THE UNIVERSITY *of* EDINBURGH

Studies of Dynamically and Statically Compressed Antimony

Amy Louise Coleman

Doctor of Philosophy
The University of Edinburgh
April 2018

Abstract

Physics at extreme conditions is not a young field; there have been decades of developments that have allowed us to generate high-pressure and high-temperature conditions in a vast array of materials. Conventionally, these extreme conditions were generated using static compression techniques; compressing a material in a diamond anvil cell which could then be heated or cooled, with structural information deduced using synchrotron radiation. These techniques are still invaluable for extreme conditions research although the pressures and temperatures that are accessible to them are limited by the strength of the diamond anvil cells and their ability to withstand extreme temperatures.

The necessity for access to pressure-temperature states that are beyond the scope of the conventional diamond anvil cell is driven by the need to characterise extreme environments such as planetary interiors. It was long believed that materials in high pressure-temperature states would exhibit relatively simple, high-symmetry crystal structures, but recent research has proven that, conversely, there is an abundance of complex structural behaviour at these extreme conditions.

One means of attaining pressure-temperature states beyond those accessible using static compression techniques is to impart a large amount of energy into a material in a comparatively short period of time (milliseconds to nanoseconds); this is known as dynamic compression. Dynamic compression can be generated using impact techniques or, alternatively, via laser ablation. Access to the most extreme conditions is commonly achieved by generating a shockwave which compresses the sample with the fastest achievable compression wave. Not only does this type of compression facilitate access to the most extreme states, it also allows us to explore the physics of impact phenomena and other such situations involving rapid energy transfer.

Dynamic compression occurs on short timescales and, as such, there is a considerable challenge in implementing diagnostics to study the behaviour of compressed materials. Furthermore, because complexity is commonplace in extreme conditions, it is vital that any diagnostics should be able to provide data of high enough quality that this complexity may be resolved. The advent of 4^{th} generation light sources (x-ray free electron lasers) has afforded us the opportunity to obtain extraordinarily high quality data on dynamic compression timescales.

In the interest of refining analytical techniques when utilising this novel technology, materials exhibiting complex crystal structures should be investigated. Antimony is an element which is known, under static compression, to transform from a Peierls-distorted rhombohedral phase ($R\bar{3}m$) to an incommensurately modulated host-guest structure ($I'4/mcm(00\gamma)000s$), a structure with an incredibly high level of complexity. The complexity of this host-guest phase, and the relatively low pressure at which it forms, makes antimony an ideal candidate for testing the resolution achievable using these 4th generation light sources. Furthermore, it is interesting to observe whether such a complex phase can form on the short timescales of dynamic compression.

In this work antimony is both statically and dynamically compressed and the results of both experiments are compared. A static phase diagram is constructed for antimony up to 31 GPa and 835 K, confirming the location of a previously theorised triple point and suggesting the location of an additional triple point. Three solid phases are characterised and data are found to agree with the pre-existing static compression studies. The nature of the host-guest phase is investigated and the guest "chains" are found to remain intact even at the highest temperatures and pressures, a result which has not previously been observed in high pressure-temperature host-guest structures.

Dynamic data from shock-compression experiments at pressures up to 59.3 GPa are plotted alongside the static data and contrasting phase behaviour is discussed. Four solid phases are identified along with one liquid phase. Observation of the host-guest phase in shock-compressed antimony confirms that highly complex crystal structures are able to form on the nanosecond timescale.

Lay Summary

The study of materials in extreme conditions, such as at high-pressures, is important in that it helps us to understand the physics of environments such as the depths of our oceans or the interiors of planets. Furthermore, it can be useful in the synthesis of novel materials, and the ability to generate high-pressure states can be used to test the structural integrity of materials in extreme conditions.

Typically, high-pressure states have been generated by compressing a material between two diamonds (in a diamond anvil cell). This cell can then be heated or cooled and data can be collected at extreme pressures and temperatures. The pressures which are accessible using these techniques are limited by both the finite strength of the diamonds and also the diamond anvil cell's ability to withstand extreme temperatures.

An alternative method of compressing a material is to generate a shockwave or a dynamic compression wave using a laser pulse; this wave propagates through the material, compressing it in a fraction of a second. Because of the speed at which this energy is imparted into the material, the pressures and temperatures generated are much higher than those achievable using a conventional diamond anvil cell.

While the rapid rate of energy transfer of a laser-generated compression pulse is ideal for creating extreme conditions, it does mean that studying the state of the compressed material is extremely difficult; it is not easy to obtain high quality data from something which occurs so rapidly. Conventionally, x-rays generated at synchrotron facilities have been used to study materials compressed in diamond anvil cells but these x-rays are not sufficiently bright to obtain data from dynamic compression experiments.

Fortunately, the last decade has seen the advent of 4^{th} generation light sources; these 'free electron lasers' are able to provide X-ray pulses that are much brighter

than those produced by a synchrotron and also have a much shorter duration, allowing accurately-timed snapshots of a dynamic compression event to be taken.

In this thesis both diamond anvil cell and laser-driven dynamic compression techniques are used to investigate antimony, an element that exhibits complex behaviour and thus makes it ideal for testing the resolution of these techniques. Comparisons are made between the results of these two very different compression techniques.

Declaration

I declare that this thesis was composed by myself, that the work contained herein is my own except where explicitly stated otherwise in the text, and that this work has not been submitted for any other degree or professional qualification except as specified.

Parts of this work have been published in [1] and chapter 3 has been submitted for publication.

[Amy Louise Coleman, April 2018]

Acknowledgements

I would like to like to express my most sincere gratitude to my supervisor, Professor Malcolm McMahon, for his continuing support and guidance throughout my PhD research. His vast knowledge of high-pressure physics, ingenuity in complex crystallographic analysis and boundless enthusiasm for the research make him a genuinely inspirational supervisor to work with, and I cannot thank him enough for such an engaging and valuable introduction to both static and dynamic compression.

Additionally, I would like to thank my second supervisor, Dr Stewart McWilliams, for countless energetic meetings and many frantic diagrams scribbled on numerous whiteboards. I believe his absolute tenacity in the face of experimental adversity has made me a better physicist, and his powerful optimism has been extremely motivational during the more difficult periods of data analysis and thesis writing.

I could not possibly write this thesis without extending my warmest thanks to Dr Richard Briggs and Dr Martin Gorman, both of whom have held positions as post-doctoral researchers during my time in the McMahon group. They have taught me how to successfully conduct high-pressure research, as well as introducing me to some real-world applications of statistics (to varying degrees of success).

I would like to extend my gratitude to my friends and colleagues in CSEC for their camaraderie and advice. In particular, Ed, Graham, Miriam, Robin, Duncan and Veronika. I am grateful to the other members of the McMahon group, Keith, Michael, Sarah and Christian, for their assistance during experimental campaigns. I must also express my gratitude to the beamline staff at DLS, the LCLS and the Jupiter laser facility at LLNL, and to thank them for their assistance with numerous successful experiments. I would especially like to thank Dr Simon Macleod of AWE for use of his pressure cells and assistance during beamtime, Dr David McGonegle of the University of Oxford for the integration of diffraction data from the LCLS and more discussions about strength than anyone expected, and Carol Davis of LLNL for several masterclasses in target fabrication.

I would like to give thanks to the talented scientists who have accompanied me from the beginning of my physics studies; Susanna, Kirsten and Lukas, I cannot thank you enough for your friendship, countless mathematical discussions and continually amusing mnemonics. I must also give special thanks to some of the

most extraordinary and ambitious women I have had the pleasure of associating with: Sarah, Evelyn, Becky, Marie and Mary-Ellen. Your faith, fortitude and confidence have been more motivational than I could ever describe.

Finally, I must thank my family, in particular, my parents: Joanne and Peter Coleman. It is impossible to encapsulate how influential they have been over the course of my studies; their encouragement and unwavering support have been completely invaluable. They are truly two of the most inspirational, impressive and good-hearted people I have had the good fortune of knowing; the entirety of this work is dedicated to them.

Contents

Abstract i

Lay Summary iii

Declaration v

Acknowledgements vi

Contents viii

List of Figures xii

List of Tables xxi

1 Introduction 1

1.1 High Energy Density Materials..... 1

1.2 A Brief History of Static Compression 2

1.3 A Brief History of Dynamic Compression..... 3

1.4 A Brief History of High Pressure Antimony..... 6

1.4.1 Static Compression of Sb..... 6

1.4.2 Dynamic Compression of Sb..... 11

1.5 Motivation for this Study..... 14

1.6 Thesis outline..... 16

1.7 The Role of the Author 17

2 Experimental Methods 18

2.1 Laser-Shock Compression 18

2.1.1 Laser Interactions with Solids 19

2.1.2 Shock Compression of Solids 23

2.1.3 Target Design 30

2.2 Static Compression 34

2.2.1 Diamond Anvil Pressure Cells 34

2.2.2 Pressure Transmitting Media 35

2.2.3 Pressure Determination 36

2.3 Crystallography and X-ray Diffraction 38

2.3.1 Periodic Crystals 38

2.3.2 Incommensurate Host-Guest Structures 41

2.3.3 Bragg's Law 43

2.3.4 Structure Factor 44

2.3.5 Powder Diffraction 46

2.4 Diagnostics 47

2.4.1 X-ray Diffraction 47

2.4.2 X-ray Diffraction Data Refinement 53

2.4.3 VISAR 54

3 Dynamic Compression of Sb at LCLS 59

3.1 Experimental Set-Up 60

3.2 The Matter in Extreme Conditions (MEC) Chamber 60
3.2.1 Drive Laser 63
3.2.2 Target Design 66
3.3 Pressure Determination 69
3.4 Dynamic Studies of Sb at the LCLS: 2015 vs. 2016 75
3.5 Results 78
3.5.1 The Sb-I and Sb-I′ Phases 80
3.5.2 The Sb-II Phase 90
3.5.3 The Sb-III phase 95
3.5.4 Liquid Sb 98
3.5.5 Unidentified Diffraction Peaks 101
3.5.6 Release Studies 104
3.5.7 Discussion 110

4 Static Compression of Sb at Diamond Light Source (DLS) 119

4.1 Compression With Pressure Transmitting Medium 119
4.1.1 Experimental Details 119
4.1.2 Experimental Results 120
4.1.3 Discussion 130
4.2 Compression Without Pressure Transmitting Medium 133
4.2.1 Experimental Details 133
4.2.2 Experimental Results 134
4.2.3 Discussion 139

5 Conclusions and Future Work 142

5.1 Conclusions 142

5.2 Future Work 144

A Distortion of Debye-Scherrer Rings (PTM data) 147

B Published Material 148

Bibliography 165

List of Figures

(1.1) The phase diagram of Sb as best understood in 1965, presented by Stishov and Tikhomirova 7

(1.2) Integrated diffraction data showing the Sb-II phase at 10.3 GPa. Upper and lower tickmarks indicate the main and modulation peaks, respectively. The insets highlight the weak modulation reflections. Figure taken from [43]. 10

(1.3) The Compressibility of Sb to 32 GPa, figure adapted from [43] . . 10

(1.4) A summary of data collected on statically-compressed Sb prior to the work conducted in this thesis [27, 39, 43]. 11

(1.5) (a) is taken from [49] and shows the dependence of the pressure of the first plastic wave (measured at the rear surface of the sample) on the thickness of the sample. (b) shows a radiograph from [50] used to identify the existance of two plastic waves in Sb. (c) is taken from [51] and shows the two waves from (b) along with wave profiles calculated from Warnes' data [49]. 13

(1.6) Sb PV data collected using dynamic compression techniques prior to this thesis. 14

(1.7) Peak brilliance vs photon energy of various light sources. 15

(2.1) A diagram showing laser ablation on the surface of a typical dynamic compression target. 19

(2.2) An illustration of the differing rise times of shock (a) and ramp (b) drive laser pulses. 21

(2.3) An example of a PT plot with a Hugoniot (from shock compression) and an isentrope (from ramp compression). The shaded region represents the area in PT space that is able to be explored using dynamic compression experiments beginning at ambient conditions. 22

(2.4) An illustration of the Rayleigh line connecting the initial state and the shocked state on the Hugoniot curve. Also shown is the propagation of a shock front through a target. 23

(2.5) A steady shock front propagating through a cylinder of cross sectional area A 25

(2.6) An illustration of the Rayleigh lines connecting the initial state and the final state on the Hugoniot curve for a multi-wave process. Also shown is the propagation of multiple shock fronts through a target. 29

(2.7) The transmission of X-rays through a 10μm thick Sb sample, plotted as a function of photon energy. The transmission of Sb foils at a photon energy of 10 keV, as used in this experiment, is $\sim$40 % 31

(2.8) A deconstructed Sb target. In practice the Sb layer is deposited directly onto the kapton and the rear LiF window is attached with a $\sim$ 1μm glue layer. 32

(2.9) Basic diamond anvil cell configuration. 34

(2.10) On the left the DAC on the stage is shown prior to insertion into the vessel. On the right hand side the vessel is shown, mounted on the I15 beamline. 35

(2.11) Pressure and volume data for various candidate pressure calibrant materials at room temperature and 800 K. 37

(2.12) Figure a) shows the possible vector choices in a two-dimensional Bravais lattice. The cell to the right is the primitive unit cell as it is the smallest possible tessellating unit within the lattice. Figure b) shows the convolution of a two-dimensional lattice and a basis. 39

(2.13) An illustration of how Miller indices are used to describe crystal planes (a) along with some examples of crystal planes within unit cells and their corresponding Miller indices (b). 41

(2.14) The incommensurately modulated host-guest structure of Sb-II in projection down the c-axis. The host atoms are shown in a lighter shade whilst the guest chains are darker. The incommensurate modulation is not visible in this image as it occurs along the c-axis. 42

(2.15) An illustration of Bragg's law. Two incoming x-ray beams are reflected from lattice planes. The path difference between the incoming and reflected beams is given by $2d_{hkl}sin\theta$ where d_{hkl} is the spacing between the crystal planes and θ is the angle between the incoming x-rays and the plane-normal. 43

(2.16) An illustration of diffraction from a crystal plane in an ideal powder sample. The large number of crystallites randomly orientated about the azimuth mean that a ring of intensity is produced by diffracted x-rays; the Debye-Scherrer ring. 46

(2.17) A schematic of a synchrotron facility with the path of the electrons shown by the black arrows. The electrons are initially accelerated in the linear accelerator before being further accelerated in the booster synchrotron. Once their energy is high enough (GeV regime) they are released into the storage ring where they may be accessed by the beamlines where the experiments are conducted. 48

(2.18) a) Quasi-monochromatic radiation from an undulator source (K=0.1) transitioning to broad band wiggler radiation (image adapted from [91]). b) Undulator radiation source. c) Wiggler radiation source. 49

(2.19) A schematic showing the formation of microbunches in an XFEL undulator. Initially electrons are not microbunched but the interaction between the transverse velocity of the bunch and the transverse magnetic field from the previous bunch causes bunching of the electrons, where the period of the bunches is equal to the period of the emitted radiation. 51

(2.20) An early method of measuring the rear surface velocity of an explosively shocked target. The metal pins detect contact with the rear surface of the target. Image taken from [49]. 54

(2.21) A schematic showing a Mach-Zehnder interferometer used in the VISAR diagonstic. The incident beam enters a beam splitter and travels through two paths of the same geometrical path length but different optical path length. An etalon may be used to control the optical path length of one of the beams. They are then recombined before leaving the interferometer. Image taken from [99] 55

(2.22) A diagram showing the basic setup for the VISAR diagnostic at the OMEGA laser facility. Image taken from [99] 56

(2.23) VISAR interference fringes for ramp (a) and shock (b) compression. Image taken from [100] 57

(2.24) VISAR interference fringes for a shock compression event from two separate interferometers. The upper, right pane shows the possible rear surface velocity profiles from channel 1 (dotted lines) and channel 2 (dashed lines). The lower right panel shows the true solution where the profiles from the two interferometers agree. Image taken from [99]. 58

(3.1) An aerial view of the LCLS. The MEC end station is located at the end of the far experimental hall [105]. 60

(3.2) Typical experimental setup at MEC. The target holder (detailed in the inset) is positioned at the centre of the vacuum chamber and the drive laser and XFEL (green and red respectively) are focused on the targets with the CSPAD detector positioned in transmission geometry. Image from [96] 61

(3.3) A CAD image showing the standard configuration of the CSPADs used at MEC in May 2016 [106]. 62

(3.4) Raw diffraction data showing the detector coverage at MEC in the 2016 experimental campaign. The signal from the CSPADs has been transformed so that the Debye-Scherrer rings appear as straight lines. 63

(3.5) A typical quasi-flat-topped drive pulse from the MEC Nd:Glass drive beam. 64

(3.6) Typical interference fringes (left) and rear surface velocity profile (right) from a shocked target at MEC. This profile corresponds to a pressure state of 12 GPa. 65

(3.7) FIB images taken using a Zeiss energy selected backscatter detector. Both the side profile (a) and flat face (b) of the Sb target are shown with the presence of columnar grains. 67

(3.8) An overlay of an ambient diffraction pattern taken from the Sb target and the calculated diffraction intensities with a fibre texture where the c-axis is parallel to the target normal. 68

(3.9) Target plates (labelled P7, P8 and P9 mounted on the target plate holder along with the calibrant targets to the right. 69

(3.10) The dashed line shows the EOS calculated using a single U_S-u_p relation and the solid line shows the three-part EOS. The data points from Warnes [49] and McQueen and Marsh [48] are shown as triangles, squares and circles on the plot. 70

(3.11) On the left a distance vs time plot shows the propagation of waves at the Sb/LiF interface. On the right, the principal Hugoniot curves of Sb and LiF are expressed in terms of P and u_p, along with the reflected Sb Hugoniot. 72

(3.12) Diffraction data from the 2015 experimental campaign at the LCLS. Tickmarks show ambient Sb-I peaks and the $(1\bar{1}2)$ peak of the compressed Sb-I phase is indicated in grey. 76

(3.13) Interference fringes collected using the VISAR diagnostic for an Sb target in the 2015 experimental campaign at the LCLS. The shock breakout is not planar, and reflectivity is lost in many areas after shock breakout, greatly complicating the analysis. 77

(3.14) Integrated diffraction profiles from shock-compressed Sb along with tick marks showing the calculated peak positions for the structures at the relevant pressures. The diffraction profiles are from (i) ambient Sb-I, (ii) compressed Sb-I, (iii) Sb-I′, (iv) Sb-II, (v) Sb-III, (vi) Sb-III and liquid and (v) liquid. 79

(3.15) The R$\bar{3}$m structure of ambient Sb shown in two different orientations. The right hand view (not to scale with the left) shows the structure viewed along the c axis. 80

(3.16) Observed and calculated diffraction peaks from a Le Bail fit of Sb at ambient conditions. Peak positions are indicated by the tick marks below the integrated pattern. 81

(3.17) The rhombohedral structure of the Sb-I phase is shown on the left, along with a simple cubic structure on the right. The added bonds illustrate a distorted cube within the rhombohedral structure and a corresponding undistorted cube in the simple cubic structure. . 82

(3.18) c/a ratio vs pressure plot for the Sb-I phase on-Hugoniot. Data from previous room-temperature work by Schiferl [112] and Degtrareva [43] are also shown. 83

(3.19) Profile (a) shows ambient Sb-I peak positions in black and Sb-I at 1.9(3) GPa in red. In profile (b), the compressed (101) and (1$\bar{1}$2) peaks are still visible but it is difficult to distinguish the compressed (104), (2$\bar{1}$0) and ambient (20) peaks. In profile (c) the simple cubic peaks are labelled in blue. 84

(3.20) A 2D square lattice is shown in three different orientations (rotated 15° in each direction from the central position). The two candidate structures for the Sb-I′ phase are shown; the rhombohedral structure is compressed uniaxially (by 30% in this figure) before being rotated, and the simple cubic structure with strength is rotated and then compressed (also by 30%). The subtle difference between the two structural candidates is indicated. . . . 85

(3.21) The two competing structures of Sb-I′ are shown by dashed lines. On the left a simulation of the rhombohedral structure is shown by a white dashed line and on the right the strained simple-cubic structure is shown over the same raw diffraction pattern, collected at 7.9(6) GPa. 86

(3.22) The same integrated diffraction profile of Sb at 7.9 GPa is shown with fits to both of the candidate Sb-I′ phases; the upper plot shows a simple cubic structure fitted to the profile (not accounting for strength) while the lower plot shows a rhombohedral structure fitted to the profile. 87

(3.23) Rear surface velocity profiles from the VISAR diagnostic for the Sb-I, Sb-II and Sb-III phases 6.6, 11.7 and 14.6 GPa respectively. Wave splitting is evident in the Sb-II profile. The second increase in velocity in the Sb-III profile occurs due to re-shock within target. 90

(3.24) Observed and calculated diffraction peaks from a Le Bail fit of Sb-II at 11.8 GPa. Peak positions are indicated by the tick marks below the integrated pattern with a, b and c showing the Sb-I′ phase (fitted with a simple cubic structure), the ambient Sb-I phase and the Sb-II phase, respectively. 92

(3.25) The on-Hugoniot data collected in this experiment alongside the stability regions of Sb-I and Sb-II reported by Degtyareva [43] (shown by lines at room temperature), the Sb-I→Sb-II transition point reported by Schiferl [35] (marked by a star) and the melt data reported by Klement [27]. 93

(3.26) The integrated and raw diffraction pattern showing ambient Sb-I peaks and compressed Sb-II at 11.8 GPa. The four arrows indicate the (2200), (1001), (2110) and (3100) Sb-II peaks (in order of increasing 2θ). 94

(3.27) The $Im\bar{3}m$ structure of Sb-III. 95

(3.28) Observed and calculated diffraction peaks from a Le Bail refinement of Sb-III at 18.9 GPa. Peak positions are indicated by the tick marks below the integrated pattern with a and b showing the ambient Sb-I phase and the Sb-III phase, respectively. 96

(3.29) Texture is present in the Sb-III phase as shown by the textured bcc Debye-Scherrer rings indicated with arrows in the raw data, with corresponding integrated peaks marked by a star. 97

(3.30) A waterfall plot showing the onset of the liquid phase. The (101) bcc peak is indicated on the plot. 98

(3.31) Diffraction profiles showing the onset of melting. a) shows uncompressed Sb-I along with Sb-III diffraction peaks at 24.6 GPa, b) shows uncompressed Sb-I along with Sb-III at 37.6 GPa and broad liquid features and c) shows that most of the Sb-I and Sb-III signal has been masked by the broad liquid signal at 57.2 GPa (pressures determined using the VISAR diagnostic as these data were collected from LiF window targets). 100

(3.32) A waterfall plot showing the unidentified peaks present in the Sb-I′ diffraction data. The arrows indicate an unindexed peak and the grey shaded region highlights the ambient (104) peak which is broadened, possibly due to an unexplained overlapping peak. . . 101

(3.33) A waterfall plot showing the unidentified peaks present in the Sb-I′, Sb-II and Sb-III diffraction data. 102

(3.34) A Rietveld refinement of diffraction data collected 5.5 ns on release following shock compression to 17 GPa. Sb-I, Sb-I′ and Sb-II phase markers are labelled a, b and c, respectively. The grey shaded regions represent data excluded from the fit. 105

(3.35) The $P - u_p$ relations for Zr, Sb, Nd and LiF. Plotted using data from the shockwave database. 106

(3.36) A distance vs time plot generated using the output from the HYADES code. The shock breakout and diffraction data collection time are indicated on the graph. 107

(3.37) Diffraction data collected 5.5 ns on release from a peak pressure of 19 GPa. The smooth nature of the Sb-I Debye-Scherrer rings shows loss of texture upon recrystallisation. 108

(3.38) A waterfall plot showing data collected on release from targets without a LiF window. The peak pressure state of each of these shots was ∼17 GPa. 108

(3.39) Integrated diffraction profiles from shock-compressed Sb along with tick marks showing the calculated peak positions for the structures at the relevant pressures. The diffraction profiles are from (i) ambient Sb-I, (ii) compressed Sb-I, (iii) Sb-I′, (iv) Sb-II and (v) Sb-III. The broad feature which appears around 30° in profiles (vi) and (vii) marks the onset of liquid diffraction. 111

(3.40) The volumetric compression of Sb obtained at the LCLS. Hugoniot EOS data obtained from this study are shown using filled black symbols, and points obtained using a LiF backing window in this study are shown using filled grey symbols. The grey shaded lines shows the isothermal compressibility data at 300 K for the Sb-I, Sb-II and Sb-III phases [43]. Unfilled circles show data obtained from previous dynamic compression studies using velocimetry measurements [48, 49] 114

(3.41) The known components of the Sb phase diagram after obtaining on-Hugoniot data at the LCLS. Melt curve (to ∼9 GPa) from [27], room temperature data from [43]. 117

(4.1) The structures of the Sb-I, Sb-II and Sb-III phases. 120

(4.2) Integrated diffraction patterns showing three distinct phases of Sb observed under static-compression: the rhombohedral A7 phase (Sb-I), the incommensurate host-guest phase (Sb-II) and the bcc phase (Sb-III), all collected at ∼475 K. 121

(4.3) The c/a ratio versus pressure for the Sb-I phase, as obtained at a series of different temperatures at Diamond Light Source (DLS) along with on-Hugoniot data obtained at LCLS (as described in the previous chapter). Data from previous room-temperature work by Schiferl [112] and Degtrareva [43] are shown for comparison. . 123

(4.4) Tickmarks show the position of peaks fitted to an integrated diffraction pattern from the Sb-II phase at 19.1 GPa and 770 K. Even at high temperatures the (1001) and (2101) guest peaks are still clearly visible. 124

(4.5) Raw diffraction images and integrated profiles showing the Sb-II phase at a) 19.4 GPa and 475 K, and b) 6.2 and 720 K. The weak modulation peaks that arise from interactions between the host and guest substructures are visible in both profiles and the recrystallisation of the sample is evident in the 2D images. 125

(4.6) A plot showing the ratio of host to guest peak c lattice parameters of the Sb-II phase versus pressure across several isotherms. 126

(4.7) The variation in 2 theta around the azimuth of the two strongest peaks of the Sb-II phase: the (3100) peak between 9.7 and 9.8 degrees 2θ and the (2110) peak around 9.4 degrees 2θ. 126

(4.8) The static phase diagram of Sb to 31 GPa and 835 K. The Sb-I, Sb-II, Sb-III and liquid phases are shown along with the Sb-I → Sb-II room temperature transition point as reported by Degtyareva and Schiferl [43, 112]. 128

(4.9) The compressibility of Sb to 31 GPa at room temperature. Analysis of Sb-II data using the composite and IM models are shown in comparison to the density measurements made by Bridgman in 1941 [28]. 130

(4.10) The Sb phase diagram with phase boundaries as determined from the static compression experiments. Downward pointing triangles, circles, squares, upward pointing triangles and diamonds show Sb-I, Sb-I', Sb-II, Sb-III and Sb-III & Liquid data points obtained from the dynamic compression experiments. Black and grey filled data points show data collected without and with a rear LiF window, respectively. 131

(4.11) Pressure vs V/V_0 for Sb-I data collected using no PTM analysed at the maximum and minimum possible temperatures. Also shown are data sets collected using a PTM at constant temperatures. . . 135

(4.12) An integrated diffraction pattern showing Sb I under static compression and raw Sb I diffraction profiles highlighting the presence of the Cu_2Sb peak 136

(4.13) Raw Sb I diffraction profiles highlighting the presence of the Cu_2Sb peak 137

(4.14) Raw x-ray powder diffraction data from three consecutive data points along an isotherm, immediately prior to the Sb-I to Sb-II transition. The images illustrate recrystallisation of the Cu_2Sb which is present in the sample. 138

(4.15) Warped plot of Sb-I x-ray powder diffraction under static compression without a PTM. 138

(4.16) d spacings of Sb, W and Ta peaks at 300 K and 650 K. 141

(A.1)Figure showing distortion of the Debye Scherrer rings in the Sb-II phase at 300 K, 475 K and 650 K. 147

List of Tables

(2.1) The 7 crystal systems and corresponding unit cell restrictions and allowed centring. The centring options shown in brackets indicate choices that could also be expressed as alternative centring with a different choice of axes. 40

(3.1) Pressure calculations using only VISAR data (P_{VISAR}) and combined VISAR/x-ray diffraction data ($P_{combined}$) for each of the Sb phases observed on dynamic compression. The best and worst agreement between the methods (highest and lowest ΔP) is shown for each phase, with the exception of Sb-II where the variation in ΔP across the collected data was negligible. 74

(4.1) Volume, pressure and lattice parameters of Sb-I immediately prior to transition to Sb-II. Data collected using static compression techniques. 139

Chapter 1

Introduction

1.1 High Energy Density Materials

Prior to the invention of the deep sea submarine in the late 1800s, and the first successful space voyage in 1961, the human experience was largely limited to the surface of the Earth, an environment which exhibits a relatively limited range of pressure-temperature conditions. While this domain is convenient for human habitation, it is not entirely representative of the vast expanse of matter in the surrounding universe. From the crushing pressure in the depths of our oceans to the blistering cores of both our own planet and the millions of other celestial bodies, the physics that we experience in our daily lives is not quite the same as the physics that governs these extreme pressure-temperature environments. The alteration of atomic bonds and the changes in kinetic energy of atoms due to high pressure and temperature states, can lead to material behaviours that are markedly different to those seen at ambient conditions such as changes in melting temperatures [2], insulator to metal transitions [3], chemical changes [4] and changes in refractive index [5].

The field of high energy density (or, equivalently, high pressure) materials is of interest not just in the sense that it provides a framework for understanding the universe around us; it also has practical, material applications, especially in the synthesis of novel materials [6]. The vast advancement of technology over the past century has facilitated unprecedented opportunities to explore high-pressure, high-temperature states through both static and dynamic compression

techniques; the former involving compression over seconds, minutes, hours or even days and the latter involving a more rapid transfer of energy on timescales of milli to femto seconds. As well as improvements in compression techniques, the development of diagnostic tools has played a vital role in the progression of the field, meaning that once we have achieved these extreme conditions, we can begin to understand the physics that governs such high-pressure systems. It is these technological advancements which have enabled the work in this thesis to be conducted.

1.2 A Brief History of Static Compression

In 1900 Percy Bridgman enrolled at Harvard University to study physics [7]. Some five years later he began his work in the field of high pressure, utilising the crude techniques of the time which typically involved compressing materials using steel cylinders and reaching pressures of less than 1 GPa (10,000 bars). Bridgman revolutionised the field by implementing a new compression technique which involved compression between two tapered, tungsten-carbide anvils and enabled much higher pressure regimes to be accessed without mechanical failure of the system. In 1946 Bridgman was awarded the Nobel Prize in Physics for his pioneering work on the physics of high pressures [8].

The compression technique devised by Bridgman allowed pressure states of up to 10 GPa to be routinely accessed, but in the scheme of extreme compression physics, this pressure is still relatively low. The successor of Bridgman's compression cell made use of anvils made from diamond which not only enabled higher pressure states to be achieved, but also enabled the use of optical spectroscopic techniques as a means of characterising the compressed materials due to the optically transparent nature of the diamonds [9, 10].

Subsequent developments of the diamond anvil cell (DAC) included the addition of a gasket material which confines the compressed sample between the two diamonds, and the development of pressure gauge materials which, when included in the sample chamber, provide a way to reliably diagnose the pressure state that has been achieved (discussed in section 2.2). In more recent years much more ambitious modifications to the conventional DAC have been made such as the inclusion of resistive heating or cryogenic cooling capabilities so that high pressure states can be explored at various different temperatures. Presently, techniques

using double stage DACs have been utilised to access pressures in excess of 1000 GPa [11].

1.3 A Brief History of Dynamic Compression

Compression by means of a shockwave is not a novel concept; theoretical considerations of discontinuities in fluid flows were published in the late 19th century by William Rankine and Pierre Henri Hugoniot [12, 13]. It is this work that forms the basis of much of our present understanding of dynamic compression; the work instigated by these two men led to the formation of the Rankine-Hugoniot Equations (see section 2.1.2) which are used to this day to describe the nature of shock-compressed materials.

It is perhaps unsurprising that experimental dynamic compression finds its origins in a military environment, specifically, during the second world war [14, 15]. Some of the earliest research papers on the physics of shock waves in condensed matter concerned the propagation of shock waves in water and were published in the 1940s by Navy scientists [16]. After WWII, the ensuing Cold War generated a high level of interest in the study of ballistics and, as a consequence, the invention of the two-stage light-gas gun in 1948, a device widely used in shock physics experiments [17]. The development of aircraft and ballistic missiles demanded study of supersonic flow, something which has also contributed to today's understanding of shock wave environments [14].

In 1956, physicists Bancroft, Petersen and Minshall published a paper in which they claimed to have observed a polymorphic phase transition in iron at 13 GPa (130 kbars) using shock compression techniques [18]. The results of the experiment disagreed with those obtained by the static compression techniques of Nobel Prize winner Percy Bridgman. Bridgman observed the phase transition to occur at a higher pressure and did not believe that there was enough time in a dynamic compression experiment for the phase transition to occur [19]. In later work, Bridgman realised that the pressure scale he was using was inaccurate and that by using increased force and adding shear stresses to the iron sample, the phase transition occurred in a much shorter time [16]. This led Bridgman to conclude that the dynamic compression results of Bancroft *et al.* were accurate.

Following the conception and physical realisation of the laser in the 1950s,

physicists Askaryon and Morez demonstrated, in 1963, that shock pulses could be created in metals using this new technology [20]. The compression waves in their work were generated through laser-induced vaporisation at the surface of the material. This technique was further developed by Anderholm who introduced a laser-transparent overlay to create a 'confined surface', allowing higher pressures to be achieved within the material [21]. In the following years, the choice of overlay material, including optically-opaque materials, and the ability to combine layers of overlay materials, was investigated in the work of O'Keefe and Yang [22, 23]. The idea to use various different materials as an overlay has been key in reaching high pressures in dynamically compressed materials, laying the foundations for modern impedance matching techniques which are used to pick an overlay or 'ablator' which will allow the desired pressures to be achieved, as described in this thesis in section 2.1.3.

The first in-situ, x-ray diffraction experiment on a shock-compressed sample was conducted in 1972 by physicists Johnson and Mitchell [24]. This seminal work reported a phase transition in boron nitride, observed using flash x-ray diffraction techniques and, for the first time, showed conclusively that the shockwave process is not characterised by "chaos" on the atomic level. The ability to characterise structural transformations on the short timescales of shock compression was the first step towards more thorough comparison between the behaviour of materials under dynamic and static compression. It took many years to develop x-ray diffraction techniques until they were able to be used as a standard diagnostic in dynamic compression experiments; indeed, it was not until 2005 that the $\alpha \rightarrow \epsilon$ transition in iron was unambiguously characterised in a shock-compression experiment [25]. This important work showed that the phase transition observed by Bancroft in 1956, was the same structural transition observed by Bridgman in his static experiments. The use of x-ray diffraction as a diagnostic in dynamic experiments marked a considerable development in the field, as crystal structures could be investigated directly without having to infer structural information from static experiments.

Presently, the task of refining methods of dynamic compression continues; recent work has exemplified the ability to compress diamond to 5 TPa (50 Mbars) with the use of ramp-compression techniques [26]. As well as refining compression techniques and target design, much effort has been put into improving diagnostics for use in dynamic compression experiments. In order to fully resolve the structure of a material, diffraction data are necessary and historically these have not

been accessible to dynamic compression experiments due to the short timescales over which they occur: in order to collect analysable data from phenomena occurring on such a short timescale, an extremely brilliant x-ray source is required. Early dynamic compression experiments made use of interferometry techniques to measure wave-profiles and infer information about structural phase transitions in elements based upon structures which were resolved using static compression techniques [18]. Even in the early dynamic compression work, it was recognised that materials may not behave the same way under rapid pressure loading as they do in a static compression environment and that "only x-ray or neutron diffraction *at pressure* can definitely establish the structure of a given high-pressure polymorph" - W. Klement, 1963 [27].

Over the last decade there have been great advancements in x-ray diffraction capabilities with the advent of free electron lasers (FELs), known as 4th generation light sources. Facilities that house these state-of-the-art x-ray systems are able to offer femtosecond x-ray pulses, the brilliance of which is such that phenomena occurring on the nanosecond timescales of dynamic compression are able to be observed. One such facility is the Linac Coherent Light Source (LCLS) at the SLAC National Accelerator Laboratory, and it it this facility which has hosted the dynamic experiments reported in this thesis. The basic operating principle of these 4th generation light sources is discussed in section 2.4.1.

The actualisation of ultra-bright, ultra-fast light sources has opened up a whole new era of investigation into the structural behaviour of materials at extreme pressures and temperatures and it is presently the work of the scientific community to refine experimental techniques in order to obtain data of optimal quality. The work described in this thesis focuses on an element that is known, upon static compression, to exhibit a series of interesting and complex structural transitions. One of the aims of this work is to probe the nature of such complex transitions and to explore the rapidity of formation of extremely intricate structures. The quality of data needed to fully resolve such complex structures is remarkably high and so this work aims to showcase the capability of 4th generation light sources to provide data which is of comparable quality to that which may be attained at a synchrotron. Furthermore, this thesis will compare data obtained using both dynamic and static techniques in the interest of exploring the consequences of rapid pressure loading.

1.4 A Brief History of High Pressure Antimony

1.4.1 Static Compression of Sb

This thesis focuses on compression experiments on the group-15 element, Sb. High-pressure studies of Sb date back to the early work of Bridgman in 1941 using static techniques. This showed little more than a similarity to Bi (also a group-15 element) in terms of a phase transition with a similar volume change ($\sim 4\%$) but occurring around 8.5 GPa, a notably higher pressure than the same transition seen at 2.5 GPa in Bi [28, 29].

It was not until the 1960s that the next static compression work involving Sb was published. In 1963, Klement *et al.* used piston cylinder compression to map out the melt curve of Sb to just below 7 GPa, with a triple point reported at 5.7 GPa and ∼840 K [27]. Results were measured using differential thermal analysis, meaning that still no structural analysis had been conducted on Sb.

This changed in 1965 when the first x-ray diffraction studies on room-temperature, statically-compressed Sb were conducted by Vereshchagin and Kabalkina [30]. This paper reported two reversible phase transitions, the first of which was reported to occur around 7 GPa and the second around 8.59 GPa. The ambient structure of Sb is rhombohedral A7, this is known as the Sb-I phase. In this study the authors found that the cell angle α in this A7 structure increased with increasing pressure, leading to a second-order phase transition from Sb-I to a primitive cubic structure. The second phase transition, at 8.59 GPa, was diagnosed as a primitive cubic to hexagonal-close-packed (HCP) transition.

Following this publication, a new melt-curve study was conducted by Stishov and Tikhomirova [31]; the motivation for which was the discovery of the 7 GPa room temperature transition. They believed that there may be an additional triple point in the melt curve which lined up with this initial phase transition the way that the transition at 8.5 GPa appeared to share a phase boundary with the triple point at 5.7 GPa reported by Klement. The work of Stishov and Tikhomirova largely agreed with the work of Vereshchagin and Kabalkina, except that they believed the first phase transition to be first-order, with a finite volume change. Furthermore, they reported a triple point at 0.39 GPa and ∼900 K. The best understanding of the phase diagram of Sb at this point in time is shown in figure 1.1.

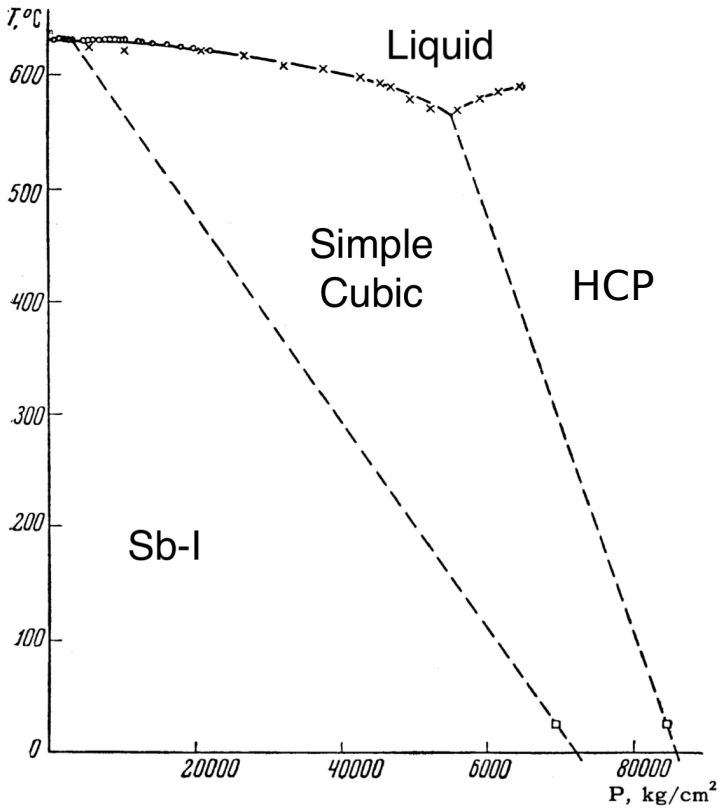

Figure 1.1 *The phase diagram of Sb as best understood in 1965, figure adapted from Stishov and Tikhomirova [31]. The phase labels have been adapted for clarity.*

In 1969 a paper was published by Kolobyanina *et al.* which used x-ray diffraction measurements to confirm that the transition from the rhombohedral phase of Sb to the simple cubic phase is in fact first-order in nature [32]. This paper also disagrees with this diagnosis of the HCP phase, stating that there are "superfluous" reflections that are observed in the diffraction pattern. Following this paper, Kabalkina, Kolobyanina and Vereshchagin published work the following year which attempted to better characterise the phase which was formerly known as HCP Sb [33]. Based on their x-ray diffraction results they re-diagnosed the HCP structure as a monoclinically distorted SnS structure. This was contradicted by a publication the following year, 1971, which characterised the structure as being tetragonal in nature [34]. Neither the monoclinically-distorted SnS structure proposed by Kabalkina, nor the tetragonal structure proposed by Duggin, showed particularly good agreement between the observed and calculated d-values.

A decade later, in 1981, Schiferl *et al.* published work which described single-

crystal structure determinations performed on Sb using x-ray diffraction as a diagnostic [35]. In this study, the simple cubic phase was not observed at all and instead the A7 structure of the Sb-I phase was found to only approach the simple cubic structure upon pressure increase until a transition to an "unknown" structure at 8.6 GPa. Schiferl theorised that the transition to the simple cubic structure was not observed because of the use of single crystal samples compressed hydrostatically in a diamond anvil cell with ethanol used as the pressure transmitting medium. The previous studies by Vereshchagin, Kolobyanina and Kabalkina had used amorphous boron as a pressure vessel to subject the Sb samples to quasi-hydrostatic pressures (methods described in [36]) and Kabalkina and Kolobyanina had reported the Sb-I to simple cubic transition to be sluggish (as reported in a private communication cited in [35]) with a full transition to the simple cubic structure occurring in only 20% of cases. It is suggested that the transition to the simple cubic structure is very sensitive to shear stresses and that the hydrostatic nature of the compression in the work by Schiferl would prevent the structure from forming. This is corroborated by a study published in 1984 by Khvostantsev and Sidorov in which melting and solid-solid phase transitions in Sb were explored using hydrostatic compression [37]. This work also does not see any evidence of a compete transition to the simple cubic phase, indicating that it is only observed under non or quasi-hydrostatic conditions. An additional consideration is that the earlier work, as well as using quasi-hydrostatic compression methods, also used unfiltered Mo radiation in the process of obtaining their x-ray diffraction patterns which may have negatively impacted the quality of their data.

In 1983 a paper published by Aoki *et al.* reported the first observation of a phase transition to the bcc structure in Sb, occurring at 28 GPa [38]. The phase was found to persist to at least 43 GPa. This paper used a diamond anvil cell for compression and water as a pressure transmitting medium. The appearance of the bcc phase in Sb was not unexpected as it had been observed previously in Bi and the two elements are isostructural at ambient conditions.

In 1986 the first heated static-compression study of Sb utilising x-ray diffraction was published by Iwasaki and Kikegawa [39]. Diamond anvil cells were used to compress the sample hydrostatically and sodium chloride powder was used as a pressure transmitting medium. The simple cubic phase was not observed and the paper identifies the subsequent phase as a heavily distorted face centred tetragonal structure. Indexing the observed diffraction lines in terms

of a monoclinic unit cell (approximately twice the volume of that assigned by Kabalkina *et al.*) gave improved agreement between the observed and calculated d values. The data agreed with a phase boundary which forms a straight line between the phase transition repeatedly reported at 8.6 GPa at room temperature and the triple point at 5.7 GPa and ∼840 K reported by Klement. Further work was conducted by Iwasaki and Kikegawa in 1990 in an attempt to better characterise this mystery phase which has previously been identified as hcp, monoclinically distorted SnS structure, and a tetragonal structure [40]. This work used shorter wavelength radiation to obtain more x-ray diffraction peaks to aid in the solution of the structure. This paper described the phase as a distorted body centred tetragonal structure with each atom surrounded by 8 nearest neighbours and 10 atoms per unit cell.

In 2000, ten years later, the debate over the structure of this mystery phase was finally brought to an end. Improvements in experimental technique and equipment allowed significantly higher quality x-ray diffraction data to be obtained and McMahon *et al.* were able to index the structure as a body centred tetragonal (bct) "host" and a bct "guest" [41]. This incommensurate host-guest structure was first solved for the Bi-III phase and subsequently found to be isostructural with this mystery Sb phase, now known as Sb-II. This result was verified by the work of Schwarz in 2003 [42].

The high quality of x-ray diffraction data attainable using modern techniques facilitated the discovery of an additional solid phase of Sb: Sb-IV. This phase was successfully indexed by Degtyareva *et al.* in 2004 as an incommensurate composite phase with a monoclinic host-guest structure [44]. The phase was found to exist over a small pressure region (8.2 to 9 GPa on pressure increase) at room temeprature, forming between the Sb-I and Sb-II phases. The ability to thoroughly characterise such a phase is a perfect demonstration of the marked improvements in the field; the modulation peaks in diffraction patterns from incommensurately modulated host-guest structures are significantly less intense than the host and guest atom peaks as they arise due to interactions between the atoms [43, 45]. The subtlety of the modulation peaks is illustrated in figure 1.2; that these peaks can be detected and indexed is an impressive feat.

Figure 1.3 shows the compressibility of Sb as determined in the more recent work by Degtyareva [43] and the early work by Bridgman [29]. In the work carried out by Bridgman, the crystal structures of the Sb phases were not diagnosed; the compressibility data is plotted from measurements of pressure and absolute

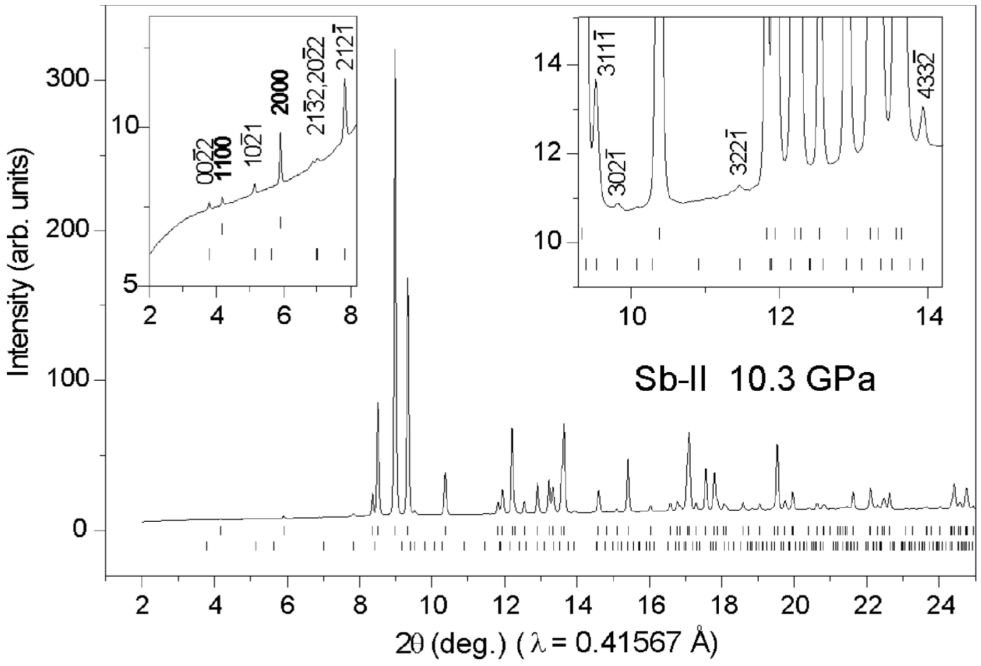

Figure 1.2 *Integrated diffraction data showing the Sb-II phase at 10.3 GPa. Upper and lower tickmarks indicate the main and modulation peaks, respectively. The insets highlight the weak modulation reflections. Figure taken from [43].*

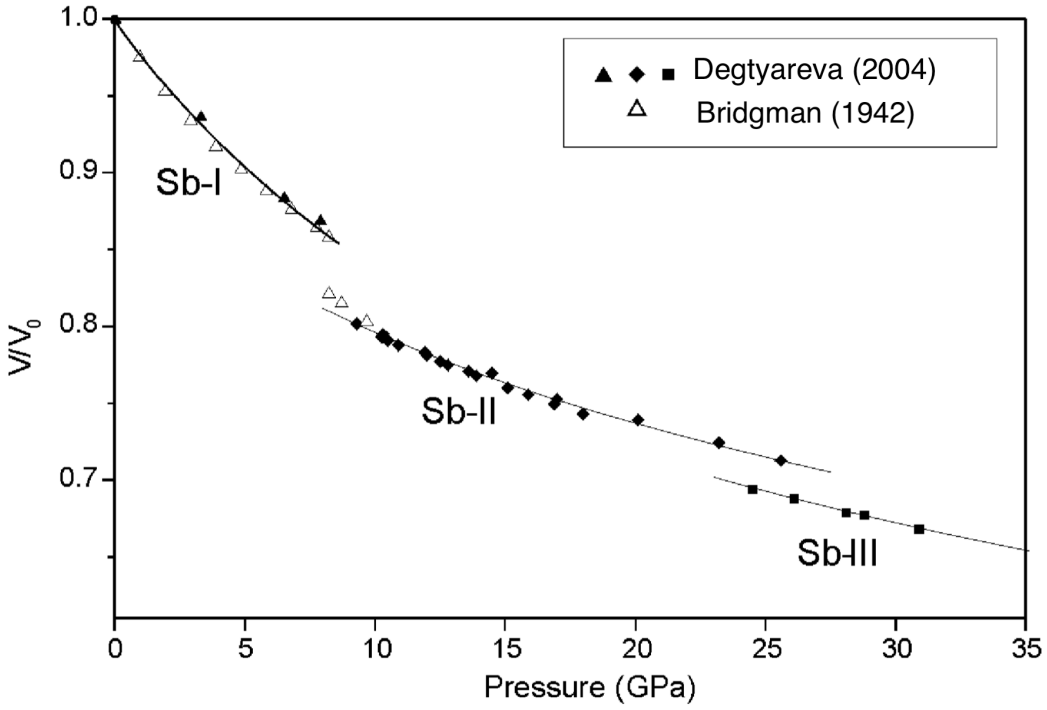

Figure 1.3 *The compressibility of Sb to 32 GPa, figure adapted from [43]*

volume. These density measurements agree well, but it is the conversation about the *structures* of the phases of Sb that has drastically changed since the beginning of high pressure Sb research. Figure 1.4 summarises the most recent pressure-temperature information on the various structures of statically-compressed Sb that was available prior to the work in this thesis. The evolution of our understanding of the nature of Sb under compression is an archetypical example of the need for progression of not only compression techniques to generate uniform compression but also of diagnostics so that complex phenomena may be accurately characterised.

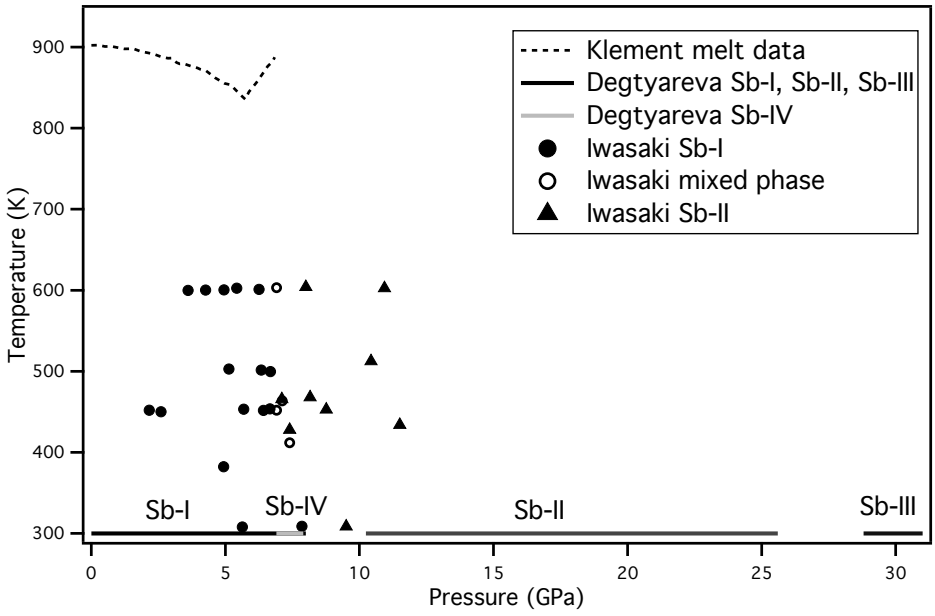

Figure 1.4 *A summary of data collected on statically-compressed Sb prior to the work conducted in this thesis [27, 39, 43].*

1.4.2 Dynamic Compression of Sb

The first work on high pressure Sb which utilised dynamic compression methods was published in 1957 and appears in a paper on the dynamic compression of Bi [46]. This early work used a block of baratol to initiate an explosive impact, generating compression through the propagation of a shockwave in the sample. The velocity of the rear surface of the shocked material is measured, and from this velocity measurement a pressure is calculated using conservation equations (this method is discussed in section 2.4.3). In this paper, one line is devoted to Sb and states that a striking increase in transition pressure is observed as the

sample thickness is reduced.

Similarly, in a paper published in 1959 on shock compression of Al, there is a small paragraph dedicated to preliminary Sb measurements which states that a transition is observed at 9.5 GPa in contrast to Bridgman's static work which indicated a transition pressure of 8.4 GPa [47]. This paper also indicated a multiple wave structure in Sb (see section 2.1.2).

In 1960, a paper published by McQueen and Marsh reported equation of state information on nineteen elements that had been dynamically compressed by means of using explosive systems to accelerate thin metal plates [48]. This work reports Sb data more thoroughly than the previous two dynamic compression papers, but acknowledges that the results are less extensive than for other elements due to issues arising from the phase transitions that occur within the material and subsequent multi-wave structures. This paper is the first to offer a PV Hugoniot (a locus of PV states accessible via shock compression, detailed in section 2.1.2) for Sb and shows a dip in the PV curve corresponding to a mixed phase region. The paper does not offer structural data and all results reported are based on velocimetry measurements.

Work on dynamically compressed Sb was continued in 1967 when Warnes published a paper which investigated a shock-induced phase transition in Sb, again by measuring the velocity of the rear surface of the compressed sample [49]. This paper detailed a dependence of the pressure of the first compression wave in the multi-wave region on the thickness of the sample of the Sb being compressed; the thicker the sample the lower the pressure of the first plastic wave, as recorded at the rear surface of the material. The transition pressure was found to decrease with sample thickness to 20 mm, before decreasing more slowly up to 50 mm, as shown in figure 1.5 (a).

In contrast to the first plastic compression wave, Warnes found the pressure of the second plastic wave to be independent of the sample thickness up to 20 mm, after which it decreased linearly with thickness. Significant effort was made in this work to understand and characterise the multi-wave compression in the Sb sample. Warnes theorised that the initial plastic wave induced a metastable state in the Sb which was followed by a relaxation into a higher-density phase. He theorised that this relaxation would cause rarefaction waves to propagate in all directions, attenuating the pressure of the first plastic wave and impeding the progress of the second plastic wave; once the metastable material behind the first

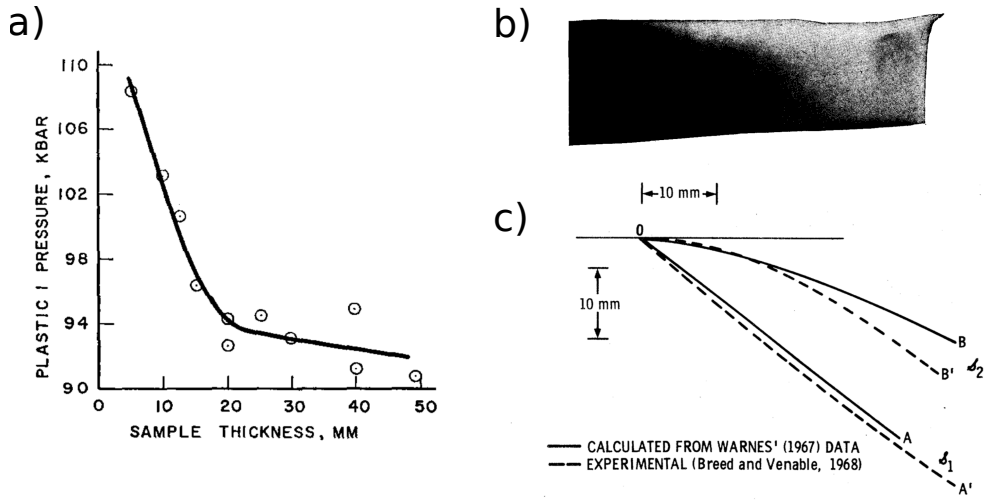

Figure 1.5 *(a) is taken from [49] and shows the dependence of the pressure of the first plastic wave (measured at the rear surface of the sample) on the thickness of the sample. (b) shows a radiograph from [50] used to identify the existance of two plastic waves in Sb. (c) is taken from [51] and shows the two waves from (b) along with wave profiles calculated from Warnes' data [49].*

plastic wave had settled to an on-Hugoniot state, the second plastic wave could progress through that material at its characteristic velocity. This interpretation stated that there was a 0.6 μs delay in the formation of the second plastic wave based on x-ray radiographs that were later published by Breed and Venable [50]. These results indicated a relaxation time (time taken to relax from a metastable state to an on-Hugoniot state) of 3 μs in samples thinner than 20 mm [51].

The continuation of this work by Breed and Venable was published in 1968 with the use of flash radiographs to illustrate the formation of the separate compression waves [50], as shown in figure 1.5 (b), and (c). They concluded that the initial compression wave decelerates as it progresses through the sample while the second compression wave accelerates to some higher final velocity; this is taken to mean that the phase transition does not occur at a constant rate. Interestingly, in Bi (an element with similar reconstructive phase transitions to antimony) the transition pressure was not found to vary with sample thickness [52]. Breed and Venable state that the transition between Sb-I and Sb-II occurs on a timescale on the order of 2 - 3 μs, which is surprisingly long in comparison to the nanosecond timescale that such a transition was estimated to occur on in Bi [52] and an order of magnitude larger than relaxation times observed in iron [53].

Prior to the work in this thesis, the understanding of dynamically compressed

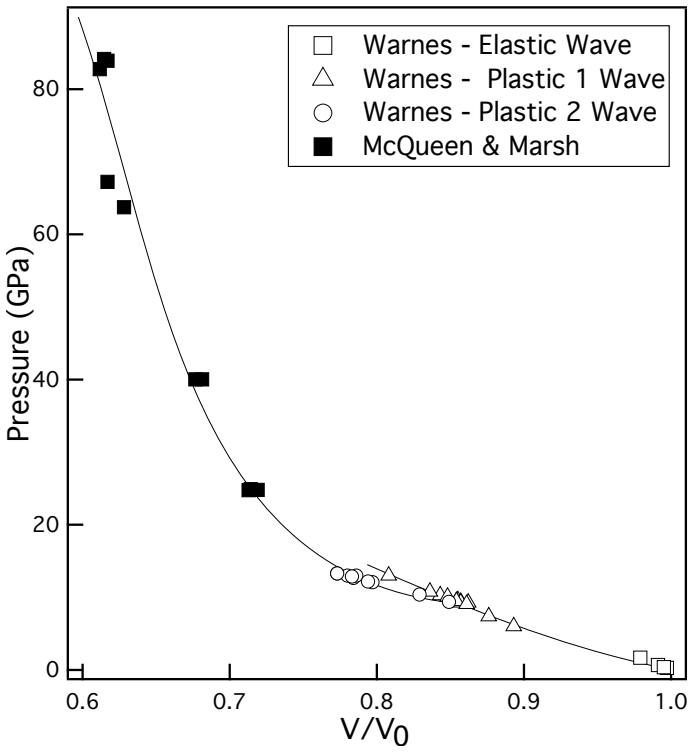

Figure 1.6 *Compression data for Sb using explosively generated shock waves [48, 49].*

Sb was as such: it was believed that there is a shallow region in the Hugoniot where the compression wave splits into a multi-wave structure and that a phase transition following explosively-generated shock-compression occurs on a microsecond timescale. A plot summarising the pressure-volume relationship, as it was understood prior to this work, is shown in figure 1.6. No x-ray diffraction experiments have so far been conducted on Sb under dynamic compression and all structural information has been inferred from static compression studies.

1.5 Motivation for this Study

One of the main obstacles in the field of dynamic compression has, for many years, been the inability to obtain high-quality diffraction data on the incredibly short timescales of such experiments. State-of-the-art light sources such as LCLS and the upcoming European XFEL (as shown in figure 1.7), offer peak brilliances which are around 8 orders of magnitude higher than those provided by the best synchrotrons. This means that these new facilities provide the ability to obtain diffraction data not only on incredibly short timescales but also of very high

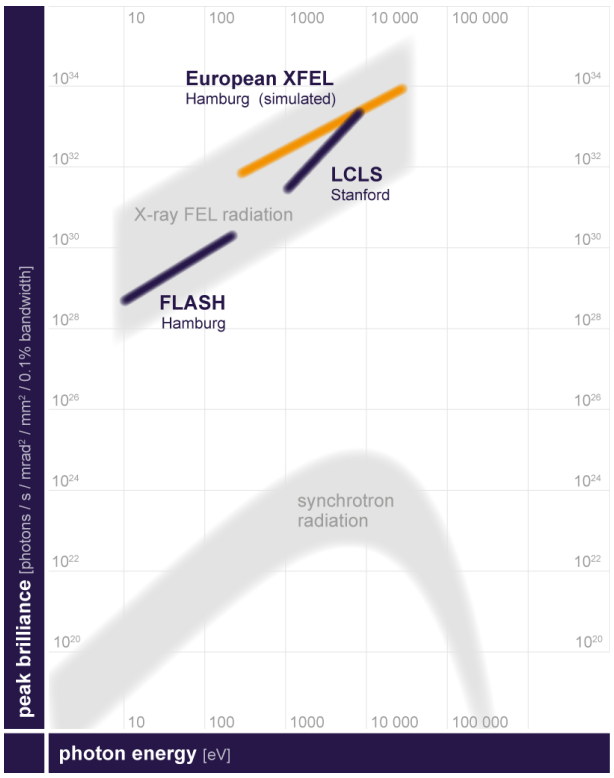

Figure 1.7 *The peak brilliance and photon energy of various light sources is shown. As shown in this plot there is a marked increase in brilliance in the 4th generation light sources such as European XFEL in comparison to standard synchrotron radiation. Image from [54]*

quality. Continuing advancements in dynamic compression techniques allow us to explore PT regimes which have previously been inaccessible. In such regimes there is predicted to be a wealth of complex behaviour; for instance, predictions have been made that aluminium adopts an incommensurate host-guest structure above 3.2 TPa [55]. It is important to diagnose, therefore, whether we will be able to characterise such complex structures once we are able to access these pressure regimes.

Sb is known to form an incommensurate host-guest structure (Sb-II) above 10 GPa which persists over a modest stability region (∼15 GPa); this is a readily accessible pressure regime for a dynamic compression experiment. In the interest of testing our ability to refine complex structures using dynamic compression techniques, this work aims to obtain diffraction data from the Sb-II phase. Prior to this work, no incommensurate host-guest structures had been diagnosed with

x-ray diffraction using dynamic compression techniques, so it is interesting to investigate whether such a highly complex structure is able to fully form on nanosecond timescales.

Furthermore, as there have been discrepancies between reports of phase behaviour in Sb at high pressures, this work aims to conduct static compression experiments on Sb and compare these results to the dynamic compression studies to determine whether there are any differences in the behaviour of Sb under different pressure loading regimes.

1.6 Thesis outline

This introductory chapter has provided a brief background of the dynamic and static compression techniques that are used in this thesis, as well as an overview of the Sb research which has been conducted prior to this thesis. The remainder of the thesis is presented as follows:

Chapter 2 is divided into four subsections. The first presents the theory of laser-induced shock compression, including laser-material interactions, conservation equations, the origin of the Hugoniot curve, and how these concepts inform the practical design of dynamic compression targets. A brief overview of the practical workings of static compression using a DAC are then detailed in the second subsection of this chapter. The third subsection discusses crystallography and the theoretical underpinnings of x-ray diffraction as it is the primary diagnostic in both the static and dynamic compression experiments. The final subsection of this chapter contains a practical discussion of the diagnostics used in this work (x-ray diffraction and VISAR) as well as an introduction to the facilities at which these experiments were conducted.

Chapter 3 describes the dynamic compression experiments conducted on Sb for this thesis. There is discussion of the solid phases that were observed and characterised using a combination of x-ray powder diffraction and VISAR diagnostics.

Chapter 4 presents the results of static compression experiments conducted on Sb. This chapter is divided into two sub-sections; the first details the results of compression with the use of a pressure transmitting medium (PTM) while the second section describes similar experiments without the use of a PTM. These

results are analysed independently are are compared to the dynamic compression experiments.

Chapter 5 summarises the findings of the work conducted for this thesis and discusses ideas for future research both on Sb and also using 4th generation light sources in general.

1.7 The Role of the Author

As with most research, this work is collaborative in nature and this section aims to clarify the role of the author in the experiments and analysis of the data. The dynamic experiments were led by the McMahon research group at Edinburgh University (Prof. M.I. McMahon, Dr R. Briggs, Dr M. G. Gorman and the author) and while target preparation and data collection were a collaborative effort, the data analysis was primarily conducted by the author with texture and strain analysis conducted by Dr D. R. McGonegle of the University of Oxford. The static compression experiments were also a collaborative effort between the McMahon group and Dr S. G. Macleod of the Atomic Weapons Establishment (AWE), with data analysis conducted solely by the author.

The role of the author in the papers included at the end of this thesis is also described. In reference [1], experiments were conducted by the author along with Prof. M.I. McMahon, M. Stevenson and Dr S. G. Macleod. The author conducted the data analysis, constructed the figures and wrote the paper. The simulations described in reference [56] were conducted by the author, who also wrote the paper, constructed the figures and presented the findings at the joint AIRAPT-25 and EHPRG-53 high-pressure conference in Madrid (2015). The data to which the simulations are compared were obtained by the author along with Dr R. Briggs and Dr M. G. Gorman. Finally, in reference [57] the author assisted in the collection and analysis of the data while the paper and figures were constructed by Dr R. Briggs.

Chapter 2

Experimental Methods

In this thesis, the results of x-ray powder diffraction experiments utilising both dynamic and static compression techniques are described. This chapter summarises the experimental methods and diagnostics used in each of these types of experiment, and is split into four main sections. The first discusses the theory of dynamic compression and gives an overview of how this compression technique is implemented. The second section describes the methods used to generate static compression; the third presents a theoretical consideration of x-ray diffraction and crystallography; and the fourth discusses the practical realisation of the diagnostics and the analysis techniques used in this work.

2.1 Laser-Shock Compression

Generating a dynamic compression wave in a material may be done in several different ways; using explosive detonation [58], using gas-gun driven plate impact [59] or via laser ablation. The latter is the method used in this thesis and is unique in that it is able to provide the highest pressures, even into the TPa regime [26] and that it allows phenomena to be studied on shorter timescales (nanoseconds rather than microseconds). The dynamic compression experiments conducted in this thesis make use of laser-driven shock-compression. This section of the thesis will explain this compression technique, as well as providing a brief overview of the theoretical background of the method based on chapters 1 through 3 of reference [60].

2.1.1 Laser Interactions with Solids

When compressing a material with a laser-driven shockwave, it is important to consider the mechanism involved in transferring energy from the incident laser pulse to the material that is to be compressed (the material of interest). When an intense laser beam is incident on a surface, a fraction of the energy of the laser pulse is absorbed in a thin layer near the surface of the material. The absorption of this energy causes heating and generates a plasma which expands outwards away from the surface of the material [61]. As the plasma is expanding away from the surface of the material, conservation of momentum necessitates the formation of a pressure wave travelling in the opposite direction, as shown in figure 2.1.

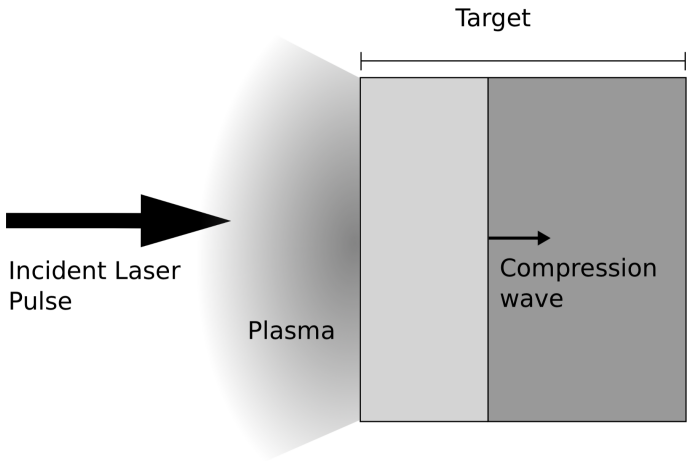

Figure 2.1 *A diagram showing laser ablation on the surface of a typical dynamic compression target.*

The critical density of the plasma, n_{cr}, is that at which the laser frequency is equal to the plasma frequency; at this density the oscillation of plasma electrons inhibits the propagation of light. At densities lower than n_{cr} the laser light continues to penetrate deeper into the material, while at densities higher than n_{cr} the plasma response is more rapid than the laser oscillation and the electric field is blocked. By assuming that all laser absorption occurs at n_{cr}, as described in equation 2.1, then the laser ablation pressure may be approximated using equation 2.2. Here ω, λ and I are the angular frequency, wavelength and intensity, respectively, of the incident laser. m_e and m_p are electron and proton rest masses, respectively, ε_0 is the permittivity of free space, c is the speed of light, α is the fraction of the incident laser energy that is absorbed by the material and Z^* represents the

ionisation state of the material at critical density.

$$n_{cr}[cm^{-3}] = \frac{\omega^2 m_e \varepsilon_0}{e^2} \approx \frac{1.1 \times 10^{21}}{(\lambda[\mu m])^2} \tag{2.1}$$

$$P = \left((2\pi c)^2 \frac{m_e m_p \varepsilon_0}{e^2 Z^*}\right)^{1/3} \left(\frac{2\alpha I}{\lambda}\right)^{2/3} \tag{2.2}$$

From equation 2.1 we see that the critical density of the plasma is dependent on the inverse square of the wavelength of the incident laser pulse; this means that the critical density at which energy is absorbed into the material is higher in the instance of shorter wavelength incident radiation. Equation 2.2 also shows that the pressure generated by the laser pulse in the material is proportional to the intensity$^{2/3}$ of the incident laser pulse, where intensity is given by equation 2.3. Here we see that by using high-energy laser pulses and laser beams with smaller spot sizes (tighter focus), higher pressures are able to be generated. In the experiments detailed in this thesis the typical laser intensities are around 10^{13} W/cm^2.

$$Intensity = \frac{Energy}{Area \times Time} \tag{2.3}$$

At the critical plasma density n_{cr}, energy is absorbed into the material from the laser pulse via collisional absorption (inverse Bremsstrahlung absorption). This process involves the absorption of an incident photon by a free electron in the plasma, causing it to become more energetic. These energetic electrons, oscillating in the laser field, then collide with the ions in the plasma which consequently absorb energy and accelerate. During this process, excess heat and x-rays are generated and if the laser pulse is incident on the material of interest this can cause undesirable heating in the material. To overcome this issue, dynamic compression targets may be designed such that the laser is incident on an 'ablator' material; this is a material which absorbs the laser energy and forms the compression wave while shielding the material of interest. The compression wave then propagates forward travelling from the ablator into the material of interest.

The compression wave generated by this process is maintained for the duration that the laser pulse is incident on the surface of the target. Once the pulse has

ended, a release wave forms and propagates behind the compression wave into the target. This release wave (discussed in section 2.1.3) commonly travels faster than the propagating compression front as it propagates though compressed material, and once it has caught the compression front, both the velocity and peak pressure of the front will decrease. For this reason, it is important to consider the sound speeds and thicknesses of the target materials when designing laser drive pulses.

Ramp and Shock Compression

Dynamic compression can occur using two different mechanisms: ramp compression and shock compression. In laser-driven dynamic compression, the profile of the incident laser pulse can determine the compression regime; shock compression is generated by an incident pulse with an incredibly short rise time, whereas ramp compression pulses involve a slower increase to maximum intensity over the duration of the pulse, as shown in figure 2.2.

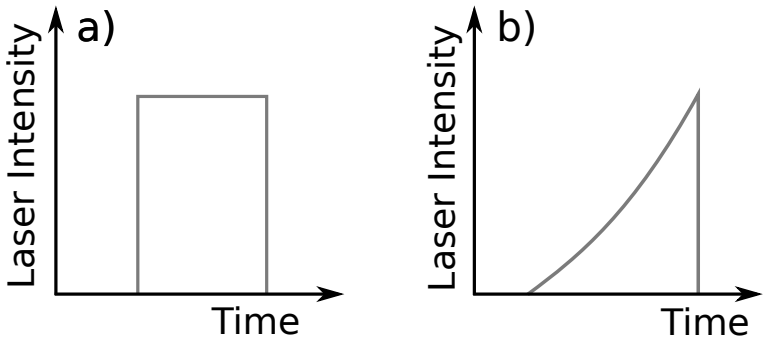

Figure 2.2 *An illustration of the differing rise times of shock (a) and ramp (b) drive laser pulses.*

To understand the difference between ramp and shock compression, it is helpful to imagine a 1-dimensional chain of atoms. The progression of a shock wave pushes the atoms so they come into contact with their nearest neighbours, thus shortening the interatomic distance in an almost instantaneous manner: the timescale of compression of this nature is smaller than the vibrational period of the material [62]. The rapid energy transfer and large entropy increases involved in this process cause large heating effects.

Ramp-wave driven compression also involves the atoms in the material being forced into their nearest neighbours, but due to the sloping nature of the pulse, the process is slower (by a few or a few tens of nanoseconds) and the characteristic timescale is longer than that of the vibrational period of the material. This type

of compression involves less of an increase in entropy than shock compression and high pressures may be achieved at lower temperatures [63]. Depending on the compressibility of the target material, ramp compression is not always a viable compression method [26]. When the front of a ramp pulse travels through a material it compresses it, meaning that the speed of sound in this denser region is higher. The tail end of the compression wave will therefore speed up in this denser region and, in more compressible materials, given that the propagation distance is sufficiently long, the tail will catch up to the front of the pulse, steepening it and turning it into a shock wave [63]. The propagation of a ramp pulse can be modelled using simulations in order to effectively design pulses to obtain desired experimental results [62, 64, 65]. Once an ideal pulse shape has been found using simulations, laser facilities such as OMEGA and NIF are able to make use of multiple laser beams in order to craft a pulse which meets very precise design specifications. Ramp compression has had great success in recent experiments reaching a range of pressures, from the GPa range up to 5 TPa [26, 65].

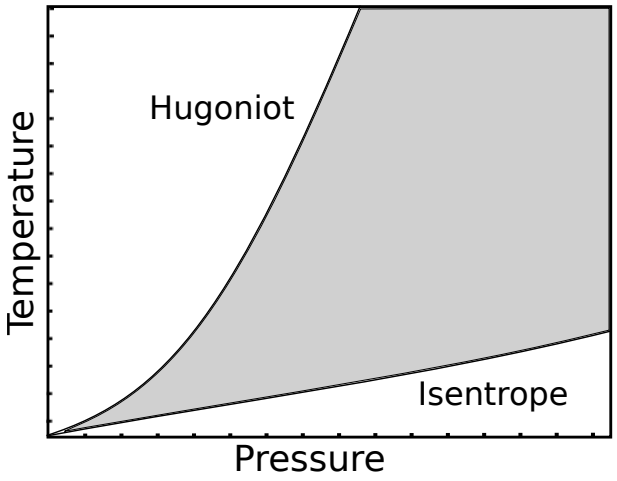

Figure 2.3 *An example of a PT plot with a Hugoniot (from shock compression) and an isentrope (from ramp compression). The shaded region represents the area in PT space that is able to be explored using dynamic compression experiments beginning at ambient conditions.*

The compression pathways for shock and ramp compression differ due to the rate of loading and associated temperature gradients. Figure 2.3 illustrates an example pressure-temperature plot with the grey region indicating the PT states that are accessible using dynamic compression techniques. The upper bound of this region is given by a Hugoniot curve which represents states accessible using shock compression (discussed in section 2.1.2). Ramp compression is quasi-isentropic in nature and allows access to states below the Hugoniot curve. The temperatures associated with ramp compression are lower, but as there are still

heating effects associated with the compression mechanism, there is also a lower bound to the region that is accessible via quasi-isentropic compression. The dynamic compression work in this thesis uses only shock-compression, the physics of which is discussed in the following section.

2.1.2 Shock Compression of Solids

A shock wave can be considered to be a discontinuity in pressure (P), density (ρ) and energy (E) that propagates through a material at a speed faster than the sound speed of the material at ambient conditions. Figure 2.4b shows the propagation of a shock front through a typical target package. Until the shock front reaches the rear surface of the target, there are two discrete states in the material of interest; uncompressed material in front of the shock front, and compressed material behind the front. The shock front itself is the discontinuity between these two states and by considering a series of conservation equations between the compressed and uncompressed states we are able to construct the Rankine-Hugoniot equations; these are invaluable in calculating physical properties from parameters which are determined experimentally.

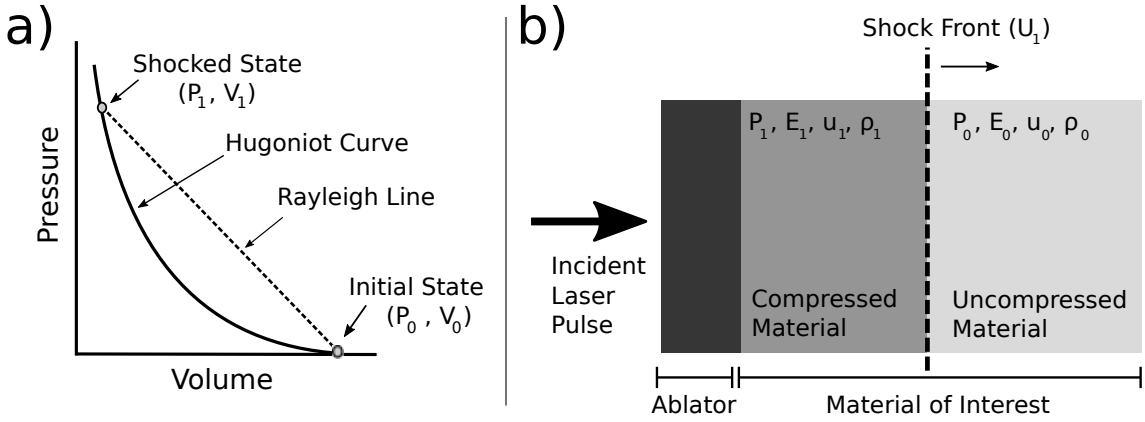

Figure 2.4 *a) illustrates the compression pathway (the Rayleigh line) which connects the initial state and the shocked state on the Hugoniot curve. b) shows the progression of a shockwave through a typical target material. Variables shown here include pressure (P), volume (V), density (ρ), shock velocity (U_S), particle velocity (u_p) and energy (E) with uncompressed and compressed states denoted by subscripts 0 and 1 respectively.*

Prior to deriving the Rankine-Hugoniot equations, it is important to define the terms that are used. As well as P, ρ and E described above, these conservation equations also make use of particle velocity (u_p) and shock velocity (U_S). Particle

velocity is the average velocity of the particles in the material of interest that are accelerated by the shock wave, while shock velocity is the velocity of the propagating shock front. To understand the difference between the two, one may imagine an object floating on a lake [60]. A boat, travelling parallel to the shore and further out into the lake than the object, passes by, sending out a wave in its wake. The floating object moves with the water slowly towards the shore, this is representative of u_p. Contrastingly, the wave rushes towards the shore, here this is analogous to U_S.

Rankine-Hugoniot Equations

In order to derive the Rankine-Hugoniot (RH) equations, it is useful to consider a one-dimensional shock front propagating through a tube of compressible material with cross sectional area A, over some time δt (where $\delta t = t_b - t_a$) as shown in figure 2.5. The subscripts 0 and 1 signify ambient and compressed material, respectively. We assume here that the uncompressed material is at ambient conditions and that u_0 and P_0 are equal to zero. L_C and L_U represent the lengths of the tube that contain the compressed and uncompressed material, respectively, at time t_a, while L'_C and L'_U represent the lengths of the compressed and uncompressed material at a later time (t_b). As the shock front progresses through the tube over time δt, the amount of material that remains uncompressed decreases. The amount of compressed material increases but as it is denser than the uncompressed material, the total volume of material within the tube decreases, meaning that L'_C and L'_U may be expressed by equations 2.4 and 2.5.

$$L'_C = L_C + U_S \delta t - u_1 \delta t \tag{2.4}$$

$$L'_U = L_U - U_S \delta t \tag{2.5}$$

Firstly, we may consider the conservation of mass on either side of the shock front which has progressed for time δt. At time t_a, in the uncompressed region ahead of the shock, the mass may be expressed as $\rho_0 L_U A$ where A is the cross sectional area of the cylinder. The mass of the compressed material behind the shock at time t_a may be expressed as $\rho_1 L_C A$. Conservation of mass requires that the total mass at time t_a be equal to the total mass at time t_b, yielding equation

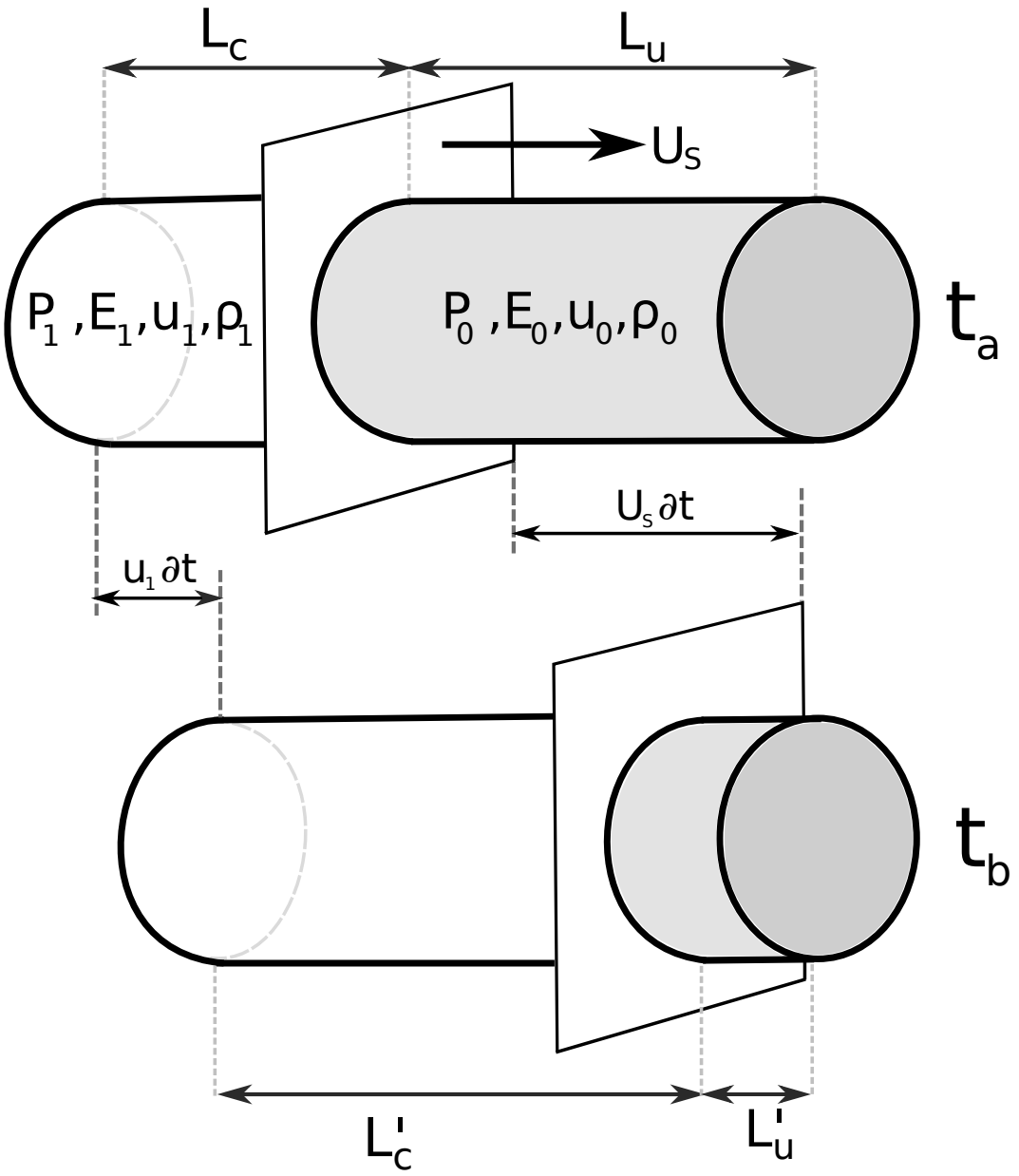

Figure 2.5 *A steady shock front propagating through a cylinder of cross sectional area A at a shock velocity U_S over time δt where $\delta t = t_b - t_a$.*

2.6 which, using equations 2.4 and 2.5, may be expressed as equation 2.7, the first RH equation.

$$\rho_0 L_U A + \rho_1 L_C A = \rho_0 L'_U + \rho 1 L'_C A \tag{2.6}$$

$$\rho_0 U_S = \rho_1 (U_S - u_1) \tag{2.7}$$

In addition to the conservation of mass, momentum is also conserved across the shock front. Momentum may be expressed in terms of mass $\times$ velocity. At time t_a the momentum of the material in the tube may be expressed as $\rho_1 L_C A u_1$, while at time t_b the momentum of the material is given by $\rho_1 L'_C A u_1$. The difference between these two terms is equal to the momentum imparted by the force, F ($F = (P_1 - P_0)A$) acting to the right in this system over time δt. This gives equation 2.8 which may be expressed as the second RH equation, equation 2.9 using equations 2.7, 2.5 and 2.4.

$$(P_1 - P_0)A\delta t = \rho_1 L'_C A u_1 - \rho_1 L_C A u_1 \tag{2.8}$$

$$P_1 - P_0 = \rho_0 U_S u_1 \tag{2.9}$$

The third RH equation is derived from the conservation of energy across the shock front. As the shock front propagates through the material, it changes both the kinetic and internal energy; this change is equal to the work done on the system by the shock front. The work done is equal to force multiplied by distance through which it acts ($PAu_1\delta t$). The kinetic energy term is given by $1/2 \times$ mass $\times$ velocity^2 which may be expressed as $1/2\ (\rho_1 L_C A)u_1^2$ at time t_a and $1/2\ (\rho_1 L'_C A)u_1^2$ at time t_b. The internal energy per unit mass is denoted by E, meaning that the total internal energy in the tube at time t_a may be written as $E_0(\rho_0 L_U A) + E_1(\rho_1 L_C A)$ and the total internal energy in the tube at time t_b may be written as $E_0(\rho_0 L'_U A) + E_1(\rho_1 L'_C A)$. Energy is conserved when the work done on the system is equal to the change in the total energy (kinetic and internal). Using the previous two RH equations and expressing the system in terms of the specific volume (V=$1/\rho$), the third RH equation, equation 2.10, may be derived from this conservation of energy.

$$(E_1 - E_0) = \frac{1}{2}(P_1 + P_0)(V_0 - V_1) \tag{2.10}$$

These three Rankine-Hugoniot equations (2.7 2.9 and 2.10), also commonly referred to as the jump equations, describe the relationship between the physical variables P, V, u_p, U_S and E, and are incredibly useful when making calculations based on parameters measured experimentally.

These RH equations allow us to construct a curve in PV space, as shown in figure

2.4a, known as the Hugoniot curve. This curve is a locus of points accessible through shock compression, with each PV point on the curve representing the final state of a single shock compression. It is important to note that the thermodynamic compression pathway is *not* along the Hugoniot curve, it is instead represented by a straight line known as the Rayleigh line which connects the initial and final states of shock compression. In rearranging the RH equations, one may obtain an expression (equation 2.11) that highlights the dependence of the slope of the Rayleigh line on the magnitude of the shock velocity; when compressing to higher pressures (larger values of P_1), the value of U_S will be greater resulting in a concave Hugoniot curve.

$$U_S = V_0\sqrt{\frac{P_1 - P_0}{V_0 - V_1}} \tag{2.11}$$

To better understand the relationship between these parameters, one can consider, specifically, the relationship between U_S and u_p. For most metals, this relationship is described by a linear relationship given by equation 2.12 where c_0 is the sound speed in the material at ambient conditions and s_1 is an experimentally determined constant.

$$U_S = c_0 + s_1 u_p \tag{2.12}$$

This relationship between U_S and u_p is commonly referred to as the equation of state (EOS). This EOS is useful for extrapolating experimentally obtained data in order to construct a Hugoniot curve in PV space by substituting in the constants c_0 and s_1 into equation 2.9 to give equation 2.13.

$$P_1 - P_0 = \frac{c_0^2 V_0}{V_0 - s_1(V_0 - V_1)} \tag{2.13}$$

Multi-Wave Shock Compression

In practice, this model of a single shock wave propagating through a material is not always accurate. Before compressing plastically in three dimensions, materials are compressed elastically and uniaxially by an elastic wave (known also as an "elastic precursor") which can travel ahead of the plastic shock front at (or near)

the longitudinal sound velocity. The pressure above which plastic compression occurs is material dependent and also depends upon the distance that the elastic wave has propagated into the material (or, equivalently, the time of propagation), as well as peak pressure [66, 67]. The pressure of this elastic precursor decreases with propagation distance into the target until, eventually, it stabilises at some pressure which may be referred to as the Hugoniot Elastic Limit (HEL). In the instance of a relatively weak shock compression or a higher HEL (where the shock front has not overdriven the elastic precursor before it reaches the rear surface), it is possible to observe a separate elastic compression wave as well as a plastic shock compression wave in velocimetry wave profiles. However, this was not the case for the Sb studied in this thesis. There was no observation of the elastic precursor in the Sb data, this is perhaps not surprising as the amplitude of this precursor has been observed to be small in other heavy metals such as bismuth ($\sim$0.2 GPa) [68, 69].

The separation of the elastic and plastic compression waves is not the only multi-wave mechanism in shock compression. While a linear $U_S - u_p$ relationship (equation 2.12) is fitting for many metals, it is not always a suitable approximation; this is especially true in instances when a phase transition occurs, resulting in a much denser phase. A non-linear $U_S - u_p$ relationship results in a more complex Hugoniot curve. In this instance, illustrated in figure 2.6, the shock wave splits up into two plastic compression waves as a single Rayleigh line is not sufficient to reach the final state on the Hugoniot curve. The initial shock wave compresses the material from the state P_0, V_0 to P_1, V_1 and the second wave compresses it from P_1, V_1 to P_2, V_2.

There is a high-pressure regime in which splitting of the shock front is not observed; this occurs when the gradient of the Rayleigh line extending from the initial point is steep enough that it bypasses the peak in the Hugoniot curve. The lower pressure boundary for this regime may be found by extending the gradient of the initial Rayleigh line until it intersects the Hugoniot curve, as shown in figure 2.6. At the lower boundary of this "overdriven" regime, the velocity of the second shock wave, which increases with pressure, is equal to the velocity of the initial wave and thus their Rayleigh lines must have the same gradient. At higher pressures, further into the overdriven regime, the second wave is faster than the first meaning that it overtakes it and only a single wave profile is observed.

In the case of this splitting of a plastic compression wave, the RH equations discussed previously can be generalised in order to make calculations relating to

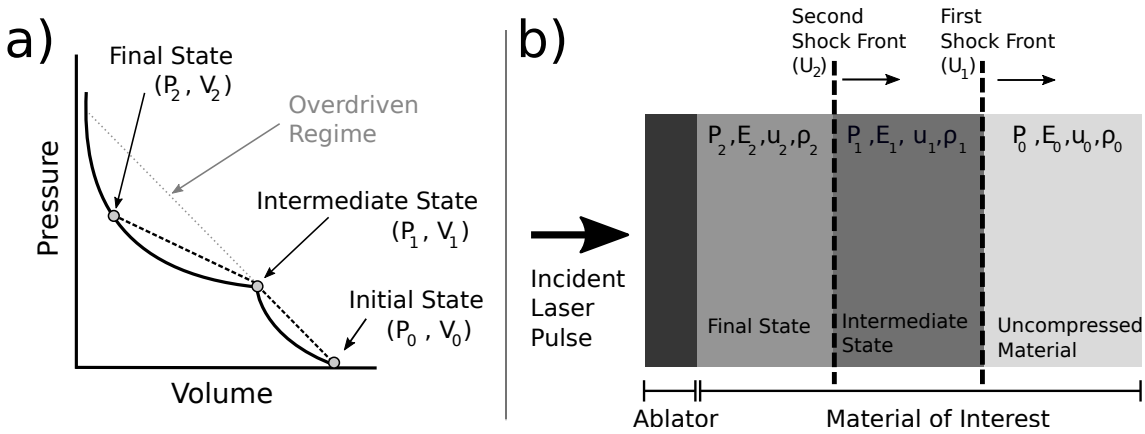

Figure 2.6 *a) illustrates the compression pathway (the Rayleigh lines) between an initial state and the final shocked state on the Hugoniot curve when shock wave splitting occurs. b) shows the progression of two shockwaves through a typical target material.*

the final compressed state of the material, denoted by the subscript 2.

$$\rho_1(U_2 - u_1) = \rho_2(U_2 - u_2) \tag{2.14}$$

$$P_2 - P_1 = \rho_1(U_2 - u_1)(u_2 - u_1) \tag{2.15}$$

$$E_2 - E_1 = \frac{1}{2}(P_2 + P_1)(V_1 - V_2) \tag{2.16}$$

Here equations 2.14, 2.15 and 2.16 refer to the conservation of mass, momentum and energy respectively. It should be noted that the initial state of the material need not be ambient for Hugoniot calculations to be valid. The Hugoniot calculations discussed in the single-shock case in the previous section refer to the principal Hugoniot, this is the Hugoniot that begins from an ambient, zero pressure, state. It is possible to construct Hugoniot curves that begin from some initial state which is at a higher pressure, indeed it is necessary to do these calculations when compressing a material that is not initially at ambient conditions. Equations 2.14, 2.15 and 2.16 may be used in the case of a single shock compression where subscript 1 represents the starting condition of the material (which need not necessarily occur as the result of shock compression) and subscript 2 denotes the state of the material after shock compression.

2.1.3 Target Design

When conducting a dynamic compression experiment, one of the most important parts of the experiment is the design and construction of targets. As discussed in section 2.1.1, an ablator material is commonly included at the front of the target package. One of the advantages of using an ablator is that it shields the material of interest from the high temperatures associated with plasma ablation but it may also smooth out small-scale variations in the incident pulse, promoting a steady shock front [70]. Commonly, plastics are used as ablator materials as they are relatively inexpensive to obtain, easy to manipulate and do not generate x-ray diffraction signal, the latter being particularly advantageous when x-ray diffraction is used as an experimental diagnostic. When conducting shock compression experiments at facilities such as LCLS it is necessary to construct a large number (hundreds) of targets; at such facilities a compression event ("shot") can occur every ∼4 minutes over the course of one or several 12-hour shifts. As described previously, a single shock compression gives one on-Hugoniot data point so in order to build up a comprehensive data set it is necessary to shoot a large number of targets. For this reason, it is also important that the target design is highly reproducible. In the Sb work conducted for this thesis, 50 μm thick black kapton was used as the ablator material.

Another feature to consider in target construction is the impedance of the neighbouring layers in the target. Shock impedance (Z) is defined in equation 2.17.

$$Z = \rho_0 U_S \tag{2.17}$$

Let us consider the consequences for pressure and particle velocity in two extreme cases: the first case is that of a shock front propagating from a material into a vacuum, where $Z = 0$. In this instance, the transmitted pressure is zero. At an interface, not only is there transmission of a wave but, by conservation laws, there is also reflection. In this first case, the reflected pressure is of opposite sign to the incident wave; this signifies a "release" wave which acts to lower the pressure in the material. The second case addresses a situation where a shock front propagates into a material of infinite impedance ($Z = \infty$). In this instance the reflected pressure is equal to the incoming value and rather than a release wave lowering the pressure in the original material, the reflected wave acts to

increase the pressure. In practice, impedances fall between these two extremes. It is important to consider, when designing a target, that when a shock passes from material A to material B, the pressure in A will increase if B is of a higher impedance and the pressure in A will decrease if B is of a lower impedance. The amount the pressure is altered by the passage of a shock front into a neighbouring material is dependent on the difference in impedance between the materials on either side of the interface, this is discussed further in section 3.3 and illustrated in figure 3.11.

Another aspect of target design that must be considered is the thickness of the layers of the target. Firstly, the speed of shock propagation through each layer must be characterised so that the diagnostics are correctly timed, this will be discussed further in section 2.4.1. Additionally, if x-ray diffraction is used as a diagnostic, it is important to consider the x-ray signal that will be obtained from the material of interest. Figure 2.7 shows the transmission of x-rays through a 10 μm thick Sb foil with a 10 keV incident x-ray beam, as used in the dynamic experiments conducted for this thesis. 40% transmission is a suitable value for these experiments; if the transmission is too high then there is not enough scattering signal and if it is too low then the material absorbs too much of the incident x-rays. The ideal thickness of a target is one absorption length which, for Sb being probed by 10 keV x-ray radiation, is equal to 11 μm [71].

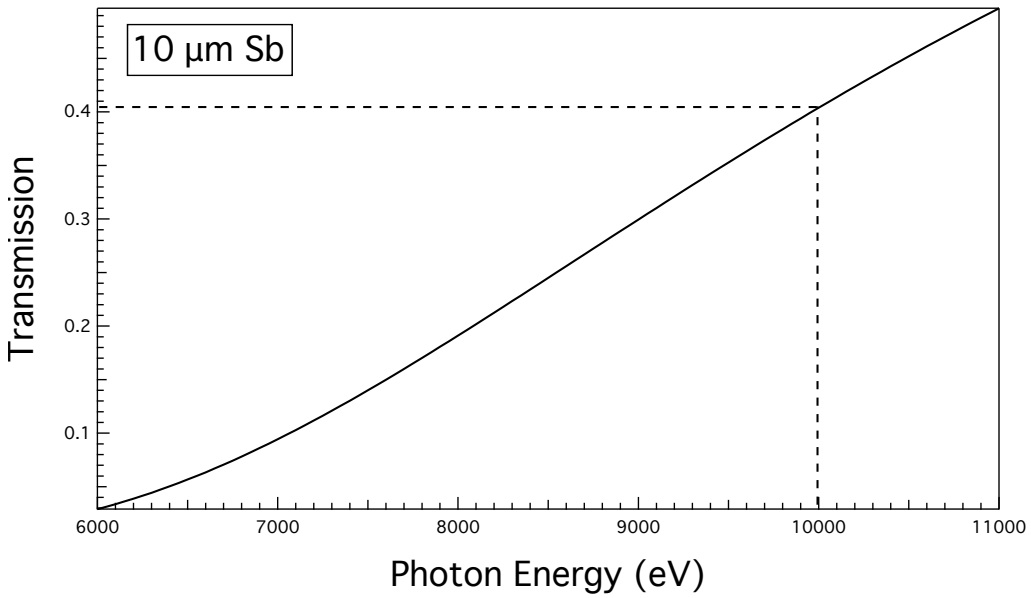

Figure 2.7 *The transmission of X-rays through a 10µm thick Sb sample, plotted as a function of photon energy. The transmission of Sb foils at a photon energy of 10 keV, as used in this experiment, is ∼40 %*

Commonly, the ablator material and the material of interest layers are attached using very thin ($\sim 1\mu$m) glue layers, however for this work, the Sb was deposited directly onto the black kapton ablator. While many of the targets were comprised purely of black kapton and deposited Sb, several targets were constructed with a rear LiF single-crystal window, as shown in figure 2.8. This LiF crystal was 150 μm thick and was attached with a $\sim 1\mu$m glue layer. The purpose of this LiF crystal was to create an interface between the rear surface of the Sb layer and a material which had higher impedance than the vacuum of the experimental chamber. This meant that the pressure did not decrease as rapidly when the shock front had traversed the full extent of the Sb layer, and high pressures could be maintained in the Sb sample for longer periods of time due to the less severe release wave in comparison to when a vacuum neighbours the Sb layer.

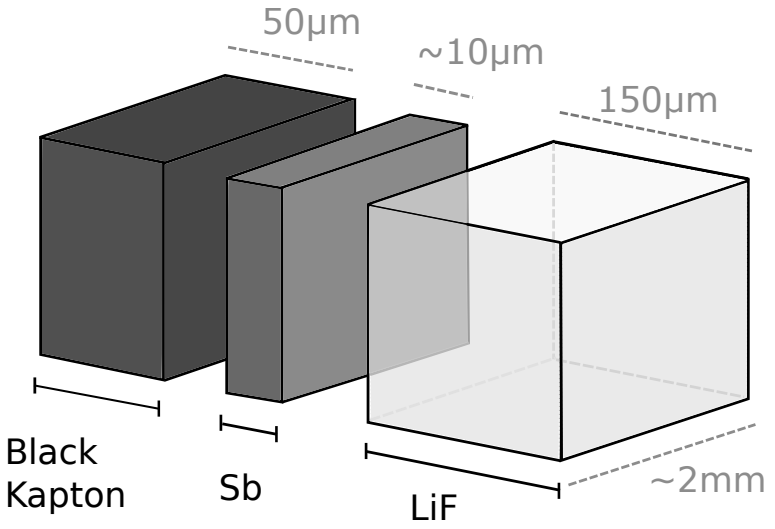

Figure 2.8 *A deconstructed Sb target (not to scale). In practice the Sb layer is deposited directly onto the kapton and the rear LiF window is attached with a $\sim 1\mu$m glue layer.*

When x-ray diffraction data are collected before the shock front reaches the rear surface of the material of interest, the data is said to be collected "on compression" and any sample volumes that are yielded by fitting the x-ray diffraction data correspond to on-Hugoniot points, allowing a pressure to be calculated. When data are collected after the shock front has reached the rear surface of the material of interest, this data is said to be collected "on release". This data does not correspond to on-Hugoniot points as the state of the material is not induced by a single shock; it is the result of a combination of the initial shock compression and subsequent reflected wave interactions. While data collected on release are often more difficult to interpret, due to the multiple wave interactions, it is useful, especially in observing the structural behaviour of a material as pressure

is decreased slowly (in the case where a LiF window is used). Unless otherwise stated, the data collected during the dynamic compression experiments in this thesis were collected on compression.

When designing targets for dynamic compression experiments, it is incredibly useful to simulate the target package and incident laser pulse using hydrodynamic simulation code such as HYADES [72]. This code takes an input which specifies the target geometry and compression pulse profile in order to calculate pressure states in the target throughout the compression event. The program divides the specified target into a series of cells which together form a mesh. Each of these cells has an associated pressure, volume and energy state and the EOS and conservation equations are applied to each cell as the compression pulse progresses through the simulated target. HYADES then provides an output in the form of thermodynamic data describing each of these cells; this may be processed and used to interpret the wave interactions within the target. HYADES has been used to successfully model and plan dynamic compression experiments where EOS data is available [56]. These simulations inform the design of not only the target package but also the drive laser pulses so that the desired pressure states are achieved in the material of interest. They also help to estimate the propagation time of the shock front through the target so that the diagnostics may be properly timed. These simulations are also invaluable in interpreting the wave interactions within the target; there will be both reflected and transmitted waves when a shock front crosses any interface, as discussed previously.

2.2 Static Compression

This section describes the practical methods of compression using a diamond-anvil pressure cell (DAC) and the techniques used for pressure determination.

2.2.1 Diamond Anvil Pressure Cells

In a diamond-anvil cell (DAC), the sample which is to be compressed is placed between two diamond anvils and is confined by a metallic gasket, as shown in figure 2.9. Force is applied to backing plates which sit behind the diamonds, causing the distance between the diamond faces to decrease, consequently increasing the pressure on the sample as a result of reducing the volume in which the sample is confined. Commonly, it is not just the sample which is confined between the diamonds and the gasket; a pressure calibrant and a pressure-transmitting medium (PTM) are also present alongside the sample in the cell.

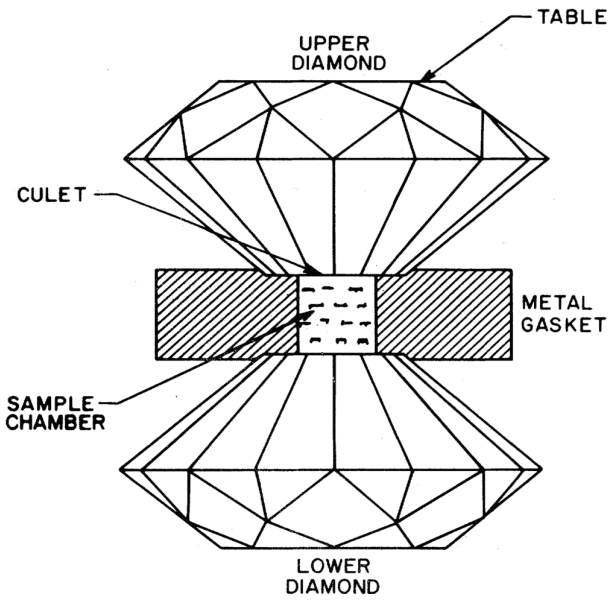

Figure 2.9 *Basic diamond anvil cell configuration, figure taken from [73].*

For the work reported in this thesis, Livermore-type diamond-anvil cells were used in order to perform resistive heating of the sample [74]. This experimental setup used a gas membrane to allow remote control of the cell pressure, something which is essential during high-temperature data collection. The outer body of the DAC was resistively heated by a Pt-Rh alloy wire coil that wrapped around the outside, with heat being transferred to the sample via thermal conductivity. The

temperature within the cell was measured by a thermocouple placed in contact with the DAC and insulated from the surrounding equipment by ceramic beads. The cell, heater and thermocouple were mounted onto a stage (as shown in figure 2.10) where the gas membrane was attached and the stage was then placed into a vessel. The vessel was mounted in the experimental chamber in the path of the incident x-rays (shown on the right hand side of figure 2.10) and was evacuated. Heating under vacuum inhibits unnecessary heat loss and is essential to stop discolouration of the diamonds due to oxidation at high temperatures. The vessel was connected to a cooling system of circulating cold water and a gas input so that the membrane could be controlled externally (both shown in figure 2.10). This setup permits access to temperatures of up to 1200 K with maximum achievable pressure varying depending on the size of the diamond cutlets; during these studies the maximum temperature and pressure achieved were 835 K and 31 GPa respectively.

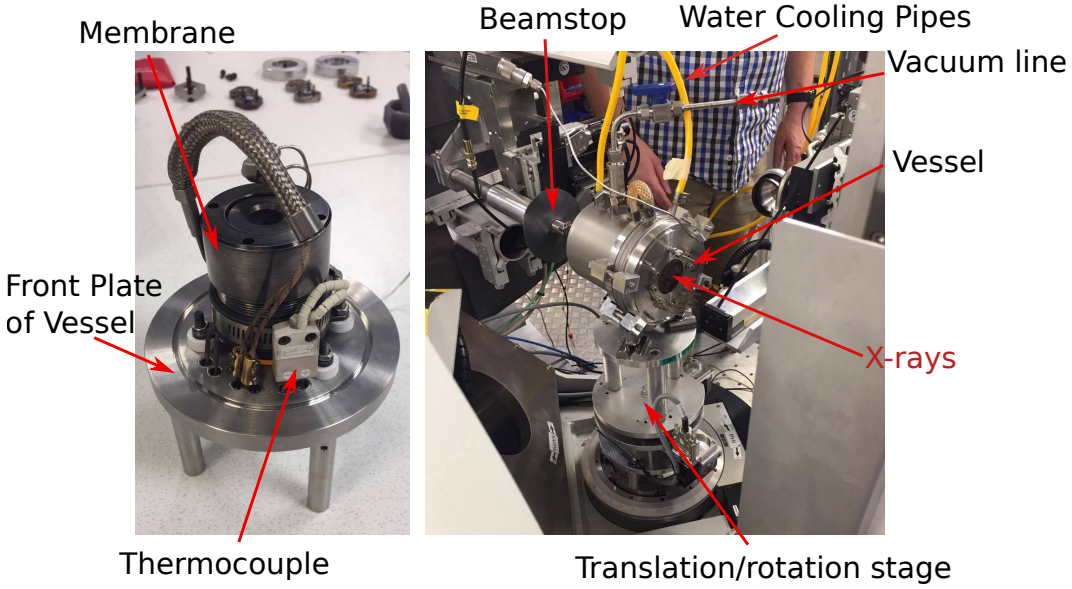

Figure 2.10 *On the left the DAC on the stage is shown prior to insertion into the vessel. On the right hand side the vessel is shown, mounted on the I15 beamline at the Diamond Light Source.*

2.2.2 Pressure Transmitting Media

Compression in a diamond-anvil cell is achieved by applying force to the backing plates behind the diamonds, which sit parallel to each other, while the gasket confines the sample radially. As the compressing force applied to each of the backing plates is axially symmetric, uniaxial stress on the sample in this plane

can be larger than the radial stress; these conditions are considered to be non-hydrostatic. Non-hydrostatic compression can be advantageous in the specific study of shear strength and elastic moduli as a function of pressure [75]. However, the presence of non-hydrostatic stress can lead to broadening of diffraction lines; when a powder sample is compressed, inhomogeneous compression of the crystallites which constitute the sample can result in shifts in the diffraction peaks [76].

To minimise non-hydrostatic compression conditions, a liquid pressure transmitting medium can be loaded into the cell alongside the sample which promotes uniform compression across the sample, rather than along one axis. When selecting a material to use as a pressure transmitting medium it is important to select something with a high hydrostatic limit which will not solidify in the pressure regime of study and to select something which will not react with the sample. When a pressure transmitting medium was used in these experiments, mineral oil was selected as the material of choice.

2.2.3 Pressure Determination

There are various different pressure-calibration methods that can be used in static-compression experiments such as ruby fluorescence and internal pressure calibrants [77]. This work used only the Livermore-type diamond-anvil cells which are enclosed within a vessel that imposes limitations upon laser access to the cell, meaning that use of ruby fluorescence as a method of pressure determination was not possible.

Pressure determination via the use of an internal pressure calibrant involves loading a small amount of a material with a well-characterised equation of state (EOS) into the diamond-anvil cell alongside the sample. By fitting the x-ray diffraction pattern, the volume of the pressure calibrant material can be calculated meaning that the pressure can be determined using the EOS. For these high-temperature experiments, thermal EOS were used meaning that the temperature of the pressure calibrant had to be well characterised [78].

Ideally, the pressure calibrant should consist of a material which does not undergo any structural transitions in the pressure-temperature regime that the experiment is being conducted in; typically transition metals such as Cu, Ta, Au and W are used as pressure calibrants. There are many factors which must be taken

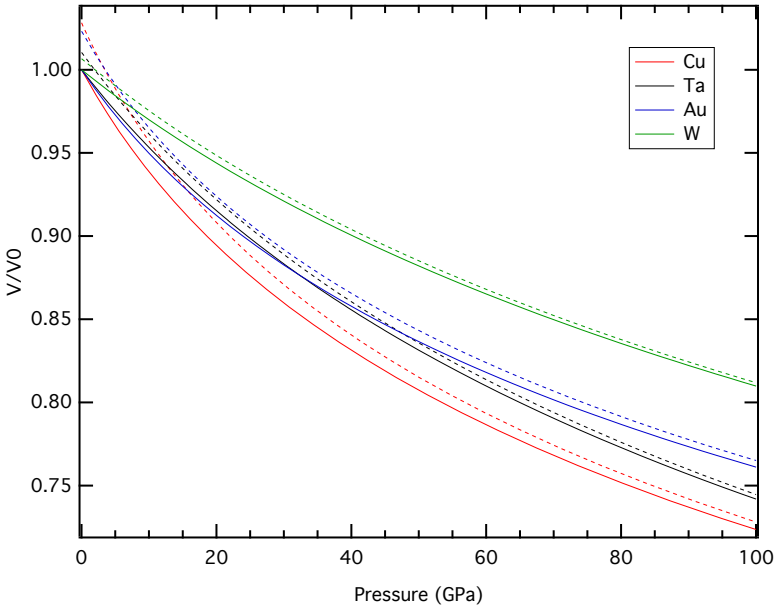

Figure 2.11 *Compressibility of candidate pressure calibrant materials: Cu, Ta, Au and W shown by red, black, blue and green lines respectively. Solid lines represent data at 300 K while dashed lines represent data at 800 K. All results calculated using published thermal EOS [78].*

into consideration when selecting a pressure calibrant material, for instance the compressibility of the material which is used as a calibrant is important; if the region of interest is low pressure, it is necessary to use a calibrant which undergoes a volume change which is significant enough to give an accurate pressure reading in that regime. Figure 2.11, calculated using published thermal EOS equations [78], shows PV data for a series of typical pressure calibrant materials at both room temperature and 800 K. For a material that experiences phase transitions at low pressures, Cu could be a good choice of pressure calibrant as it experiences the greatest change in volume in the low-pressure regime. When choosing a calibrant is is also important to consider potential reactions between the sample and the calibrant at high pressure-temperature conditions. Another factor to consider is the location of the calibrant diffraction peaks; it is difficult to fit a diffraction pattern and give a reliable value of the volume of the calibrant if the diffraction peaks all lie underneath the diffraction peaks of the sample. The intensity of the pressure calibrant peaks is also something which should be taken into consideration, it is important to load enough of the pressure calibrant material into the cell to obtain a strong enough diffraction signal to enable reliable fitting as well as considering the x-ray absorption of the material.

2.3 Crystallography and X-ray Diffraction

> "Only x-ray or neutron diffraction *at pressure* can definitely establish the structure of a given high-pressure polymorph."
>
> W. Klement, 1963

The primary diagnostic used in both the static and dynamic experimental work described in this thesis is x-ray diffraction. The following section gives an overview of the underlying theory of basic crystallography and x-ray diffraction based on chapters 4, 5 and 6 from Ashcroft and Mermin's *Solid State Physics* [79], chapter 1 in Hook and Hall's *Solid State Physics* [80], chapters 1 and 2 from reference Kittel's *Introduction to Solid State Physics* [81], and the first three chapters from Waseda's *X-ray Diffraction and Crystallography* [82]. The techniques used to obtain x-ray diffraction data are described in section 2.4.1, and the refinement techniques used are described in section 2.4.2.

2.3.1 Periodic Crystals

A crystal is a solid material which is made up of a series of repeating, identically structured units in space. The periodic array in which these repeated structural units are arranged is known as the Bravais lattice, or the crystal lattice. Atoms are attached to each lattice point of this infinite lattice and this describes the structure of a crystal. The Bravais lattice is defined by three non-parallel, lattice vectors $\mathbf{a}_1$, $\mathbf{a}_2$, and $\mathbf{a}_3$, as shown in equation 2.18, where u, v and w can take any integer value. It is important to distinguish between an infinite lattice and a finite crystal; while the Bravais lattice can indeed be considered to extend infinitely, a physical crystal fills only a finite area of the infinite lattice.

$$\mathbf{R} = u\mathbf{a}_1 + v\mathbf{a}_2 + w\mathbf{a}_3 \tag{2.18}$$

When the vector $\mathbf{R}$ describes a translation between identical points on the lattice, the lattice vectors $\mathbf{a}_1$, $\mathbf{a}_2$, and $\mathbf{a}_3$ form a parallelogram that describes the unit cell: a cell that tesselates and acts as a building block for the crystal structure. It is possible that there may be multiple different sets of unit vectors that may be selected within a lattice, as illustrated in two-dimensions in figure 2.12a.

Frequently a preferential choice of lattice vectors will become apparent based on symmetries within the crystal. The length of these unit cell vectors along with the angles between them are commonly referred to as the lattice parameters.

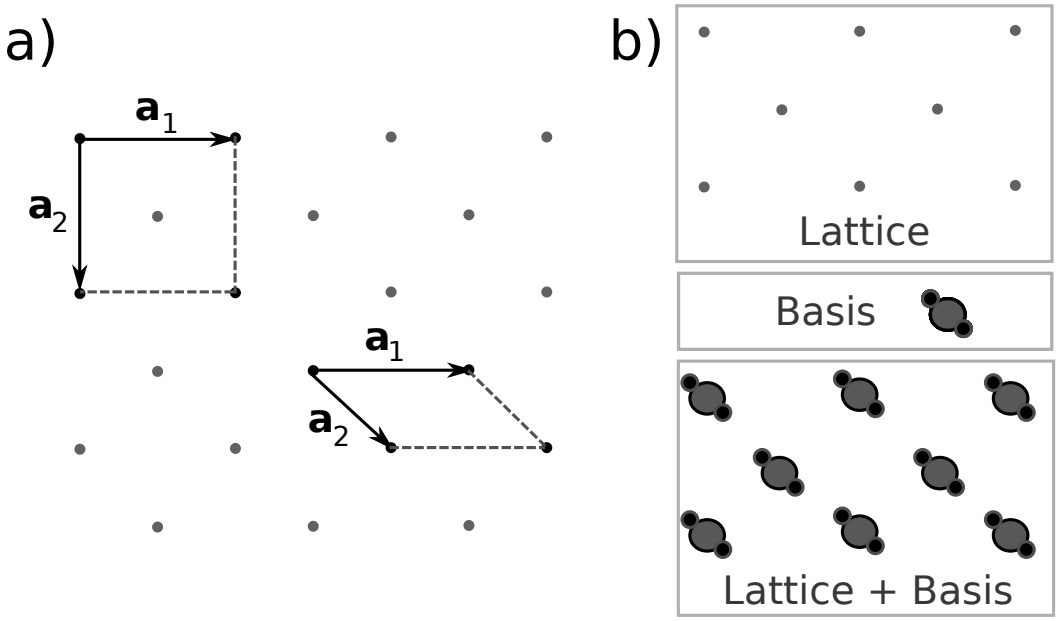

Figure 2.12 *a) shows the possible vector choices in a two-dimensional Bravais lattice. The cell to the right is the primitive unit cell as it is the smallest possible tessellating unit within the lattice. b) shows the convolution of a two-dimensional lattice and a basis.*

In order to describe a crystal structure, a basis of atoms is needed as well as a lattice; this basis of atoms is attached to each lattice point in an identical fashion. There can be any number of atoms attached to a lattice point, and the position of any given atom within the unit cell is described by equation 2.19 with $0 \leq x, y, z \leq 1$. The entire crystal structure can be described as a convolution of the Bravais lattice and the crystal basis, as illustrated in figure 2.12b.

$$\mathbf{r} = x\mathbf{a}_1 + y\mathbf{a}_2 + z\mathbf{a}_3 \tag{2.19}$$

Periodic crystal structures may be described in terms of symmetries. A symmetry operation is an operation which is performed on the crystal, resulting in a final state that is identical to the initial state. In considering the crystal lattice itself, it is evident that there is translational symmetry present; we have already defined a vector $\mathbf{R}$ which transforms one lattice point to an indistinguishable lattice point. While all perfect crystals exhibit translational symmetry in all three dimensions, there are a series of other symmetry operations (rotation about a line, inversion

Crystal System	Unit Cell Restrictions	Allowed Centring
Triclinic	none	P
Monoclinic	$\alpha = \gamma = 90°$	P, C (I)
Orthorhombic	$\alpha = \beta = \gamma = 90°$	P, C (A, B), I, F
Tetragonal	$a = b$, $\alpha = \beta = \gamma = 90°$	P, I
Trigonal	$a = b$, $\alpha = \beta = 90°$, $\gamma = 120°$	P (R)
Hexagonal	$a = b$, $\alpha = \beta = 90°$, $\gamma = 120°$	P
Cubic	$a = b = c$, $\alpha = \beta = \gamma = 90°$	P, I, F

Table 2.1 *The 7 crystal systems and corresponding unit cell restrictions and allowed centring. The centring options shown in brackets indicate choices that could also be expressed as alternative centring with a different choice of axes. The lattice parameters are given by a, b and c with α, β and γ denoting the angles within the unit cell.*

through a point and reflection in a plane) which apply only to certain crystal structures. The allowed symmetry operations for a periodic crystal is known as its point group, of which there are 32. The 7 crystal systems, shown in table 2.1, contain 32 point groups.

These 7 crystal systems may also be described in terms of centring of lattice points: primitive (P), body centred (I), face centred (F), base centred (A, B or C depending on which faces are centred), and rhombohedral (R). The combination of crystal systems and allowed centring gives 14 allowed Bravais lattices. When considering the possible combinations of these 14 Bravais lattices, the 32 point groups and additional symmetry operations due to translational symmetry of the crystal (screw axes and glide planes) there are 230 configurations of symmetry elements in crystalline solids; these are referred to as space groups and these are described thoroughly in the International Tables for Crystallography Volume A [83].

Within the crystal lattice, planes can be defined with the use of Miller indices. Figure 2.13a shows an example of a plane which crosses the $\mathbf{a}_1$, $\mathbf{a}_2$, and $\mathbf{a}_3$ axes at some values $(1/h)$, $(1/k)$ and $(1/l)$ respectively where. The miller index of this plane is (hkl) where h, k and l are integer values ≥ 0. In the instance when a plane intercepts the negative section of the axis, the accepted notation is to place a bar over the number, rather than using a negative sign. Figure 2.13 illustrates several examples of planes inside cubic lattices along with their Miller indices. Each of these planes corresponds to a possible reflection or a peak in an integrated x-ray diffraction profile, this will be discussed further in section 2.3.3.

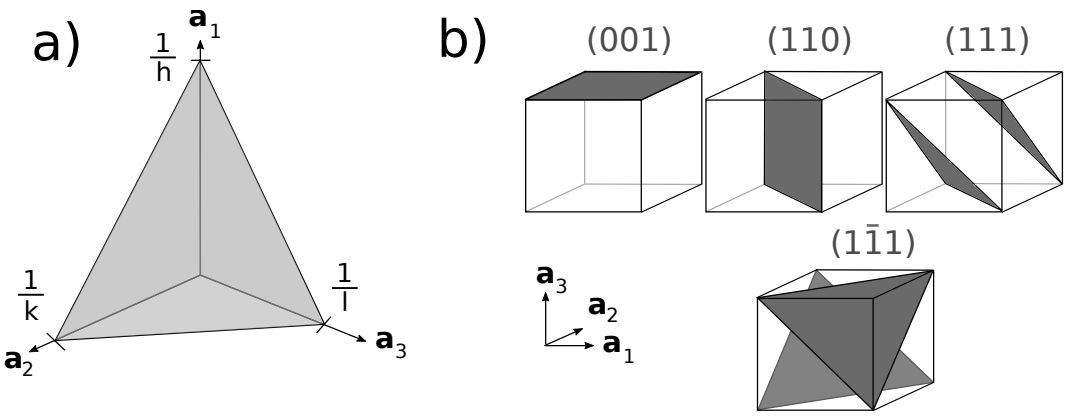

Figure 2.13 *An illustration of how Miller indices are used to describe crystal planes (a) along with some examples of crystal planes within unit cells and their corresponding Miller indices (b).*

2.3.2 Incommensurate Host-Guest Structures

As mentioned in the previous section, periodic crystals are known to exhibit translational symmetry in three dimensions; this, however, is not true of aperiodic crystals [84]. While an aperiodic crystal still retains long-range order, the unit cell cannot be translated linearly along three independent directions resulting in periodic repetitions. There are three classes of aperiodic crystals: incommensurately modulated structures, composite crystal structures and quasicrystals. As the structure of Sb-II is known to be an incommensurately modulated, composite host-guest structure [41–43], it is this class of aperiodic crystal which is discussed in this section. Figure 2.14 shows the host-guest structure of Sb-II, a structure where the tetragonal host is incommensurately modulated with the tetragonal guest "chains" along the c-axis.

A *modulated* structure has an average three dimensional periodic structure where the atoms are displaced from their average position by some modulation function. In an *incommensurate* structure, the ratio of the period of this modulation function to the periodicity of the lattice is not a rational number. The result of this irrational ratio is that the real structure of the crystal is not periodic. In an *incommensurately modulated* structure, atoms are displaced relative to their average lattice-periodic positions by a modulation whose wavelength is incommensurate with the average periodic lattice. A composite structure is made up of two or more interpenetrating lattice-periodic subsystems, in Sb-II these subsystems are the host and guest components. In an incommensurate composite structure these subsystems are mutually incommensurate. The subsystems of an

incommensurate composite structure be modulated themselves as a result of the interactions between them.

In order to describe crystal planes in incommensurate structures, the superspace formalism constructed by De Wolff in 1974 [85] may be used. In this 4 dimensional superspace, crystal planes in incommensurate structures can be described using Miller indices, though they require an additional parameter m. In this $(hklm)$ notation, the planes that comprise the average (host) structure have indices where $m = 0$ $(hkl0)$, and when characterised using x-ray diffraction, these resulting reflections are known as the 'main' reflections.

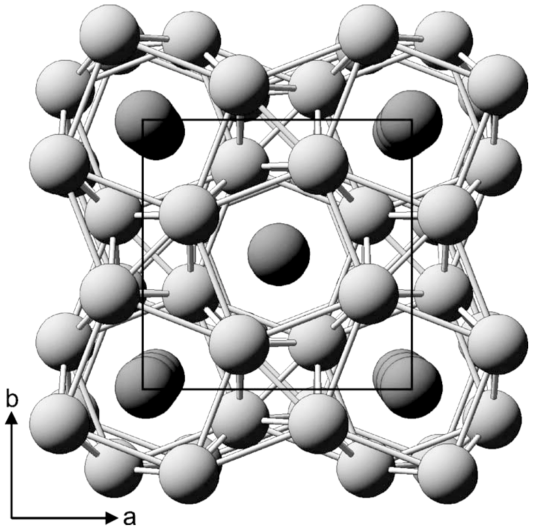

Figure 2.14 *The incommensurately modulated host-guest structure of Sb-II in projection down the c-axis.The host atoms are shown in a lighter shade whilst the guest chains are darker. The incommensurate modulation is not visible in this image as it occurs along the c-axis. Figure from [45]*

Reflections that have indices $(hk0m)$ occur as a result of the guest structure and $(hk00)$ reflections arise from crystal planes that are common to both the host and the guest structures. In the diffraction patterns of these host-guest structures there can be additional reflections that do not occur as a result of the crystal planes in either the host or guest structures. These reflections occur as a consequence of the interaction between the host and guest subsystems, which are incommensurately modulated and are described by indices with both $m \neq 0$ and $l \neq 0$. While this is a very brief description of the superspace formalism that is used to describe these incommensurately modulated host-guest composite structures, the interested reader may find a more detailed description in references [86, 87].

2.3.3 Bragg's Law

Crystal structures can be studied using the diffraction of photons, neutrons and electrons. It is the translational symmetry of the crystal that enables us to use diffraction in this way; the regularly spaced, repeating units act as a diffraction grating for the incident radiation if the wavelength is comparable to the spacing between the units. In this thesis the primary diagnostic used in both the dynamic and static experiments is x-ray diffraction.

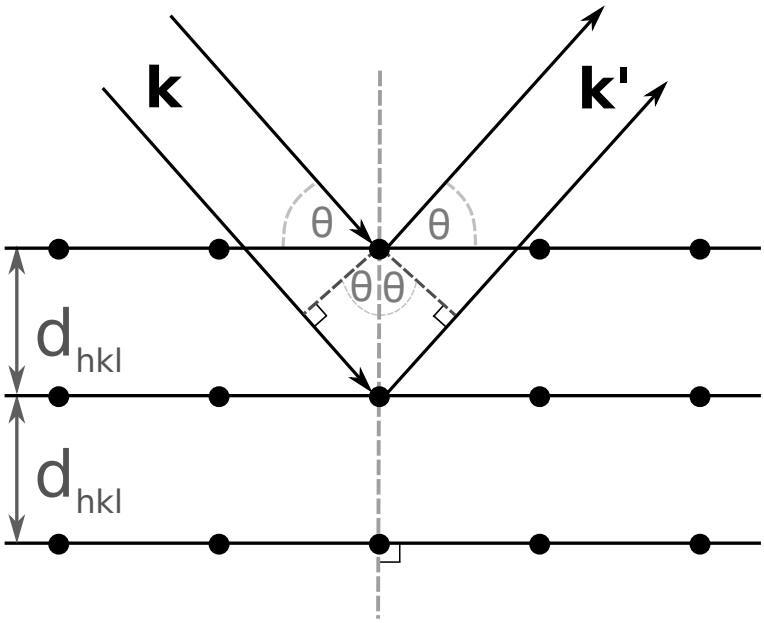

Figure 2.15 *An illustration of Bragg's law. Two incoming x-ray beams are reflected from lattice planes. The path difference between the incoming and reflected beams is given by* $2d_{hkl}sin\theta$ *where* d_{hkl} *is the spacing between the crystal planes and* θ *is the angle between the incoming x-rays and the plane-normal.*

As described above, a crystal can be described in terms of a series of planes which can be be described using Miller indices. The Bragg formalism states that incident radiation is specularly reflected from these planes and when reflections from adjacent planes interfere constructively then diffraction peaks are observed. Figure 2.15 illustrates a scenario in which two incoming x-ray beams (with wave-vector **k**) are incident (at an angle θ to the plane normal) on lattice planes which are separated by a distance of d_{hkl}. They are reflected at an angle equal to the angle of incidence and the resulting, reflected beams are described by a wave-vector **k'**. Bragg's law gives the criteria for constructive interference and is shown in equation 2.20 where λ is the wavelength of the incident radiation and n is some

integer.

$$n\lambda = 2d_{hkl}sin\theta \tag{2.20}$$

In evaluating Bragg's law an important point is reiterated; diffraction can only occur when the wavelength of the incident radiation is of a similar order of magnitude to the crystal lattice - specifically, Bragg reflection can only occur when $\lambda \leq 2d_{hkl}$. Typically, to probe matter on the atomic scale. an x-ray wavelength of approximately 1 Å is necessary; this corresponds to an x-ray energy of 12.4 keV where photon energy is given by $E = hc/\lambda$ (with h equal to Planck's constant and c equal to the speed of light in vacuum).

The inter-planar spacing d_{hkl} can be related to the Miller indices via a series of equations, depending on the crystal system. An example of this is shown in equation 2.21 which describes the relationship between d_{hkl} and the Miller indices for a cubic structure. This relationship is a powerful one; it allows the calculation of lattice parameters from the observation, and correct indexing, of a diffraction peak.

$$d = \frac{a}{\sqrt{h^2 + k^2 + l^2}} \tag{2.21}$$

2.3.4 Structure Factor

X-ray radiation is an electromagnetic wave which is characterised by an electric field that vibrates at constant frequency perpendicular to the direction of motion. The nucleus of an atom is relatively heavy compared with electrons so it scatters x-ray radiation very much less strongly than electrons; the scattering ability of an atom depends purely on the number and distribution of its electrons. It is reasonable, then, to assert that the scattering ability of a material increases with its atomic number. It also follows that the intensity of the Bragg peaks I_{hkl} (the diffracted x-rays) contains information about the positions of the atoms in the crystal. The peak intensity is, in fact, proportional to the structure factor (F_{hkl}) of a material, as shown in equation 2.22.

$$I_{hkl} \propto |F_{hkl}|^2 \tag{2.22}$$

The structure factor is a description of how a material scatters radiation; it is the vector sum of all waves from all atoms in a given unit cell. F_{hkl} is expressed by equation 2.23 where the sum is over all of the N atoms in the unit cell and f_j is the form factor; a term which quantifies the scattering efficiency of the atoms. In this equation x_j, y_j and z_j are the positional coordinates of the atom and have the $\mathbf{a}_1$, $\mathbf{a}_2$, and $\mathbf{a}_3$ lattice vector dimensions and directions.

$$F_{hkl} = \sum_{j=1}^{N} f_j exp\Big[2\pi i(hx_j + ky_j + lz_j)\Big] \tag{2.23}$$

This equation informs us that sometimes there will not be any intensity in a Bragg peak as a result of diffraction from a crystal plane; this is known as a systematic absence. As an example we may consider the face centred cubic (fcc) structure. Here there are four atoms in a unit cell, and we may define the position of these atoms in the unit cell as being on the origin, x_j, y_j and z_j = (0, 0, 0), and one at the centre of each of the adjacent faces, x_j, y_j and z_j = (1/2, 1/2, 0), (0, 1/2, 1/2) and (1/2, 0, 1/2). These values of x_j, y_j and z_j may be substituted into equation 2.23 to yield equation 2.24.

$$F_{hkl} = f\Big(exp\big[0\big] + exp\Big[\pi i(h+k)\Big] + exp\Big[\pi i(k+l)\Big] + exp\Big[\pi i(h+l)\Big]\Big) \tag{2.24}$$

$$F_{hkl} = f\Big(1 + (-1)^{h+k} + (-1)^{k+l} + (-1)^{h+l}\Big) \tag{2.25}$$

Equation 2.24 may be simplified to give equation 2.25 and here we see that F_{hkl} can take only two values: if h, k and l are *all* even or *all* odd then we have $F_{hkl} = 4f$. Any other combination of solutions (i.e mixed parity) will result in a 0 sum. This means that for a fcc structure, only reflections where h, k and l are either all odd or all even are observed; the other reflections interfere destructively and no Bragg peak is observed. A series of selection rules can be calculated similarly using the structure factor for various different crystal structures.

2.3.5 Powder Diffraction

Generally, in the description of diffraction using Bragg's law given in section 2.3.3, we consider a single crystal, for which the diffraction maxima for each plane would appear as a spot of intensity. This is not the case when the x-ray diffraction is performed on a powder sample which contains, ideally, a large number of randomly orientated crystallites. The many orientations of the crystallites about the azimuth (φ), mean that the crystal planes within the crystallites will also be orientated randomly about the azimuth. Rather than a single diffraction spot occurring as a result of diffraction from many identically orientated crystal planes, the result of powder diffraction is the sum of intense spots from randomly orientated crystallites over all azimuthal angles.The sum of these contributions yields a ring of intensity, known as a Debye-Scherrer ring, shown in figure 2.16.

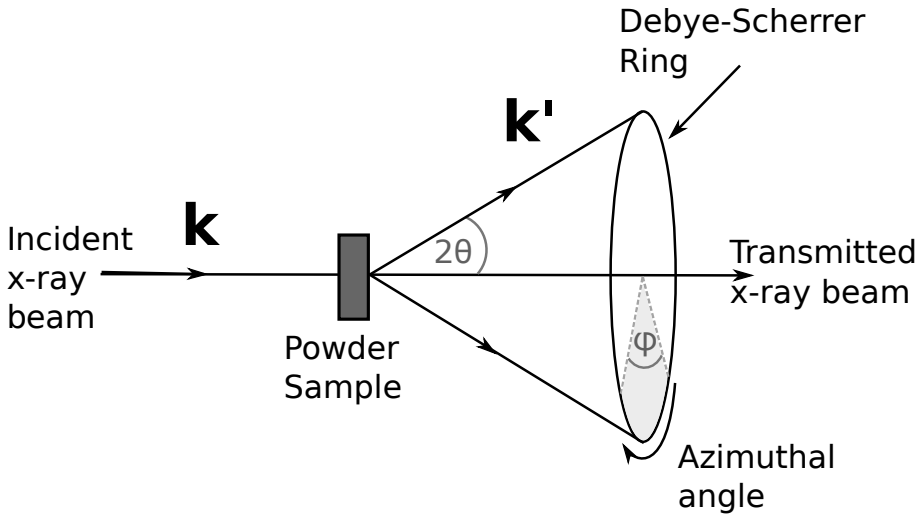

Figure 2.16 *An illustration of diffraction from a crystal plane in an ideal powder sample. The large number of crystallites randomly orientated about the azimuth mean that a ring of intensity is produced by diffracted x-rays; the Debye-Scherrer ring.*

Commonly, powder samples are not 'perfect' in that their grain orientation may be preferential; this is referred to as sample *texture*. When there is preferred orientation within the powder sample, there may not be any crystallites which satisfy the Bragg condition for certain azimuthal angles. If the Bragg condition is not satisfied then there will be no diffracted intensity; for textured samples this means that rather than a smooth Debye-Scherrer ring, the diffraction profile will consist of a spotty ring of varied intensity [88].

2.4 Diagnostics

2.4.1 X-ray Diffraction

The primary diagnostic used in both the static and dynamic compression experiments conducted in this thesis is x-ray diffraction. In this section, the basic operating principles of the two types of x-ray facilities used in this work, namely synchrotrons and FELs, will be briefly described.

Synchrotron X-ray Diffraction - Diamond Light Source

There are several difficulties in using a DAC in conjunction with an x-ray diffraction diagnostic; one such difficulty is the limitation imposed on the 2θ coverage by the edges of the cell. In many cases this can be addressed by altering the experimental geometry, however this is not always the case when additional equipment, for instance a vacuum casing around the cell in the instance of cell heating (see section 2.2.1), is used. In order to attain high quality x-ray diffraction data from a collimated and high-brilliance x-ray source, the data collected during the static compression experiments described in this thesis were collected from a synchrotron facility: Diamond Light Source (DLS).

As was shown in figure 1.7, synchrotrons are sources of high-brilliance radiation. The way that this x-ray radiation is produced at synchrotron facilities is as such: an electron gun is used to generate bunches of electrons via thermionic emission which are accelerated linearly using a pulsed electric field until their energy reaches several MeV [89]. The electron bunches are then accelerated further by being injected into a booster synchrotron until their energy reaches the GeV regime (3 GeV for DLS), at which point they are passed into the storage ring, as shown in figure 2.17. Throughout the whole process, the electrons are kept under vacuum to avoid the collisional losses that would occur if they were travelling through air. When electrons are accelerated to relativistic velocities (approaching the speed of light), they generate electromagnetic radiation; this is the synchrotron radiation which is generated at facilities such as DLS. The storage ring comprises a series of straight sections (24 at DLS) interspersed with bending magnets which maintain the curvature of the path of the electrons within the ring. Synchrotron radiation is produced when a magnetic field curves the path

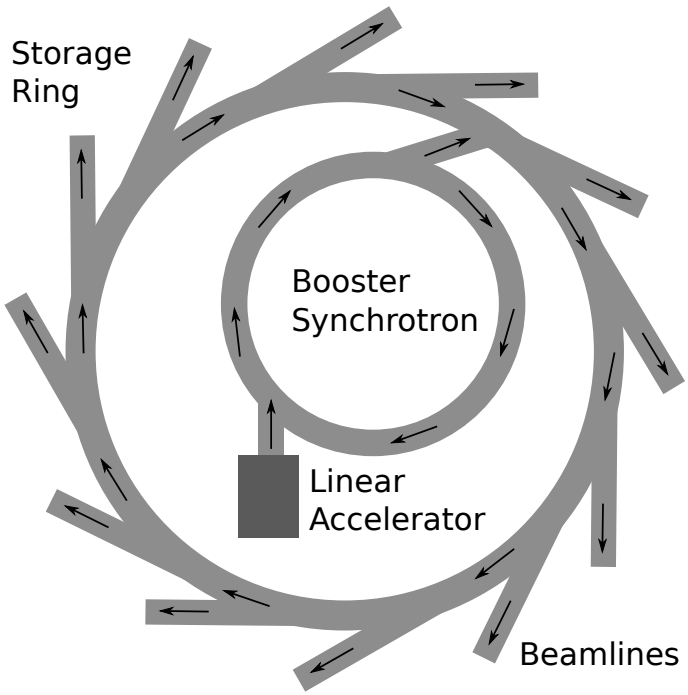

Figure 2.17 *A schematic of a synchrotron facility with the path of the electrons shown by the black arrows. The electrons are initially accelerated in the linear accelerator before being further accelerated in the booster synchrotron. Once their energy is high enough (GeV regime) they are released into the storage ring where they may be accessed by the beamlines where the experiments are conducted.*

of an electron travelling close to the speed of light; radiation is produced over a broad spectrum ranging from infrared to x-rays.

In the straight sections of the storage ring there are various insertion devices; these are magnetic structures used to create x-ray beams. There are two main types of insertion device used in a synchrotron: wigglers and undulators. An undulator consists of a periodic array of dipole magnets with alternating polarity. These magnets produce a magnetic field which acts perpendicularly to the direction of propagation of the electrons. The strength of this perpendicular magnetic field is varied along the path, causing the electrons to oscillate transverse to their direction of motion. The wavelength of this electron oscillation is dictated by the spacing of the magnets, while the wavelength of the emitted radiation depends on the strength of the magnetic field. A wiggler also consists of an array of magnets which repeatedly bend the path of the electron, typically with fewer magnets than an undulator. The radiation which is produced can span a broad range of x-ray wavelengths and may be adjusted by altering the magnetic field [90]. Insertion devices such as undulators and wigglers may be characterised by a parameter

'K' as described in equation 2.26 [91]. Here B_0 represents the on-axis magnetic field, m_e is the electron rest mass, λ_p is the magnetic period and γ is the Lorentz factor.

$$K = \frac{ceB_0\lambda_p}{mc^2 2\pi} = 0.934 B_0 \lambda_p \tag{2.26}$$

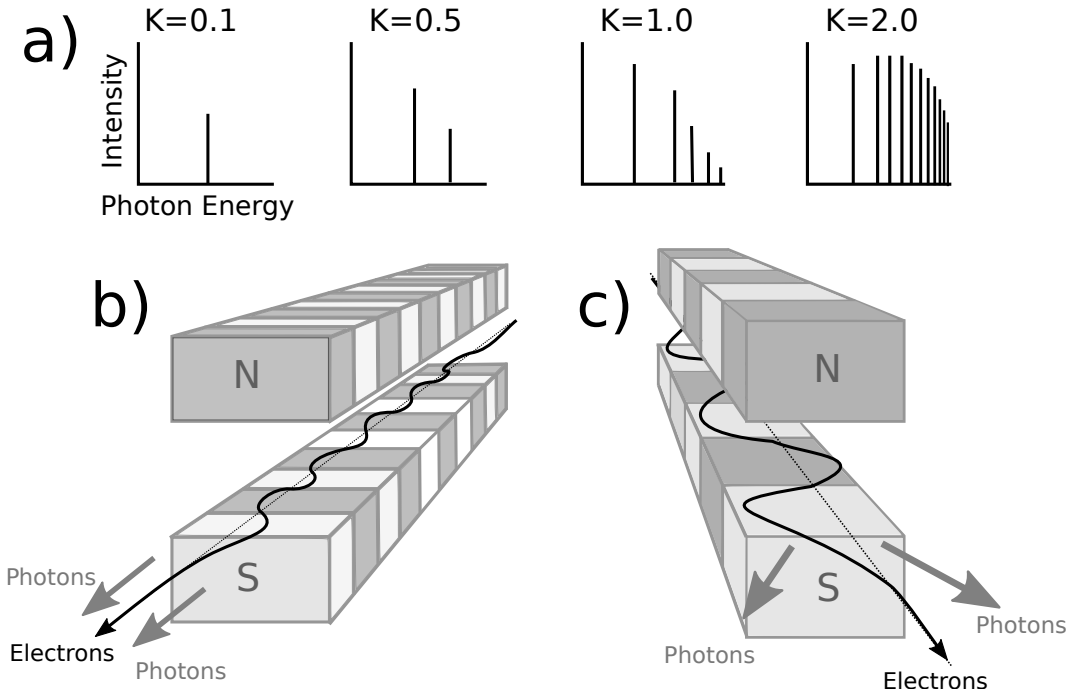

Figure 2.18 *a) Quasi-monochromatic radiation from an undulator source (K=0.1) transitioning to broad band wiggler radiation (image adapted from [91]). b) Undulator radiation source. c) Wiggler radiation source.*

Wigglers have fewer magnets than undulators but typically these magnets are stronger resulting in $K \gg 1$. As shown in figure 2.18, the radiation which is emitted from a wiggler is a superposition of the radiation emitted in each oscillation. The angular distribution of this emitted radiation is dependent on the angle at which the electrons are deflected. Undulators typically have a larger number of dipole magnets than wigglers but operate at a reduced field strength with $K < 1$. In an undulator, the deflection of the electrons is less than that in a wiggler; it is approximately the same magnitude of the angle of emitted radiation resulting in constructive interference between the radiation emitted from each oscillation. Undulators emit a narrow cone of radiation with intensity peaks occurring at specific wavelengths; as shown in equation 2.27, the wavelength of the emitted radiation is proportional to $L/2\gamma^2$ where L is the undulation

period and γ^2 is the relativistic Lorentz factor for the electrons (as described in equation 2.28 where v is the velocity of the electron) [92]. The electron approaches the undulator at relativistic speed (approaching the speed of light) and, due to relativistic effects, the undulator period appears contracted in length by the Lorentz factor γ. In the electron's frame of reference, the emitted wavelength is equal to L/γ. In the laboratory frame of reference, the radiation is Doppler shifted, resulting in a correction factor of 2γ; the combination of these effects results in the γ^2 term in equation 2.27. The undulation period L, is typically a few centimetres in magnitude [93], so in order to generate wavelengths that are in the x-ray regime, it is evident from equation 2.27 that γ is required to be very large. The requirement for a large γ value is the reason that it is vital that the electrons are accelerated to GeV energies.

$$\lambda = \frac{L}{2\gamma^2}\left(1 + \frac{K^2}{2}\right) \tag{2.27}$$

$$\gamma = \frac{1}{\sqrt{1 - \frac{v^2}{c^2}}} \tag{2.28}$$

From the insertion devices the radiation may then be transmitted to a beamline where experiments are conducted; the work in this thesis was conducted on the I-15 Extreme Conditions beamline, which makes use of a wiggler to produce high-energy x-rays up to 100 keV which are necessary for penetrating into the DAC. On the beamline the beam is passed through a monochromator to select the wavelength of the x-rays. Typically, a monochromator consists of a pair of single crystals, orientated so that the Bragg condition is satisfied for the desired wavelength; the I15 beamline at DLS makes use of a Si (111) double crystal monochromator which permits x-ray wavelengths between 20 and 80 keV. A series of mirrors may be used to focus the beam and a pinhole may be used to further reduce the beam size. The DAC is then placed in the path of the beam and diffraction data are collected with the use of a detector (specifically, a Mar345 image plate detector at DLS).

X-ray Free Electron Lasers - LCLS

X-ray free electron lasers (XFELs) are fourth generation light sources which, as shown in figure 1.7, are capable of generating x-ray radiation that has a peak spectral brightness which is 10^9 times greater than conventional synchrotron radiation. The XFEL operational mechanism is as such: a linear accelerator is initially used to accelerate electron bunches to relativistic speeds before they are passed into an undulator as described previously. The radiation produced in an XFEL undulator still obeys equation 2.27, however there is a key difference between third and fourth generation light sources: coherence. In a synchrotron light source, each electron emits radiation independently resulting in a less coherent light source. In an XFEL, the emitted radiation is intense enough to perturb the electron bunches as they pass through the undulator, causing them to form micro-bunches, as illustrated in figure 2.19.

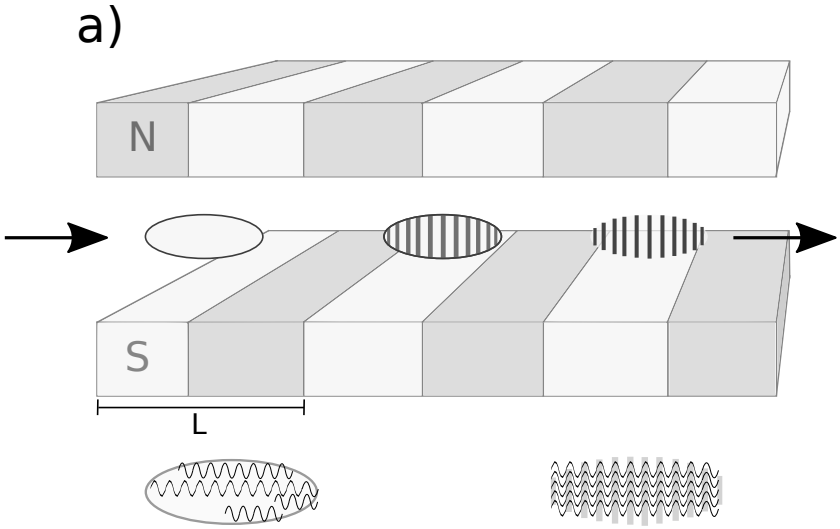

Figure 2.19 *A schematic showing the formation of microbunches in an XFEL undulator. Initially electrons are not microbunched but the interaction between the transverse velocity of the bunch and the transverse magnetic field from the previous bunch causes bunching of the electrons, where the period of the bunches is equal to the period of the emitted radiation.*

After entering the undulator, any given electron will emit a wave, the transverse magnetic field of which, combined with the transverse electron velocity, generates a Lorentz force which pushes the electrons into microbunches (the faster electrons will catch up with the slower ones). Destructive interference occurs between radiation emitted at non-resonant wavelengths, and as the electrons move through the undulator, progressively more electrons bunch together until the number of

coherent photons in each bunch reaches values around 10^{12} with electron energies of up to ∼15 GeV [94]. The periodicity of these microbunches is equal to the periodicity of the emitted radiation. Within a microbunch, the electrons oscillate in phase (as shown in figure 2.19) and consequently their emitted radiation is coherent. The E-field of the waves emitted by the individual electrons sum together, unlike in the instance of incoherent bunches when the intensity of the incoherent radiation is summed. As the wave intensity is proportional to the E-field, the total intensity of the emitted radiation from these coherent electrons is proportional to N^2 rather than N, where N is the number of electrons in the bunch. This process is known as self amplified spontaneous emission (SASE); the emission of radiation by the electrons at the beginning of the undulator acts as seed radiation in the main part of the undulator [95]. The wave intensity is amplified as the bunches progress through the undulator up to some saturation point which exists due to energy losses in the electrons as they transfer energy to radiation and consequently decelerate with respect to the x-rays [92]. The wavelength of the produced radiation may be tuned by altering the undulator magnetic field amplitude or period; this is advantageous in that it allows experiments to be conducted with various different x-ray energies.

The increase in intensity of the emitted radiation is exponential in nature, meaning that sufficient radiation is produced after a single pass through the undulator; this differs from conventional laser systems where mirrors are used to create cavities to allow more passes through the system. The sufficiency of this single-pass through the undulator is actually vital to the practical realisation of XFELs as, due to the high-energy nature of x-rays, they penetrate mirrors rather than being reflected by them and as such, constructing a laser-cavity for x-rays would be incredibly difficult. The research described in the dynamic experiments in this thesis was conducted at the Linac Coherent Light Source (LCLS) in Stanford, the world's first hard XFEL. The undulator hall at this facility is 132 m long, housing thousands of magnets. The radiation energy may be tuned to any value between 2.5 and 12 keV in the 1^{st} harmonic, with pulse lengths varying from 50 to 300 fs.

After passing though the undulator, the electrons are collected in a beam dump with the use of an electromagnet while the x-ray beam progresses to the end station where experiments are conducted. This experiment was conducted at the Matter in Extreme Conditions (MEC) end station of LCLS. The samples were compressed using a dual arm Nd:Glass optical laser, where pulses in each arm

can vary between 1 to 25 J and 2 to 200 ns. A full description of the MEC end station is available in reference [96]. Details of the MEC setup during the data collection in this thesis are given in section 3.2.

2.4.2 X-ray Diffraction Data Refinement

Once diffraction data hve been collected, the raw diffraction images (from either the Mar345 detector at DLS or the Cornell-SLAC pixel array detectors (CSPADs) at LCLS) may be integrated to give 1-D line outs. Le Bail [97] and Rietveld [98] refinements may be conducted in order to optimise the lattice parameters and determine the best fitting structural model. Both Le Bail and Rietveld refinements make use of least-squares fitting procedures to optimise the fit between observed and calculated data. The calculated data is based on an initial structural model which, in order for the fitting to be successful, must be close to the final solution. For Le Bail refinement the symmetry and space group of the structure must be defined along with initial approximations of the unit cell lattice parameters a, b, c, α, β and γ. These parameters are used, along with some arbitrary initial peak intensity, to calculate a structure factor to initialise the refinement. A least-squares fit is then performed to minimise the residual between the fit an the observed data, generating new calculated lattice parameters. Le Bail fitting is an iterative process and the newly calculated lattice parameters are used to determine a structure factor which is used to initialise the next iteration until the observed and calculated intensities are in good agreement. As well as refining the lattice parameters and the intensity, peak width and peak shape may also be refined using the Le Bail method.

While the Le Bail method allows us to fit the lattice parameters, the calculated intensities do not depend on the structural model so it does not inform us about the atomic positions; for this a Rietveld refinement must be conducted. The lattice parameters and peak shape parameters, as determined from a Le Bail refinement, are used to initialise a Rietveld refinement in which the peak intensities are derived from the atomic positions. This process involves refining the atomic positions and displacement parameters.

2.4.3 VISAR

Pressure states within a target may be determined from velocimetry information : knowing the rear surface velocity of a shocked target enables us to calculate pressure using the Rankine-Hugoniot Equations and an EOS, as described in section 2.1.2. In addition to this, the wave profile determined form the rear surface of the target are very useful in observing phase transitions and melting behaviour of dynamically compressed materials. In many of the early dynamic compression experiments described in section 1.4.2, the velocity of the rear surface of a dynamically-compressed target was measured via physical contact with a series of electrical pin contacts, as shown in figure 2.20. The "I" pins were placed at the Sb-air gap interface in order to measure the time at which the shock wave enters the target while the "A" pins were placed at measured distances away from the Sb target [49].

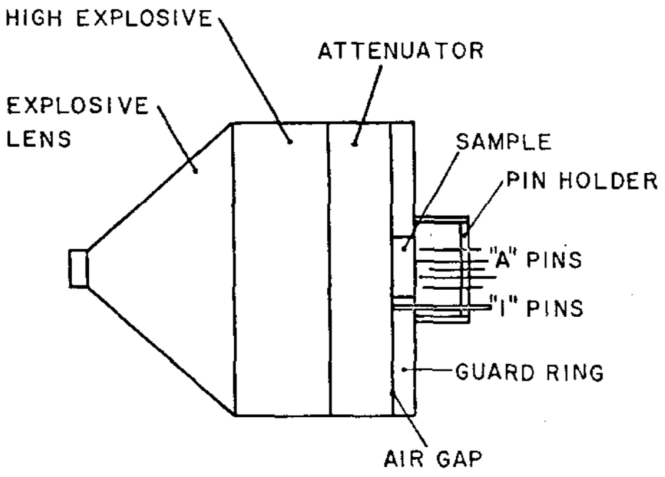

Figure 2.20 *An early method of measuring the rear surface velocity of an explosively shocked target. The metal pins detect contact with the rear surface of the target. Image taken from [49].*

Presently, more sophisticated methods are used to determine the rear surface velocity of a shocked sample: one such method is interferometry. The Velocity Interferometry System for Any Reflector (VISAR) system uses coherent light, typically from a 532 nm laser, which is incident on the rear surface of the target. In order for the diagnostic to be operational the rear surface of the target must be reflective; if this is not the case then it is common practice to "flash" coat it with a thin layer of a reflective material such as aluminium. The reflected light is then split and passed into two Mach-Zender interferometers where, in each interferometer, the beam is split again and traverses two different paths which

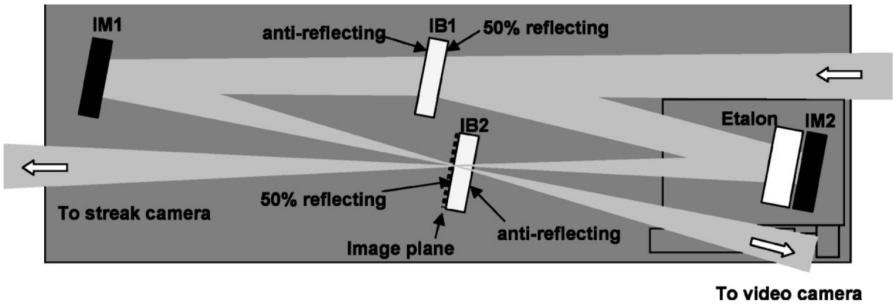

Figure 2.21 *A schematic showing a Mach-Zehnder interferometer used in the VISAR diagonstic. The incident beam enters a beam splitter and travels through two paths of the same geometrical path length but different optical path length. An etalon may be used to control the optical path length of one of the beams. They are then recombined before leaving the interferometer. Image taken from [99]*

have the same geometrical path length but different optical path lengths. An etalon (commonly made of fused silica) may be used to vary one of the optical path lengths; the optical time delay τ is given by equation 2.29 where h is the etalon thickness, n is the refractive index of the etalon and c is the speed of light [99].

$$\tau = \frac{2h}{c}(n - 1/n) \tag{2.29}$$

The two beams are then combined before leaving the interferometer, as shown in figure 2.21, and produce an interference fringe pattern. The fringe pattern from each interferometer is recorded on a streak camera with high temporal resolution, as shown in figure 2.22. As the target encounters the compression wave, its particles are accelerated typically to several kilometres per second which induces a Doppler shift in the interference fringes recorded by the streak camera. The magnitude of the fringe shifts allow us to calculate the velocity of the rear surface of the target using equation 2.30 which describes the velocity per fringe (VPF). Here λ represents the wavelength of the incident laser light and δ is a term which accounts for dispersion in the etalon (0.0318 for a 532 nm incident laser wavelength).

$$VPF = \frac{\lambda}{2\tau(1 + \delta)} \tag{2.30}$$

We see that the sensitivity of the fringe shifts is dependent on the optical time

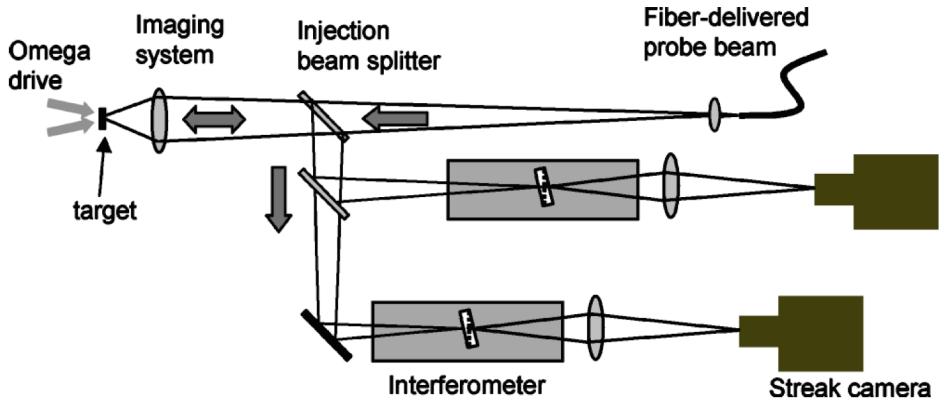

Figure 2.22 *A diagram showing the basic setup for the VISAR diagnostic at the OMEGA laser facility. Image taken from [99]*

delay introduced by the etalon in the interferometer. Such fringe shifts are shown in Figure 2.23 for both shock and ramp compression. As expected, the discontinuity in pressure which is characteristic of a shock wave is visible as a discontinuous jump in the fringes (and velocities) of the shocked sample. The ramp compression is characterised by a smoother shift in the interference fringes which corresponds to the more gradual increase in pressure.

In the case of a shock wave, the discontinuous jump in the fringes looks identical for integer multiples of fringe jumps, it is for this reason that a second interferometer, with a different etalon and thus different VPF, is used. Figure 2.24 illustrates the necessity for a secondary interferometer. A rear surface velocity profile is obtained from the interference fringes by means of a fast Fourier Transform (FFT). There are multiple different solutions for the rear surface velocity from channel 1, it is not until it is compared with the possible solutions from channel 2 (whose interferometer has a different etalon that does not have a thickness that is a multiple of the first etalon) that one obvious solution where the two agree is found.

In the experiments conducted in this thesis, two types of targets were utilised, one with Sb on the rear surface and one where a LiF window was attached to the rear surface, as described in section 2.1.3. In the instance when the rear surface of the target is a LiF window, the velocity measured by the VISAR diagnostic is the particle velocity u_1 at the interface between the Sb and the LiF. Knowledge of the impedance of the materials and the Hugoniot curves allows the particle velocity in the Sb sample to be calculated. In the instance that a LiF rear window was not used in the target design, equation 2.31 was used to approximate the free

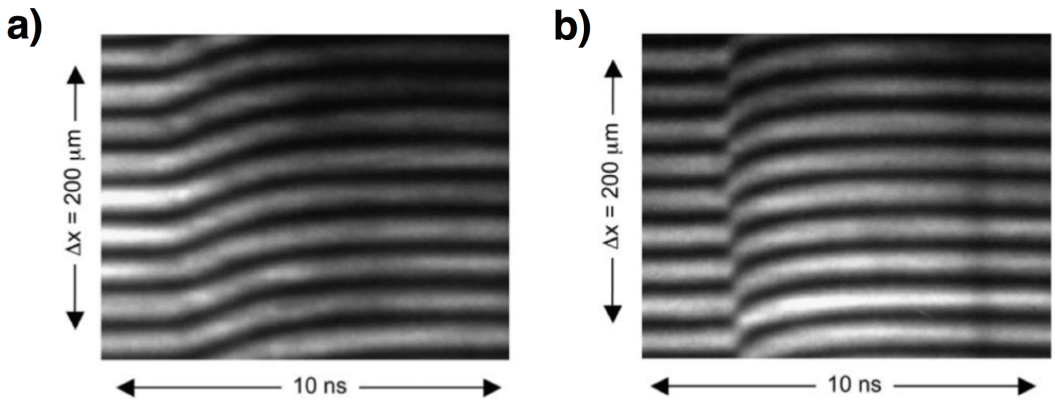

Figure 2.23 *VISAR interference fringes for ramp (a) and shock (b) compression. Image taken from [100]*

surface velocity U_{FS}, the velocity of the rear surface of the target in a vacuum.

$$U_{FS} = 2u_p \tag{2.31}$$

Once the value of u_1 has been determined, is is possible to calculate U_s and then pressure using equations 2.12 and 2.9. The theory of the VISAR analysis technique is discussed in more detail in Dolan's 2006 report 'Foundations of VISAR analysis' [101].

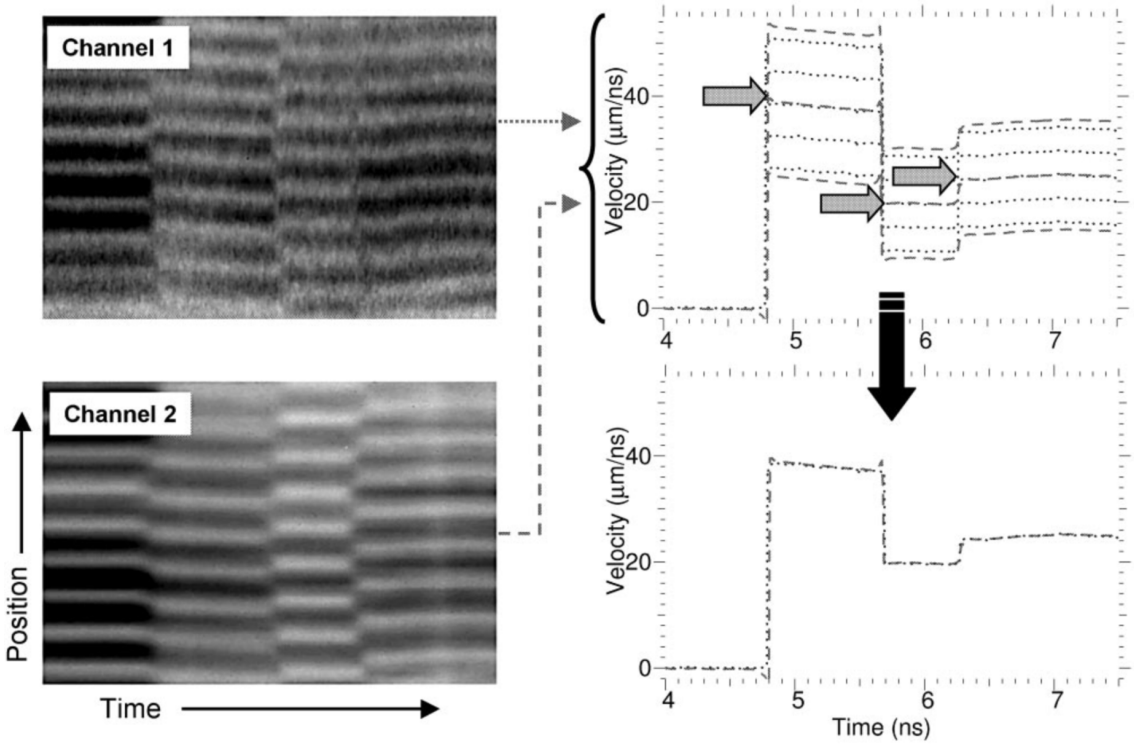

Figure 2.24 *VISAR interference fringes for a shock compression event from two separate interferometers. The upper, right pane shows the possible rear surface velocity profiles from channel 1 (dotted lines) and channel 2 (dashed lines). The lower right panel shows the true solution where the profiles from the two interferometers agree. Image taken from [99].*

Chapter 3

Dynamic Compression of Sb at LCLS

The energy loading associated with shockwave compression is incredibly rapid and it has been shown that atoms can mobilise and rearrange themselves on the picosecond timescale [102]. However, until recently, the formation of structures that exhibit extremely high complexity (such as incommensurate host-guest structures) had not been observed on dynamic compression using x-ray diffraction techniques. The ability to resolve complex structures requires x-ray diffraction data of the highest quality, and it is only through a concerted effort in improving x-ray diffraction techniques for ultrafast experiments [103, 104] that such data is accessible to us presently. The ability to obtain extremely high-quality diffraction data on the short timescales of dynamic compression has been exemplified in recent work by Briggs *et al.* who reported observation of an incommensurate host-guest phase in Sc with disordered chains [57].

Prior to the work described in this thesis, there had been no dynamic compression experiments conducted on Sb in which x-ray diffraction data were collected; all structural information in the previous dynamic studies was inferred from static compression experiments. From static experiments it is known that the Sb-II phase has an extremely complex structure (the incommensurate host-guest structure) and so, in order to identify this phase under dynamic compression, it is vital that the data collected is of the highest quality.

This chapter discusses the dynamic compression of Sb at the Matter in Extreme Conditions (MEC) end station of the LCLS in May 2016 [96] and details the ways

in which the data quality was optimised. The experimental set up, including laser drive specifications, target design, and experimental methods, are presented along with a description of pressure determination and overview of experimental data. Unless otherwise stated, the data discussed in this section were collected on compression (before the compression wave had reached the rear surface of the target) and was compressed by a shock wave. The Rankine-Hugoniot equations were found to be appropriate for analysis. The observed phase transitions are discussed along with a brief overview of data collected on release.

3.1 Experimental Set-Up

3.2 The Matter in Extreme Conditions (MEC) Chamber

The dynamic compression data reported in this thesis were collected at the Matter in Extreme Conditions (MEC) end station at the LCLS. As discussed in section 2.4.1, electron bunches are generated in the injector and accelerated to relativistic speeds by the linac before passing into the undulator where they generate x-ray radiation. The undulator hall at the LCLS is 132 m long, and the MEC station (one of seven stations at the LCLS) is situated at the far experimental hall, shown in figure 3.1.

Figure 3.1 *An aerial view of the LCLS. The MEC end station is located at the end of the far experimental hall [105].*

Laser compression experiments are conducted in vacuum conditions to avoid interaction between the incident laser pulse and air during ablation. Figure 3.2 shows the geometry of the vacuum chamber at MEC which is ∼2 m in diameter: the drive laser (shown in green) is incident on the target, as is the XFEL (shown in red). The target plate holder was positioned in the chamber between the Cornell-SLAC pixel array detectors (CSPADs) and the incident drive laser (100 to 500 μm spot size) and XFEL beam (50 μm spot size) as shown in figure 3.2 and again in figure 3.3. This meant that the diffraction data were collected in a transmission geometry, so data collected on compression would contain diffraction peaks from uncompressed material ahead of the shock front.

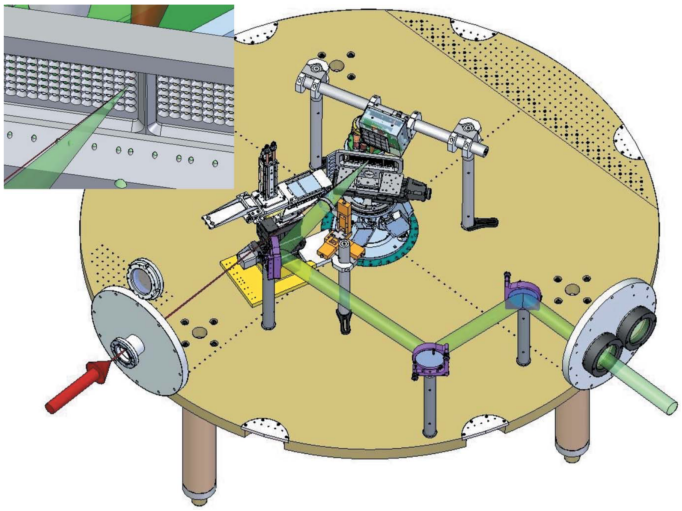

Figure 3.2 *Typical experimental setup at MEC. The target holder (detailed in the inset) is positioned at the centre of the vacuum chamber and the drive laser and XFEL (green and red respectively) are focused on the targets with the CSPAD detector positioned in transmission geometry. Image from [96].*

At MEC there are a variety of 'standard configurations' of the chamber that may be chosen by users ahead of their experimental campaign. The use of these means that the facility runs efficiently; teams who wish to use the same configuration are scheduled to run experiments successively so that minimum time is spent reconfiguring the chamber. For many materials, the 2θ location of diffraction peaks may be simulated ahead of the experiment and a standard configuration (and x-ray energy) may be selected so that these peaks are detected optimally. The configuration of CSPAD detectors used for the collection of data reported in this thesis (collected in May 2016) is shown in figure 3.3. This configuration of detectors meant data could be collected between 20 and 100° in 2θ.

The diffraction signal is detected on each of these CSPADs and these data

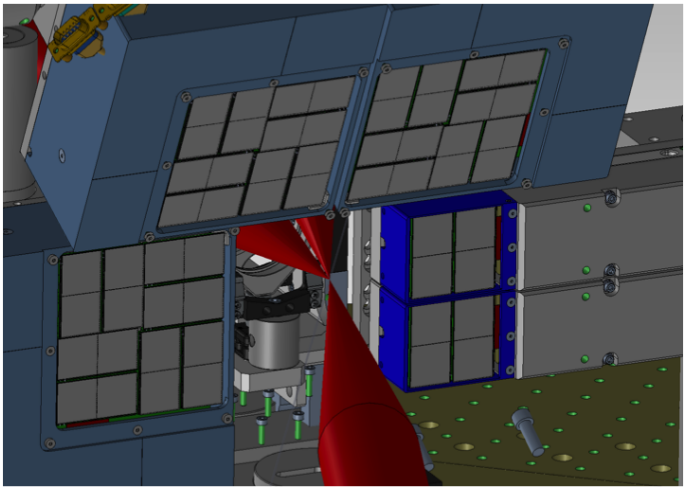

Figure 3.3 *A CAD image showing the standard configuration of the CSPADs used at MEC in May 2016 [106].*

must then be combined so that contributions from all of the detectors are included in the integration of the diffraction pattern. In order to combine the information from each of the CSPADs, they must be carefully calibrated. Prior to beginning an experimental campaign, diffraction patterns are obtained from standard x-ray diffraction calibrants such as CeO_2, MoO_3 or LaB_6 whose diffraction patterns are well characterised; this is used to calibrate the detectors [107]. As mentioned previously, the transmission geometry means that any data collected on compression will contain diffraction signal from uncompressed material. These uncompressed peaks may be used to check the calibration of the CSPADs (if the x-ray energy is known) as the lattice parameters of uncompressed Sb have been well characterised [43].

Figure 3.4 shows diffraction from an Sb target collected at MEC. The constituent signal from all of the CSPADs has been combined and the data has been transformed so that the Debye-Scherrer rings appear as straight lines. This figure highlights the importance of selecting an appropriate standard configuration; the lack of a large plate detector means that there are substantial gaps in the collected data.

As well as calibrating the CSPADs, it is incredibly important to align the incident beams on the target. A yttrium-aluminium-garnet (YAG) crystal may be placed in the target holder and, utilising its fluorescent properties, can be used to align the drive laser and the XFEL so that x-ray data is collected from the precise section of the target where the drive is incident.

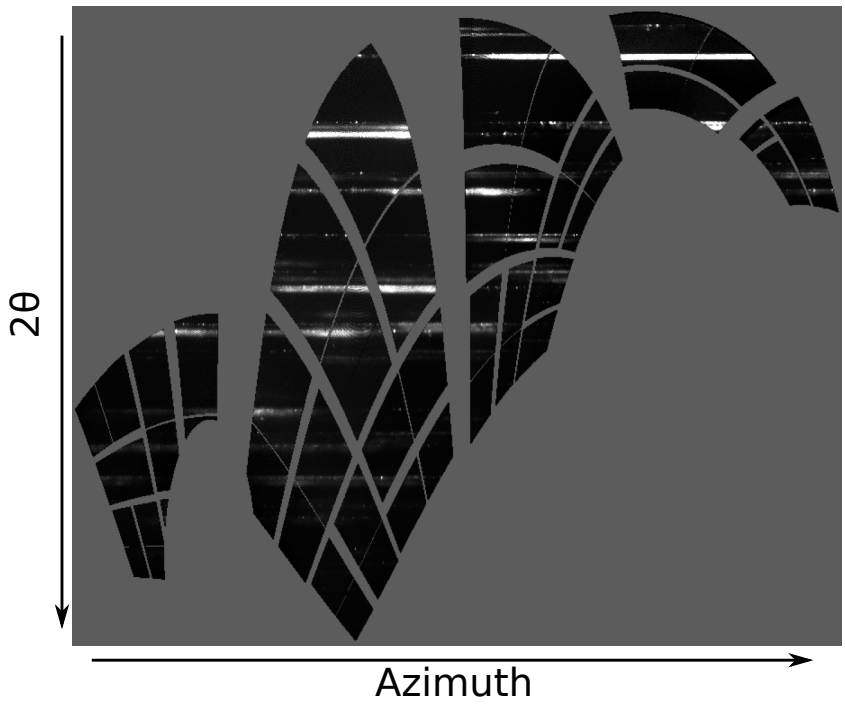

Figure 3.4 *Raw diffraction data showing the detector coverage at MEC in the 2016 experimental campaign. The signal from the CSPADs has been transformed so that the Debye-Scherrer rings appear as straight lines. The diffraction is taken on compression from a Sb target shocked to 1.9 GPa (ambient peaks are also present). Variations in the intensity around the Debye-Scherrer rings indicate the presence of texture within the sample. Note the areas of azimuth - 2θ space not covered by the four detectors.*

MEC also provides a VISAR diagnostic and this was used during the experiment. This diagnostic makes use of a 532 nm wavelength laser which is incident on the rear surface of the target, at an angle normal to the target surface. An optical camera was also positioned in the target chamber so that the rear surface of the targets could be viewed from the control room prior to being shot by the laser. This meant that any targets that appeared damaged or dislodged could be rejected.

3.2.1 Drive Laser

At MEC the Nd:Glass, long-pulse optical drive laser operates as a two arm system. Each of the arms (labelled AB and EF) can provide a pulse with energy between 1 and 25 J and a pulse length between 2 to 200 ns. These arms can be used successively, permitting a shot to be taken every 3.5 minutes, or they may be used in unison for higher energy drive pulses, allowing a shot to be taken every 5

minutes. A combination of single-arm and multi-arm shots were taken throughout the Sb experiment with drive energies ranging from 1.8 to 20 J. The drive pulse length used in this experiment was 20 ns, meaning that the drive was maintained until after the shock wave had traversed the entirety of the Sb layer in the target.

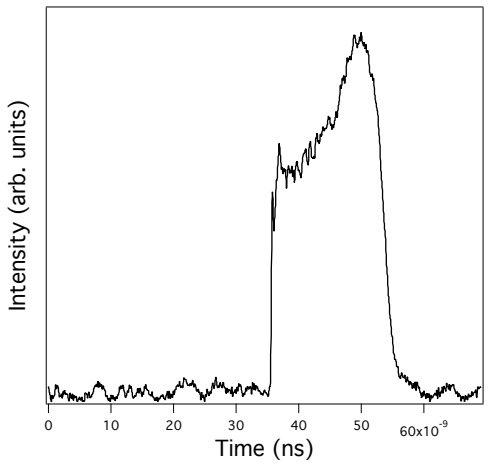

Figure 3.5 *A typical quasi-flat-topped drive pulse from the MEC Nd:Glass drive beam.*

As discussed in section 2.1.1, a shockwave is driven by a pulse with a sharp rise in intensity to a near-constant state; a more gradual increase in intensity will result in ramp compression. The pulses used in this experiment were characterised by a rapid (100 ps) rise in intensity followed by a more gradual rise in the intensity over the duration of the pulse; these are referred to as quasi-flat-topped pulses, an example of which is shown in figure 3.5. These quasi-flat topped pulses have been shown to yield constant values of ablation pressure when plastic ablators are used [70, 108].

Phase plates are used to promote homogeneous intensity distribution in an incident laser pulse [109]. This experimental configuration did not make use of phase plates as a previous experiment conducted at LCLS in May 2015 found their quality to be poor. Instead, the drive beam spot size was defocussed to between 100 and 500 μm. As no phase plates were used, the shape of the incident drive spot was checked at regular intervals during the experiment. In 2015 it was found that the phase plates contributed to drive instabilities due to localised regions of high intensity within the laser spot. Regions of higher intensity in the drive beam mean that these areas of the target are driven more strongly, leading to a non-planar shock front propagating in the material and subsequent spatial pressure gradients in the target. These spatial pressure gradients significantly complicate the analysis of the data and make interpretation of the pressure states within

the target decidedly more complex. As well as acting as a heat shield, another advantage to using a 50 μm thick ablator layer is that it smooths small-scale variations in the the drive beam [70].

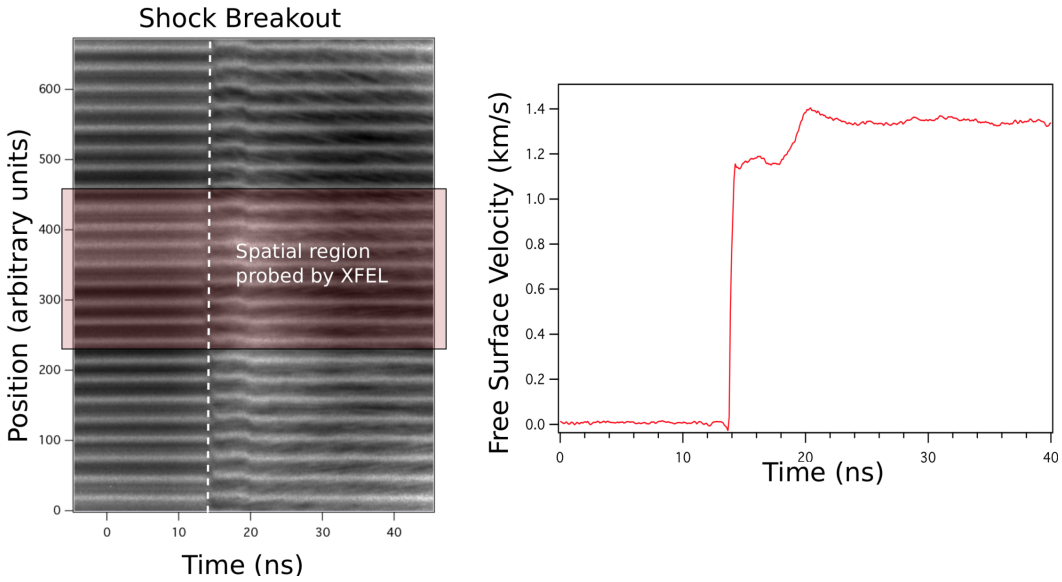

Figure 3.6 *Typical interference fringes (left) and rear surface velocity profile (right) from a shocked target at MEC. This profile corresponds to a pressure state of 12 GPa.*

The planarity of the drive may be assessed using the VISAR diagnostic. Figure 3.6 shows interference fringes as recorded on the streak cameras and the corresponding wave profile of a typical shot. The area highlighted in red indicates the section of the target that was probed by the 50 μm $\times$ 50 μm XFEL beam, the analysis of the interference fringe movement is conducted in this region to ensure that the VISAR and x-ray diffraction data are measuring the same pressure state. The rear surface velocity profile shows an additional jump in velocity at around 20ns, this is due to re-shock within the target caused reflected waves travelling from the Sb/vacuum interface, back to the Sb/kapton interface and again back to the rear surface of the target.

In a small number of low-pressure shots there was a certain amount of non-planarity in the shock breakouts shown in the VISAR data. In the case of extreme non-planarity, these shots were rejected from the data set as they do not represent a well-defined pressure state. Small variations in the time of breakout are represented in the calculated values of pressure by larger error bars as the VISAR velocity data used in the calculation (discussed in section 3.3) has a greater uncertainty. In the instances were the non-planarity occurred at the upper and lower edges of the VISAR image, possibly due to delamination of the

target, there was less of an issue as the VISAR analysis was conducted over the middle section of the streak camera only.

3.2.2 Target Design

The targets used in these experiments consisted of 8 to 10 μm of antimony deposited onto a 50 μm thick black kapton ablator. These deposited targets were fabricated by Paul Mirkarirmi of the Lawrence Livermore National Laboratory. Because of the high shot rate at the LCLS, it was vitally important that the targets could be produced in large quantities, with a high level uniformity between targets. As discussed in section 2.1.3, it is common to bond layers of a target together with a glue layer; any variation in the thickness of which will affect the propagation time of a shock front through a target. In the interest of timing an x-ray pulse correctly so that a diffraction image is taken once a shock front has progressed a certain distance through a target, uniform glue layers are of extremely high importance. In this experiment, the deposition of Sb directly onto the ablator material meant that variation in timing in the targets was much less of an issue. The deposition of the Sb was not entirely uniform across the targets, with thicknesses of Sb varying between 8 and 10 μm. However, each target was characterised with the use of a micrometer and the 10 μm targets were selected preferentially. Furthermore, the deposition process meant that there was a notable amount of fibre texture present in the targets. This is illustrated in the diffraction data shown in figure 3.4 where the Debye-Scherrer rings are not smooth and uniform as is expected of diffraction from a perfect powder (see section 2.3.5) but rather they have significant variations in intensity around the azimuth.

In the interest of characterising this texture, a series of focused ion beam (FIB) images were taken of the Sb targets, as shown in figure 3.7. The images were taken using a Zeiss energy selected backscatter detector (EBS). These images show columnar grains with widths on the order of 0.5 μm. Figure 3.7a) shows the side profile Sb target with a protective coating on the top of the target after milling and these long grains can be seen to extend into the target along the direction of compression. Figure 3.7b) shows the uncoated rear surface of the target.

One of our collaborators, Dr D. R. McGonegle, of Oxford University, calculated the position of the diffraction peaks if the sample had a fibre texture where the c-axis was parallel to the sample normal and found that it agreed well with the

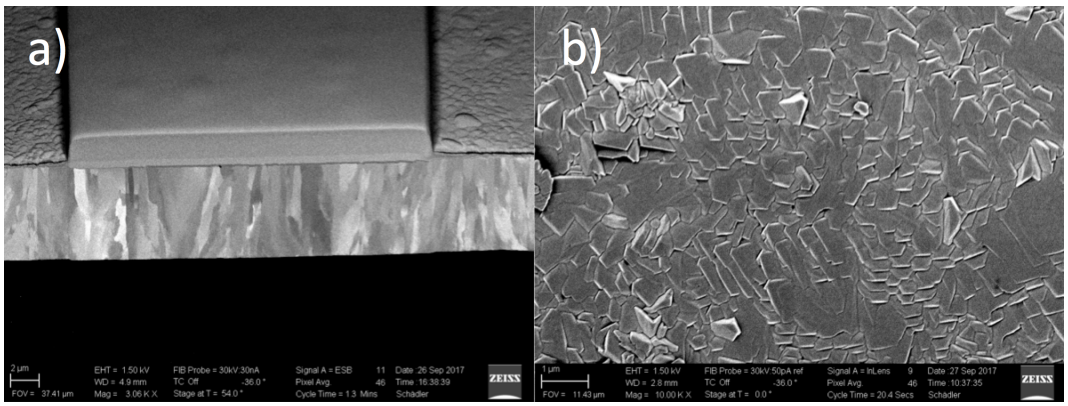

Figure 3.7 *FIB images taken using a Zeiss energy selected backscatter detector. Both the side profile (a) and flat face (b) of the Sb target are shown with the presence of columnar grains.*

ambient diffraction data collected from the Sb target as shown in figure 3.8. As the compression of the targets occurs normal to the front face, this indicates that the samples are compressed along the *c*-axis. Additionally, the texture width was found to be ∼15 degrees. In a perfect fibre textured sample (with a fibre width of 0), all grains have a fibre orientation parallel to the sample normal (and random azimuthal angle). A ∼15 degree width indicates that there is some distribution of the angle between the fibre direction of each grain and the sample's normal.

As shown in figure 2.7, the 10 μm thick Sb samples absorb around 60% of the incident 10 keV x-rays; the x-ray diffraction from the 10 μm targets was sufficient to resolve even the most complex structure (the incommensurate host-guest structure of the Sb-II phase). In an experiment conducted at LCLS in May 2015, some Sb targets were shock-compressed and probed using 8.8 keV incident x-rays. These targets were also fibre-deposited onto a black kapton layer though the thickness of the Sb layer was considerably less, ∼4 μm. The diffraction signal from these targets was not sufficient to perform any meaningful data analysis. Some of the deposited thicknesses of the Sb layers in the targets from this initial run reached ∼12 μm though there was significant delamination in these targets, rendering them unusable.

Several targets were constructed with a rear 500 μm thick LiF window which was flash coated with a thin ∼ 100 nm Al layer at the Sb interface, as illustrated in figure 2.8. These LiF windows were attached using glue; as the shock front has traversed the entirety of the material of interest by the time it reaches this interface, the uniformity of the glue layers is not of great importance. Nonetheless, a micrometer was used to characterise the glue layers and they were found to be

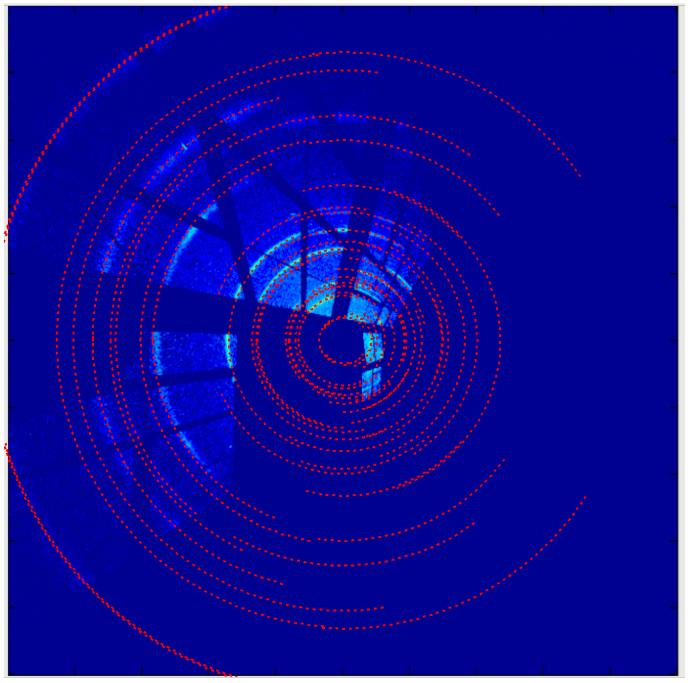

Figure 3.8 *An overlay of an ambient diffraction pattern taken from the Sb target across the CSPADs (2θ increasing radially outwards from the centre) and the calculated diffraction intensities with a fibre texture where the c-axis is parallel to the target normal.*

$\sim$1 μm with a variation of approximately 1 μm. As well as lessening the release of the pressure at the rear of the Sb layer, these flash coated LiF windows are useful when melting occurs in the target. When the material of interest transitions in to a liquid phase there can be an associated loss of reflectivity at the rear surface meaning that the VISAR diagnostic is no longer viable. If there is a flash coated LiF window in contact with the melted sample, its movement will be detected by the VISAR diagnostic.

Once constructed, the targets were mounted, with uniform orientation, onto target plates using UV-curing glue. The target plates were then screwed into the target plate holder as shown in figure 3.9. The capability of the target holder to accommodate a large number of targets is incredibly useful; the experiment is conducted in a vacuum chamber (with a typical vacuum of 10^{-5} mbar) which must be vented in order to make changes within the chamber and this is a time consuming process. The equipment is set up such that the vacuum chamber is vented as little as possible over the course of a 12 hour shift, to wit: the target plate holder is placed on a mechanical stage which may be operated remotely so that successive targets may be placed in the path of the beam from the control room.

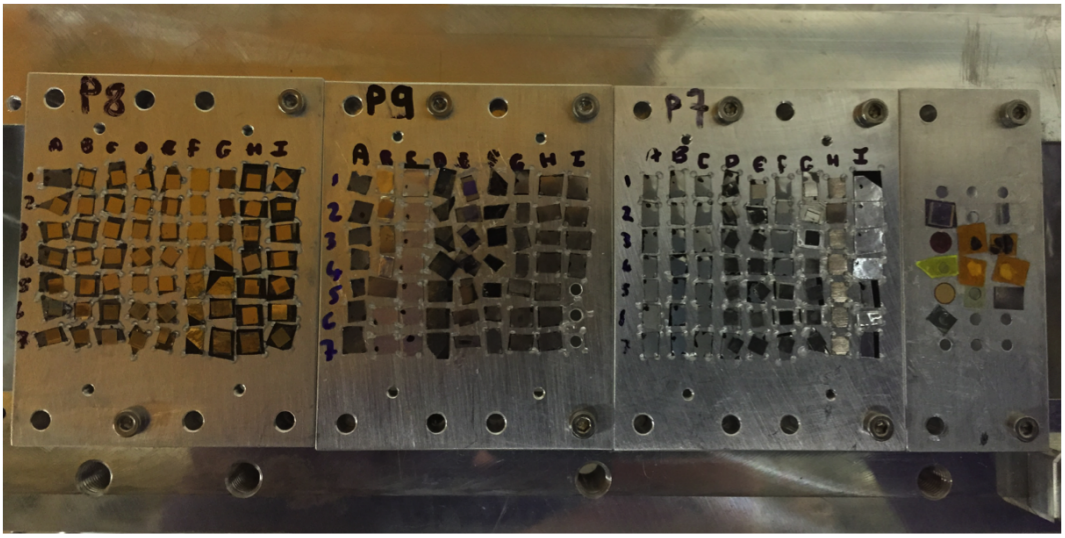

Figure 3.9 *Target plates (labelled P7, P8 and P9 mounted on the target plate holder along with the calibrant targets to the right.*

3.3 Pressure Determination

Establishing an EOS

The pressure can be calculated from the rear surface velocity, measured using the VISAR diagnostic, with the use of an EOS model and the Rankine-Hugoniot equations, as described in section 2.4.3. An EOS can be constructed from preexisting experimental data; for Sb we have used data collected above 20 GPa from McQueen and Marsh [48] and data collected below 20 GPa from Warnes [49]. The data from Warnes includes a distinction between two plastic compression waves, the implications of this for our experiment are discussed further in section 3.5.2. Figure 3.10 shows the McQueen and Warnes data along with an EOS based on a single U_S-u_p relation fitted to the data set (shown using a dashed line) and a three-part EOS fitted to the data set (shown using a solid line).

The three part EOS is constructed as follows: below u_p= 0.50 km/s (10.6 GPa), a linear U_S-u_p relation (see equation 2.12) described by equation 3.1 accurately fits the data. This includes the ambient bulk sound speed of 2.50 km/s which is calculated using the ambient density (6.698 g/cm^3) and bulk modulus (42 GPa) of Sb. Above u_p = 0.62 km/s, the linear U_S-u_p relation is described by equation

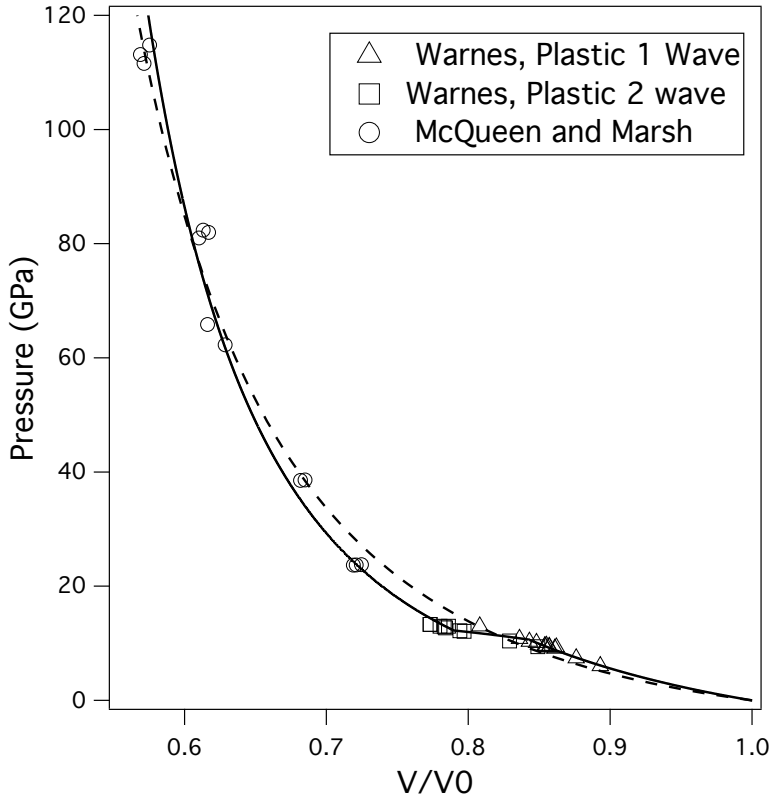

Figure 3.10 *The dashed line shows the EOS calculated using a single U_S-u_p relation and the solid line shows the three-part EOS. The data points from Warnes [49] and McQueen and Marsh [48] are shown as triangles, squares and circles on the plot.*

3.2, and these two regimes are joined by a linear interpolation in U_S-u_p.

$$U_S = 2.50 + 1.36u_p \qquad (u_p < 0.5km/s) \tag{3.1}$$

$$U_S = 1.93 + 1.65u_p \qquad (u_p > 0.62km/s) \tag{3.2}$$

$$U_S = 2.25 + 1.50u_p \qquad (all\ u_p) \tag{3.3}$$

The Sb EOS determined using a single U_S-u_p fit is defined by equation 3.3. From these U_S-u_p relations the pressure may be calculated using Rankine-Hugoniot equations, specifically pressure may be calculated using equation 2.9 and volume using equation 3.4. These calculations allowed the construction of the PV curve

shown in figure 3.10.

$$V = \frac{U_S - u_p}{U_S \rho_0} \tag{3.4}$$

VISAR Pressure

Once this EOS had been established it could be used to determine the pressure of the Sb sample from the VISAR diagnostic. The streak cameras used as part of the diagnostic measured the motion of the interference fringes over sweep windows of either 50 or 20 ns duration. The majority of the data were collected using the 50 ns sweep windows as, even though this provides poorer temporal resolution, it was easier to time the data collection so that the shock breakout occurred within the sweep window of the streak camera. As discussed in section 2.4.3 the motion of the interference fringes was used to measure the rear surface velocity, from which the particle velocity u_p was determined using the assumption that the rear surface velocity is equal to $2u_p$. From this the shock velocity U_S was calculated using the EOS, meaning the pressure could be calculated using the Rankine-Hugoniot relations, as described in equation 2.9. The validity of the $2u_p$ assumption for a free surface is shown by the agreement between the LiF and non-LiF data points. The agreement between these data points in Sb is shown in figure 3.40 towards the end of the chapter. This use of the $2u_p$ approximation is also reported in recent research published on high-pressure Sc [57].

In the instance of velocimetry information being obtained from a target using a LiF rear window, the determination of the pressure state is slightly different. The method of determining the pressure state in the Sb layer using the velocity of the target at the interface between the Sb and LiF layers requires knowledge of impedance matching techniques, as introduced in section 2.1.3. A full mathematical description of how to calculate the pressure state in a material on both sides of a boundary is given in chapter 3 of reference [60], but it is also possible to determine the pressure in the Sb layer through geometric consideration of the Hugoniot curves of Sb and LiF.

The initial shock front travels through the Sb layer, compressing the material to a point on the Sb principal Hugoniot where it reaches the Sb/LiF interface. The impedance of LiF is lower than that of Sb, meaning that when a shockwave is incident on the boundary between these two layers, a shockwave is transmitted

into the LiF and a release fan propagates back into the Sb layer, reducing the pressure. Release waves are generally handled as isentropes, however, the Hugoniot and the isentrope are the same to second order in compression [60]. For practical purposes here, the pressure state generated by the release fan propagating back into the Sb is treated as being on a reflected Hugoniot curve.

As shown in figure 3.11, when the initial shock front (S1) has reached the interface between the Sb and LiF layers (point a), a shock front is propagated forwards into the LiF layer (S2) and the pressure state in the LiF is described by a point on the LiF principal Hugoniot (shown in the figure to the right, point b). Simultaneously, a release fan (modelled as a reflected Sb Hugoniot in the (P, u_p) diagram) propagates backwards into the Sb layer, lowering its pressure. The lower pressure state in the Sb, in this treatment, thus lies on a reflected Sb Hugoniot with the initial conditions (P_a, u_a), so the Sb Hugoniot is reflected about point a. In order for these two materials to remain physically joined together once the shock front has reached the interface, the new pressure in the LiF (point b) must be equal to the new pressure in the Sb layer; it is evident that the only (P, u_p) condition which meets this requirement is the point where the principal LiF Hugoniot and the reflected Sb Hugoniot intercept (point b).

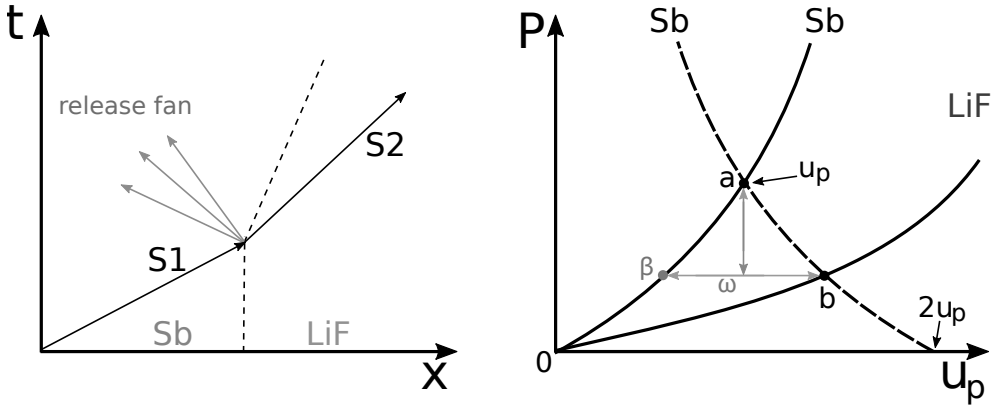

Figure 3.11 *On the left a distance vs time plot shows the propagation of waves at the Sb/LiF interface. On the right, the principal Hugoniot curves of Sb and LiF are expressed in terms of P and u_p, along with the reflected Sb Hugoniot.*

The (P, u_p) plot may be used to calculate the pressure state in the Sb immediately before the shock front reaches the interface (point a); this is the pressure state of the compressed Sb in the x-ray diffraction data collected on compression. In experiments using a LiF window, the pressure state in the LiF (point b) may be measured using the particle velocity from the VISAR diagnostic. Point β may then be found, this is the value on the Sb Hugoniot which has the same pressure

as point b on the LiF Hugoniot. From simple geometry, we see that the initial pressure state in the Sb (point a) occurs at a value of u_p which is half of the distance between points b and β (a distance of $\omega/2$). Once the value of u_p in the Sb layer is known, the pressure may be determined from the principal Hugoniot.

For both the kapton/Sb targets and the kapton/Sb/LiF targets, the uncertainty in the pressure (as determined from the VISAR diagnostic alone) is derived from the uncertainty in the peak free surface velocity. This uncertainty may come from fluctuations in the free surface velocity in one VISAR trace or from the level of agreement between the VISAR traces from each of the interferometers (referred to as VISAR 1 and VISAR 2).

Pressure determination from x-ray diffraction and VISAR

The methods of determining the pressure from the VISAR data discussed in the previous section require knowledge of an accurate EOS. Given the limited amount of previous data that exists for shock-compressed Sb, it is prudent to scrutinise the pressures calculated using these methods. By combining the value of u_p determined using the VISAR diagnostic and the volume determined using x-ray diffraction, it is possible to calculate the pressure state without the use of an EOS, i.e. to determine the EOS independently.

For each shot, the x-ray diffraction data were fitted with the relevant structure and refined using the JANA 2006 software [110]. Unitcell software [111] was used to analyse the peak positions of the diffraction data and calculate an uncertainty in the volume yielded by the fitted structure. The shock velocity U_S, was calculated using equation 3.5 (from the Rankine-Hugoniot equations) with u_p determined from the VISAR diagnostic and a V_0 of 30.20 Å^3/atom for Sb [43].

$$U_S = \frac{u_p}{1 - (V/V_0)} \tag{3.5}$$

A second Rankine-Hugoniot relation (equation 2.9) can then be used to determine the pressure. The uncertainty in the pressure is propagated from the uncertainty in the value of u_p from the VISAR data and the uncertainty in V from the x-ray diffraction data. This method of pressure determination has been used in recently published work on shock-compressed scandium [57]. The validity of this method was checked by comparing the results to pressures determined

Shot	Phase	P_{VISAR} (GPa)	$P_{combined}$ (GPa)	ΔP (GPa)
263	Sb-I	4.49(14)	4.5(4)	0.01
266	Sb-I	5.9(2)	6.9(6)	1.0
104	Sb-I′	11.2(4)	11.3(13)	0.1
103	Sb-I′	11.4(5)	12.1(14)	0.7
168	Sb-II	12.3(8)	11(2)	1.3
98	Sb-III	18.2(7)	18(1)	0.2
171	Sb-III	20.3(6)	18(2)	2.3

Table 3.1 *Pressure calculations using only VISAR data (P_{VISAR}) and combined VISAR/x-ray diffraction data ($P_{combined}$) for each of the Sb phases observed on dynamic compression. The best and worst agreement between the methods (highest and lowest ΔP) is shown for each phase, with the exception of Sb-II where the variation in ΔP across the collected data was negligible.*

using the VISAR data and prior EOS measurements. Table 3.1 shows the best and worst agreement between the pressure calculated using only the VISAR data (P_{VISAR}) and the pressure calculated using both the VISAR and x-ray diffraction data ($P_{combined}$) for the Sb phases observed under shock compression, where ΔP denotes the difference between the pressures calculated using both methods.

The large uncertainty in the $P_{combined}$ value in the Sb-II and Sb-III phases originates from the unitcell fitting of the Bragg peaks. Sb-II is a highly complex phase, and some of the peaks overlap with the ambient Sb-I peaks. Peak overlap may lead to slight mis-fitting of the peak position so these fits have a larger uncertainty associated with them. The Sb-III profiles were taken early on compression so the relative intensity of the Sb-III peaks to the ambient Sb-I peaks was low; this can contribute to a higher uncertainty in the fit to the diffraction pattern. Greater uncertainties in the fits are propagated forward and lead to higher uncertainty in the $P_{combined}$ value.

It should be noted that the method of determining the pressure using combined VISAR and x-ray diffraction data ($P_{combined}$) is very sensitive to small changes in the rear surface velocity U_{FS} measured by the VISAR diagnostic; it is vital that the VISAR data is of the highest possible quality to ensure reliable pressure determination. The difference in the timing and position between the x-ray and VISAR measurement also requires the steadiest possible loading conditions. The pressures quoted in this thesis were calculated using the combined method unless the target made used of a LiF window at the rear surface, in which case the impedance matching method was used.

3.4 Dynamic Studies of Sb at the LCLS: 2015 vs. 2016

The data reported in this thesis were collected at the LCLS in 2016, however, preliminary data were also collected at the LCLS in 2015. While the data from this initial experimental campaign is not included in the main results of thesis, the 2015 experiment is discussed in this section in the hopes of highlighting the importance of refining experimental design.

In section 3.2.1 the use of phase plates in the 2015 and 2016 experimental campaign was briefly discussed; it was found that the phase plates created 'hot-spots' in the drive beam leading to non-planar shockwaves propagating in the sample. The phase plates were removed for the 2016 campaign to promote drive planarity. The use of laser focusing, rather than phase plates, was not the only change made to the experimental set up at the facility.

In 2015 the single 825 $\times$ 830 pixel CSPAD quad detector which was available at the LCLS, allowed access to a 2θ range of 20 to 80°. While this range encapsulated the most intense peaks in the diffraction signal from Sb phases at the x-ray energy used in the experiment (8.8 keV), a much larger 2θ range was accessible in the 2016 experiments. By using two further CSPAD quads, data were obtained between 20 and 110°. Furthermore, the x-ray energy was increased to 10 keV in 2016 meaning that more reflections were able to be observed within the accessible 2θ range.

Another definite improvement between the 2015 and 2016 experimental campaigns was the introduction of standard configurations at the LCLS. This system allowed users who wanted to use the same experimental configuration in the chamber to interleave shifts meaning that there was time for valuable data analysis between the shifts. This time is invaluable as the occasionally unpredictable nature of scientific experiments means that experimental plans must sometimes be revised *in-situ*, and the luxury of being able to more thoroughly analyse data mid-campaign can ultimately lead to more fruitful experiments.

The main improvement between the 2015 and 2016 experimental campaigns was the alteration of the Sb targets. The initial experiment used targets which still had a 50 μm kapton layer but the deposited Sb layer was only 4 - 5 μm thick.

The thinner Sb layer was chosen in order to avoid delamination of the targets though ultimately this led to many experimental difficulties. The transmission of 8.8 keV x-rays through a 4.5 μm Sb layer is 56% and while the diffraction signal was of high enough quality to identify the Sb-I phase, the thin nature of the targets and some difficulties with timing at the facility made it extremely difficult to obtain x-ray diffraction data on compression. As an approximation, one may consider the propagation of a shock front at ambient sound speed (2.5 km/s for Sb) through the target. In a target 4.5 μm thick, this leaves only a 1.8 ns window in which to obtain diffraction data on compression, and as the material is shocked to higher pressures the shock velocity increases, thus reducing this window of time further. Additionally, it is advantageous to time an x-ray pulse so that the shock front has propagated far enough into the target that enough material is in the compressed state to provide a strong diffraction signal; again this is difficult when the time interval in which data may be obtained on compression is so small. At the LCLS, x-ray pulses are able to be timed to 0.5 ns accuracy which, while highly impressive, was not accurate enough to obtain useful data on compression from these thin Sb targets. One of the few x-ray diffraction profiles collected on compression is shown in figure 3.12. Here we see that while the $(1\bar{1}2)$ peak of the compressed Sb-I phase is visible, the diffraction signal from this phase is not particularly strong and no other peaks from the compressed phase can be discerned.

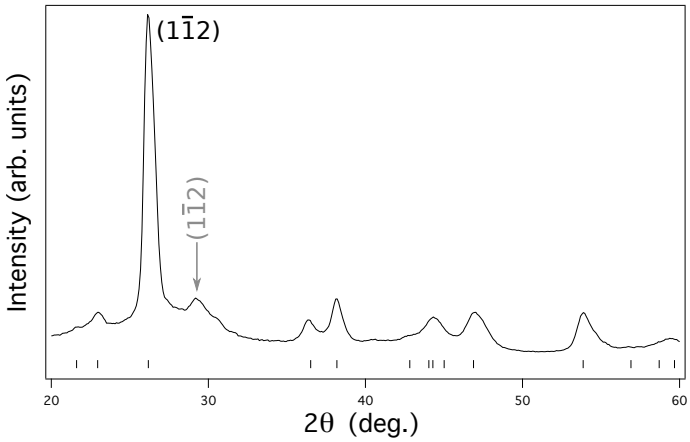

Figure 3.12 *Diffraction data from the 2015 experimental campaign at the LCLS. Tickmarks show ambient Sb-I peaks and the* $(1\bar{1}2)$ *peak of the compressed Sb-I phase is indicated in grey.*

Furthermore, the VISAR data showed extreme non-planarity of shock breakout, as illustrated in figure 3.13, making it very difficult to conduct meaningful analysis. While the use of phase plates could have contributed somewhat to

this issue, it seems more likely that there was some variation in thickness of the Sb layers which was not effectively characterised.

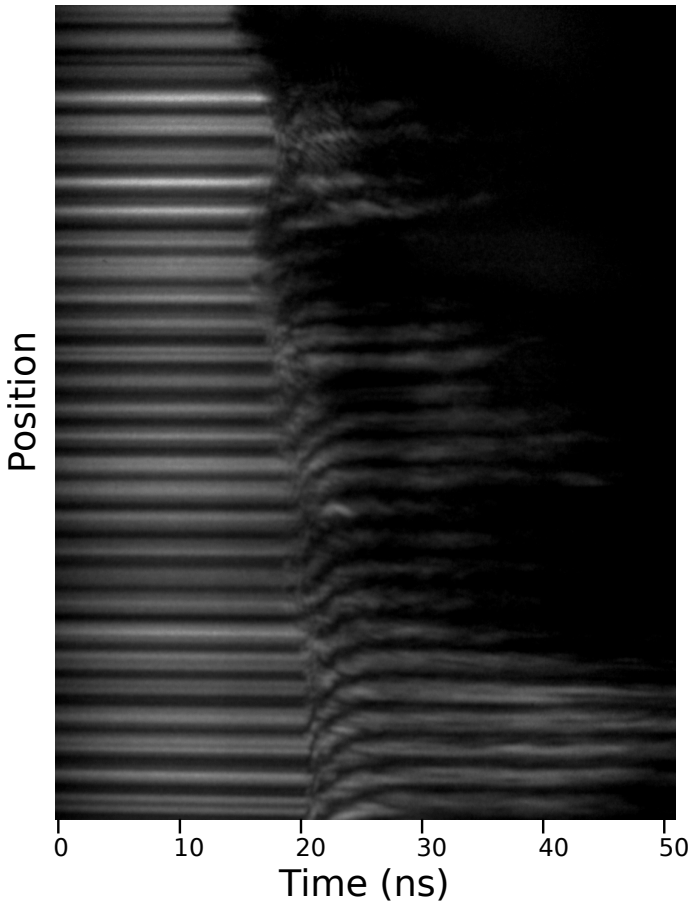

Figure 3.13 *Interference fringes collected using the VISAR diagnostic for an Sb target in the 2015 experimental campaign at the LCLS. The shock breakout is not planar, and reflectivity is lost in many areas after shock breakout, greatly complicating the analysis.*

In 2016 the Sb targets consisted of 10 μm thick layers of Sb, as discussed in section 3.2.2. The thicknesses of these targets were more thoroughly characterised and the VISAR data showed planar breakouts (as in figure 3.6). These thicker targets meant that the window in which x-ray data were able to be collected on compression was much larger. The quality of x-ray diffraction data was very high, meaning that not only was the incommensurate host-guest structure of the Sb-II phase able to be resolved but also subtle features in the 'simple cubic' phase were able to be detected (this will be discussed further in section 3.5.1). Overall, the various improvements made to the experimental method between the 2015 and 2016 experimental campaigns meant that high-quality data was able to be collected, as shown in the following sections.

3.5 Results

In this section the results from the experimental campaign at the LCLS in 2016 are discussed. Figure 3.14 provides a preliminary overview of distinct phases that were identified during the experiment, each of these will be discussed in further detail in the following subsections. The pressures indicated on the plot are those obtained from initial VISAR analysis during the experiment, these pressures were later re-calculated using the combination method described in section 3.3; the figure serves only as an introductory preview of the phases as seen during the experiment.

The Sb-I phase is observed in profile (i) at ambient conditions and again in profile (ii) along with compressed material of the same structure. The tickmarks indicate the diffraction peaks from the $R\bar{3}m$ structure of ambient Sb-I [43]. Indeed, in each of these profiles the ambient peaks are present, this indicates that the diffraction data were collected on compression as diffraction peaks are present from the uncompressed material ahead of the shock wave. In profile (iii) a clear simplification of the diffraction from the compressed material is observed. This diffraction pattern is distinct from the Sb-I phase but does not show enough complexity to be explained by the incommensurate host-guest structure of Sb-II. This was a surprising observation during the experiment as this new phase is not reported by the most recent static compression studies [43]. The structural identity of this new phase is discussed in section 3.5.1. Upon further pressure increase the diffraction pattern becomes markedly more complex, as shown in profile (iv) where new peaks are observed around 24°; this heralds the onset of the Sb-II phase. Profile (v) shows another simplification of the compressed phase; based on previous static studies [35, 43] this phase (Sb-III) is known to have a bcc structure. Profiles (vi) and (vii) show the onset of diffraction signal from liquid Sb, as characterised by the broad feature around 30°; this is discussed further in section 3.5.4.

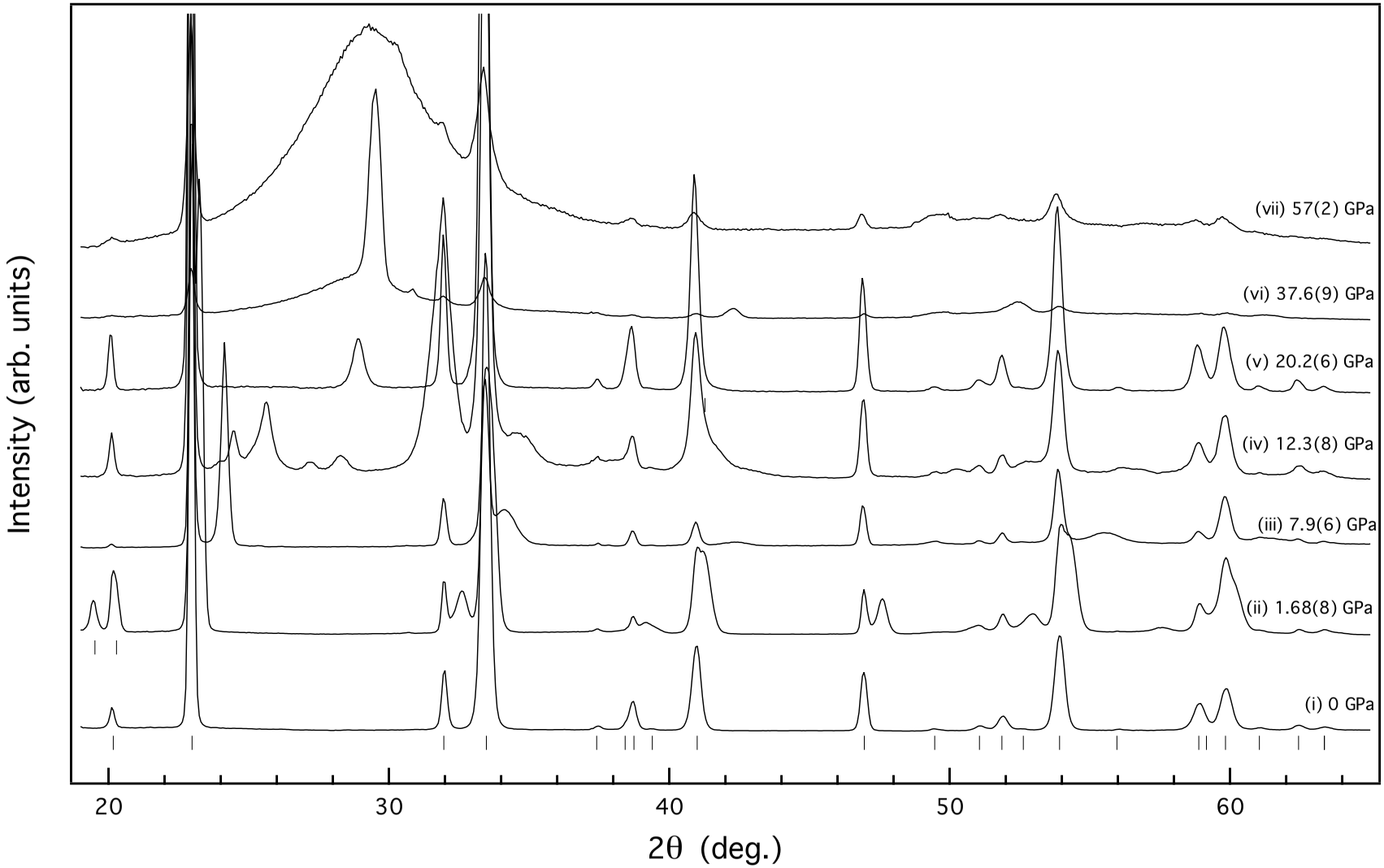

Figure 3.14 *Integrated diffraction profiles from shock-compressed Sb as a function of pressure.*

3.5.1 The Sb-I and Sb-I′ Phases

At ambient conditions, Sb crystallises in the rhombohedral A7 structure (space group $R\bar{3}m$, atom on $(0, 0, u)$ with $u = 0.234$) which is a Peierls-distorted simple cubic structure [44], as shown in figure 3.15. The right hand side of figure 3.15 shows the unit cell with the c-axis normal to the page; as discussed in section 3.2.2 this was found to be the dominant orientation of the grains in our textured samples. One can visualise the compression by imagining the drive pulse incident on the page. A fibre textured sample differs from a single crystal sample; in our fibre textured samples the c axes of the grains are aligned parallel to the foil normal but have a random azimuthal orientation about that axis. Furthermore, there is a texture width present in the sample meaning that the c-axis is only aligned to the normal within a certain angle (characterised by Dr D. R. McGonegle of The University of Oxford, as being 15° in the Sb samples used in this work) [88].

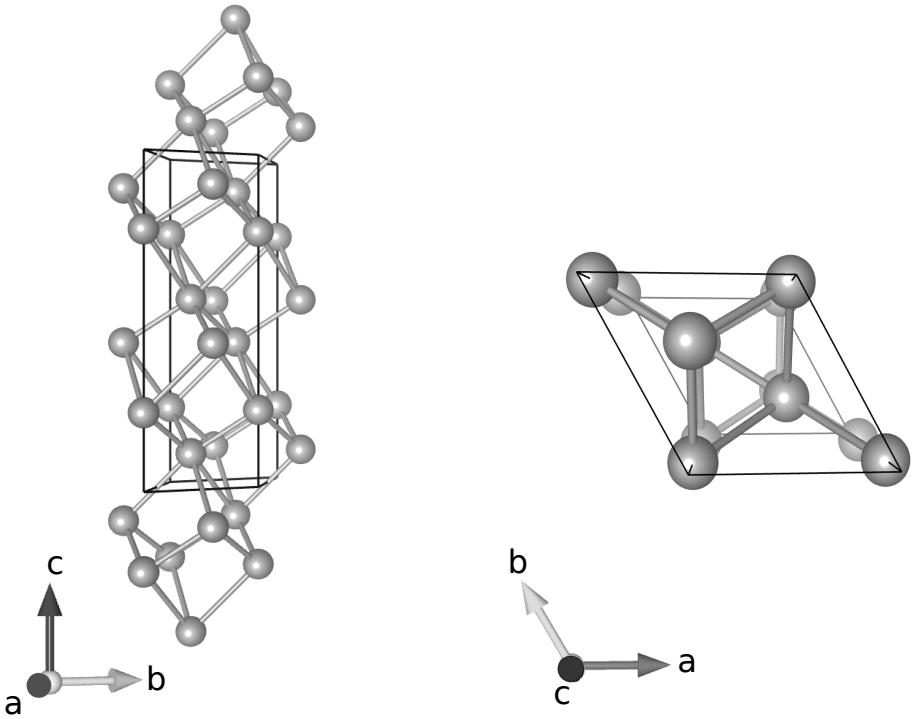

Figure 3.15 *The $R\bar{3}m$ structure of ambient Sb shown in two different orientations. The right hand view (not to scale with the left) shows the structure viewed along the c axis.*

In order to check the calibration of the detectors, an integrated x-ray diffraction pattern from an exposure without a laser drive pulse (an x-ray diffraction pattern showing only ambient Sb) was analysed using a Le Bail refinement, as shown in

figure 3.16. This fit yielded lattice parameters $a = 4.306(2)$ Å and $c = 11.297(2)$ Å, values which agree well with previously published lattice parameters of ambient Sb: $a = 4.308$ Å and $c = 11.297$ Å [43]. This indicates correct calibration of the detectors, something which is of great importance when adding together the contributions from constituent CSPAD detectors (as discussed in section 3.2). Furthermore, the agreement of these lattice parameters with those obtained in previous studies confirms that the wavelength of the incident x-ray radiation in this experiment is well characterised. The high quality of the x-ray diffraction data is exemplified in this diffraction pattern; a high number of diffraction peaks are visible in the integrated pattern. It should be noted that the intensity of the diffraction peaks observed here are somewhat different to those observed in previous powder diffraction studies [43]; this is due to the textured nature of the sample and subsequent loss of diffraction intensity at certain azimuthal angles. This is most notable in the (104) peak which is much less intense than in the case of perfect powder diffraction.

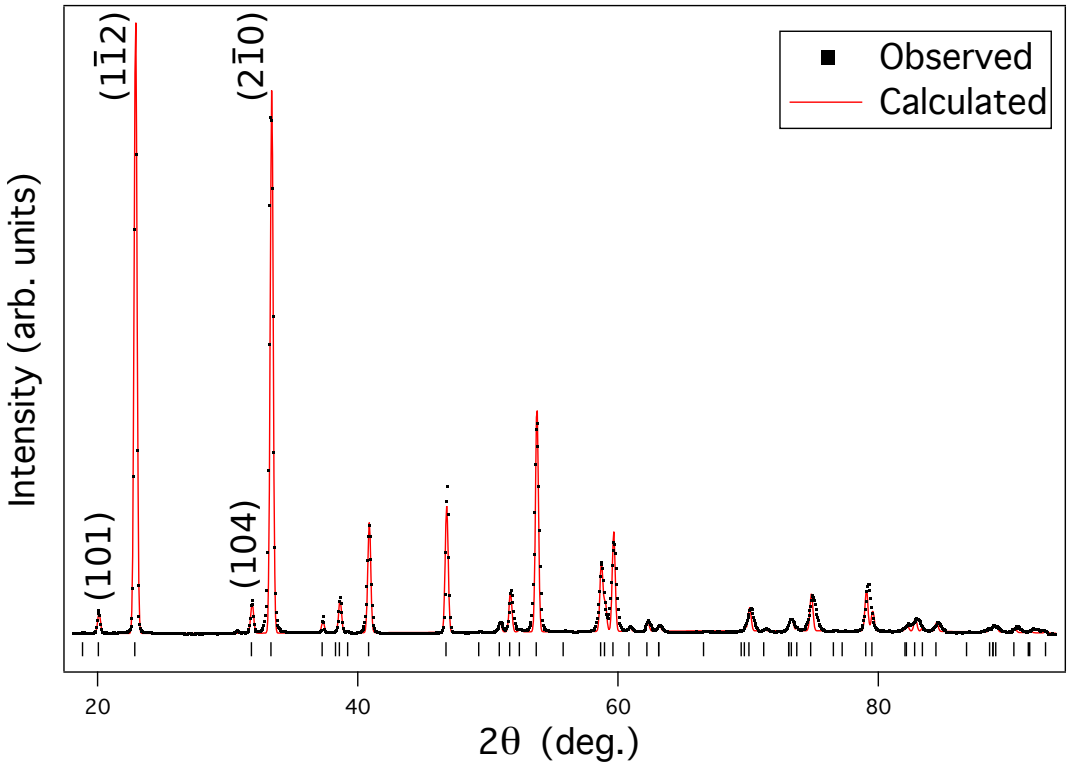

Figure 3.16 *Observed and calculated diffraction peaks from a Le Bail fit of Sb at ambient conditions. Peak positions are indicated by the tick marks below the integrated pattern.*

The Sb-I ($R\bar{3}m$) and simple cubic ($Pm\bar{3}m$) structures are shown in figure 3.17. The highlighted atoms illustrate the transition from a distorted to an undistorted cube. As discussed in section 1.4.2, early static compression studies of Sb have

reported both a continuous [30] and discontinuous [32, 33] complete transition to the simple cubic phase at around 7 GPa, as diagnosed using x-ray diffraction. More recent work using both single crystal [112] and powder diffraction [39, 43] techniques have since found no evidence of such a transition to the simple cubic phase, instead reporting a direct transition to the host-guest phase, Sb-II.

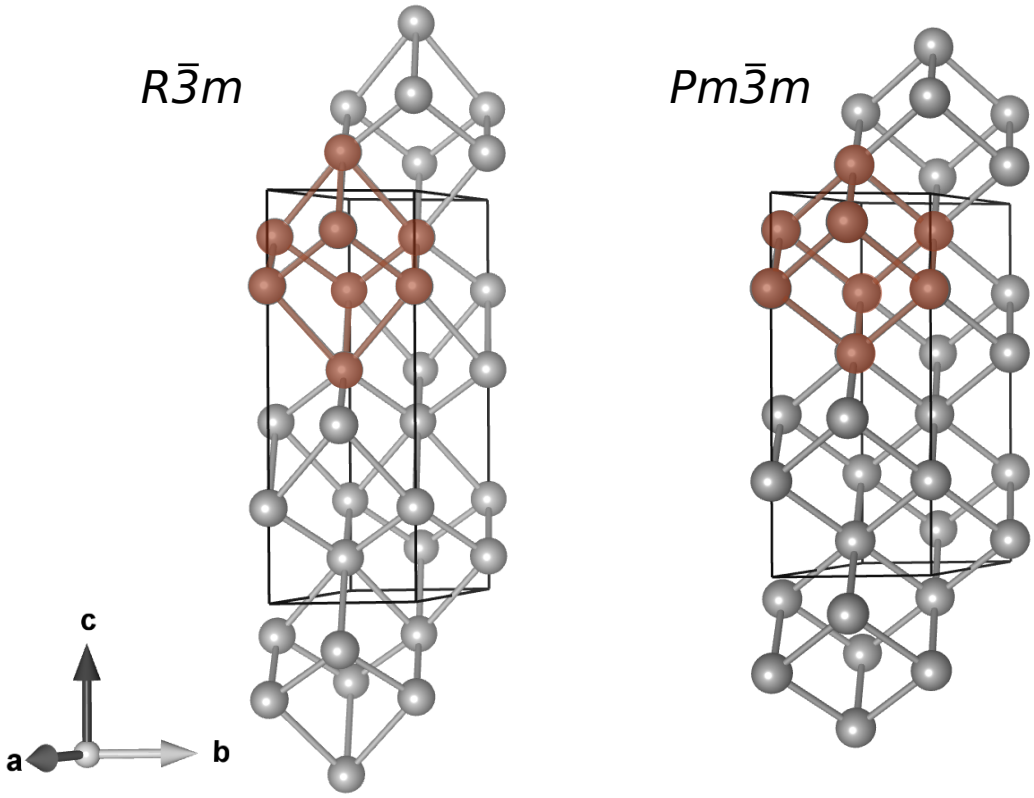

Figure 3.17 *The rhombohedral structure of the Sb-I phase is shown on the left, along with a simple cubic structure on the right. The added bonds illustrate a distorted cube within the rhombohedral structure and a corresponding undistorted cube in the simple cubic structure.*

A relaxation of the Peierls distortion in Sb-I with increasing pressure was observed as the simple cubic structure (which is characterised by a c/a ratio of $\sqrt{6}$ and u=0.25) was approached. This is illustrated in figure 3.18 which shows the c/a ratio of the Sb-I phase decreasing towards $\sqrt{6}$. Between 1.9 and 4.5 GPa there is evident disagreement with previous data obtained under static compression; the dynamic compression data points show a much more rapid decrease in the c/a value with pressure. For data collected between 5.8 and 6.9 GPa, it was not possible to obtain a c/a ratio. Due to overlap of the compressed and ambient Sb-I diffraction peaks, there were not sufficient clearly identifiable diffraction peaks from the compressed material to perform any meaningful refinement. Figure 3.19 illustrates this point; in profile (b) it is difficult to distinguish between the $(2\bar{1}0)$

peak from the ambient Sb, and the (104) and $(2\bar{1}0)$ peaks from the compressed Sb. In figure 3.18 this data is shown as a line at $\sqrt{6}$. While it is not possible to determine the exact c/a ratio or verify whether it is indeed $\sqrt{6}$, the volume difference between attempted fits is negligible and thus the volume is still used for pressure determination (as discussed in section 3.3). It is possible, however, to establish that the data collected in this pressure interval do not represent a cubic structure of Sb. This is because the (101) peak is present in all of the diffraction patterns in this region and if the structure were to transition from rhombohedral to cubic, this peak would disappear as a consequence of u becoming equal to 0.25.

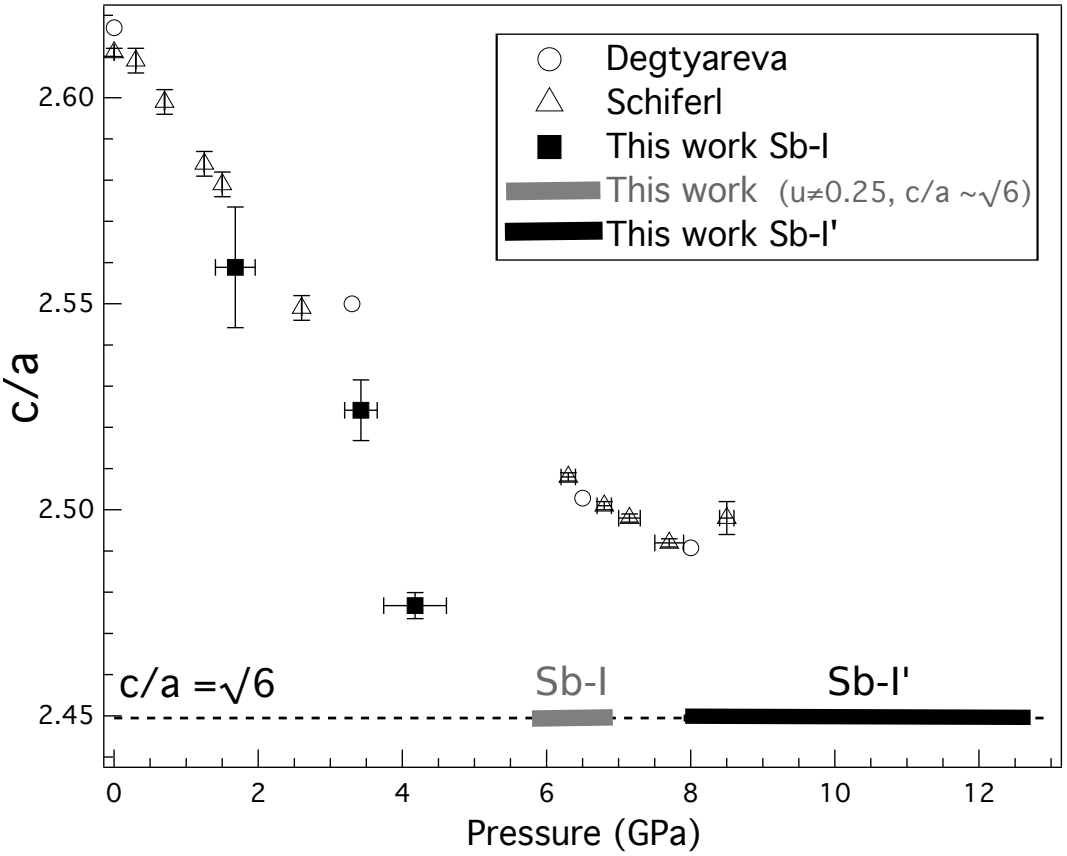

Figure 3.18 *c/a ratio vs pressure plot for the Sb-I phase on-Hugoniot. Data from previous room-temperature work by Schiferl [112] and Degtrareva [43] are shown by empty triangles and circles respectively.*

Between 7.9 and 12.7 GPa, the diffraction pattern of the compressed material is distinct from the Sb-I phase, this is most notably indicated by the apparent merging of the (104) and $(2\bar{1}0)$ peaks of the $R\bar{3}m$ structure, as these are the most intense merging peaks. This new phase, Sb-I′, was initially fitted with a simple cubic structure but, for some of the peaks, a disagreement between the observed and calculated peak positions of up to ± 0.002 Å was found. Analysis of the raw

diffraction images indicated that there were small variations in the d-spacings of the Debye-Scherrer rings around the azimuth. Such azimuthal variations can be indicative of strength within the sample. However, for textured samples this can also be indicative of a phase change [88].

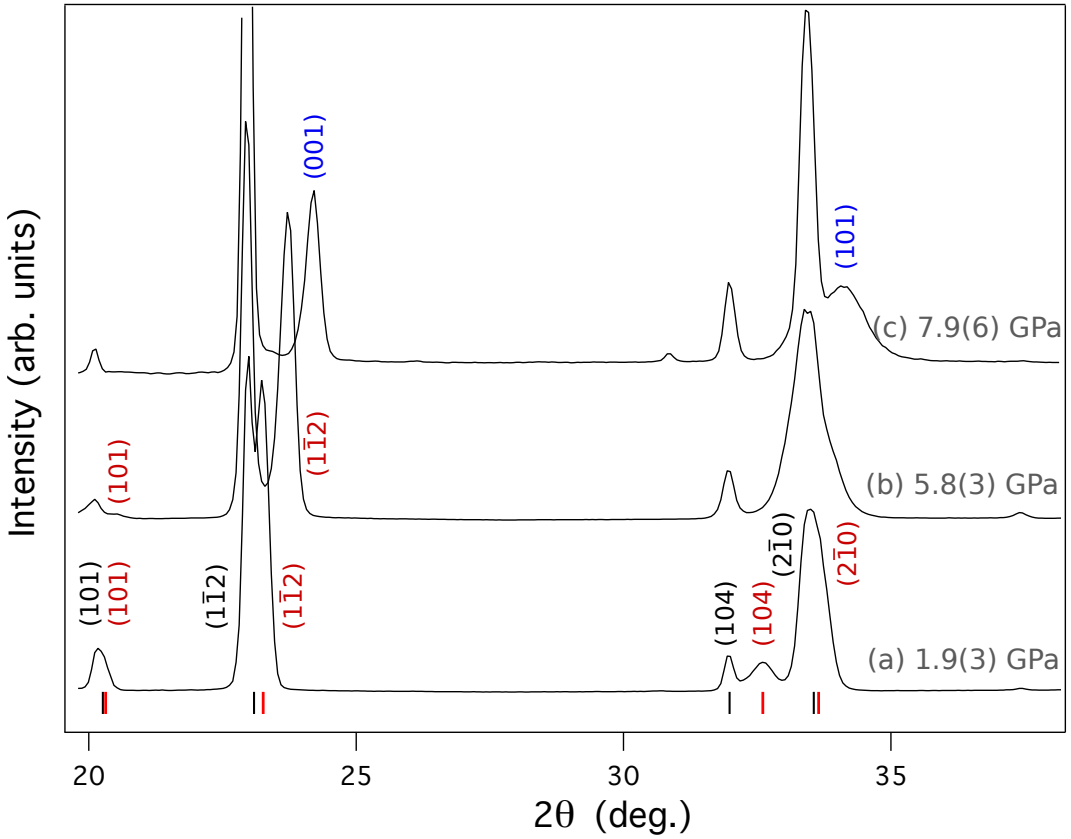

Figure 3.19 *Profile (a) shows ambient Sb-I peak positions in black and Sb-I at 1.9(3) GPa in red. In profile (b), the compressed (101) and (1$\bar{1}$2) peaks are still visible but it is difficult to distinguish the compressed (104), (2$\bar{1}$0) and ambient (2$\bar{1}$0) peaks. In profile (c) the simple cubic peaks are labelled in blue.*

Two candidate structures were identified for the Sb-I′ phase; simple cubic with strength, and a rhombohedral structure without strength. These two structures are extremely similar, as represented in two dimensions in figure 3.20 which was created by our collaborator Dr D. R. McGonegle. Figure 3.20 shows a square grid, rotated to the left and right by 15°, as this is the texture width of our sample. The rhombohedral candidate structure is modelled by non-hydrostatic compression followed by rotation while the simple cubic structure is modelled by rotation followed by non-hydrostatic compression. As is evident from the figure, these two structures are indistinguishable in the instance of zero texture width; indeed, even the case of maximum rotation achievable in our sample and relatively

large compression (figure 3.20 shows 30% vertical compression, ie it is 70% of its original length), the difference between the two structures is subtle.

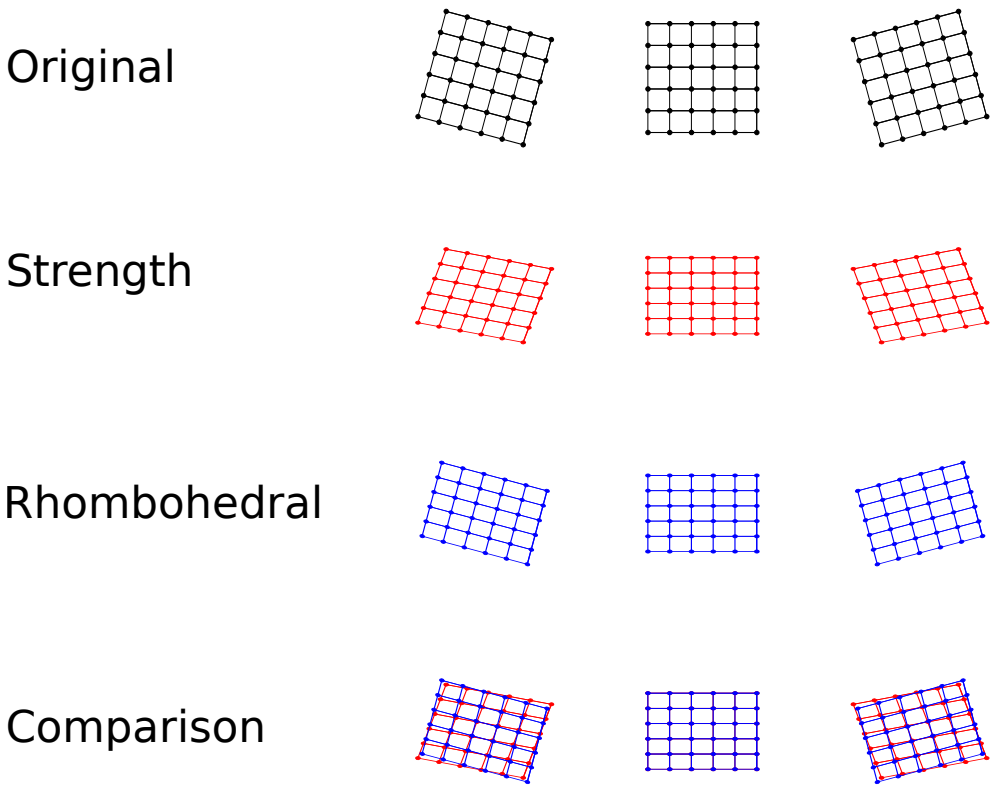

Figure 3.20 *A 2D square lattice is shown in three different orientations (rotated 15° in each direction from the central position). The two candidate structures for the Sb-I′ phase are shown; the rhombohedral structure is compressed uniaxially (by 30% in this figure) before being rotated, and the simple cubic structure with strength is rotated and then compressed (also by 30%). The subtle difference between the two structural candidates is indicated.*

Distinguishing between these similar structures was greatly complicated by the presence of texture in the sample which meant that there were significant azimuthal gaps in the diffraction data, but also by the limited coverage of the CSPAD detectors. Simulation of the simple cubic with strength and rhombohedral structure without was conducted by Dr McGonegle. The simple cubic structure with strength was fitted to the data using the methods detailed in reference [113]. The rhombohedral structure was fitted by converting longitudinal and transverse strains from the simple cubic with strength fit to c and a parameters for the rhombohedral structure; as shown in figure 3.20 the structures are the same for zero texture width. Dr McGonegle then wrote a code that assumed that the fibre direction was along the c-axis and assigned a texture

width. This code calculated the position of the diffraction intensities for each plane of the rhombohedral structure and fitted this to the real diffraction data. Simulations of these competing structures are shown, alongside raw diffraction data, in figure 3.21. The rhombohedral candidate structure is shown in figure 3.21 (a) and the simple cubic candidate structure with strength is shown in figure 3.21 (b) using white dashed lines that do not cover the entire azimuth; this is because the texture of the sample was accounted for in the simulation. Because $u = 0.25$ in the rhombohedral candidate structure, it is possible to define a unit cell with a halved c lattice parameter. The Miller indices shown in figure 3.21 do not reflect a rhombohedral structure where the c parameter has been halved, instead the same convention as the $R\bar{3}m$ structure of Sb-I has been maintained for clarity.

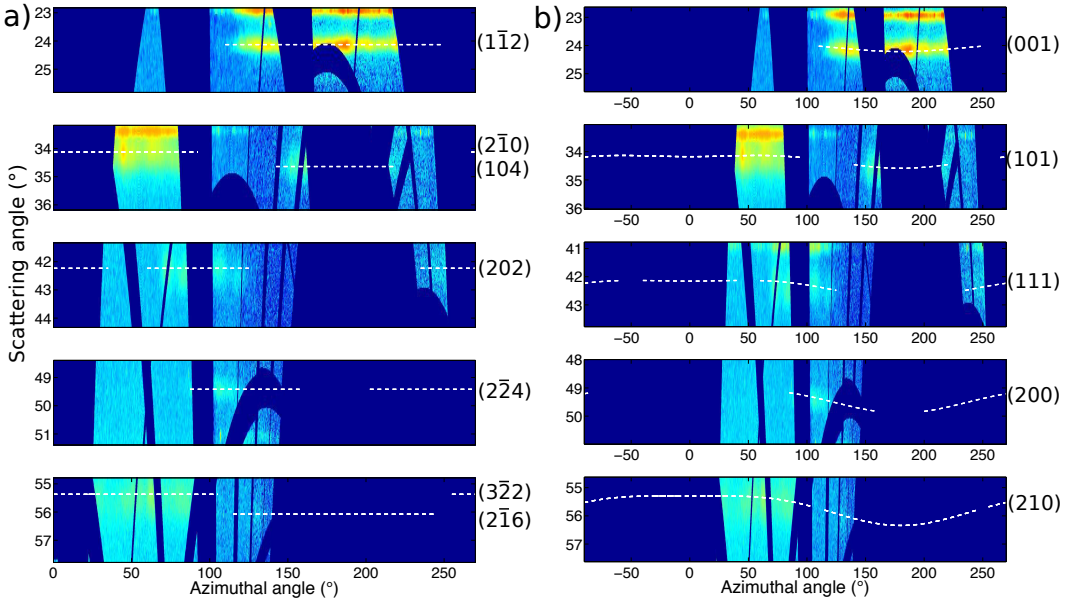

Figure 3.21 *The two competing structures of Sb-I′ are shown by dashed lines. On the left a simulation of the rhombohedral structure is shown by a white dashed line and on the right the strained simple-cubic structure is shown over the same raw diffraction pattern, collected at 7.9(6) GPa.*

In principle, to differentiate between the two competing structures, the intensity patterns in the Debye-Scherrer rings could be analysed. If the Sb-I′ phase did indeed have a simple cubic structure, the intensity peaks in the (104) and (2$\bar{1}$0) Debye-Scherrer rings should combine when these peaks merge, resulting in a (101) simple cubic peak with the combined texture of the (104) and (2$\bar{1}$0) peaks from the Sb-I $R\bar{3}m$ structure. If the new rhombohedral structure with $c/a < \sqrt{6}$ is the correct structure, the (104) peak should appear at a higher 2θ than the (2$\bar{1}$0)

peak (unlike in the Sb-I phase where $c/a > \sqrt{6}$ and the (104) peak appears at a smaller 2θ than the $(2\bar{1}0)$ peak). Unfortunately, this technique could not be used in this specific situation as the nature of the texture and the 2θ variation of the peaks in the simple cubic structure with strength made it impossible, with the limited detector coverage of this experiment, to differentiate between the two candidate structures. It may be possible to distinguish between these two candidate structures in the future with comprehensive detector coverage, for instance, at European XFEL.

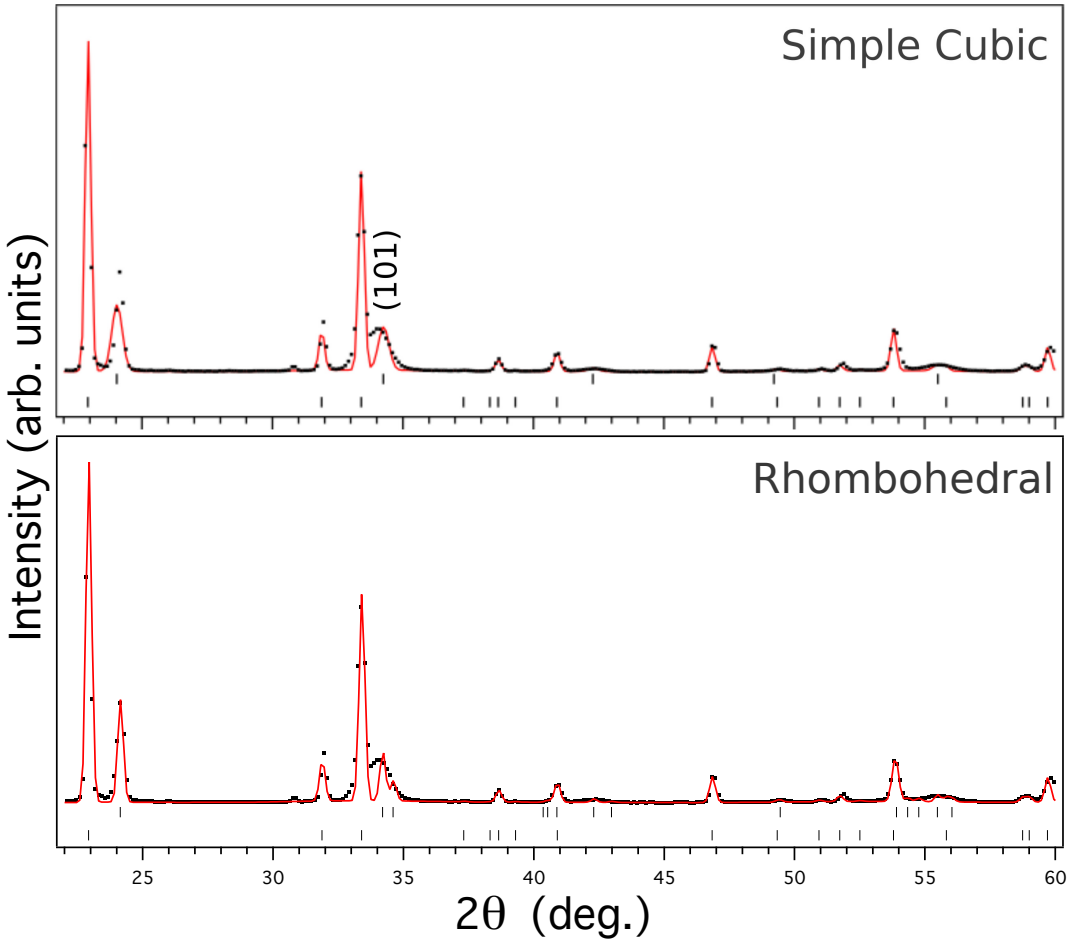

Figure 3.22 *The same integrated diffraction profile of Sb at 7.9 GPa is shown with fits to both of the candidate Sb-I′ phases; the upper plot shows a simple cubic structure fitted to the profile (not accounting for strength) while the lower plot shows a rhombohedral structure fitted to the profile. In each of the plots the upper tick marks indicate peaks from the candidate phase and the lower tick marks indicate peaks from the ambient Sb-I. The observed diffraction pattern is shown using black dots, the calculated fit is shown by a red line.*

Figure 3.22 shows the peak positions of the two candidate structures fitted to an integrated diffraction pattern from the Sb-I′ phase at 7.9 GPa. The fitted simple

cubic structure ($a = 2.977$) does not account for strength effects and so a slight misfitting of the peaks is observed. As this is a Le Bail fit and, as such, is weighted more heavily by the more intense peaks, the mis-fit here is most strongly observed in the (101) peak, indicated in the figure. The simple cubic fit shown in figure 3.22 (without strength) yields a V/V_0 of 0.874 while the analysis done by Dr D. R. McGonegle (accounting for strength in the simple cubic structure) gives a V/V_0 of 0.863(4) (where V_0 is 30.2 Å^3/atom for Sb [43]). The rhombohedral candidate structure ($a = 4.225(5)$, $c = 10.13(2)$) gives a V/V_0 of 0.864(2). The volumes yielded by both the simple cubic with strength and the rhombohedral fits are very close in value, meaning that there is no appreciable change to the calculated pressure depending on which candidate structure is used in the analysis. While it is not possible to differentiate between the two candidate structures with this data set, it is possible to clearly identify that the phase is distinct from the Sb-I phase.

Density functional theory (DFT) calculations have been conducted by Wang *et al.* which indicate a transition from the normal rhombohedral A7 structure of the Sb-I phase to other A7 variants prior to the transition to the Sb-II phase [114]. These calculations show a kink in PV at around $V/V_0 = 0.876$, which is indicative of an evolution of the structural parameters (c/a and u). This agrees very well with the data we have collected at LCLS; the highest pressure Sb-I data point having $V/V_0 = 0.888(4)$ and the lowest pressure Sb-I′ data point having $V/V_0 = 0.864(2)$ (as calculated for a strained simple cubic structure by Dr D. R. McGonegle). As mentioned previously, the simple cubic phase is characterised by $c/a = \sqrt{6}$ and $u = 0.25$. The first A7 variant structure described by Wang *et al.* is a a pseudo-cubic structure with $c/a = \sqrt{6}$ and $u \neq 0.25$, this was found to be the favourable structure from the kink at $V/V_0 = 0.876$ on compression until $V/V_0 = 0.863$ beyond which point, further on compression, the second A7 variant is found to be the favourable structure; this is characterised by $c/a > \sqrt{6}$ and $u = 0.25$. The calculations in this paper found the differences between the two structures to be sufficiently small (≤ 2 meV/cell) that the pressure region 5.7 to 6.6 GPa should be considered to be a region of coexistence. While the pressures given in this paper may not be directly applicable to the work conducted at the LCLS due to the high temperature at which the experimental data were collected, the volumes at which the calculations predict the A7 variant structures to exist agree well with our observation of the Sb-I′ phase.

The work by Wang *et al.* acknowledges the previous contrasting reports of

experimental observation of a simple cubic structure prior to the transition to the Sb-II phase (as discussed in section 1.4) and hypothesises that uniaxial stress could indeed be a contributing factor to these disparate experimental results. They note that the c/a ratios in their calculations are in fact smaller than those observed experimentally and that while no deviatoric stresses are present in their calculations, when applied to experimental results, they correspond to a strained configuration. They express that it is conceivable that, as the Peierls-like distortion of Sb-I is a uniaxial effect, it may be sensitive to uniaxial stress along the C_3 axis (equivalent to the c axis), and that these A7 variant structures may not be observed under hydrostatic compression along another axis. The grains in the Sb targets used at the LCLS were orientated such that the compression acted along the c axis; our observation of the Sb-I$'$ thus corroborates this theory.

3.5.2 The Sb-II Phase

This section presents the first observation of an incommensurate host-guest structure with ordered chains formed under dynamic compression, using x-ray diffraction techniques. The VISAR diagnostic showed evidence of a two-wave structure in the data where the Sb-II phase was observed, as illustrated in figure 3.23. The shallow region in the P-V curve in figure 3.10 suggests the existence of this two wave structure, as there is a region on the Hugoniot curve that is inaccessible via a single Rayleigh line (as discussed in section 2.1.2). The initial peak in the rear surface velocity profile for Sb-II occurs as the initial plastic wave (compressing the sample to Sb-I′) reaches the rear surface. This is followed by the second plastic wave which compresses the sample to the final Sb-II state.

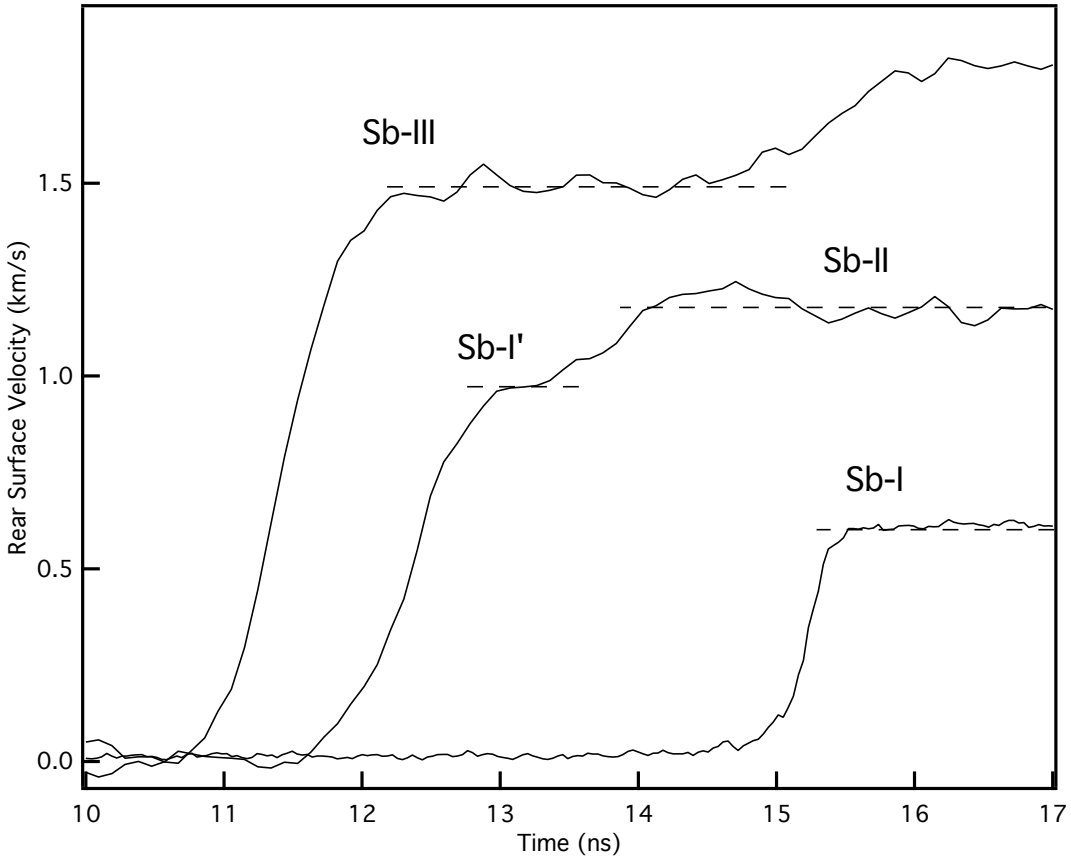

Figure 3.23 *Rear surface velocity profiles from the VISAR diagnostic for the Sb-I, Sb-II and Sb-III phases 6.6, 11.7 and 14.6 GPa respectively. Wave splitting is evident in the Sb-II profile. The second increase in velocity in the Sb-III profile occurs due to re-shock within target.*

The analysis of VISAR data which show a two-wave structure requires use of the multi-wave Rankine-Hugoniot equations, given by equations 2.14, 2.15 and 2.16. Due to the extremely shallow nature of the dip in the Sb Hugoniot, the

treatment of the Sb-II data using the multi-wave analysis does not differ greatly to the single-wave analysis used previously. Analysis of the Sb-II data shown in the middle profile in figure 3.23 using the single-wave analysis yields a pressure of 11.76 GPa while the two-wave analysis for the same shot gives a pressure of 11.81 GPa. An additional advantage to conducting multi-wave analysis is that additional data points may be obtained from the initial wave: in analysing both waves, velocity, volume and pressure information is obtained for both the Sb-II and the Sb-I′ phase.

In the Sb-II x-ray diffraction data collected on compression it proved difficult to obtain data where the Sb-II peaks had higher intensity than those from the Sb-I′ and ambient Sb-I phases. Figure 3.24 shows a Le Bail fit of the Sb-II phase at 11.8 GPa; there is reasonable agreement between the observed and calculated intensities shown in the figure, with small misfits observed in fitting the Sb-I′ phase with a simple cubic structure, as discussed in section 3.5.1. The intensities of the Sb-II peaks are significantly less than those from the Sb-I phase, this is because the data was obtained early enough on compression that the dominant diffraction signal was from the uncompressed material ahead of the first shock front. On release, however, it was possible to obtain diffraction data where the intensity of the Sb-II peaks were (relatively) greater. With this release data it was possible to perform a Rietveld refinement of the structure, this is shown in figure 3.34 in section 3.5.6.

In contrast to the incommensurate host-guest phase observed in shock compressed Sc [57], the diffraction peaks that are attributed to guest reflections ($(hk0m)$ guest-only peaks) are observed, indicating that the guest chains are ordered in Sb-II. This is the first structural resolution of a shock-compressed, incommensurate host-guest structure with ordered chains, thus confirming that such highly reconstructive phase transitions are able to occur fully on nanosecond timescales.

The Sb-II phase was observed in this experiment between 11(2) and 14(2) GPa; this is a considerably smaller stability region than that observed for Sb-II formed on static compression at room temperature (observed between 10.2 and 25.6 GPa) [43]. This could be due to kinetic inhibition of the transition from the rhombohedral structure of Sb-I to the incommensurate host guest structure of Sb-II; this transition is highly reconstructive and the data collected at the LCLS suggest that transitions to simpler structures such as simple cubic, rhombohedral or bcc are favoured, decreasing the stability region of the Sb-II phase.

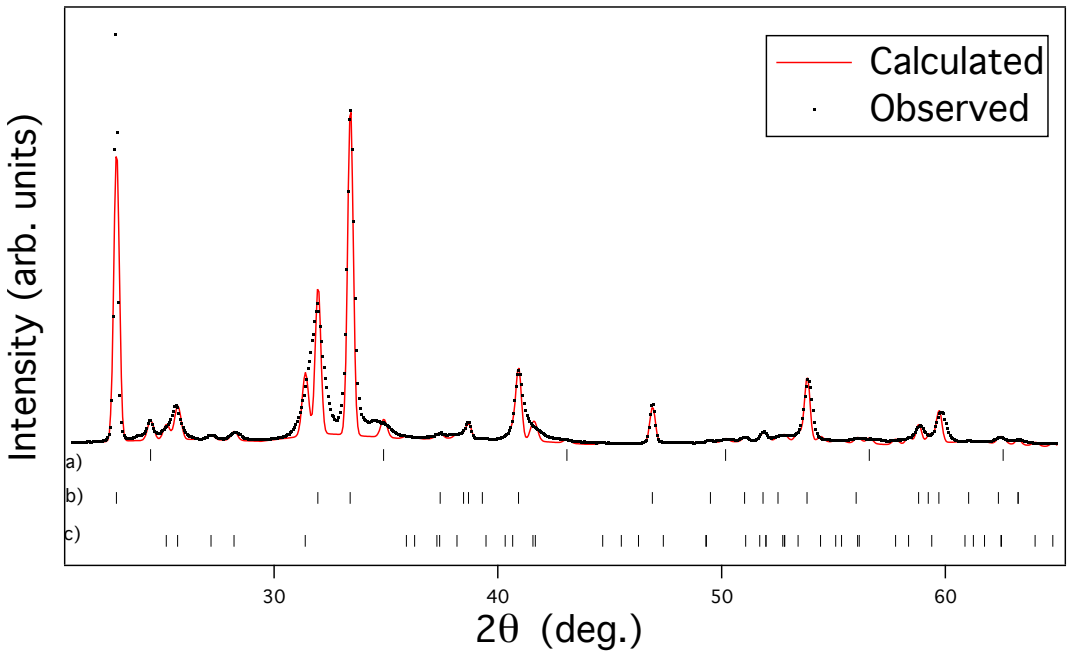

Figure 3.24 *Observed and calculated diffraction peaks from a Le Bail fit of Sb-II at 11.8 GPa. Peak positions are indicated by the tick marks below the integrated pattern with a, b and c showing the Sb-I′ phase (fitted with a simple cubic structure), the ambient Sb-I phase and the Sb-II phase, respectively.*

As discussed in section 1.4.2, previous dynamic studies have reported the presence of a two wave structure in dynamically compressed Sb at pressures similar to those studied here [49, 50]. These dynamic experiments were conducted using gas guns and found that the second plastic compression wave was delayed in forming by 0.6 μs. Evidently our results do not show such a significant delay; if this were the case then the second wave would not have been observed in our data on the few-nanosecond timescales of these experiments. If the Sb-I→Sb-II phase transition point reported by Degtyareva and Schiferl [35, 43] is joined to the minimum in the melt curve reported by Klement [27] (as shown in figure 3.25), we see the dynamic onset of Sb-I′ as the Hugoniot enters the equilibrium stability region of Sb-II. The Hugoniot conditions determined in our experiment (from $P_{combined}$ and V from x-ray diffraction) agree well with data collected on longer-duration plate-impact experiments (as shown by the good agreement between our data and previous results in figure 3.40) which indicates that the shock response is not strongly sensitive to experimental timescale. It is possible that the sluggish transition reported in these earlier papers around 8.8 to 11.3 GPa represents severely kinetically delayed transformation to Sb-II and it is in this regime that we observe the Sb-I′ phase. In the interest of better understanding this behaviour

and reconciling the present work with previous gas gun experiments, it would be useful to obtain further data on the timescales of the previous work. Modern techniques facilitate the use of x-ray diffraction as a diagnostic in plate-impact shockwave experiments; this would allow structural diagnosis on the timescales of gas gun experiments [115]. It would certainly be interesting to characterise the strain-rate dependence of the Sb-I→Sb-I′→Sb-II transitions.

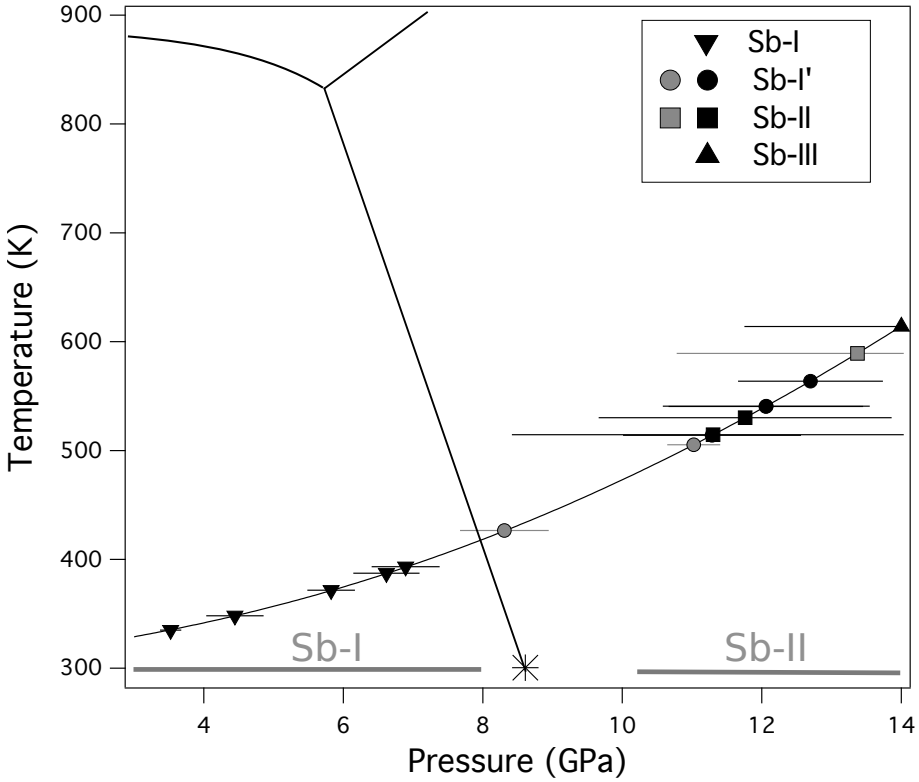

Figure 3.25 *The on-Hugoniot data collected in this experiment alongside the stability regions of Sb-I and Sb-II reported by Degtyareva [43] (shown by lines at room temperature), the Sb-I→Sb-II transition point reported by Schiferl [35] (marked by a star) and the melt data reported by Klement [27]. Grey and black points represented data collected using a LiF window and a Sb free surface, respectively.*

While the diffraction data showed that the variation in azimuthal intensity around the Debye-Scherrer ring was retained after the Sb-I→Sb-I′ transition, figure 3.26 shows a distinct difference in the appearance of the Debye-Scherrer rings in the Sb-II phase. The (2200), (1001), (2110) and (3100) peaks of the host-guest phase are indicated by arrows in the figure and the raw diffraction image above shows that, though faint, these rings exhibit much less intensity variation compared with the ambient diffraction rings on either side of these four peaks. This is perhaps not surprising given that the Sb-I→Sb-II transition is highly reconstructive; the smoother nature of the Sb-II rings also indicates that the grain size is smaller

than in the ambient Sb.

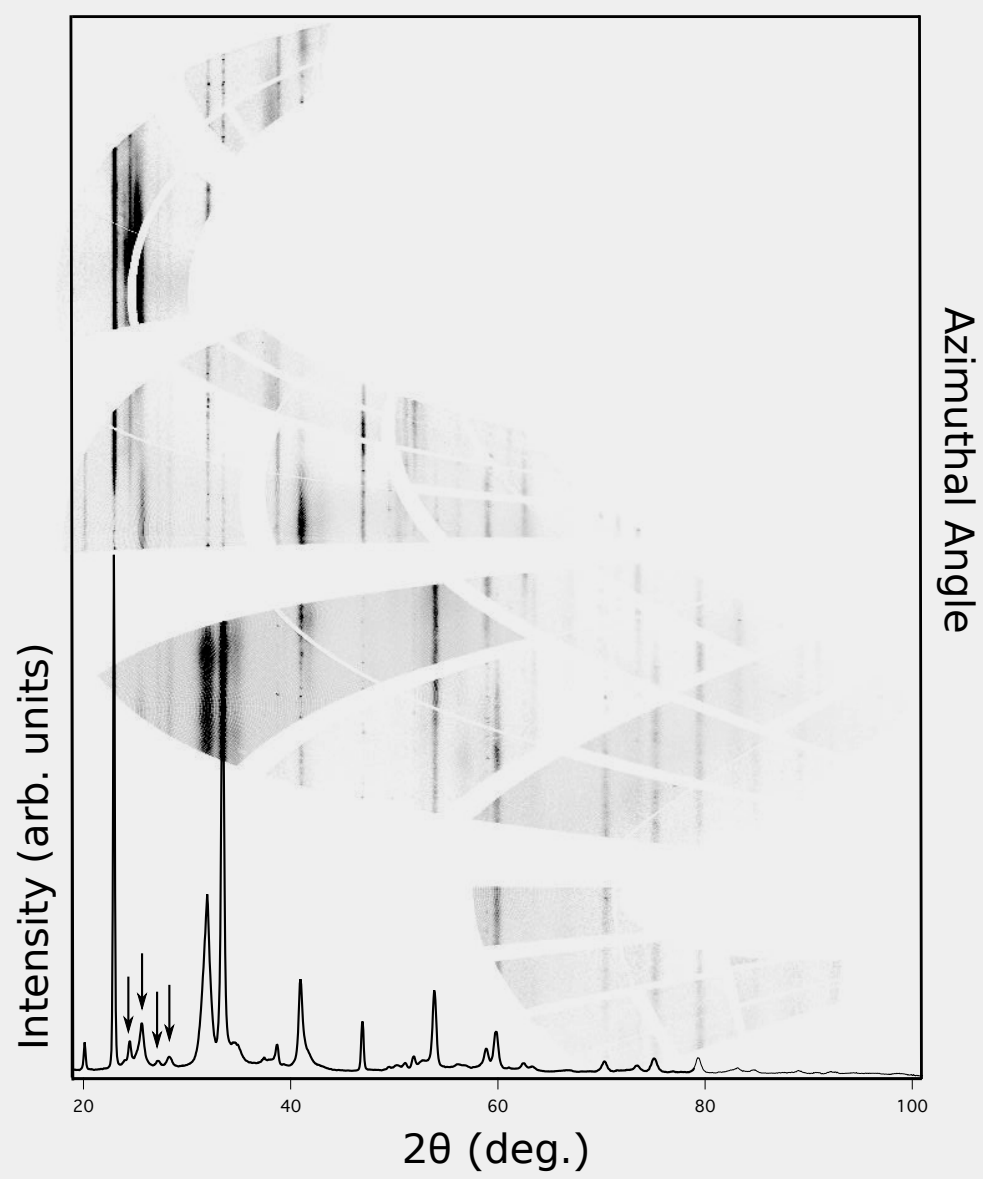

Figure 3.26 *The integrated and raw diffraction pattern showing ambient Sb-I peaks and compressed Sb-II at 11.8 GPa. The four arrows indicate the (2200), (1001), (2110) and (3100) Sb-II peaks (in order of increasing 2θ). These peaks show markedly less azimuthal intensity variation than the Sb-II peaks immediately to either side.*

3.5.3 The Sb-III phase

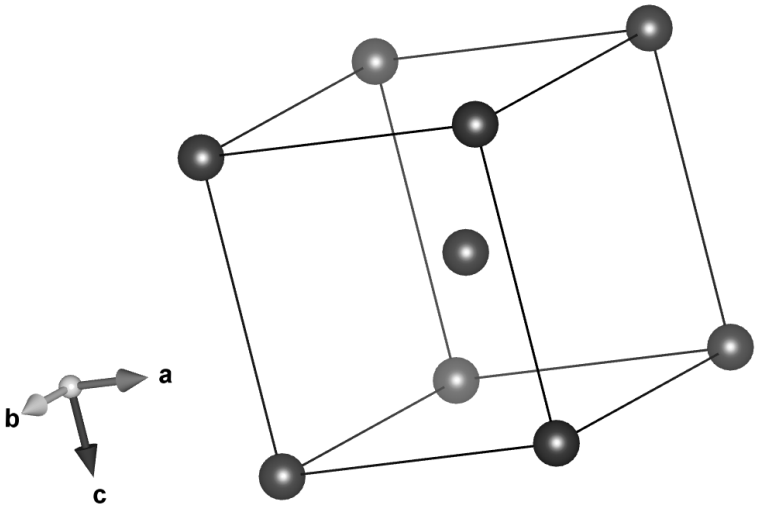

Figure 3.27 *The $Im\bar{3}m$ structure of Sb-III.*

The Sb-III phase (bcc structure, space group $Im\bar{3}m$) was observed on pressure increase from 14.6(14) GPa. There was no indication of two-wave structures from the VISAR data; the absence of a two-wave structure in the wave profiles for the Sb-III phase (as exemplified in figure 3.23) indicates that the overdriven regime has been reached and that the on-Hugoniot points are once again accessible via a single Rayleigh line. This means that the phase transition that occurs is directly from Sb-I phase to the Sb-III phase with the $Im\bar{3}m$ structure, as shown in figure 3.27

Figure 3.28 shows a Le Bail refinement of an integrated diffraction pattern featuring peaks from both uncompressed Sb-I and Sb-III. This fit gives an a lattice parameter of 3.515(2) Å and a corresponding V/V_0 of 0.719(1) Å^3. It is difficult to compare these lattice parameters to the static compression, room temperature data obtained by Degtyareva as at this V/V_0 the Sb sample was still in the Sb-II phase in that study [43]. The formation of the bcc structure at 14.6(14) GPa is markedly lower in pressure than observed in static compression experiments conducted at room temperature where Sb-III is reported only above 28.8 GPa [43]. Figure 3.40 (shown later in section 3.5.7) shows a PV plot containing the data obtained in this study, the room temperature static-compression data from Degtyareva and the pre-existing dynamic compression data from gas gun experiments. In this figure a Birch-Murnaghan fit is used to extend the Sb-III room temperature PV curve from Degtyareva to lower P.

In the diffraction pattern shown in figure 3.28, the weakness of the Sb-III peaks can be attributed to the smaller fraction of the Sb material that has been compressed into this phase. Many of the Sb-III diffraction profiles were obtained at times when the shock wave had not propagated far into the Sb; the higher pressure of the Sb-III phase in comparison to the other phases of Sb means that the shock front propagates more quickly and timing the x-ray diffraction diagnostic is consequently more difficult.

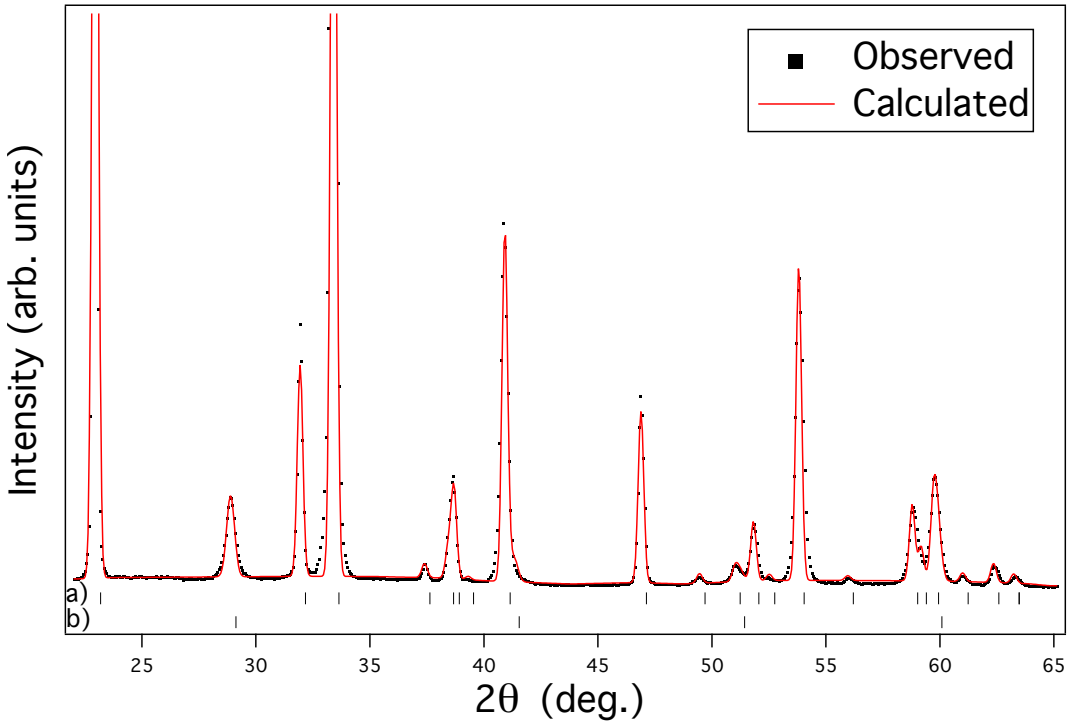

Figure 3.28 *Observed and calculated diffraction peaks from a Le Bail refinement of Sb-III at 18.9 GPa. Peak positions are indicated by the tick marks below the integrated pattern with a and b showing the ambient Sb-I phase and the Sb-III phase, respectively.*

Much like in the Sb-I and Sb-I′ phases, notable variation in intensity around the azimuth is observed in the Sb-III diffraction patterns, as illustrated in figure 3.29. In comparing the texture of the uncompressed Sb-I diffraction peaks and the Sb-III peaks, there is no obvious relationship between the patterns, unlike in the case of the Sb-I to Sb-I′ transition which is not very reconstructive in nature and so the same texture is maintained. There is more azimuthal variation in intensity in the Sb-III diffraction than in the Sb-II patterns, this is perhaps unsurprising given that the Sb-I→Sb-II transition is significantly more reconstructive than the Sb-I→Sb-III transition.

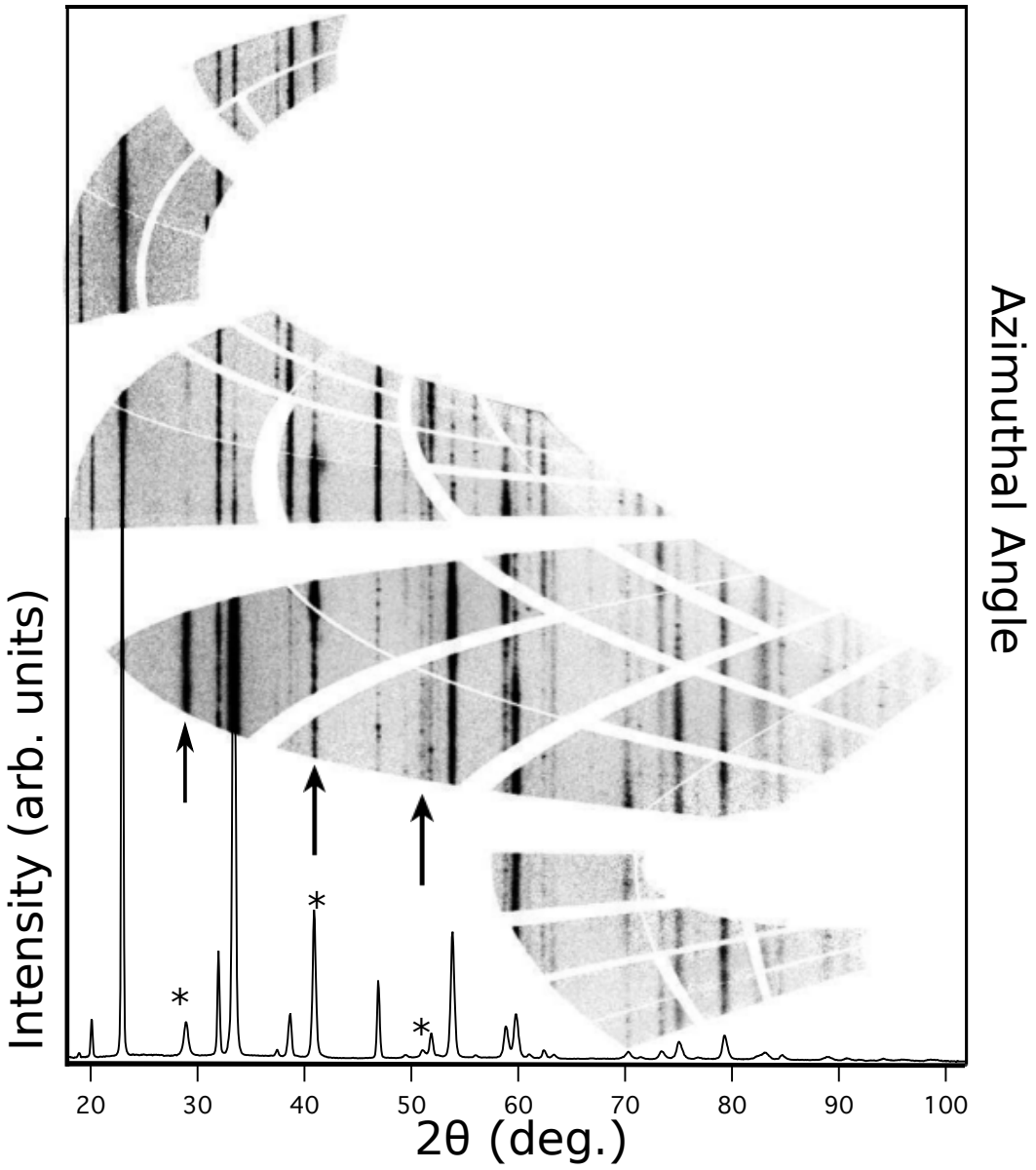

Figure 3.29 *Texture is present in the Sb-III phase as shown by the textured bcc Debye-Scherrer rings indicated with arrows in the raw data, with corresponding integrated peaks marked by a star.*

3.5.4 Liquid Sb

There has been relatively limited work conducted to characterise the melt curve of Sb. As discussed in section 1.4, early work was conducted by Klement [27] and Stishov [31] which used static compression techniques alongside differential thermal analysis to map out the melt curve of Sb to ∼7 GPa. More recently, work has been published by Chiba *et al.* which reports structural analysis of liquid Sb using the multianvil high-pressure apparatus and energy dispersive x-ray diffraction techniques [116]. There have, however, been no dynamic compression studies of melting in Sb to date.

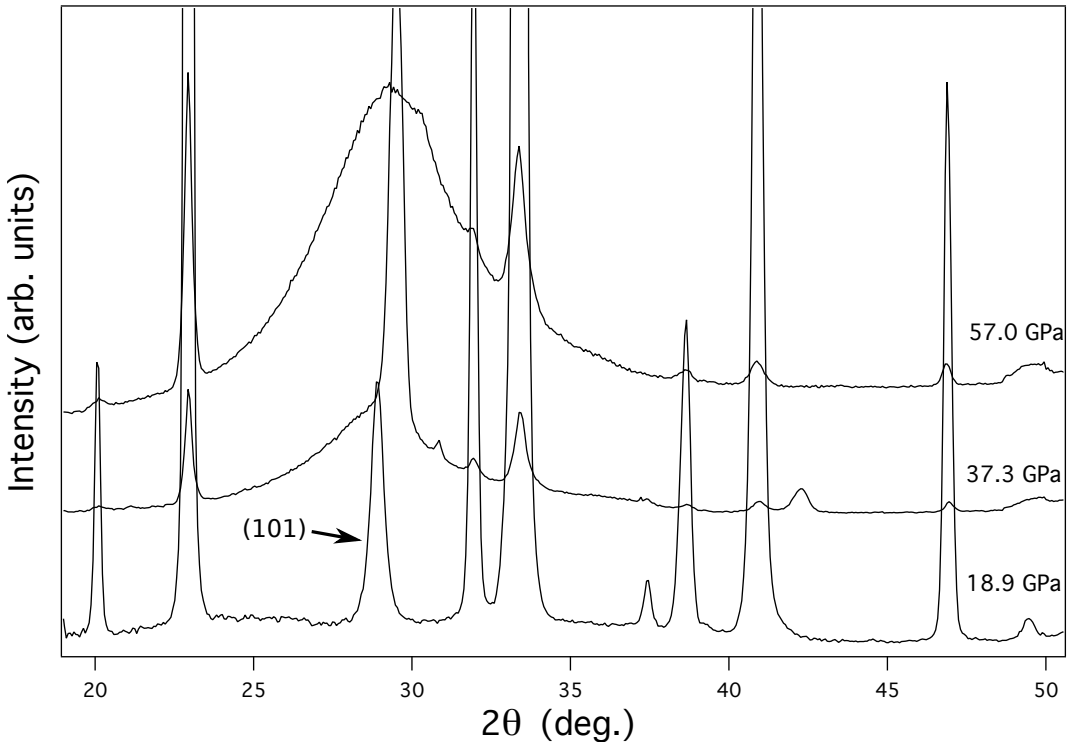

Figure 3.30 *A waterfall plot showing the onset of the liquid phase. The (101) bcc peak is indicated on the plot.*

Figure 3.30 shows the onset of melting in the Sb sample, as the first liquid peak emerges at 37.3 GPa. The onset of the liquid phase is marked by the presence of a broad peak around 30° as the crystal melts and long range order is lost. For all of the shots containing liquid diffraction, LiF windows were used in the target package and the pressures were determined using the VISAR diagnostic and the Sb EOS. The pressure obtained from the VISAR diagnostic will be somewhere between the solid and liquid Sb states in the mixed phase region, whereas the volume, determined from the bcc peak positions in the x-ray diffraction data, is that of the solid component. In the PV plot shown in figure 3.40, the "liquid

and bcc" data points are denser than data obtained from previous studies at the same pressure, this is because the V/V_0 value is based on the diffraction peaks from the solid bcc phase which has a higher density than the mixed phase density measured by the VISAR diagnostic (from which the pressure is obtained).

The observation of the liquid phase on the nanosecond timescales of these shock compression experiments is certainly no surprise; recent work published by Gorman *et al.* reported shock melting of Bi (a structurally similar element) on timescales shorter than 3 ns [117]. In Sb, the bcc and liquid phases are found to coexist between 37.6 and 59.3 GPa. The presence of both liquid and bcc diffraction in the data collected on compression indicates that the Hugoniot coincides with the melt curve over this pressure region, and that bcc is the stable solid phase at melting for these pressures. No data were collected showing liquid Sb without the presence of diffraction peaks from the bcc phase meaning that the pressure at which the principal Hugoniot leaves the melt curve and enters into the liquid phase is unknown.

It would certainly be of interest to further study the behaviour of liquid Sb. Liquid-liquid transitions have been observed in other group-15 elements; liquid P undergoes a first order transition at 1 GPa and 1300 K [118]; liquid As has been shown to exhibit an increase in coordination number with pressure, mimicking the A7 to simple cubic transition in the solid phases [116]; and it has been reported that the coordination number in liquid Bi also increases with pressure, following the relaxation of the Peierls distortion in the solid phase [119, 120]. Given that this work reports the existence of the Sb-I′ phase under dynamic compression, it would be interesting to see how liquid Sb behaves under the same rapid energy loading conditions, but this would require higher temperature experiments than performed here on the principal Hugoniot.

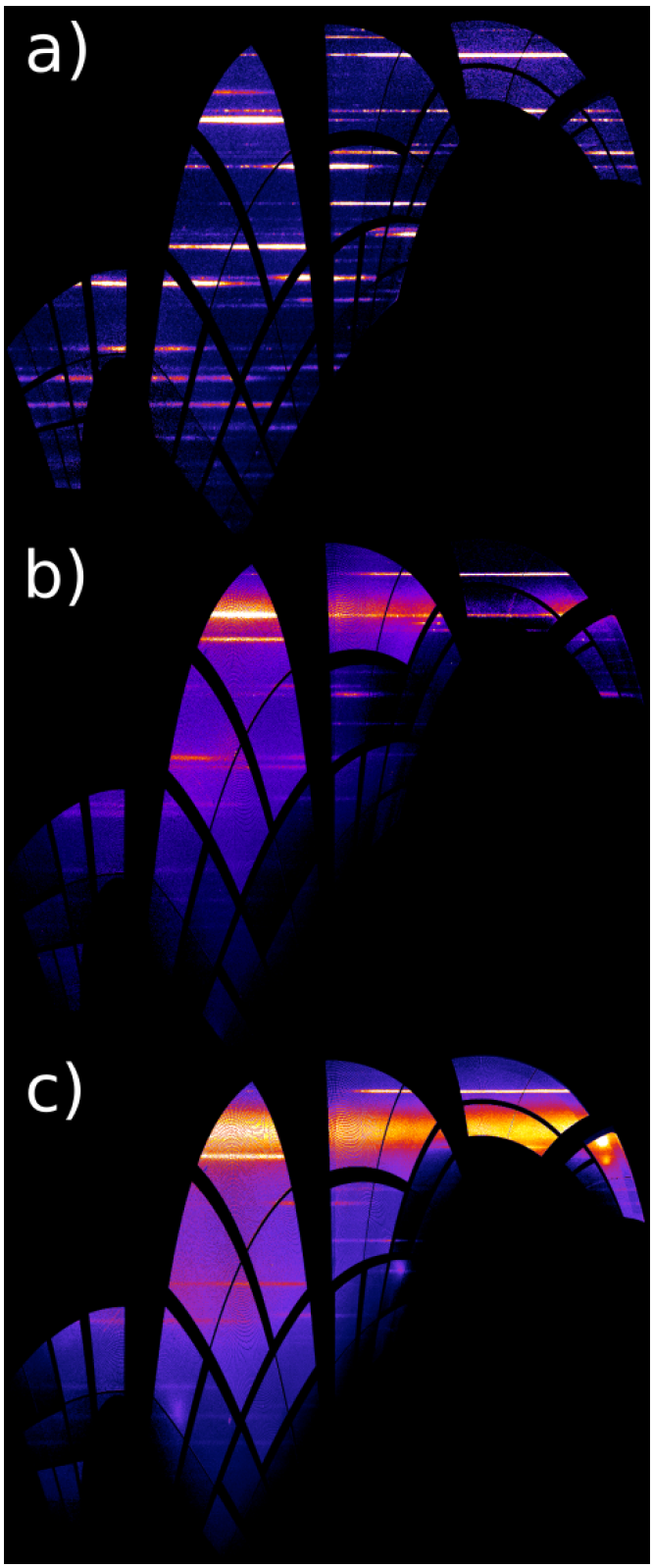

Figure 3.31 *Diffraction profiles showing the onset of melting. a) shows uncompressed Sb-I along with Sb-III diffraction peaks at 24.6 GPa, b) shows uncompressed Sb-I along with Sb-III at 37.6 GPa and broad liquid features and c) shows that most of the Sb-I and Sb-III signal has been masked by the broad liquid signal at 57.2 GPa (pressures determined using the VISAR diagnostic as these data were collected from LiF window targets).*

3.5.5 Unidentified Diffraction Peaks

As well as the aforementioned phases that were characterised in this study, we also observed some unexplained diffraction peaks. The first Sb-I′ diffraction pattern contains an uncharacterised peak around 31° 2θ, as indicated by a star in figure 3.32. The next pattern (obtained at 10.9 GPa) shows the presence of a new, unidentified feature around 26° which persists throughout the rest of the Sb-I′ data. Additionally, a broadening of the uncompressed Sb-I (104) peak is observed (highlighted in grey in figure 3.32) as another peak grows underneath it.

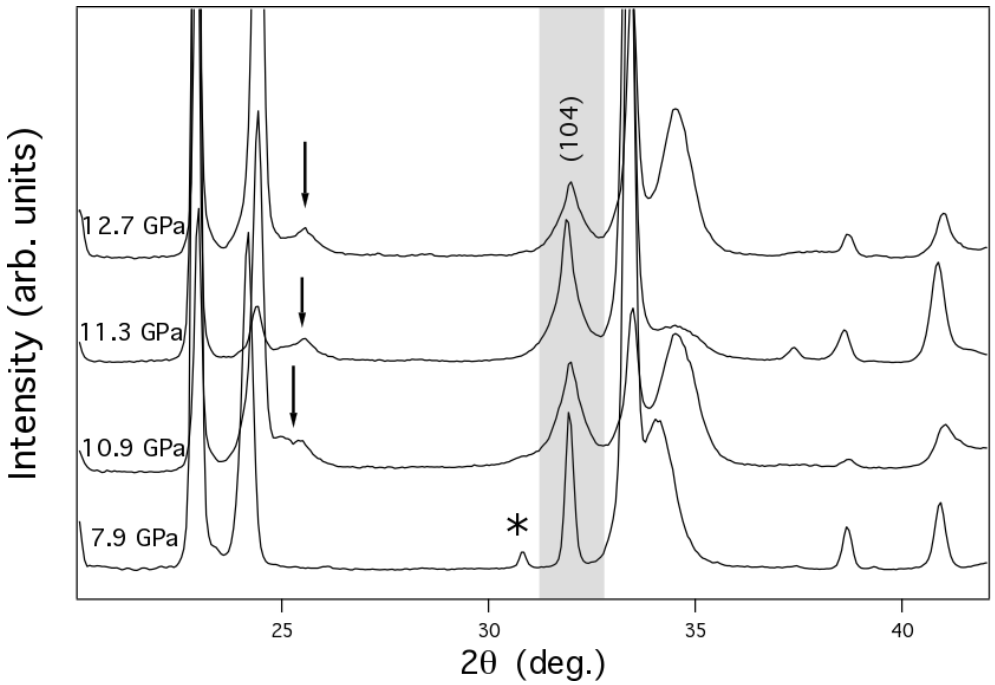

Figure 3.32 *A waterfall plot showing the unidentified peaks present in the Sb-I′ diffraction data. The arrows indicate an unindexed peak and the grey shaded region highlights the ambient (104) peak which is broadened, possibly due to an unexplained overlapping peak.*

As well as persisting on increasing pressure for the remainder of the Sb-I′ phase, evidence of the two unidentified features (at ∼26° and ∼31°) is observed in the Sb-II and low pressure Sb-III diffraction patterns. Figure 3.33 shows that the broadening of the (104) peak at ∼31° is present until Sb-III data is collected at 18.4 GPa. The feature at ∼26° is difficult to resolve in the Sb-II data as it overlaps with the (2200) and (1001) Sb-II peaks, though it would explain the broad nature of these peaks. This feature is observed again in the Sb-III diffraction data. Initially this was mistaken for Sb-I′ diffraction signal which would be present if the overdriven regime had not yet been reached and two plastic waves were

propagating in the sample. This interpretation was, however, rejected as there were no other Sb-I′ peaks present in the diffraction pattern and the position of the peak was at too high an angle (the volume of Sb-I′ corresponding to this peak position would be unphysical).

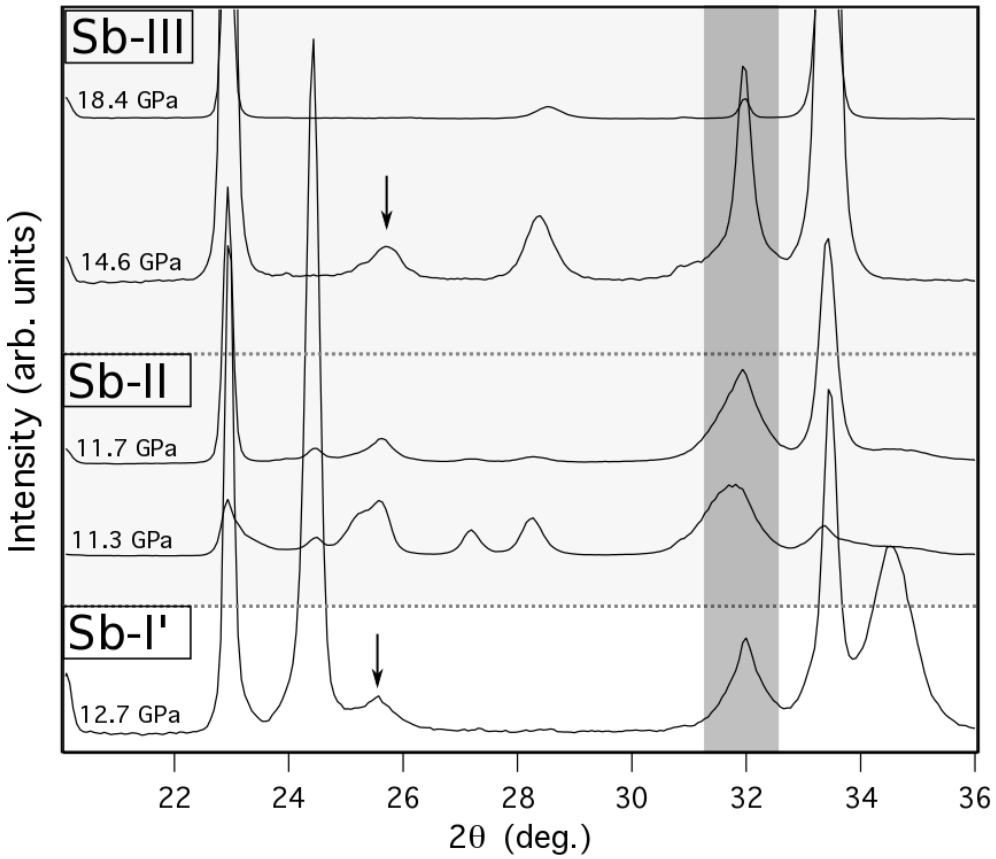

Figure 3.33 *A waterfall plot showing the unidentified peaks present in the Sb-I′, Sb-II and Sb-III diffraction data. The arrows indicate an unindexed peak and the grey shaded region highlights the ambient (104) peak which is broadened due to an unexplained overlapping peak.*

Unfortunately, as there are only two features to this unidentified phase, and at least one of the features always overlaps with another peak, it has not been possible to find a structural solution. The pre-compression x-ray diffraction data has been checked for each target to eliminate the possibility of a contaminant in the target and the raw diffraction images have been checked for unusual intensity spots. It is most unusual that these features should persist across three different phases.

It is possible that an improved understanding of this behaviour could be obtained if diffraction data were collected from the target in a transverse geometry. Presently x-ray diffraction studies are conducted using a geometry such that

the x-rays have traversed the full length of the target before they are detected; this means that diffraction intensities resulting from the compressed, released and uncompressed material are visible in the collected data, as discussed previously. By collecting diffraction data at 90° to the shock propagation, one may probe a single compressed state alone. This would mean that a more comprehensive picture could be built up of the structures that form at different depths into the target as the shockwave propagates; something which is particularly useful in the instance of multiple plastic waves propagating through the material. This would also be of use in the instance where the intensity peaks of the uncompressed material overlap with the 2θ positions of the compressed material; it would allow better resolution of the compressed material without the interference of the uncompressed peaks. Such investigations are currently being conducted by Dr E. E. McBride at the LCLS, the outcome of which is greatly anticipated [121]. Additionally, it is believed that the European XFEL will be able to provide the ability to conduct shock compression experiments with the use of transverse x-ray diffraction geometry. In addition, the projected energy of the European XFEL (10-25 keV) will allow thick samples to be probed in this geometry across a large range in 2θ.

3.5.6 Release Studies

X-ray diffraction data collected at a time after the shock front has reached the rear surface of the Sb layer of the target is referred to as being "on release". These data are often much more difficult to interpret than data collected on compression as they do not necessarily represent on-Hugoniot states, meaning that many of the equations used in the analysis of the data discussed so far are invalid. Furthermore, the pressure states of data collected on release are not determined by one, or two, forward progressing shock fronts but rather it is the result of many wave interactions between waves reflected from any boundaries between materials in a target, including dispersive release waves, as discussed in section 2.1.3.

Figure 3.34 shows a Rietveld refinement of a diffraction pattern taken ~ 5.5 ns on release. This target made use of a LiF window in order to reduce the magnitude of the release at the rear surface of the Sb so that the pressure decrease in the Sb was more gradual than in a target with a free surface in vacuum. From the VISAR diagnostic, the peak pressure (an on-Hugoniot state) was found to be 17 GPa, meaning that the Sb would initially be in the bcc phase. From the diffraction pattern fit we do not see any evidence of the Sb-III phase. The fit indicates the presence of Sb-II with lattice parameters $a_H = 7.979$ Å, $c_H = 3.860$ Å and $\gamma = 1.306$, and a V/V_0 of 0.7687 Å^3. The refined atomic coordinates of the host and guest atoms are $(0.153, x + 0.5, 0)$ and $(0, 0, 0)$, respectively. These parameters agree well with data obtained at 14.5 GPa and 300 K (a_H =7.989(1) Å, c_H =3.867(1) Å, γ =1.309(1), and x =0.156(1)) in a static compression study by Degtyareva *et al.* [43]. The fit also includes peaks from the Sb-I phase (at near-ambient conditions with $a = 4.311$ Å and $c = 11.242$ Å, corresponding to a V/V_0 of 0.998) and the Sb-I′ phase. Here the Sb-I′ phase has been fitted using a simple cubic structure, as discussed previously the difference in volume between the simple cubic and rhombohedral Sb-I′ candidate structures is very small. This fit corresponds to a Sb-I′ pressure of ~ 8.5 GPa.

The release state of this target is evidently very complex; the volumes given by fitting the diffraction profile indicate that there are three discrete pressure states within the target. In order to understand the structures present in the diffraction pattern, the HYADES simulation code (described in section 2.1.3) was used to assist in the interpretation of the wave interactions in the Sb target. As there is no existing Sb EOS file within HYADES, an alternative EOS was selected. From

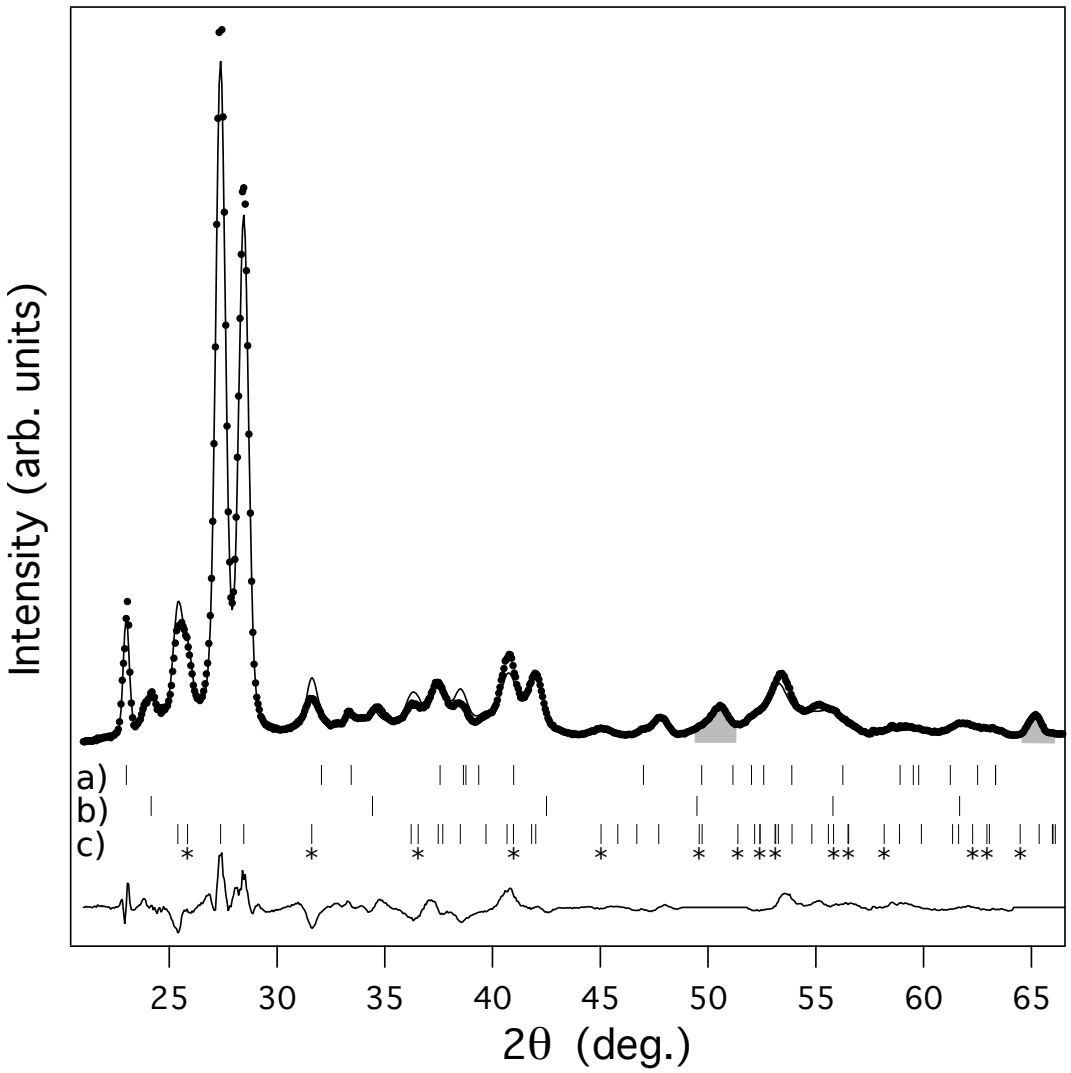

Figure 3.34 *A Rietveld refinement of diffraction data collected 5.5 ns on release following shock compression to 17 GPa. Sb-I, Sb-I′ and Sb-II phase markers are labelled a, b and c, respectively. The guest peaks in the HG structure are labelled using stars. The grey shaded regions represent data excluded from the fit.*

the library of EOS files available, Nb ($\rho_0 = 6.850$) is the most well matched to Sb ($\rho_0 = 6.698$) in terms of impedance; the second closest candidate element available in the EOS library was Zr ($\rho_0 = 6.506$). The P-u_p curves for Sb, Zr, Nd and LiF are shown in figure 3.35. Upon conducting simulations it was found that the Nd was too closely impedance matched with the LiF layer and that this was not representative of the wave interactions between the Sb and LiF layers. Consequently, the Zr EOS was used to simulate the target; although Zr has a higher impedance than Sb, it is more representative of wave interactions between materials with a difference in impedances.

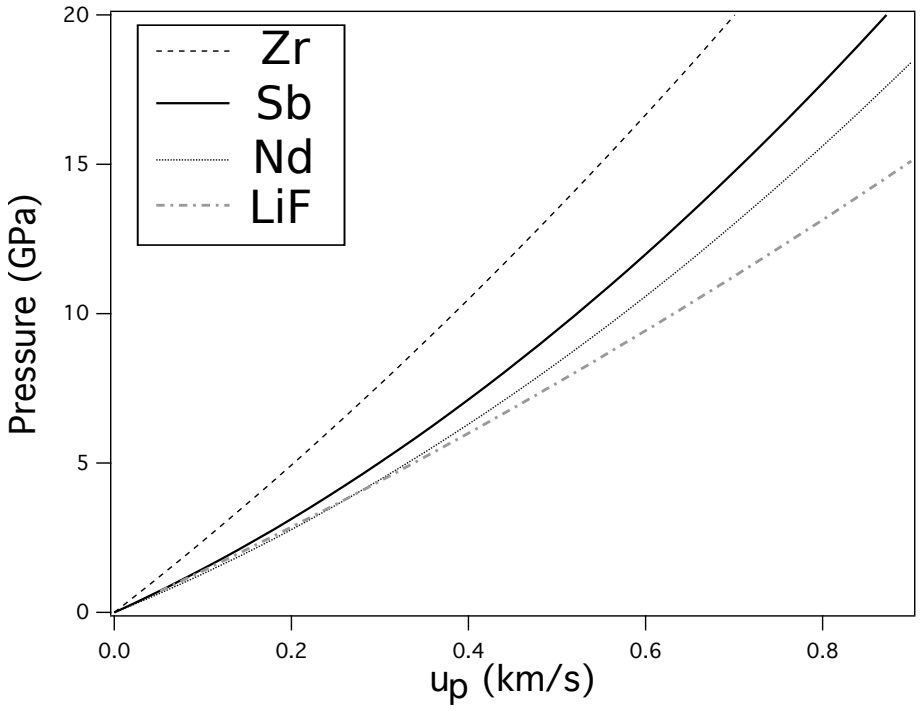

Figure 3.35 *The $P - u_p$ relations for Zr, Sb, Nd and LiF. Plotted using data from the shockwave database.*

The output of the simulation is shown in figure 3.36. The time of collection of the x-ray diffraction is 5.5 ns after the breakout (the point where the shock front reaches the rear surface of the target). The bulk sound speed is faster in Zr ($\sim$3.7 μm/ns) than in Sb ($\sim$2.5 μm/ns) so the shock front will have progressed further in the Zr simulation in the same time interval for the Sb target. We see in figure 3.36 that there are definite discrete pressure states within the Zr layer a short time after shock breakout into the LiF. It should be noted that the pressures shown in this simulation are not representative of the pressures in the Sb target due to the use of the Zr EOS in the simulation. The discrete pressure states explain the presence of the Sb-II and Sb-I$'$ diffraction intensities but as there are only two discrete pressure states in the Zr layer in the temporal region of interest, the simulation does not explain the presence of low-pressure Sb-I diffraction intensities.

The unintegrated diffraction data for this shot is shown in figure 3.37. The smooth nature of the Sb-I reflections confirm that the data was not collected on compression, as the Sb-I diffraction profiles from the targets in this experiment are characterised by highly textured Debye-Scherrer rings. This loss of texture indicates that the A7 structure has recrystallised. Given that the Sb-I reflections appear to be recrystallised from a higher pressure state and the fact that they

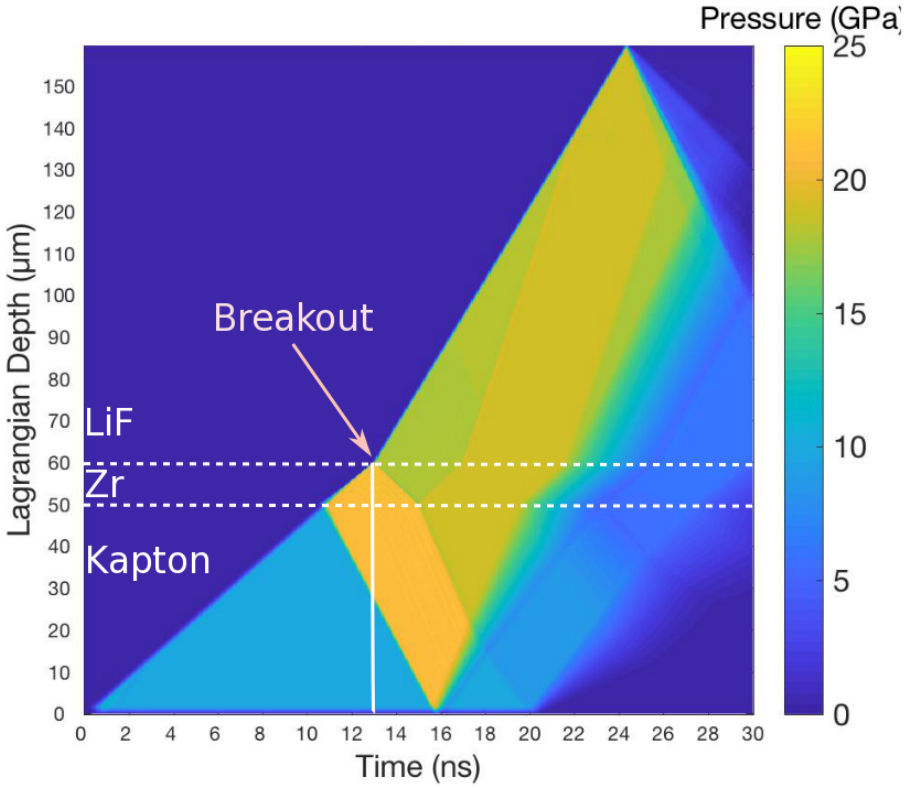

Figure 3.36 *A distance vs time plot generated using the output from the HYADES code. The shock breakout and diffraction data collection time are indicated on the graph.*

are not explained by significantly complex pressure gradients in the HYADES simulation, one may theorise that this phase occurs as a consequence of release waves from the sides of the driven region of the target. These 2-dimensional waves are not accounted for in HYADES simulations.

As well as using LiF windows to reduce the rate of pressure release in the target, data were collected on release without the use of a rear LiF window. The waterfall plot shown in figure 3.38 presents a series of integrated diffraction patterns at various time intervals on release. In each of these shots, the peak pressure state was ∼17 GPa, meaning that the crystal is released from the bcc phase.

The (101) bcc peak is indicated on the plot in the data collected at 0.2 ns before breakout. This peak is no longer visible from 3.29 ns on release but the (2110) and (3100) peaks of the Sb-II phase are visible at ∼26° and ∼27° respectively. The Sb-II phase is observed to form and the peak positions remain approximately constant over, at least, a 6.6 ns period. Fitting diffraction data collected on release is a difficult feat given that the features are broadened due to pressure gradients in the material. Additionally, wave interactions from the Sb/free surface

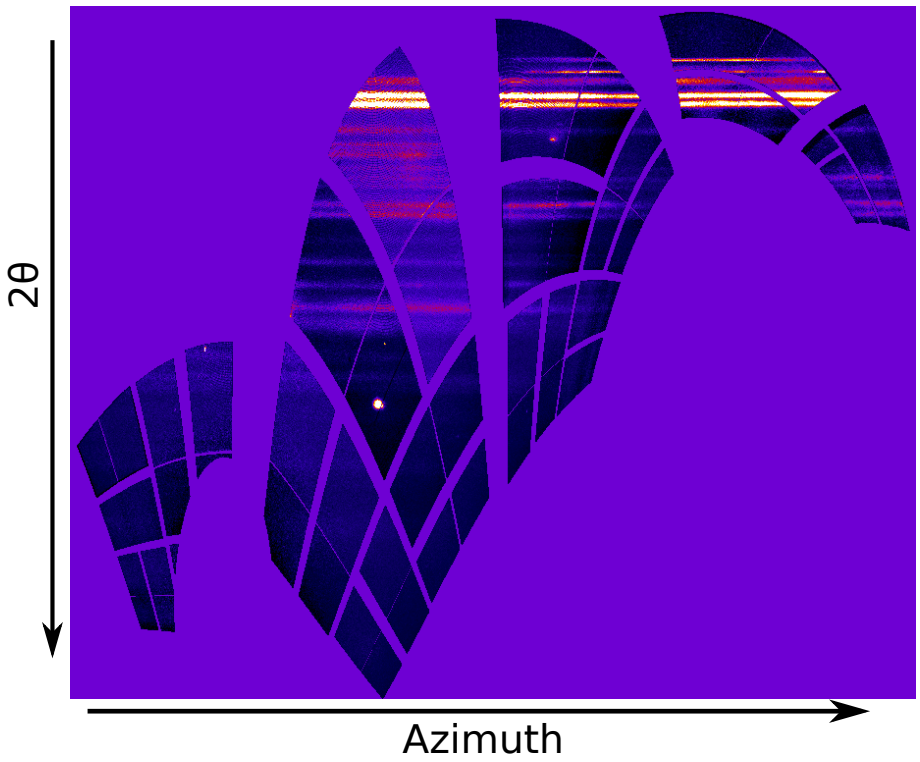

Figure 3.37 *Diffraction data collected 5.5 ns on release from a peak pressure of 19 GPa. The smooth nature of the Sb-I Debye-Scherrer rings shows loss of texture upon recrystallisation.*

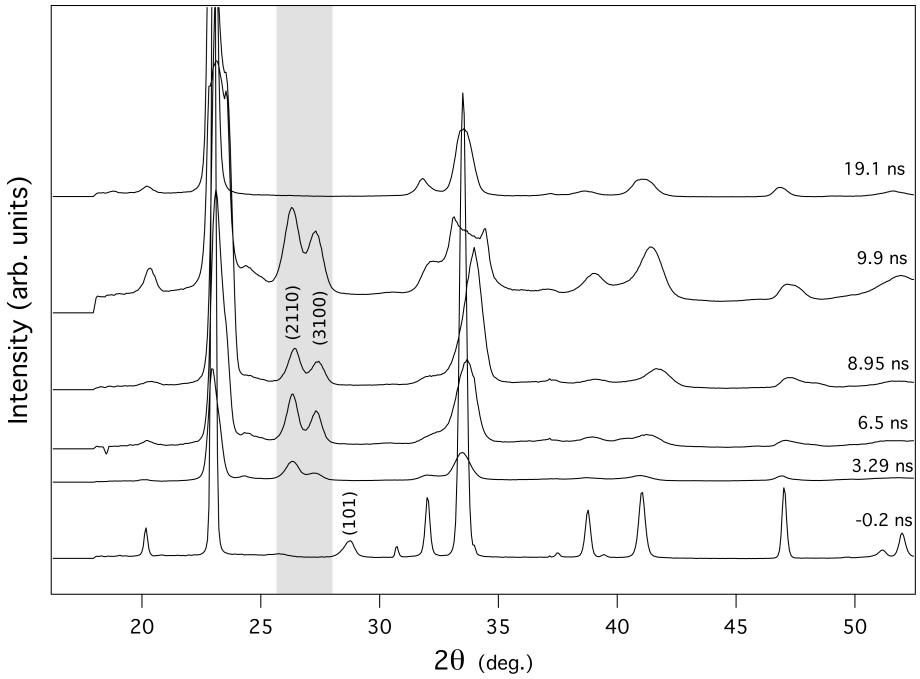

Figure 3.38 *A waterfall plot showing data collected on release from targets without a LiF window. The peak pressure state of each of these shots was ∼17 GPa. Timings are approximate*

interfaces generate significantly complex wave interactions [122]. It is evident, for instance, that not only are there diffraction peaks indicative of ambient Sb-I, there are also features which indicate compressed Sb-I is present in the target. Fully understanding the behaviour of Sb on release would require much more extensive data collection, both with and without LiF windows. As this was not the aim of this experiment, the data available for such analysis is extremely limited. Additionally, more meaningful simulation data could be obtained if an Sb EOS was available which accounted for the non-linear U_S-u_p relationship, as discussed in section 3.3.

In spite of the complex nature of the diffraction patterns, the (2110) and (3100) peaks of the Sb-II phase are clearly visible around $\sim$26° and $\sim$27° respectively. The lattice parameters obtained from a Le Bail fit of the Sb-II phase (a_H =8.295 Å, c_H =4.007 Å, and γ =1.308) indicated a V/V_0 of 0.86. That the position of these peaks remains constant in 2θ over this time period is a strong indication that the Sb-II phase has been recovered to ambient pressure. The lattice parameters of the Sb-I peaks present in these release data indicate that the Sb-I phase is also at ambient pressure when compared with the room temperature data of Degtyareva *et al.* [43] though the smeared-out, broad nature of these peaks indicates the presence of some pressure gradients within the sample. Later in time we see the disappearance of the Sb-II phase, with only broad features from the Sb-I phase remaining (this is shown at 19.9 ns in figure 3.38).

It would certainly be interesting to further explore the nature of the Sb-II phase on release. Already we have seen evidence of the Sb-III phase releasing to the Sb-II phase at 15 GPa, a pressure at which Sb-II is known to exist in the equilibrium phase diagram but at which Sb-II is not observed to form under initial shock-compression. Further experiments which make the use of LiF windows to lessen the magnitude of the release waves in the target would be necessary to conduct these studies; it would be interesting to observe whether the Sb-II phase forms over the entirety of the equilibrium Sb-II existence region on release.

3.5.7 Discussion

Sb targets were compressed between 1.9(3) and 59(2) GPa, an overview of the observed phases is shown in figure 3.39. This figure presents the same diffraction data shown in figure 3.14 at the beginning of the results section but here the structures have been characterised and refined following the analysis described in the previous sections. Tick marks on the plot indicate peak positions for each of the high-pressure structures at the relevant pressure. The pressures on this plot are calculated using the combined method discussed in section 3.3 unless a LiF window is present in the target (as in the case of profiles (iii), (vi) and (vii)), in which case the pressure is determined from the VISAR data alone. From the analysis described in this chapter it was determined that the Sb-I phase (rhombohedral A7 structure, space group $R\bar{3}m$) shown in profile (i) at ambient and (ii) on compression, was found to persist up to 4.4(4) GPa. Between 5.8(3) and 6.9(6) GPa the c/a ratio is no longer able to be accurately determined due to peak overlap but the presence of the rhombohedral (101) peak indicates that the structure is not cubic. At 7.9(6) GPa the Sb-I′ phase (profile (iii)), was observed. All data collected between 7.9(6) and 12.7(10) GPa showed evidence of the Sb-I′ phase.

Profile (iv) shows an example of a diffraction pattern obtained from the Sb-II phase (superspace group $I'4/mcm(00\gamma)0000$); this phase was observed in data collected between 11(2) and 14(2) GPa. The stability region of this phase is markedly smaller than that observed on static compression [43]. The Sb-IV phase was not observed, this is perhaps not surprising, given the incredibly small (1 GPa) pressure region over which it is stable under static compression at room temperature [44]. The Sb-III phase (bcc structure, space group $Im\bar{3}m$), shown in profile (v), was observed between 14.6(14) and 29.0(8) GPa. From 37.6(9) GPa, diffraction from liquid-Sb was observed alongside the bcc peaks (as in profile (vi) and (vii)), this is indicative of these on-Hugoniot states coinciding with the Sb melt curve.

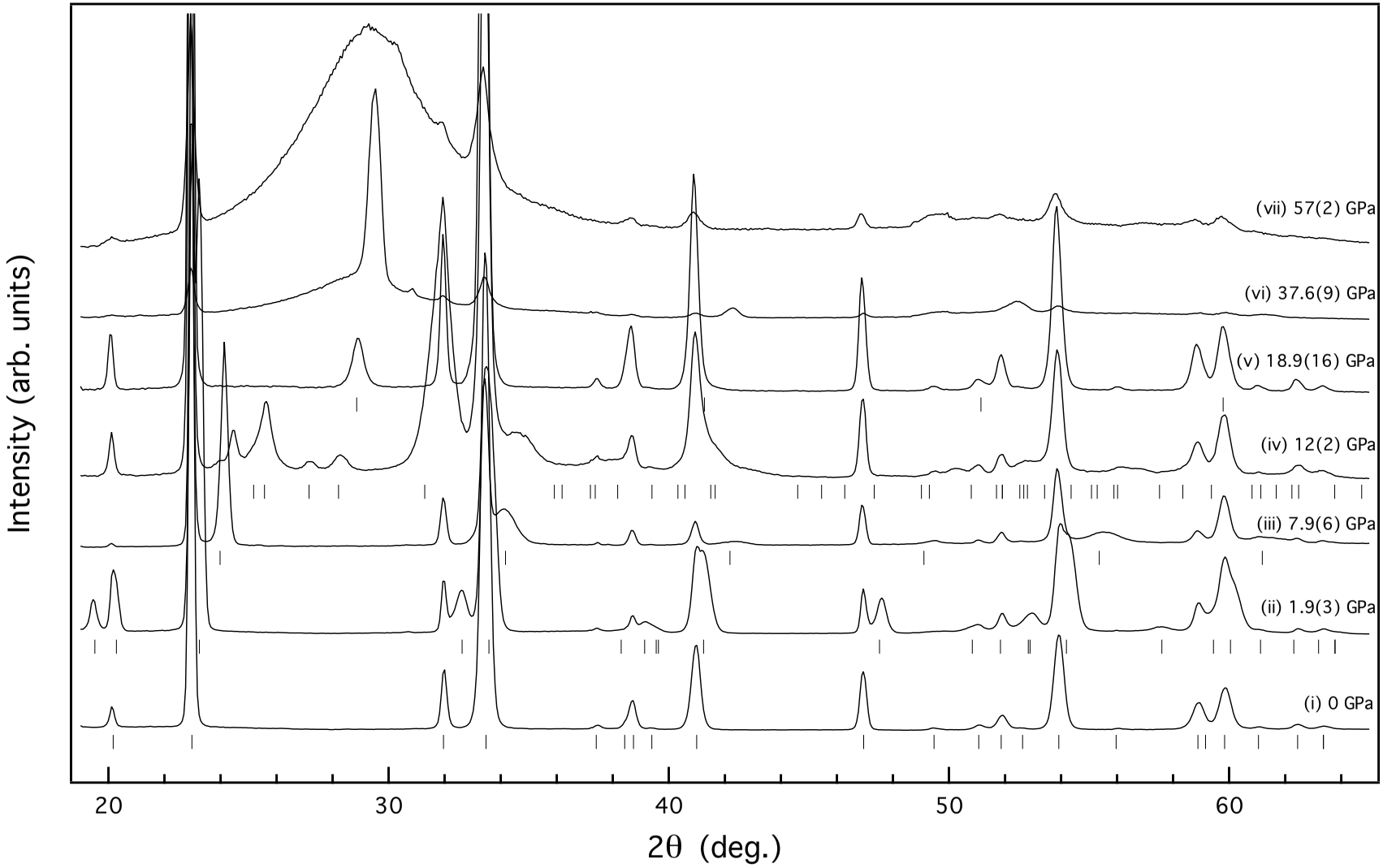

Figure 3.39 *Integrated diffraction profiles from shock-compressed Sb along with tick marks showing the calculated peak positions for the structures at the relevant pressures. The diffraction profiles are from (i) ambient Sb-I, (ii) compressed Sb-I, (iii) Sb-I′, (iv) Sb-II and (v) Sb-III. The broad feature which appears around 30° in profiles (vi) and (vii) marks the onset of liquid diffraction while the bcc phase is still present.*

Figure 3.40 shows a PV plot containing the shock compression data from the LCLS, with all data points obtained on compression. Data collected using LiF windows (P determined from pre-existing EOS) are shown in grey, while data collected without (P determined directly) are shown in black. The unfilled circles show the pre-existing data (shown earlier in figures 1.6 and 3.10) from Warnes [49] and McQueen and Marsh [48]. The grey shaded lines show the isothermal compressibility data of the Sb-I, Sb-II and Sb-III phases, collected at 300K [43]. A Birch-Murnaghan EOS (with K′=4) has been used to extrapolate the Sb-III compression curve to lower pressures so that it may be compared with the Sb-III data obtained in this work; the Sb-III phase is observed to form at a much lower pressure under dynamic compression than has previously been observed in room temperature, static compression studies, as discussed in section 3.5.3.

The data obtained in this experiment agree well with existing data from plate-impact driven dynamic compression experiments [48, 49]. There is a notable difference between the mixed bcc and liquid data points reported in this study and the pre-existing data points in the same region. The previous Sb dynamic compression experiments made measurements of u_p and U_S and subsequently calculated the volume using the Rankine-Hugoniot equations, whereas the data collected in this study directly measures volume using x-ray diffraction data, given, as observed, that each pressure condition is associated with a particular solid phase. The values of V/V_0 shown on the plot for the combined bcc and liquid data points correspond to the volume obtained by fitting the bcc peaks in the x-ray diffraction data, while the pressure is obtained from the VISAR data as these targets all have a LiF rear window. This means that the pressures shown for our data points are calculated from a rear surface velocity from a combination of the liquid and solid states, with x-ray diffraction representing only the solid component.

As mentioned previously, a notable contrast between the data obtained in this work and the results of previous static-compression experiments is the onset of the Sb-III phase at a significantly lower pressure; the bcc structure forms at 14.6 GPa under shock compression versus 28.8 GPa under static compression at 300 K [43]. This result is in contrast to the common behaviour of materials under dynamic compression, where phase transition pressures are often elevated, due to kinetic hinderance [123]. It is possible that the early onset of the Sb-III phase is due to the limited stability of the preceding Sb-II phase, which is stable under dynamic compression over a very limited pressure regime. It is plausible that a

structure as complex as the incommensurate host guest may not be energetically favourable or kinetically accessible in such high-energy, rapid-loading compression regimes.

Figure 3.40 shows good EOS agreement between the PV data obtained during this study and data from previous dynamic compression experiments [48, 49]. While the observation of a two-wave structure agrees well with previous results, the timescale on which the transition to the Sb-II phase occurs (as a consequence of the second compression wave) is found to be markedly different. Previous studies reported a 2-3 μs delay between the first and second compression waves [49, 50], whereas this thesis reports a transition to the Sb-II phase on the nanosecond timescale. This result is not entirely unexpected; the previous dynamic studies of Sb were conducted using larger targets, meaning that the timescales of the experiments were much longer. This result is not unique to Sb; the variation of completion time of phase transitions with target thickness is a phenomenon that has been reported for the $\alpha \rightarrow \epsilon$ phase transition in Fe [123]. While the thin nature of the targets used in the work reported in this thesis could account for the transition time to the Sb-II phase (on the nanosecond timescale) being smaller than that in the previous gas-gun experiments (2-3 μs), the reported delay in formation of the second plastic wave of 0.6 μs was definitely not observed in this experiment and remains poorly understood [49].

Confirming the formation of the Sb-II phase under dynamic compression was certainly a success of this experiment; the previous dynamic studies do not identify the structure of the Sb following the second plastic wave. During these early experiments the structure of the Sb-II phase was not well characterised by static compression studies and technology had not advanced sufficiently that x-ray diffraction data were able to be obtained on the timescales of shock compression studies. The values of V/V_0 reported in Sb following the second plastic wave in Warnes' paper [49] (calculated from rear surface velocity measurements) range from 0.849 at 9.4 GPa to 0.773 at 13.3 GPa, these agree well with the values of V/V_0 observed for the Sb-II phase in this experiment (0.778 at 11.3 GPa), indicating that a transition to the Sb-II was indeed being observed. As this study did not make use of x-ray diffraction, it is not possible to discern whether they observed a Sb-I$\rightarrow$Sb-II transition or a Sb-I$'\rightarrow$Sb-II transition as the difference in volume between the Sb-I and Sb-I$'$ phases is very small. It would certainly be interesting to further investigate the nature of this transition using x-ray diffraction in experiments conducted over longer time periods at a gas-gun facility.

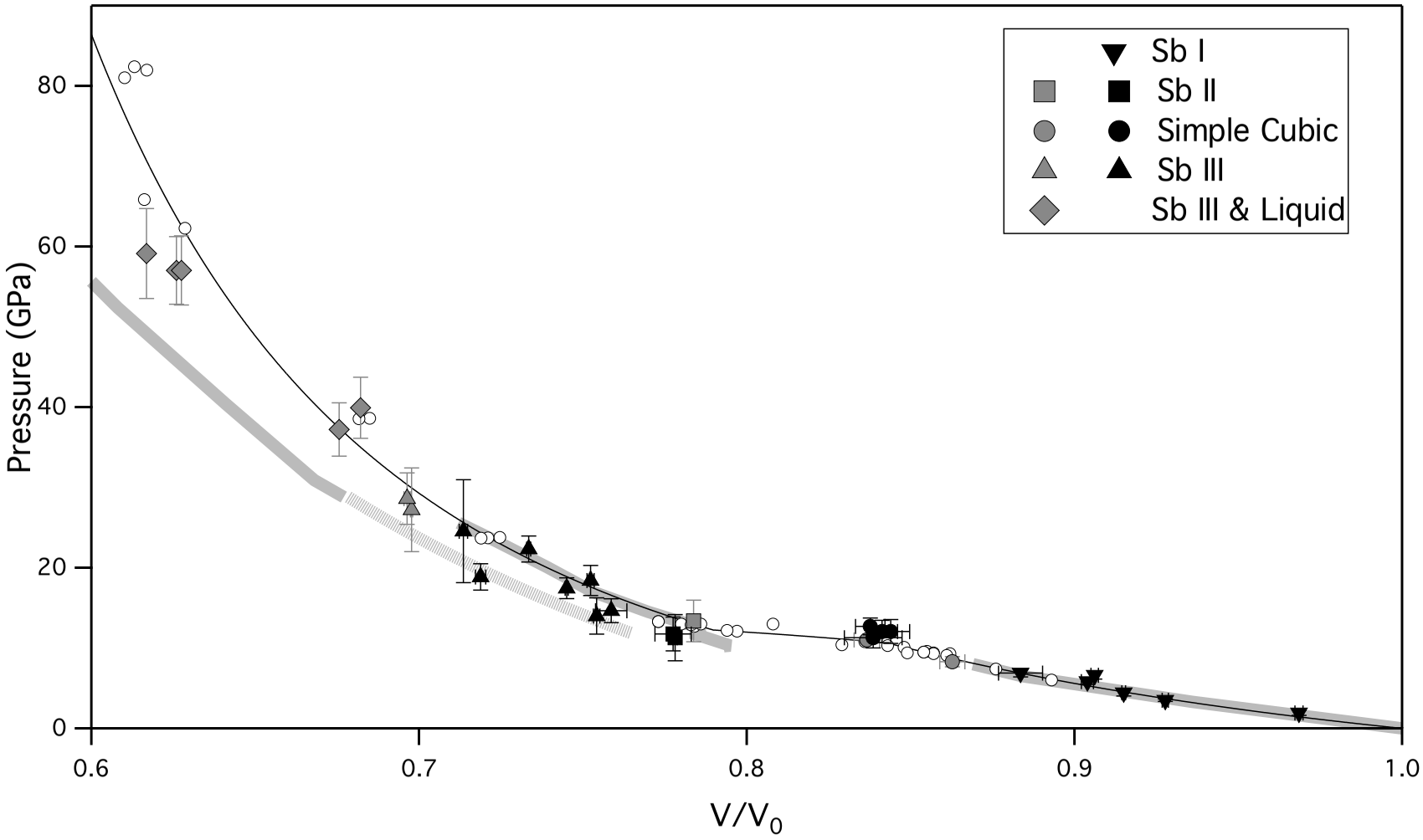

Figure 3.40 *The volumetric compression of Sb obtained at the LCLS. Hugoniot EOS data obtained from this study are shown using filled black symbols, and points obtained using a LiF backing window in this study are shown using filled grey symbols. The grey shaded lines shows the isothermal compressibility data at 300 K for the Sb-I, Sb-II and Sb-III phases [43]. Unfilled circles show data obtained from previous dynamic compression studies using velocimetry measurements [48, 49]*

Figure 3.41 shows an updated version of figure 1.4 which summarised the known components of the Sb phase diagram prior to this work. The melt curve has been extrapolated from the previous melt data published by Klement [27] using a Simon-Glatzel fit to the first data point where liquid diffraction was observed in this work; this method of melt curve extrapolation has been published recently in a paper investigating dynamically compressed Sc [57]. The relative volume of the liquid phase to the bcc phase, as observed in the diffraction data, is very low at the first point where liquid signal is observed; this is shown in profile (vi) in figure 3.39 and indicates that this point is close to the true on-Hugoniot melting point. The grey shaded areas around the melt curve show the uncertainty in this melt curve and are calculated using the uncertainty in the pressure of the first on-Hugoniot point containing liquid diffraction signal. The absence of a published Sb Hugoniot in PT space, in the solid regime, meant that theoretical calculation of such a curve was necessary to determine the value of T at which the liquid diffraction was first observed . The ambient pressure Grüneisen parameter (γ_0) was calculated to be 1.05 using equation 3.6.

$$\gamma_0 = \frac{\alpha K_T V}{C_V} \tag{3.6}$$

Here, K_T represents the isothermal bulk modulus, C_V is the specific heat at constant volume and α is the thermal expansion coefficient. This result is in good agreement with literature values of the Grüneisen parameter [124]. Due to the low Debye temperature of Sb, C_V is assumed to be in the Dulong-Petit limit and γ is extrapolated to higher pressures using equation 3.7.

$$\gamma = \gamma_0 \frac{V}{V_0} \tag{3.7}$$

Using equation 3.8, dT may be calculated and the Hugoniot curve may then be plotted in $P - T$ space [125]. It should be noted that this Hugoniot is an approximation which does not take into account the effects of solid-solid phase boundaries, and will not be sufficiently accurate for melt studies. Error bars have been omitted in T as this calculation represents only a loose estimate of the $P-T$ Hugoniot.

$$dT = -T\left(\frac{\gamma}{V}\right)dV + \frac{1}{2C_v}\left[(V_0 V)dP + (P - P_0)dV\right] \tag{3.8}$$

The co-existence of the bcc and liquid diffraction over the pressure range 37.6 to 59.3 GPa indicates that these points all lie on the melt curve and, as these are also on-Hugoniot data points, the Hugoniot is assumed to coincide with the melt curve in this regime. There have been reports of discrepancies between melt curves observed under static and dynamic compression for a series of elements such as Fe and Ta [126, 127]. These discrepancies have led to much debate over whether shock experiments measure equilibrium melt states or whether they are probing "superheated" states where a material remains solid at a higher temperature than the equilibrium melt curve [128]. As there are no static melt curve studies that have been conducted on Sb in the pressure region we observe melting here, it is not presently possible to comment on this phenomenon. It would certainly be interesting to probe the melt curve of Sb in this region under static compression in order to compare the results.

While the phase diagram of Sb has not been extensively researched above room temperatures, we certainly see strong discrepancies between the room-temperature, static-compression data and the on-Hugoniot data obtained using dynamic compression techniques. Figure 3.41 highlights these discrepancies, with the onset of the Sb-III phase in the stability region of Sb-II being particularly notable. While there are no reports of the Sb-I′ phase occurring in static compression work, there are reports of a simple cubic phase [30, 32], as discussed in section 1.4. It was theorised by Schiferl [112] that the transition to the simple cubic structure was as a result of non-hydrostatic compression in certain static compression techniques. This idea is corroborated by Wang *et al.* [114] who state that uniaxial compression could indeed be a contributing factor in the formation of the simple cubic phase. The following chapter in this thesis details static compression experiments that investigate high-pressure, high-temperature Sb. Experiments are conducted both with and without the use of a pressure transmitting material in the hopes of assessing the effect of hydrostatic and non-hydrostatic compression on the formation of the simple cubic phase.

At the time that the work described in this chapter was undertaken, there was no published research showing structural resolution of structures as complex as the incommensurate host-guest structure of the Sb-II phase on dynamic compression timescales. Work published by Dr R. Briggs and the McMahon group showed the first x-ray diffraction data on shock-compressed Sc, identifying an incommensurately modulated host-guest structure with disordered chains [57]. This work was powerful evidence of the capabilities of modern XFEL facilities

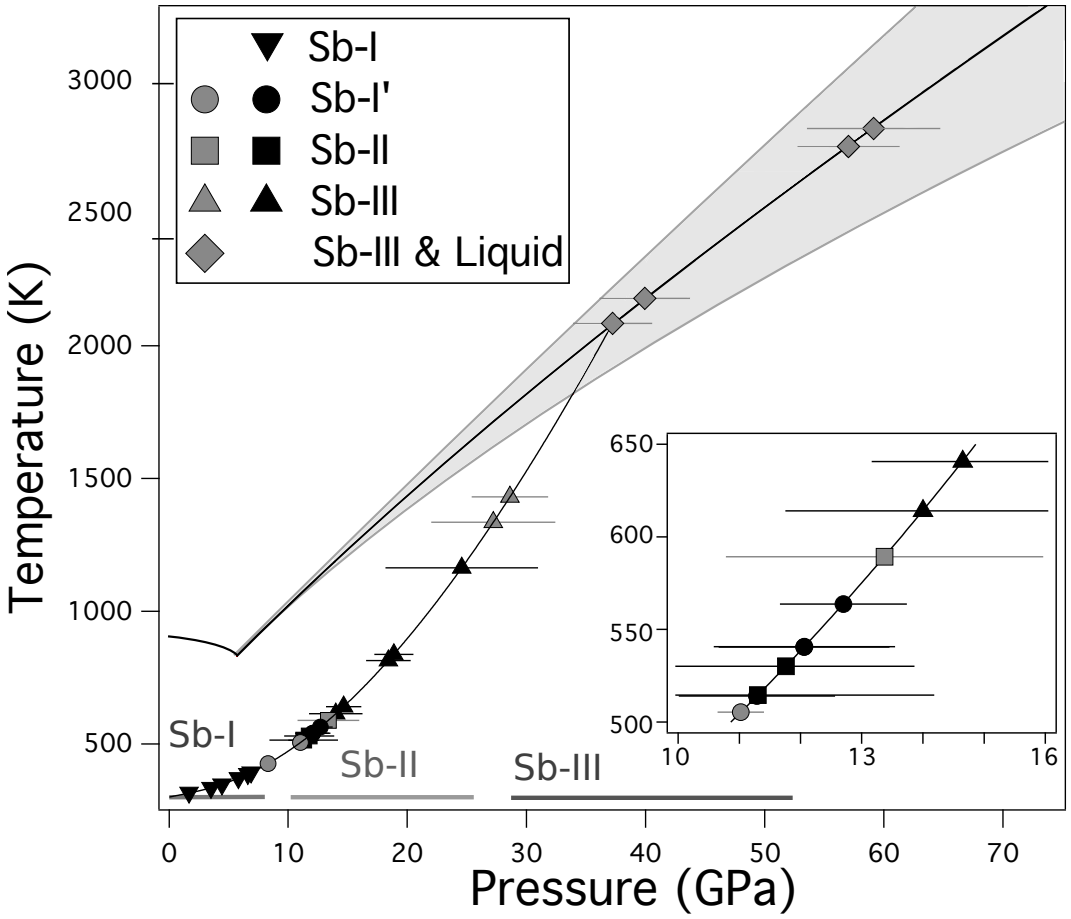

Figure 3.41 *The known components of the Sb phase diagram after obtaining on-Hugoniot data at the LCLS. Melt curve (to ∼9 GPa) from [27], room temperature data from [43].*

to produce x-ray diffraction data of unprecedented quality. The work described in this chapter is a continuation of that effort and presents the first structural resolution of an incommensurate host-guest structure with ordered chains, formed on shock-compression. Furthermore, it is a testament to the quality of the diffraction data obtained in this experiment that the Sb-I′ phase is identified as being distinct from a simple-cubic structure, possible only through diagnosis of peak displacements of ± 0.002Å from calculated positions.

The work conducted in this chapter finds that the Sb-I′ phase forms in the assumed equilibrium stability region of the Sb-II phase, as illustrated in figure 3.25. Additionally, the Sb-III phase is observed to form at 14.6 GPa, this is a much lower pressure than has been reported at 300 K in static compression experiments (28.8 GPa) [43]. In order to determine whether these discrepancies are due to the high temperatures associated with on-Hugoniot measurements at these pressures or whether they are an artefact of the compression technique, the

static work in the following chapter also aims to identify the phase boundaries at elevated temperatures in order to construct a more complete equilibrium phase diagram.

While the quality of data attainable at the LCLS is extremely high, there were some limitations to the work conducted in this chapter. Unambiguous determination of the Sb-I′ structure was not possible in this research; two candidate structures were proposed but the author was unable to establish which of these is the true structure. One of the limiting factors in this endeavour was the textured nature of the Sb targets; as the Debye-Scherrer rings were inconsistent in intensity around the azimuth it was not possible to fully characterise distortion or splitting of the rings. This was exacerbated by the incomplete coverage of the detectors around the azimuth.

In order to characterise subtle splitting or distortion of Debye-Scherrer rings, full detector coverage is required around the azimuth, as well as a substantial range in 2θ. To this end, it is with great anticipation that the author awaits the full commissioning of the European XFEL. As shown in figure 1.7, this state of the art facility will offer peak brilliances that exceed those offered at the LCLS as well as more comprehensive detector coverage, meaning that subtle features in the X-ray diffraction data may be more easily resolved. Additionally, the drive laser at the European XFEL facility will offer access to higher energy drive pulses meaning that phenomena at more extreme $P-T$ conditions may be explored. As the extent of the $P-T$ conditions that are accessible at state of the art facilities is expanded, materials that are predicted to exhibit complex behaviour in these regimes may be explored; for instance, Aluminium is predicted to exhibit an incommensurate host-guest structure at 3.2 TPa [55]. In proving that such structures are able to be resolved on the timescales of shock-compression experiments, this work validates the present diagnostics as contenders for use in these extreme pressure regimes.

Chapter 4

Static Compression of Sb at Diamond Light Source (DLS)

The following experimental results of the high-pressure, high-temperature x-ray diffraction experiments on Sb are split into two subsections within this chapter. This first details work in which a pressure transmitting medium (PTM) is present within the diamond-anvil cell in order to promote hydrostatic compression. The second half of the chapter describes work in which no PTM was present within the diamond-anvil cell in order to achieve compression which was more non-hydrostatic in nature.

4.1 Compression With Pressure Transmitting Medium

4.1.1 Experimental Details

A total of four Livermore-type diamond-anvil cells, as described in section 2.2.1, were loaded for this experiment. The Sb used in this work was the same, high-purity sample as was used for the dynamic experiments described in chapter 3, with the small pieces of Sb foil removed from the kapton backing. Three of the cells contained two layers of the Sb foil (approximately 8 to 10 μm thick) with one other cell being loaded with only one layer of Sb in the hopes of replicating the condition of the Sb in the dynamic compression experiment. However, it

was found that the single layer of Sb crumpled in the cell. The cells, which were equipped with Re gaskets, were also loaded with mineral oil to act as a PTM and included a 1-3 μm thick, small piece of Cu as a pressure calibrant. The cells were resistively heated, as described in section 2.2.1, and made use of a membrane for remote pressure control. The temperature was measured using a K-type thermocouple placed in contact with the diamond and shielded from the outer casing using ceramic beads. The pressure was then calculated using a thermal EOS [78] as described in section 2.2.

Powder x-ray diffraction data were collected on the I15 beamline at Diamond Light Source using a monochromatic x-ray source with a wavelength of 0.4246 Å and beam diameter of 20 μm. Data were collected using a Mar345 image plate detector which was positioned approximately 385 mm from the sample. After calibration of the detectors, the images were integrated using the Fit2D [129] software to generate 1D diffraction profiles. Le Bail refinements were performed using the JANA2006 software [110] and analysis was also conducted by fitting individual peaks using the Igor Pro (WaveMetrics. Inc.) software package, followed by analysis of d-spacings.

4.1.2 Experimental Results

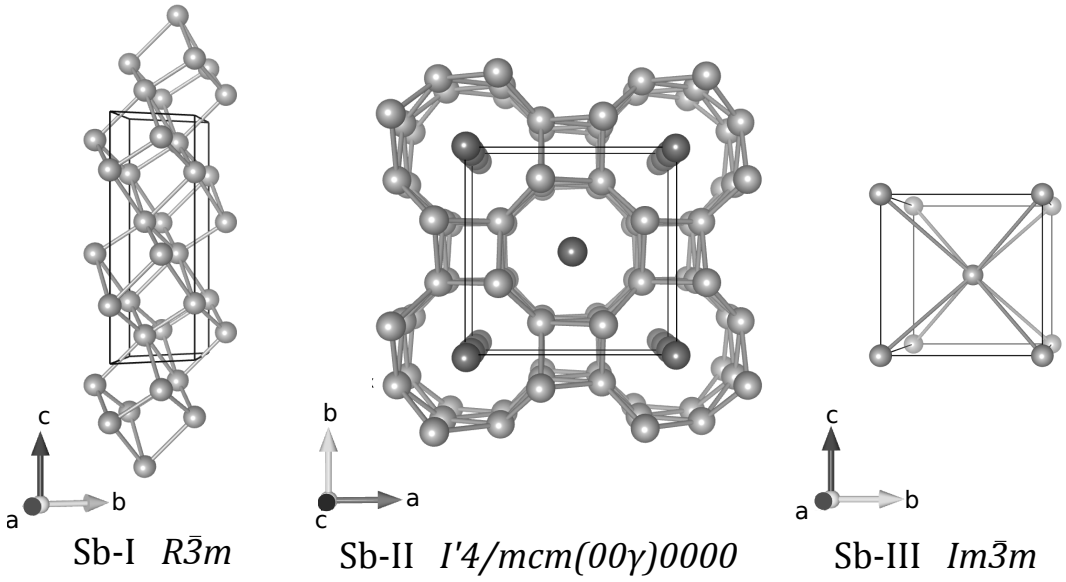

Figure 4.1 *The structures of the Sb-I, Sb-II and Sb-III phases.*

Data were collected up to ∼835 K and 31 GPa over a series of isotherms and the Sb-I, Sb-II and Sb-III phases were observed, the structures of which are

illustrated in figure 4.1. Figure 4.2 shows integrated diffraction profiles from the Sb-I, Sb-II and Sb-III phases collected on an isotherm at ∼475 K at pressures of 6.2, 23.1 and 27.6 GPa respectively. There was no evidence of the monoclinic host-guest phase (Sb-IV) in any of the data collected across all of the isotherms. As discussed previously, the Sb-IV phase has only been observed over a very small pressure region at room temperature (∼1 GPa on pressure increase [43]) and it is likely that it was not observed in this work due to a gap in the data at room temperature. As there is also no evidence of the Sb-IV phase at higher temperatures (where data were collected at smaller P intervals), it is believed that the stability region for this phase is very small indeed.

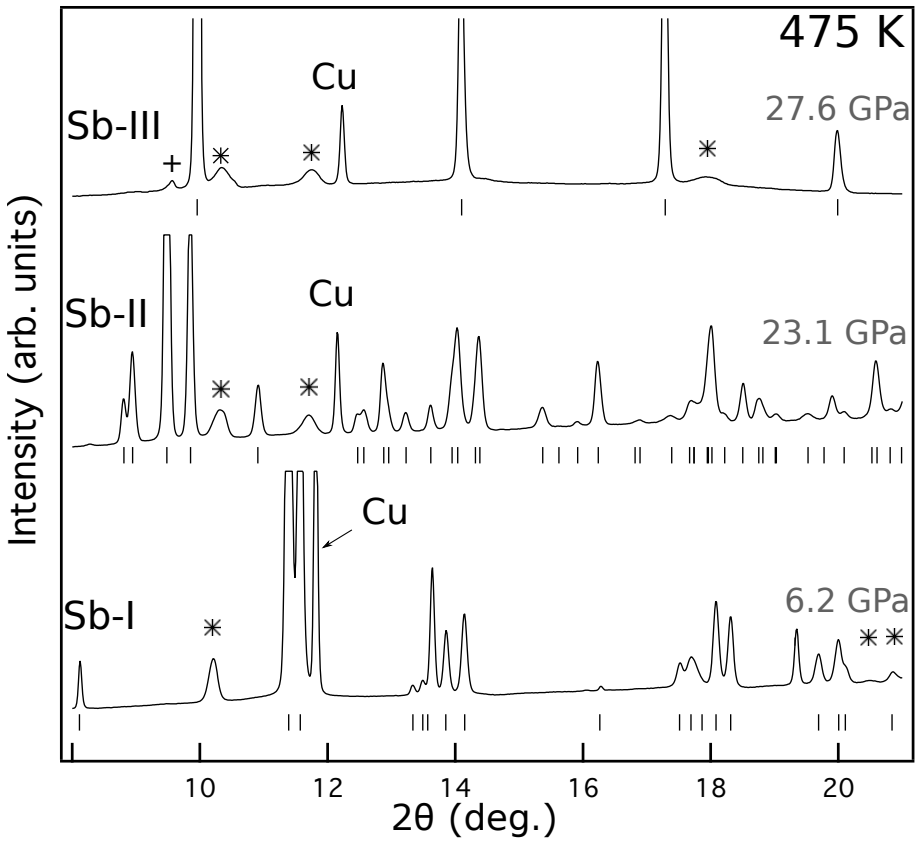

Figure 4.2 *Integrated diffraction patterns showing three distinct phases of Sb observed under static-compression at ∼475 K: the rhombohedral A7 phase (Sb-I), the incommensurate host-guest phase (Sb-II) and the bcc phase (Sb-III), at pressures of 6.2, 23.1 and 27.6 GPa respectively. Tick marks beneath the profiles show the calculated positions of the Bragg peaks for each phase. The most intense peaks from the phases have been cropped for clarity. Asterisks indicate peaks from the Re gasket, and peaks from the copper pressure calibrant are labelled as such. The most intense reflection from the Sb-II phase (the (2110) peak) is still visible in the Sb-III pattern at 27.6 GPa and is marked with a + symbol.*

There was no evidence of the Sb-I' phase that was observed in the dynamic compression experiment at any temperature. The result agrees with the previous work of Iwasaki and Kikegawa who studied the Sb-I $\rightarrow$ Sb-II phase transition to 11.5 GPa and $\sim$600 K under static compression [39] and saw no evidence of a new phase. The c/a ratios of the Sb-I phase lattice parameters, as shown in figure 4.3, decrease with increasing pressure across all of the isotherms in reasonable agreement previous static compression data obtained at 300 K [43, 112]. While this negative slope is indicative of a relaxation of the Peierls distortion, the c/a ratio never reaches the $\sqrt{6}$ value required for a transition to a simple cubic phase. The absence of a transition to the simple cubic phase was previously reported for room-temperature compression of Sb by Degtyareva and Schiferl [43, 112]; this current work confirms that the transition to a simple cubic phase is not seen, even at higher temperatures (in contrast with the dynamic compression data obtained at the LCLS as shown on the graph and described in section 3.5.1). While measurements were not made up to the melt point, linear extrapolation suggests that the c/a ratio of $\sqrt{6}$ would not be reached until $\sim$900 K, at which point the Sb would have transformed into a liquid phase.

The Sb samples used in this experiment were the same as those used in the dynamic study at the LCLS so the preferred orientation is still present within the sample, meaning that the relative intensities of the Bragg peaks were strongly effected. Nonetheless, the quality of the diffraction patterns was very high and allowed for excellent LeBail fitting of all phases, including the more complex incommensurate host-guest (HG) structure of the Sb-II phase. The $(hk0m)$ peaks in the HG diffraction patterns arise due to guest reflections and these peaks were visible in all of the Sb-II patterns, even at the highest temperatures, as shown in figure 4.4. The persistence of the $(hk0m)$ diffraction intensities indicates that long range order is maintained in the guest chains (and thus the Bragg condition is satisfied for the planes formed between the atoms in neighbouring guest chains). Commonly, at elevated pressures and temperatures, the chains of HG structures become partially disordered, as is the case for Na at 147 GPa and 300K [130], or lose long range order completely, as is the case for Rb, K and Sc [57, 131–133]. This loss of long range order in the chain subsystem is commonly referred to chain "melting". The persistence of order in the chains in the Sb-II phase even at the highest pressures and temperatures studied here (20 GPa and 835 K) shows that the interaction within the guest substructure is strong.

The high quality of the diffraction patterns also enabled the observation of weak

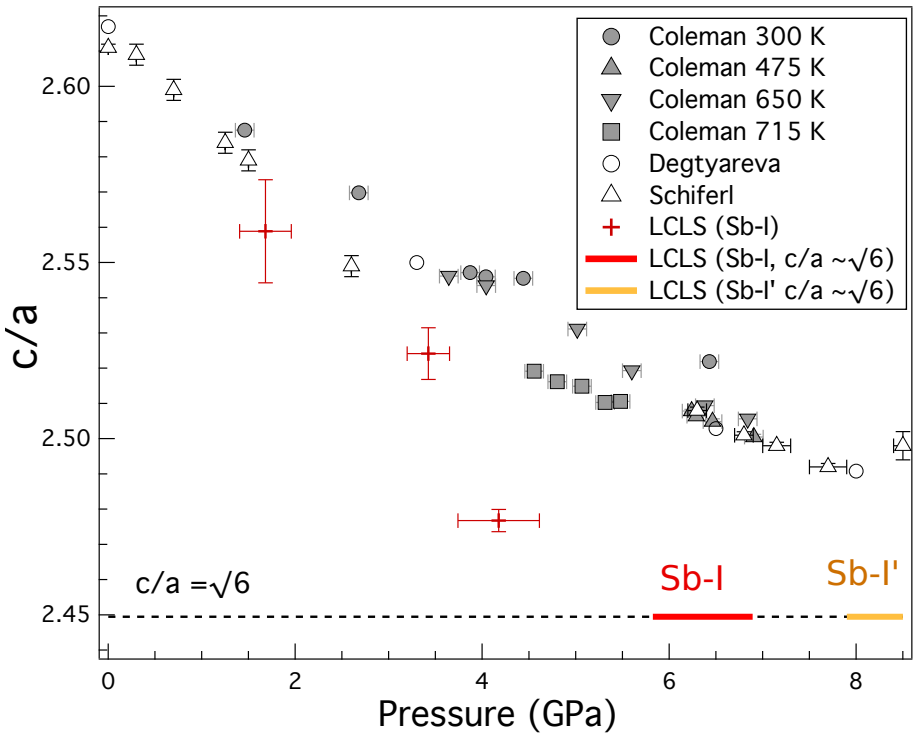

Figure 4.3 *The c/a ratio versus pressure for the Sb-I phase, as obtained at a series of different temperatures at Diamond Light Source (DLS) along with on-Hugoniot data obtained at LCLS (as described in the previous chapter). Circles, upward pointing triangles, downward pointing triangles and squares show data collected at ~300, ~475, ~650 and ~720 K respectively. Data from previous room-temperature work by Schiferl [112] and Degtrareva [43] are shown by empty triangles and circles respectively.*

$(hklm)$ ($l \neq 0$ and $m \neq 0$) modulation reflections, which arise from interactions between the host and guest substructures, as shown in figure 4.5. The modulation reflections in Sb-II are stronger than those observed in any other host-guest structures at room temperature and in this work they were observed to persist even at the highest temperatures, suggesting that the structural modulations resulting from host-guest interactions are not greatly effected by heating. At high temperatures the thermal motion of the guest atoms is much more significant than at room temperature so it is perhaps surprising that the interaction between the host and the guest remains relatively unchanged. Due to peak overlap, it was not possible to resolve enough modulation reflections to determine the nature of the P-T dependence of the structural modulations, determination of such a relationship would require single crystal data [45]. Analysis of the relative intensities of the two most intense modulation reflections (the $(212\bar{1})$ and the $(311\bar{1})$ peaks) did not yield any discernible pattern with increasing temperature though it appears that

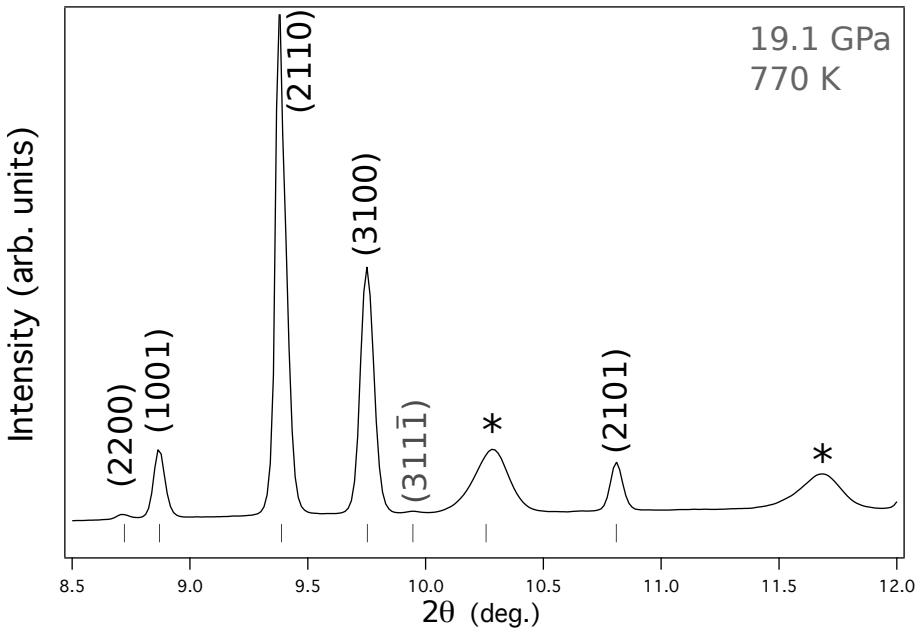

Figure 4.4 *Tickmarks show the position of peaks fitted to an integrated diffraction pattern from the Sb-II phase at 19.1 GPa and 770 K. Even at high temperatures the (1001) and (2101) guest peaks are still clearly visible.*

recrystallisation of the sample at high P-T conditions, as illustrated in figure 4.5, caused significant variations in Bragg peak intensity in the integrated diffraction profiles due to intense spots on the Debye-Scherrer rings.

The ratio of the c lattice parameters of the host and guest peaks (c_H/c_G) is plotted against pressure in figure 4.6 for a series of isotherms. The uncertainties in the lattice parameters were obtained using the UnitCell software [111], which was used to refine cell parameters based on the observed 2θ positions of peaks which had previously been indexed using the Fit2D software. While there is a universal negative trend across all isotherms and an initial degrease in c_H/c_G between room-temperature measurements and those at ∼475 K, there is no significant change in the slope of the line upon further temperature increase, even up to ∼755 K. Between the unchanging nature of the c_H/c_G ratio and the persistence of the weak modulation reflections, it appears that the relationship between the host and guest substructures in Sb-II is relatively uneffected by increased temperatures.

In the Sb-II diffraction profiles, small azimuthal variations in the radii of the Debye-Scherrer rings were observed (see appendix A); this is indicative of non-hydrostatic pressures within the sample. Such variations were negligible in the Sb-I and Sb-III phases at all temperatures. It would be expected that non-hydrostatic effects would be more significant at higher pressures, but the absence

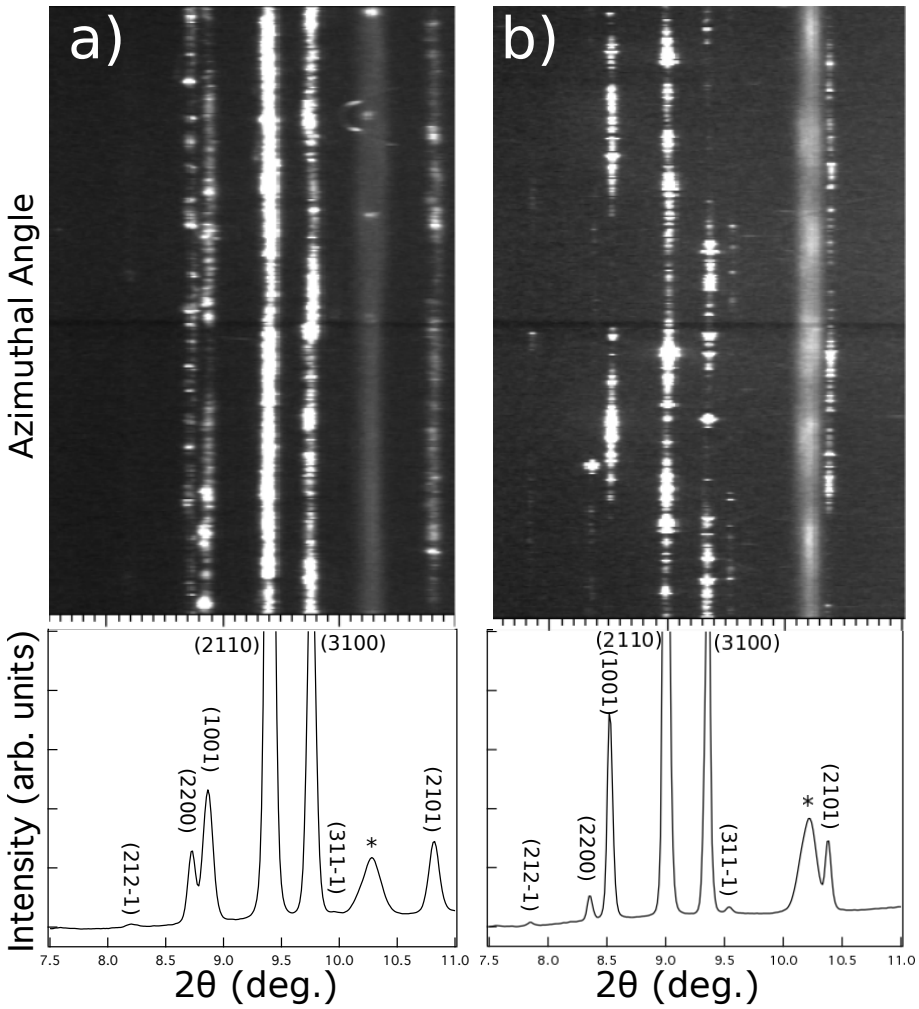

Figure 4.5 *2D raw diffraction images and integrated profiles showing the Sb-II phase at a) 19.4 GPa and 475 K, and b) 6.2 and 720 K. The 2D images are plotted as azimuthal angle versus 2θ angle plots so that Debye-Scherrer rings of constant radii are shown as straight lines. Asterisks mark the peaks from the Re gasket. The recrystallisation of the sample at high temperatures, indicated by the changed texture in the 2D profiles, results in higher intensities in the* $(212\bar{1})$ *and the* $(311\bar{1})$ *modulation peaks.*

of such effects in Sb-III suggests that they are relieved at the Sb-II → Sb-III transition. The Multifit software [134] was used to map the 2θ position of the two most intense peaks of the Sb-II phase, the (3100) peak and the (2110) peak, as shown in figure 4.7. This is significantly more variation in 2θ than is observed in the Sb-I and Sb-III phases.

Figure 4.8 shows the proposed phase diagram of Sb under static compression. The phase boundaries shown here are based on the first appearance of the new phase in the diffraction data, even if the previous phase is still present. This data is

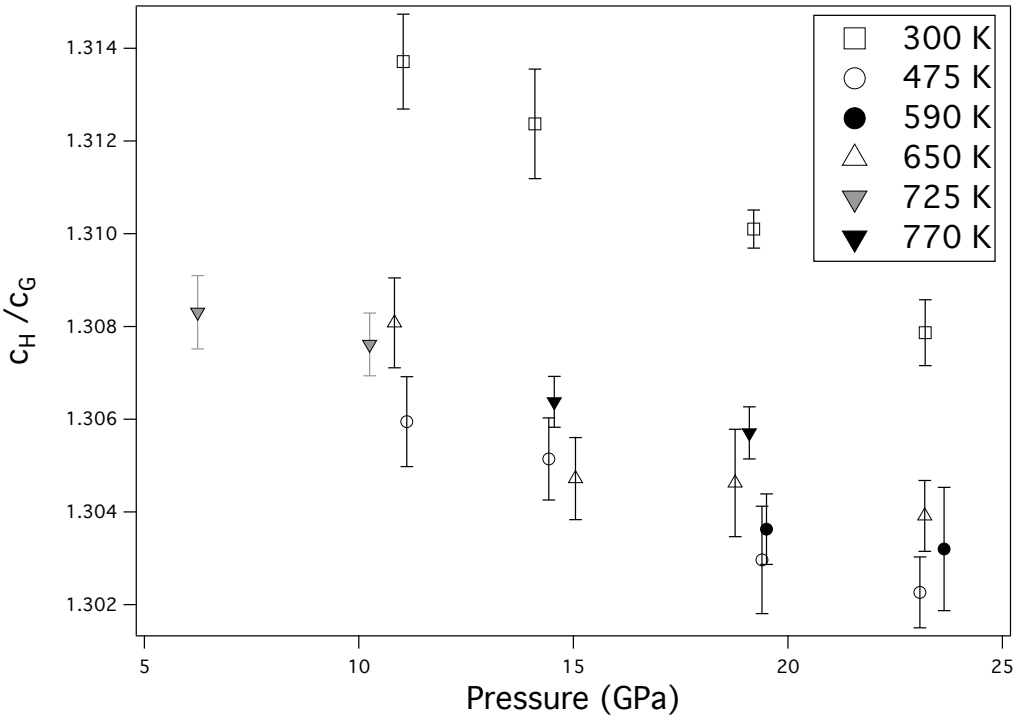

Figure 4.6 *A plot showing the ratio of host to guest peak c lattice parameters of the Sb-II phase versus pressure across several isotherms.*

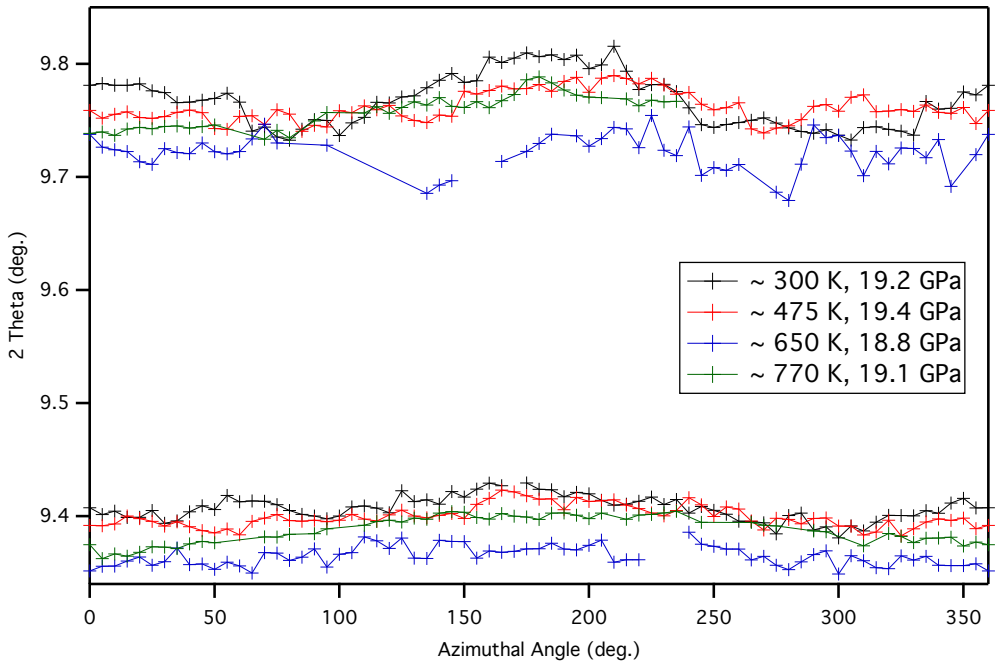

Figure 4.7 *The variation in 2 theta around the azimuth of the two strongest peaks of the Sb-II phase: the (3100) peak between 9.7 and 9.8 degrees 2θ and the (2110) peak around 9.4 degrees 2θ.*

in excellent agreement with the previous room-temperature, static-compression studies of Degtyareva and Schiferl [43, 112]; the room temperature transition reported in their studies (as marked by an asterisk on figure 4.8) agrees extremely well with our Sb-I → Sb-II phase boundary. The same phase boundary at higher temperatures agrees strongly with Iwasaki and Kikegawa and Khvostantsev and Siderov [37, 39] and coincides with a minimum in the melt curve at 5.7 GPa, as reported by Klement *et. al* [27]. This minimum is thus confirmed as a triple point between the liquid, Sb-I and Sb-II phases. The boundary between the Sb-II and Sb-III phases is measured above room temperature for the first time and has been extrapolated using a polynomial fit; this extrapolation suggests the existence of another triple point, this time between the liquid, Sb-II and Sb-III phases. Determination of the exact location of this triple point would require further data collection though it can be estimated (from the fit to the existing melt curve data and the extrapolation of the measured Sb-II → Sb-III phase boundary) that the point will occur near 13 GPa and 1200 K. It should be noted that the extrapolation of the melt curve is based on a Simon-Glatzel fit to the pre-existing melt curve data obtained using static compression techniques [27], and the first data point in which liquid diffraction signal was observed from the dynamically compressed Sb described in chapter 3. The location of the Sb-II/Sb-III/liquid triple point on the static phase diagram should be taken only as a rough approximation until further DAC studies are conducted to explore the Sb melt curve in this PT regime. The validity of this approximation is discussed in section 4.1.3.

From the static data collected here we have been able to construct a phase diagram for Sb up to 31 GPa and 835 K. The previously reported minimum in the melt curve reported at 5.7 GPa has been shown to mark a triple point between the liquid, Sb-I and Sb-II phases, with data suggesting the existence of an additional triple point between the liquid, Sb-II and Sb-III phases in the vicinity of 13 GPa and 1200 K. The absence of chain-melting in Sb-II at the highest P-T conditions, along with the persistence of satellite peaks and the unchanging nature of the c_H/c_G ratio above room temperature all suggest that the relationship between the host and guest components of the HG structure is relatively unchanged at increased temperature. This is perhaps surprising, given the greatly increased thermal motion of the guest-chains within the confines of the host framework at high temperatures.

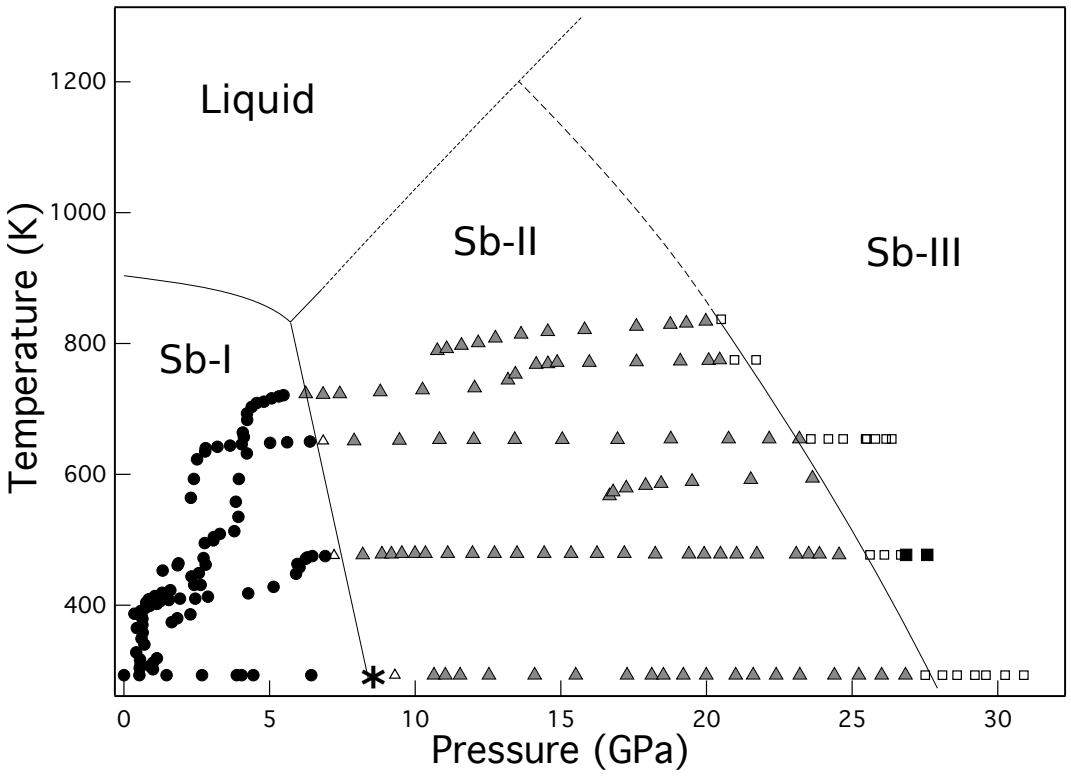

Figure 4.8 *The phase diagram of Sb to 31 GPa and 835 K. The P-T conditions under which the Sb-I, Sb-II and Sb-III phases form are shown by circles, triangles and squares respectively. Single-phase profiles are shown by filled symbols, while mixed phase profiles are shown by unfilled symbols. The Sb-I → Sb-II room-temperature transition point as reported by Degtyareva and Schiferl is shown by a star symbol [43, 112].*

Incommensurate Composite versus Incommensurate Modulated Structure

Analysis of the Sb-II phase in both this static work and the previous dynamic experiments reported in this thesis have interpreted the HG phase as a composite structure, as proposed by McMahon *et al* in 2000 [41, 43] and confirmed by Schwarz in 2003 [42]. An incommensurate composite structure comprises at least two inter-penetrating periodic subsystems. These subsystems are mutually incommensurate but, additionally, the subsystems may themselves be modulated [86]. A recent publication by Arakcheeva *et al* [135] proposed an alternative treatment of incommensurately modulated host-guest structures in Ba-IVb which they refer to as the incommensurately modulated (IM) model. The IM model describes a density wave within the structure which changes with pressure; atoms are displaced from their periodic positions on the lattice by this modulation wave.

The wavelength of this wave is incommensurate with the average periodic lattice of the structure [86]. While the incommensurate composite model (referred to as IC by Arakcheeva) describes separate host and guest components (with lattice parameters $a_H = a_G$, $b_H = b_G$, $c_H \neq c_G$), the IM model defines the superspace group and lattice parameters for the structure as a whole in the same way that just the host component is described in the composite model; in the IM model, the ($hkl0$) reflections are the main ones and the ($hklm$) (m≠0) reflections are satellites. This is unlike the composite interpretation where ($hkl0$) and ($hk0m$) represent the host and guest reflections respectively and ($hklm$) (l≠0, m≠0) reflections originate from the satellite peaks. Arakcheeva reported that the IM model was a better fit than the IC model for their single crystal Ba-IVb data and concluded that data of the highest quality was necessary to determine whether the IC or IM model was appropriate for other reported host-guest structures at high pressure.

It is interesting to consider whether the IM interpretation is appropriate for the data collected from the Sb-II phase. If the assumption is made that the Sb-II has the same structure as was proposed for Ba-IVb then in the IM model there are 20 Sb atoms in a unit cell which has a volume of $\sqrt{2}a_H \times \sqrt{2}a_H \times c_H$. In the composite model, as discussed previously, there are $8 + 2\gamma$ Sb atoms in a unit cell of volume $a_H \times a_H \times c_H$, where γ has a value of ∼1.31 in Sb-II [43]. The same data set may be analysed as both an IC and an IM structure and, as is evident from the different volume calculations, the densities calculated from each type of analysis will be different.

In 1941, Bridgman made absolute measurements of the density of Sb to 9.8 GPa [28] at room temperature using the piston displacement method. These early measurements were made without phase determination and can be compared with our data over the same pressure regime at room temperature. The Sb-I densities and the Sb-II densities yielded by both the composite and IM models are shown in figure 4.9 along with the data reported by Bridgman. The figure shows that the density calculated for Sb-II using the IC structure interpretation is in excellent agreement with the data collected by Bridgman whereas the IM model returns a density of Sb-II which is overestimated by ∼5%. Bridgman reported a 3.7% increase in density at the Sb-I → Sb-II transition, a result that is not replicated in the IM model which shows an unphysical *decrease* in the density. From this relatively simple density analysis we may conclude that the IC structure interpretation is indeed the more valid choice in the analysis of the Sb-II

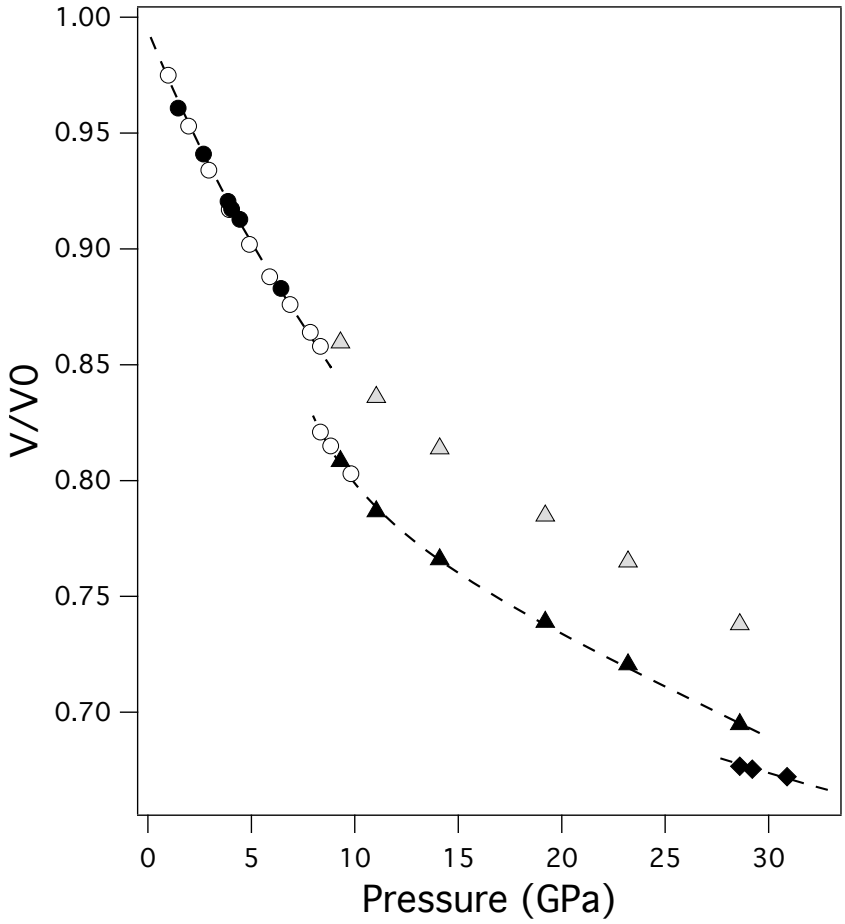

Figure 4.9 *The compressibility of Sb to 31 GPa at room temperature. Data points from Sb-I, Sb-II and Sb-III, assuming the IC model, are shown by filled circles, triangles and diamonds, respectively. The grey triangles show the volume of the Sb-II phase as calculated using the IM structure containing 20 atoms/cell described by Arakcheeva [135]. The data plotted with unfilled symbols are absolute volume measurements of Bridgman, made without phase determination [28].*

data. Unfortunately, as Bridgman did not make absolute volume measurements of Ba under pressure, this approach has not been used in analysing the IM model of Ba reported by Arakcheeva [135].

4.1.3 Discussion

Figure 4.10 shows the phase diagram of Sb as determined from the static compression experiment along with the on-Hugoniot data points collected during the dynamic compression Sb experiment at LCLS. It is evident that there are distinct differences between the two data sets. The Sb-I′ phase which was observed upon dynamic compression is not seen in the static data, neither is

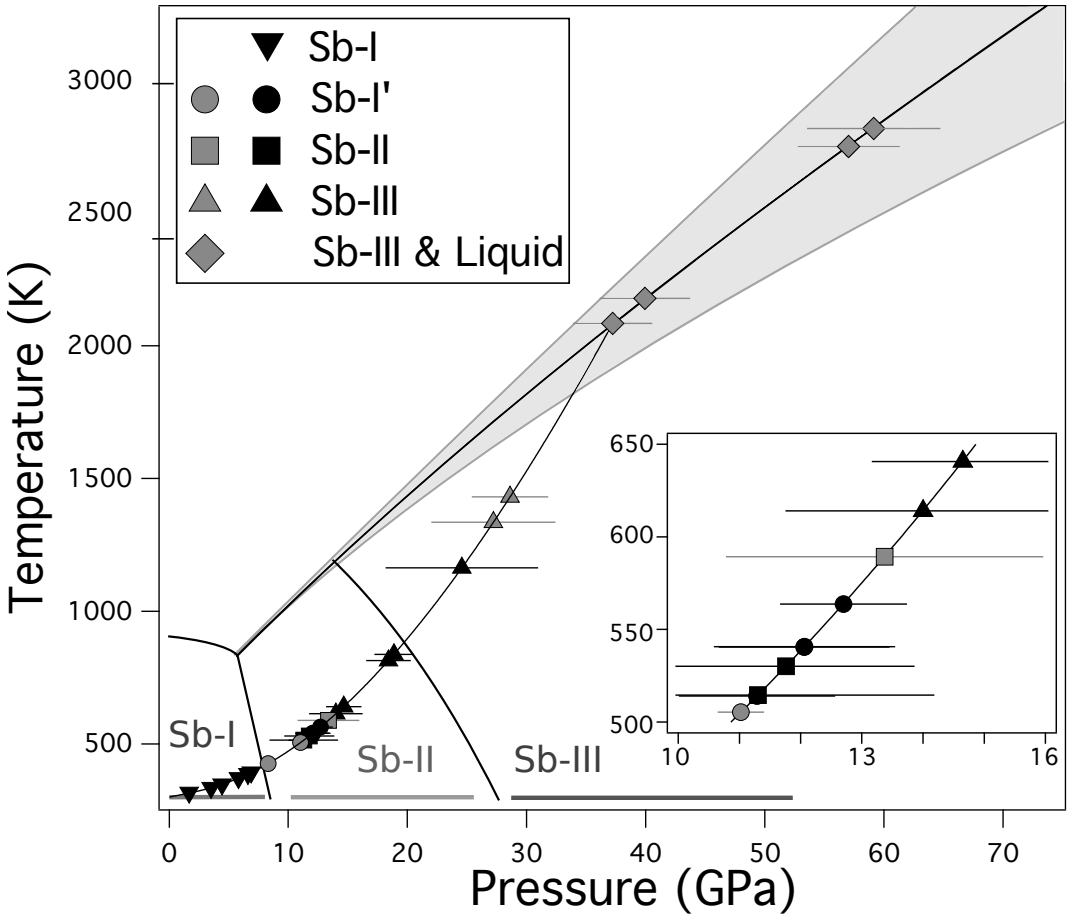

Figure 4.10 *The Sb phase diagram with phase boundaries as determined from the static compression experiments along with on-Hugoniot data from the LCLS experimental campaign. Downward pointing triangles, circles, squares, upward pointing triangles and diamonds show Sb-I, Sb-I', Sb-II, Sb-III and Sb-III & Liquid data points obtained from the dynamic compression experiments. Black and grey filled data points show data collected without and with a rear LiF window, respectively.*

the unidentified phase from the dynamic data set which spanned the Sb-I′, Sb-II and Sb-III phases. Previous literature had reported that the presence of a simple cubic phase in Sb may be dependent on uniaxial compression [35] so that absence of the Sb-I′ phase is perhaps accounted for by the use of a pressure transmitting medium. The following section reports a second DAC study conducted without the use of a pressure transmitting medium to investigate whether the simple cubic phase is observed under more uniaxial compression.

The static Sb-II→Sb-III phase boundary decreases in pressure with increasing temperature and is shown to cross the hugoniot at ∼20 GPa whereas the on-hugoniot transition pressure measured in the dynamic compression experiment

is $\sim$ 14 GPa. The stability region of the Sb-II phase is much smaller in under dynamic loading than is observed under static compression conditions. It appears that the bcc, Sb-III phase is more energetically favourable as this transition occurs at a much lower pressure under dynamic compression; this 'under-driving' of a phase transition has also been observed in dynamically compressed Bi [119] and is not presently well understood.

The static phase diagram of Sb shown in figure 4.8 uses the same melt curve as shown in figure 4.10 which is based on pre-existing static melt data [27] and the first data point in which liquid diffraction signal was observed from the dynamically compressed Sb. It is not unreasonable to assume that the on-Hugoniot melt point in the data obtained upon dynamic compression could differ from the melt point observed using static techniques, especially given the disparity between the on-Hugoniot phase transitions and the phase boundaries obtained using static compression techniques (highlighted in figure 4.10).

As discussed in section 3.5.2, it would indeed be interesting to explore the phase boundaries of Sb using gas-gun compression techniques that have characteristic compression timescales ($\sim \mu s$) that lie between those of DAC ($> s$) and laser-shock compression (ns). It has been shown that the completion time of the $\alpha \rightarrow \epsilon$ transition in Fe is highly variable depending on the shock stress and sample thickness [123]. It would be very interesting to characterise the transition to the Sb-II phase using gas gun experiments which facilitate the use of thicker Sb targets to explore the transition over longer timescales. Given the discrepancy between on-Hugoniot phase transitions and the phase boundaries observed under static compression, it appears that phase transitions in Sb may be highly sensitive to strain-rate; it is interesting to consider how a universal phase diagram may be constructed for such a material or indeed how dynamic compression of such a material may be modelled.

4.2 Compression Without Pressure Transmitting Medium

The results obtained from the hydrostatic, static compression experiments showed significant discrepancies with those obtained from dynamic compression. Additionally, early static compression studies by Vereschchagin, Kolobyanina and Kabalkina [30, 32, 33], using potentially non-hydrostatic techniques, showed the presence of the Sb-I′ phase in Sb. In order to try and understand whether these discrepancies originate from uniaxial effects, the original static Sb experiments were repeated without the use of a PTM in order to generate compression which is less hydrostatic in nature.

4.2.1 Experimental Details

Sb samples were loaded into diamond-anvil cells equipped with Re gaskets along with a 3μm thick piece of Cu foil which acted as a pressure calibrant. The Sb used was the same deposited sample as described in previous experiments in the thesis. Due to the nature of the experiment, in that there was no PTM, the cell was packed densely with Sb foil to stop the gasket hole from collapsing as the pressure was increased.

The data collection and analysis was conducted using the same instruments, programs and methods as detailed in the first half of this chapter. The sample was heated to an initial temperature which was believed to be 470 K and then pressure was increased and data were taken along this isotherm (set A). The pressure and temperature were then decreased and measurements were taken on increasing pressures along a secondary isotherm at a temperature that was believed to be 390 K (set B). (Note: the temperatures were later found to be unreliable, this is discussed in section 4.2.2) From this point forward the data collected using this diamond-anvil cell loading will be referred to as non-PTM data and the data collected in the previous static experiment, with mineral oil used as a PTM, will be referred to as PTM data.

4.2.2 Experimental Results

In this experiment, as the cells were unloaded at the end of the experiment, it was found that the ceramic insulation on the thermocouple wires had not been attached correctly, meaning that the temperature readings for the two isotherms (470 K and 390 K) were unreliable. Unfortunately this inhibited pressure determination as use of the Cu thermal EOS requires an accurate temperature input. Initial results, using the incorrect temperature data, indicated that the transition pressure from Sb-I to Sb-II was higher than that observed in the data collected without a PTM. This higher transition pressure ($\sim$ 12 GPa) agreed well with the transition pressure observed in the dynamic compression eperiment though because the values of T (and therefore P) are unreliable, this result must be closely scrutinised. The following analysis attempts to constrain the temperature (and thus the pressure) of the collected data by comparing it with previously collected hydrostatic data.

The initial constraint that can be applied to this data set is that the temperature must be between room temperature and the maximum achievable temperature of the resistively heated DAC ($\sim$1200 K). The upper temperature limit can be further constrained due to the fact that the melt curve around the Sb-I/ Sb-II transition is at approximately 850 K and there was no observation of liquid-Sb in the diffraction data. The volumes of the Sb diffraction patterns are obtained by Le Bail refinement and PV plots are shown in figure 4.11 with pressure calculated using the Cu calibration peaks and Cu thermal EOS with both the minimum (300 K) and maximum (850 K) temperatures.

Figure 4.11 shows a significant difference between the pressures obtained in the data collected with and without the use of a PTM in the same V/V_0 range. Additionally, there is a large amount of scatter in the non-PTM data. As is evident in the figure, the PTM data shows that the transition from Sb-I to Sb-II occurs in the region around 6.5 to 7 GPa (dependent on temperature), a pressure which is notably higher in the non-PTM data analysed at both the maximum and minimum temperatures. Using the position of the Cu pressure-calibrant peaks to obtain the volume of the Cu at the point of the transition and the Cu thermal EOS described previously, it can be calculated that the temperature for sets A and B would have to be -355 K and -421 K respectively in order for the transition pressure to be 6.5 GPa in agreement with the PTM data. This unphysical result and the large amount of scatter in the non-PTM data indicate that there is

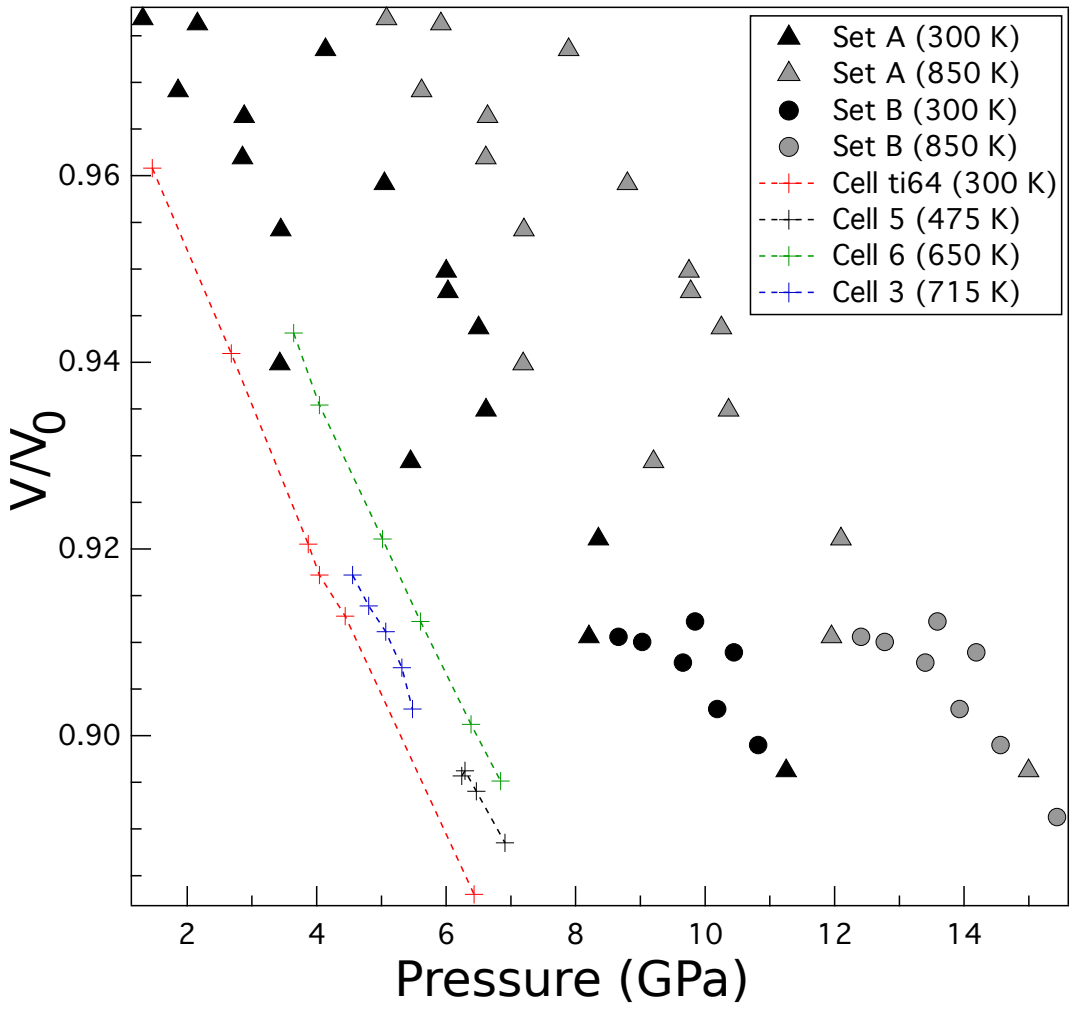

Figure 4.11 *Pressure vs V/V_0 for Sb-I data collected using no PTM (set A and set B) analysed at the maximum and minimum possible temperatures alongside data sets collected using a PTM (Cells 3, 5, 6 and ti64) at constant temperatures.*

another problem in the data analysis.

The initial data points taken on the isotherm in set A showed diffraction peaks from the Sb-I sample, the Re gasket, and the Cu pressure calibrant. However, as the pressure was increased, the Cu and the Sb reacted to form Cu_2Sb, as was seen in one of the cells in the previous static-compression experiment where the Cu and Sb were in physical contact in the cell. This is perhaps not surprising given that the Cu and the Sb had to be in contact in the densely packed cell of the non-PTM experiment. But as pressure was increased it became apparent that the extent of the reaction between the Cu and the Sb had depleted the Cu to the extent that it could no longer be used as a pressure calibrant. Figure 4.12a) shows an integrated x-ray powder diffraction pattern from set A just before

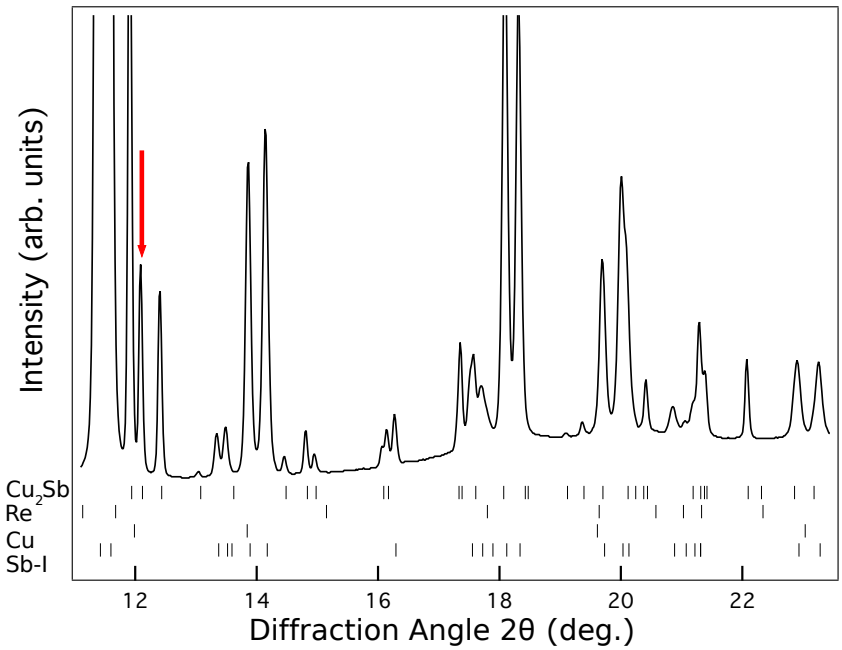

Figure 4.12 *X-ray powder diffraction profile of Sb I featuring peaks from the Re gasket, peaks from the Cu pressure calibrant and peaks from Cu_2Sb formed due to a reaction between the Cu and Sb within the cell. The red arrow indicates the peak used for pressure calibration which is in the location of the (111) Cu peak and the (112) Cu_2Sb peak.*

the transition to Sb-II. The red arrow indicates the peak which was used as the pressure calibrant (the (111) Cu peak) and unfortunately, the (112) Cu_2Sb peak overlaps with this peak making fitting the Cu peak unfeasible. As shown in the figure, there are no distinct Cu peaks that can be fitted without the presence of another peak. The inability to fit the Cu peak could account for the large scatter in the non-PTM data in figure 4.11, as the ability to fit this peak affects the volume calculation of the Cu and therefore the pressure calculated using the thermal EOS.

The onset of the Cu_2Sb peak is shown in figure 4.13; the two raw Sb-I diffraction images are obtained on the same isotherm with a) at the lowest pressure and b) at the highest pressure, immediately before the transition to the Sb-II phase. In a) the red arrow indicates the (111) Cu peak (note, no Cu_2Sb is present) and in b) the arrow indicates the same region where Cu_2Sb has formed and the (112) Cu_2Sb peak may be observed. It is evident from b) that the texture of the ring has changed markedly and there is very little evidence of the original Cu texture present. This indicates that there is no longer sufficient Cu present in the sample to use as a pressure calibrant.

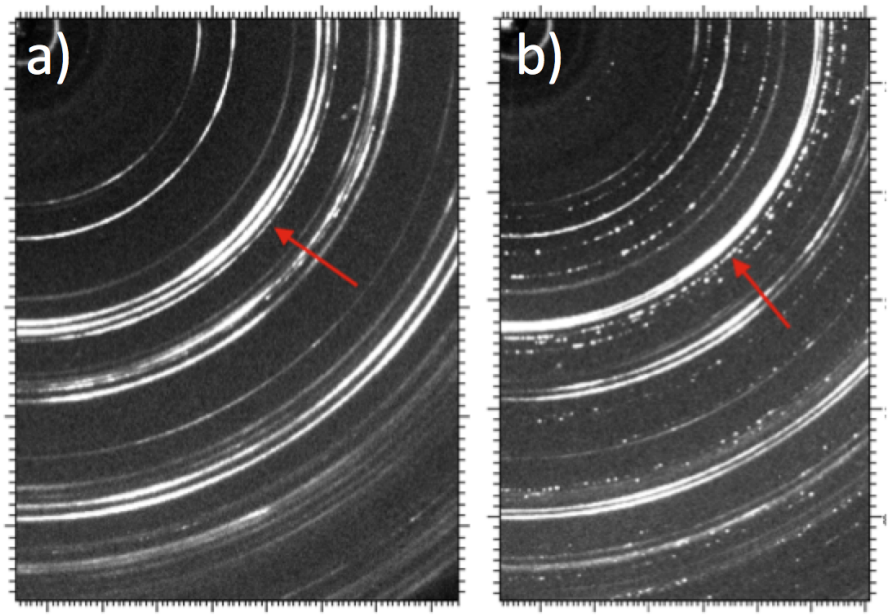

Figure 4.13 *Raw x-ray powder diffraction data from the beginning of the isotherm in set A (figure a) and the final Sb I pattern collected before the phase transition on the same isotherm (figure b). In the data shown in figure a) there is no Cu_2Sb present whereas in figure b) Cu_2Sb is present.*

It is interesting to consider the nature of this Cu_2Sb crystallisation. Figure 4.14 shows three consecutive x-ray powder diffraction patterns taken on increasing pressure along the set A isotherm. The arrows indicate the (112) Cu_2Sb peak, the texture of which visibly changes between patterns. This changing of texture between each pattern indicates that the Cu_2Sb is recrystallising upon pressure increase. If the conditions within the cell were truly non-hydrostatic, it seems unlikely that the Cu_2Sb would continue to re-crystallise in this way. Additionally, it is notable that there is not a significant amount of broadening in the diffraction peaks shown in figure 4.12 in comparison to the data collected under hydrostatic conditions (where there is not peak broadening). There is no evidence of deformation of the Debye-Scherrer rings as indicated in figure 4.15 which shows diffraction data from the Sb-I phase which has been warped so that the Debye-Scherrer rings appear as straight lines. While the lack of distortion of the Debye-Scherrer rings in the Sb-I phase agrees with the results seen in the PTM experiment, it was thought that the the lack of a PTM in this work, and the consequent uniaxial nature of the compression, would strain the sample sufficiently to observe distortions in the rings. As there was nothing loaded into the cell other than Sb and Cu, it is conceivable that the Sb is sufficiently soft under these conditions that it may act as its own pressure transmitting medium.

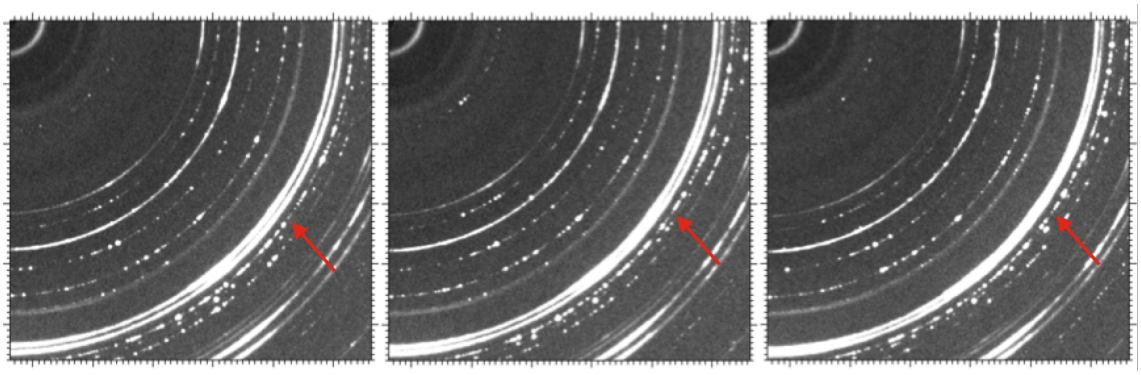

Figure 4.14 *Raw x-ray powder diffraction data from three consecutive data points along the set A isotherm, immediately prior to the Sb-I to Sb-II transition. The arrows indicate the (112) Cu_2Sb peak, the texture of which changes in each pattern indicating recrystallisation.*

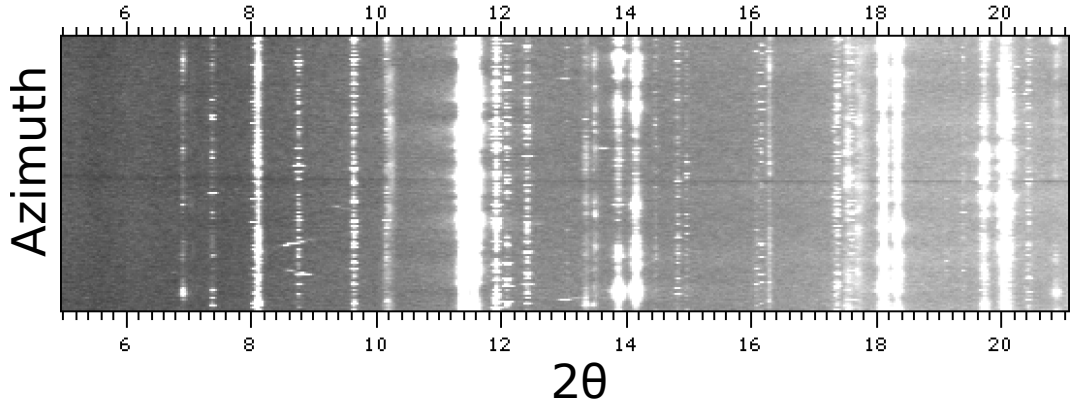

Figure 4.15 *Diffraction data from set A which has been warped to show the Debye-Scherrer rings as straight lines. This data was collected immediately prior to the Sb-I→Sb-II phase transition and shows no evidence of distortion of the Debye-Scherrer rings which would indicate strength effects within the Sb-I.*

Even though constraints can be put upon the temperature, without accurate knowledge of the Cu peak positions, it is not possible to calculate a reliable value of the pressure within the sample. However, the lattice parameters of the Sb-I and Sb-II structures can be reliably determined though Le Bail fitting of x-ray diffraction profiles. This means that for both isotherms, the c/a ratios and the volumes at the Sb-I→Sb-II transition point can be compared to the PTM data, as shown in table 4.1. It is evident that even though the transition temperature and pressure are not known for the non-PTM data, the volumes and c/a ratios agree well with the data collected using a PTM.

Furthermore, it is possible for us to conclusively rule out the appearance of a simple cubic phase in the data we collected. At the Sb-I→Sb-II transition the

Cell	PTM	Temperature (K)	Pressure (GPa)	V/V0	c/a
Cell ti64	Yes	300	6.43	0.88300	2.522
Cell 5	Yes	475	6.91	0.88852	2.500
Cell 6	Yes	650	6.84	0.89514	2.506
Cell 3	Yes	715	5.48	0.90287	2.516
Set A	No	–	–	0.89625	2.504
Set B	No	–	–	0.89128	2.479

Table 4.1 *An overview of lattice parameters, pressure and temperature (where known) at the Sb-I → Sb-II phase transition for data sets collected with and without PTM.*

c/a ratio was 2.504 and 2.484 in sets A and B, respectively; in both cases this value is higher than the $\sqrt{6}$ (= 2.449) value required for a transition to the simple cubic phase. Additionally, there was no evidence of distortion in the Debye-Scherrer rings (figure 4.15), as was seen in the dynamic compression experiments when the Sb-I′ phase was observed.

4.2.3 Discussion

It is difficult to draw impactful conclusions from this experiment where, due to a failure in experimental technique and the overlap of the Cu_2Sb peak with the primary pressure calibrant peak, it is not possible to know the temperature or the pressure of the sample. It is, however, possible to calculate structural information from the diffraction data. The volume of the sample at the Sb-I→Sb-II phase transition is not markedly different to the volumes obtained in the PTM data sets which indicates that the behaviour without a pressure transmitting medium is not drastically different at this transition. Additionally, we were able to calculate the c/a ratio of the Sb-I phase up to the transition to Sb-II and see that there is no evidence of a simple cubic or Sb-I′ phase as the value does not reach $\sqrt{6}$ prior to transition to the Sb-II phase.

The absence of a Sb-I′ phase is an interesting result, as previous reports have indicated that the formation of a simple cubic structure in Sb is dependent on non-hydrostaticity of compression [35]. It should, however, be noted that work published by Wang *et al.* [114], states that a transition to a precursor phase (simple cubic or some variant) prior to the transition to Sb-II, is conceivable if a substantial uniaxial stress component is present along the c axis. In the non-PTM experiments conducted here, many layers of the Sb foil (which was

characterised as having a preferred orientation following investigation of the texture conducted by Dr D. R. McGonegle) were loaded into the cell in random orientation. Furthermore, lack of a PTM meant that there was significant crumpling of these foils as pressure was increased in the cell, randomising the orientation of the grains in the Sb sample. In the dynamic experiments described in chapter 3, the orientation of the foils relative to the direction of compression was constant throughout the data collection and the work of Dr D. R. McGonegle showed that the *c*-axis of the Sb-I structure was normal to the surface of the target (and thus normal to the face of the forward propagating shock front). This is perhaps the reason for the observation of the Sb-I′ phase in the data obtained on dynamic compression; the uniaxial Peierls distorted rhombohedral structure of the Sb-I phase is sensitive to compression along the *c*-axis. It would be interesting to conduct further experiments to investigate this hypothesis.

In non-hydrostatic experiments, the lack of distortion of the Debye-Scherrer rings implies that there is no significant uniaxial compression occurring in the sample. Most of the data was collected in the Sb-I phase, with only a couple of patterns being obtained after the transition to Sb-II. In the PTM experiment, there were obvious distortions in the Debye-Scherrer rings in the Sb-II phase; it would be interesting to repeat this non-PTM experiment and collect diffraction patterns further into the Sb-II phase in order to compare the nature of the rings.

If this experiment were repeated, it would also be vital that the issue of the reaction between the Cu pressure calibrant and the Sb sample was addressed. Of the commonly-used pressure calibrant materials, it appears that there are no significant reactions between Sb and Ta or W. Figure 4.16 shows the d-spacings of the strongest Ta and W peaks alongside the main peaks of the Sb-I, Sb-II and Sb-III phases at room temperature and 650 K. The Ta and W peak positions were calculated using a thermal EOS [78] and the Sb peaks were obtained in the PTM experiment. In terms of peak-overlap, both Ta and W appear to be suitable candidates although both materials are less sensitive to pressure than Cu which make them less appropriate for the low pressures at which the Sb phase transitions occur.

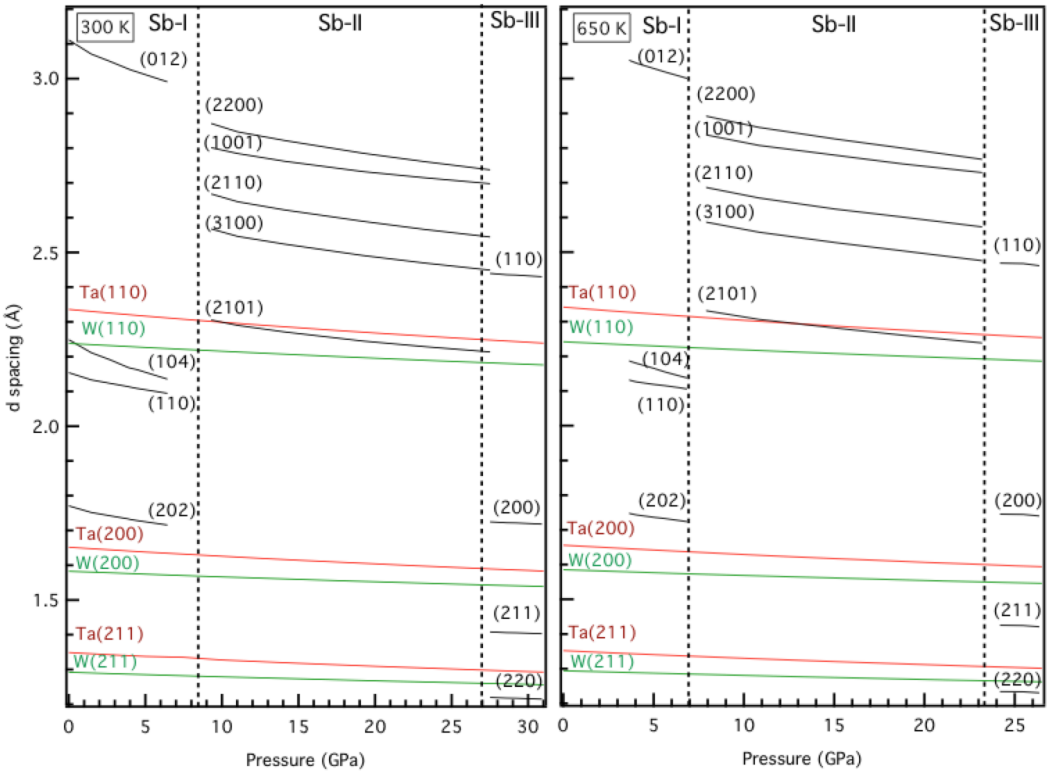

Figure 4.16 *d spacings of Sb-I, Sb-II, Sb-III, Ta and W peaks upon increasing pressure at 300 K and 600 K. The Sb data shown here was collected in the non-hydrostatic experiment described earlier in the chapter while the Ta and W peaks shown here were calculated using a thermal EOS [78]*

Chapter 5

Conclusions and Future Work

5.1 Conclusions

In this thesis both dynamic and static compression experiments have been conducted on the group-15 element, antimony. At the LCLS, *in-situ* x-ray diffraction and VISAR diagnostics were used to characterise on-Hugoniot phase transitions, including melting, on shock-compression timescales with data collected up to 59 GPa (detailed in chapter 3). The Sb-I, Sb-II and Sb-III phases were indexed, along with the identification of a new phase, Sb-I′ for which two candidate structures were proposed. Additionally, liquid diffraction data were observed, allowing a melt-curve to be approximated via extrapolation of pre-existing melt curve data obtained using static compression techniques [27]. VISAR data enabled the identification of a two-wave structure in the rear surface velocity measurements of the Sb-II phase, and a return to a single-wave profile in Sb-III indicating the overdriven regime had been entered. The x-ray diffraction data obtained at the LCLS during this experimental campaign was of unprecedented quality, enabling refinement of the highly-complex, incommensurate host-guest structure of the Sb-II phase. This is the first report of resolution of an incommensurate host-guest structure with *ordered* chains formed under shock-compression. The ability to attain such high-quality x-ray diffraction data on dynamic compression timescales shows great promise for the resolution of such complex structures at even more extreme $P-T$ conditions [55].

At Diamond Light Source, static compression experiments at elevated temperatures were conducted which made use of x-ray diffraction as a diagnostic (detailed in chapter 4). In experiments using a PTM, the Sb-I, Sb-II and Sb-III phases were observed and data were collected to 31 GPa and ∼835 K, allowing a phase diagram to be constructed and two triple points to be identified. The data obtained in this experiment agree very well with the pre-existing static compression data collected at 300 K [43], and the Sb-I→Sb-II phase boundary was found to connect the room temperature Sb-I→Sb-II transition point reported by Schiferl [35] and a minimum in the melt curve reported by Klement [27]. The high quality of the data obtained meant that the low-intensity modulation peaks of the Sb-II phase were able to be resolved, and while texture within the sample prevented any meaningful analysis of their dependence on pressure and temperature, their presence at high pressures and temperatures indicates that the interaction between the host and guest components of the structure remains strong even at extreme conditions. Indeed, the guest chains were found to remain ordered with no chain melting even at the highest temperatures, in contrast to behaviour observed in other elements such as Na, Rb K and Sc [57, 130–133].

The data collected in the dynamic and static experiments show marked disparities in phase behaviour. The Sb-I′ phase was not observed in any static compression experiments, both with and without a PTM. While this is not fully understood, it has been hypothesised that the Peierls-distorted rhombohedral structure of the Sb-I phase is sensitive to uniaxial strain along the *c*-axis [114]; this is corroborated by observation of the Sb-I′ phase in the dynamic compression experiment where the textured Sb targets were all approximately orientated with the *c*-axis parallel to the direction of shock-front propagation whereas the static compression experiments involved multiple layers of crumpled Sb-foils and this orientation was lost.

Additionally, the Sb-I′ phase was found to exist in the equilibrium stability region of the Sb-II phase, according to the phase boundaries constructed following static compression experiments. The stability region of the Sb-II phase on dynamic compression was found to be incredibly small, with the Sb-III phase forming at much lower pressures than observed statically, as illustrated in the combined static and dynamic data phase diagram in figure 4.10. It is evident that a static and dynamic phase diagram for Sb would be significantly different.

5.2 Future Work

This thesis has presented a thorough study of the behaviour of Sb under both static and dynamic compression however there remain some gaps in our understanding of the behaviour of this element at extreme conditions. Primarily, the author believes that investigation of the melt curve of Sb above ∼10 GPa using static techniques would be valuable in facilitating the juxtaposition of dynamic and static melt data. The marked difference between the onset of the phase transitions in the static and dynamic, on-Hugoniot data indicate a potential difference in the melt curve depending on the compression mechanism. The phase diagram of Sb presented in figure 4.10 includes a melt curve that is dependent upon liquid diffraction data obtained under dynamic compression, this curve may be different when measured using static compression techniques.

Furthermore, it would be interesting to explore off-Hugoniot states using dynamic compression techniques. The European XFEL is scheduled to begin operation later this year and will provide drive pulse shaping capabilities meaning that off-Hugoniot states can be investigated using specifically tailored ramp pulses. Additionally, the drive beam will provide up to 100J of energy meaning that higher pressures could be achieved; this is exciting not just for Sb research but for the high pressure community *en masse* as it facilitates access to previously unexplored pressure regimes whilst using x-ray diffraction as a diagnostic. This is particularly exciting when investigating materials which are predicted to exhibit complex structural behaviour in extreme pressure regimes; as mentioned previously aluminium is predicted to form an incommensurate host-guest structure at 3.2 TPa [55] but additionally, it is predicted to form an electride structure at 5 TPa. Electride structures are characterised by density-induced localisation of electrons at interstitial sites in the lattice, where localised electrons behave as massless pseudo-anions. Diffraction data of the highest quality will be necessary to index such structures and it is hoped that x-ray diffraction data of such quality could be attained at 4^{th} generation light sources such as European XFEL. While the 5 TPa pressure at which such structures form in Al is presently unattainable, electride structures are predicted to form in other elements such as Mg at 460 GPa [136]. Work to characterise electride structures is presently being conducted at the National Ignition Facility (NIF) and it is hoped that the high repetition rate of x-ray pulses at European XFEL (∼10 Hz) help to advance such projects.

Given the disparity between the phase transitions of Sb under static compression and laser-driven shock compression, another interesting avenue of research would be the investigation of phase transitions in Sb on timescales between the two methods. Coupling x-ray diffraction with plate-impact shockwave experiments would allow insight into the structural behaviour of Sb on the μs timescale. If, indeed, the phase transitions in Sb were found to be extremely sensitive to strain rates, it would be interesting to explore the extent to which this behaviour is exhibited in other elements.

The European XFEL facility will also provide a means to explore the effects of high strain rates in dynamically compressed materials, in comparison to materials that have been statically compressed. In materials such as Sb and Bi [68] where phase behaviour is found to be different under dynamic and static pressure loading, the study of strain rate is particularly important. As discussed in this thesis, the compression pathway of materials undergoing dynamic compression is complex, with many features to be taken into consideration such as elastic, plastic and release waves, along with phase transitions. It is important for us to be able to understand not just the final state in dynamic compression experiments, but also the processes involved in reaching the final state. At European XFEL, the ability to focus the x-ray beam down to $\sim$100 nm means that the facility will be able to provide the spatial resolution necessary to observe the behaviour of materials under dynamic compression in extraordinary detail.

The high drive beam energies of European XFEL, coupled with extensive detector coverage mean that the facility is also well suited for studying liquid phenomena under dynamic compression. Liquid-liquid phase transitions have been reported in group-15 elements such as P, As and Bi [116, 118–120] and it would certainly be interesting to investigate the behaviour of liquid Sb. Analysis of liquid diffraction patterns requires extensive 2θ coverage for Fourier analysis; at European XFEL this will be realised through both comprehensive detector coverage and x-ray energies of up to 25 keV. To date there have not been a large number of studies conducted on liquid phase transitions under dynamic compression due to technical difficulties in the practical realisation of these experiments. Hopefully the European XFEL will provide the tools necessary to instigate a wide range of dynamic liquid research.

While many results were presented in this thesis, the author believes the most important of these is found in answering the long-standing question: can highly complex structures form on the nanosecond timescales of dynamic compression

and, if so, do we have the capability to diagnose such structures? The observation and refinement of the incommensurate host-guest structure of the Sb-II phase (one of the most complex structures a single element can exhibit) conclusively answers both of these questions with a resounding yes. This work reports the first observation, via x-ray diffraction techniques, of a complete incommensurate host-guest structure with both ordered host *and* ordered guest substructures, formed under shock-compression. Furthermore, the demonstration of a Rietveld refinement of this structure speaks to the unprecedented quality of x-ray diffraction data obtainable at 4th generation light sources. Along with the diagnosis of this structure, marked differences in the phase behaviour of dynamically and statically compressed antimony are reported in this thesis. The author looks forward to future work investigating the relationship between pressure loading mechanisms (and consequent strain rates) and the behaviour of materials that are known to exhibit complex crystallographic structures.

Appendix A

Distortion of Debye-Scherrer Rings (PTM data)

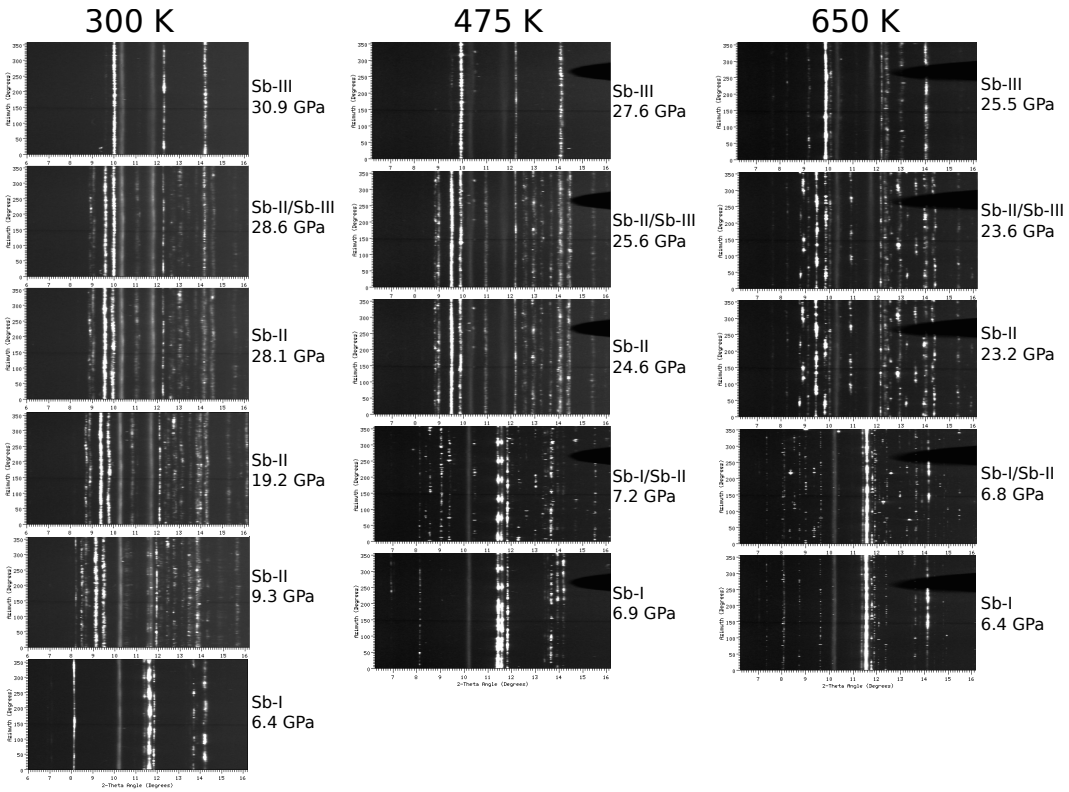

Figure A.1 *Figure showing distortion of the Debye Scherrer rings in the Sb-II phase at 300 K, 475 K and 650 K.*

Appendix B

Published Material

Phase diagram of antimony up to 31 GPa and 835 K

A. L. Coleman, M. Stevenson, and M. I. McMahon
SUPA, School of Physics & Astronomy, and Centre for Science at Extreme Conditions, The University of Edinburgh, Edinburgh, EH9 3FD, United Kingdom

S. G. Macleod
Atomic Weapons Establishment, Aldermaston, Reading, RG7 4PR, United Kingdom and Institute of Shock Physics, Imperial College London, SW7 2AZ, United Kingdom

(Received 10 January 2018; revised manuscript received 5 March 2018; published 13 April 2018)

X-ray powder diffraction experiments using resistively heated diamond anvil cells have been conducted in order to establish the phase behavior of antimony up to 31 GPa and 835 K. The dip in the melting curve at 5.7 GPa and 840 K is identified as the triple point between the Sb-I, incommensurate Sb-II, and liquid phases. No evidence of the previously reported simple cubic phase was observed. Determination of the phase boundary between Sb-II and Sb-III suggests the existence of a second triple point in the region of 13 GPa and 1200 K. The incommensurate composite structure of Sb-II was found to remain ordered to the highest temperatures studies—no evidence of disordering of the guest-atom chains was observed. Indeed, the modulation reflections that arise from interactions between the host and guest subsystems were found to be present to the highest temperatures, suggesting such interactions remain relatively strong in Sb even in the presence of increased thermal motion. Finally, we show that the incommensurately modulated structure recently reported as giving an improved fit to diffraction data from incommensurate Ba-IV can be rejected as the structure of Sb-II using a simple density argument.

DOI: 10.1103/PhysRevB.97.144107

I. INTRODUCTION

Antimony is one of the few elemental metals or semimetals that does not crystallize into a cubic or hexagonal close-packed structure at ambient conditions [1]. Instead, it forms the rhombohedral A7 structure (Sb-I), with space group $R\bar{3}m$, which is a Peierls-distorted simple-cubic (sc) structure. Under static compression at room temperature there have been various reports of a transition from the A7 structure to the undistorted sc structure. Initially this was reported to be a continuous transition occurring at 7 GPa [2], but with the improvement of x-ray diffraction techniques, the same group later reported that the transition was in fact first order [3]. However, the single-crystal study of Schiferl [4] and the later, high-resolution powder diffraction study of Degtrayeva *et al.* [5] showed that while the A7 structure approaches the sc structure on compression up to 8 GPa, the latter is never obtained. Rather, there is a first-order transition at that pressure to a tetragonal incommensurate composite structure (Sb-II) [6–8] which is stable up to 28.8 GPa (at 300 K) where it transforms to the body-centred cubic (bcc) Sb-III phase [5,9]. The structures of Sb-I, Sb-II, and Sb-III are shown in Fig. 1.

The incommensurate composite structure is an unusually complex structural form, observed first in barium [10] and subsequently in a selection of elements from Groups 1, 2, 3, and 15 [11]. The Sb-II composite structure comprises an eight-atom body-centered tetragonal host subsystem (space group $I4/mcm$) with channels running along the c axis. Within these channels run linear chains of guest atoms, which form a two-atom body-centered tetragonal guest subsystem (space group $I4/mmm$) which is incommensurate with the host along their common c axis. The same composite structure is observed in Bi between 2.8 and 7.7 GPa at 300 K [12]. It is advantageous to describe the composite structure of Sb-II in four dimensional (4D) superspace, where its superspace group is $I'4/mcm(00q_3)0000$, with $q_3 = c_H/c_G$, and c_H and c_G are the c-axis repeat distances of the basic host and guest structures, respectively. In superspace, the diffraction peaks are indexed using four integers $(hklm)$, where reflections from the host subsystem of the basic composite structure have indices $(hkl0)$, those from the guest subsystem have indices $(hk0m)$, and the $(hk00)$ reflections are common to both host and guest. Interactions between the host and guest subsystems can result in shifts with respect to the lattice periodic atomic positions, described

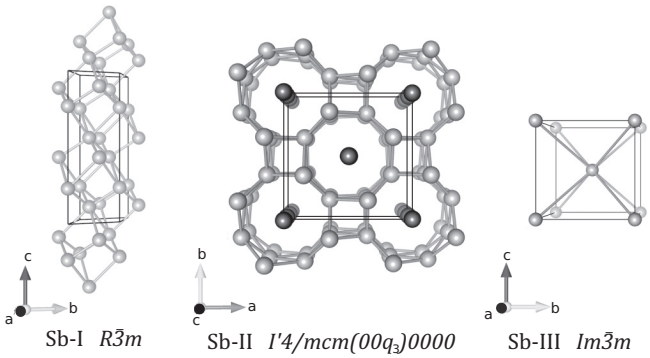

FIG. 1. The crystal structures (not to scale) of Sb-I, Sb-II, and Sb-III. In Sb-I, bonds are shown between the atoms to highlight the distorted simple cubic nature of the structure. In the host-guest structure of Sb-II, the host subsystem is shown in light gray, and the chains of guest atoms are shown in dark gray.

by modulation functions within the superspace formalism, giving rise to additional weak modulation reflections ($hklm$) with both $l \neq 0$ and $m \neq 0$. Such modulation reflections are observed in powder diffraction patterns from Sb-II at 300 K [7,12,13] and indeed are more intense in Sb-II than in the incommensurate composite structures of any other element. The total number of atoms in a unit cell of Sb-II is noninteger and is equal to $N = 8 + 2q_3$. Since the value of q_3 varies with pressure [7], N is pressure dependent.

Degyareva *et al.* reported an intraphase transition from Sb-II to another composite structure (Sb-IV) comprising body-centered monoclinic host and guest subsystems [7]. Sb-IV, with superspace group $I'2/c(q_1 0 q_3)00$, is observed only between 8.2 and 9.0 GPa on pressure increase and between 8.0 and 6.9 GPa on pressure decrease. The occurrence of an intraphase transition between two composite structures is not unique to antimony and has also been observed in barium [10] and strontium [14]. Another phenomenon observed in composite structures is the loss of long range order in the chains of guest atoms, resulting in the disappearance of the ($hk0m$) and ($hklm$) ($l \neq 0$ and $m \neq 0$) Bragg peaks. This "chain-melting" was first observed in rubidium [15,16], subsequently in potassium [17], and, more recently, it has been observed in dynamically compressed scandium at higher temperatures [18]. There have been relatively few high-temperature, high-pressure studies of Sb, although the melt curve has been determined up to ~6.5 GPa, with a triple point reported near 5.7 GPa and ~840 K [19]. It is not known, therefore, whether the incommensurate composite structure of Sb is still the stable phase under such conditions, and, if so, whether it undergoes a chain-melting transition at high temperatures even though the intensity of the ($hklm$) modulation reflections at 300 K suggests relatively strong interactions between the host and guest subsystems.

Here we report high-pressure high-temperature studies of Sb to 31 GPa and 835 K, using resistively heated diamond anvil cells. Over this P-T range we observed only the Sb-I, Sb-II, and Sb-III phases and saw no evidence of either Sb-IV or the simple cubic phase. Furthermore, we observe no evidence of any chain melting up to 835 K. Indeed, the ($hklm$) modulation reflections arising from the interactions between the host and guest subsystems were very clearly observed to the highest temperatures, suggesting that such interactions remain strong in Sb even at elevated temperatures. We also show that the alternative structural model recently reported for the structure of Ba-IVb can be rejected as the structure of Sb-II using a simple density argument.

II. EXPERIMENTAL DETAILS

Powder diffraction data were collected on beamline I15 at the Diamond Light Source, using an x-ray beam with a diameter of 20 μm and a wavelength of 0.4246 Å. Resistively heated, gas-membrane driven diamond anvil cells (DACs) [20], contained within a custom-designed vacuum vessel, and capable of heating to above 800 K [21], were utilized to collect data on Sb up to 835 K and a maximum pressure of 31 GPa. The high-purity polycrystalline Sb sample used in this experiment was obtained from Lawrence Livermore National Laboratory as a ~8 μm thick deposited layer, and small pieces were loaded into the cell along with a small piece of 5 μm thick copper foil

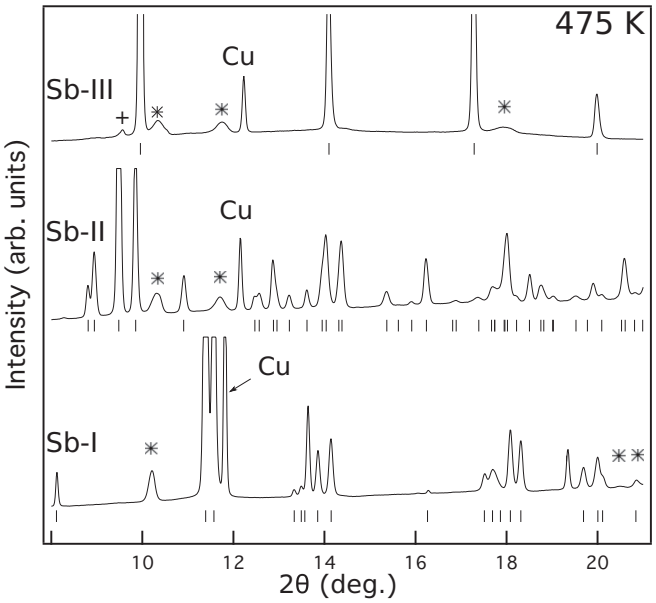

FIG. 2. Waterfall plot illustrating the diffraction patterns obtained from the three distinct phases identified during the experiment: the rhombohedral A7 phase (Sb-I), the incommensurate composite phase (Sb-II), and the bcc phase (Sb-III). The data shown were collected on an isotherm at ~475 K, at pressures of 6.2, 23.1, and 27.6 GPa, respectively. Peaks from the rhenium gasket are marked with asterisks and the copper pressure calibrant peaks are labeled as such. The weak peak marked with a + in the profile from Sb-III is the remnant of the intense (2110) reflection from Sb-II that remains after the onset of the transition to Sb-III. The most intense peaks from all three phases have been cropped for clarity.

which was used for pressure calibration. A small amount of mineral oil was used as a pressure transmitting medium and rhenium was used as the gasket material with a sample chamber diameter of 80 μm. The sample pressure was obtained from the thermal equation of state (EoS) of copper published recently by Sokolova *et al.* [22]. In one DAC a partial reaction was observed between the Sb sample and the copper pressure calibrant to form Cu_2Sb. This reaction occurred only in the DAC used to collect data at ~650 K and arose because the copper was loaded into this cell such that it was in direct contact with the Sb sample. Four separate data collections were conducted, comprising isothermal compressions at approximately 300, 475, 650, and 720 K. Data were collected only on pressure increase, and the sample temperature was measured using a K-type thermocouple which was attached to one of the diamond anvils, close to the sample. The diffraction data were collected using a Mar345 image-plate detector which was placed approximately 385 mm from the sample. The 2D diffraction images were integrated using the FIT2D software [23] and the resulting 1D profiles were analyzed using both the JANA2006 software system [24] and individual peak fitting followed by least-squares analysis of d spacings. Analysis of the effects of nonhydrostaticity on the sample were analyzed using Multifit [25].

III. RESULTS AND DISCUSSION

Figure 2 shows a series of diffraction patterns collected on pressure increase at ~475 K. At this temperature we observed

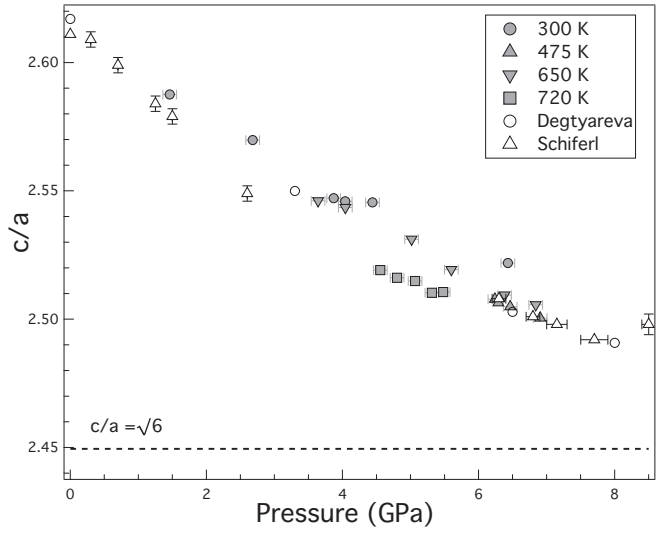

FIG. 3. The c/a ratio of Sb-I versus pressure, as obtained at different temperatures. Circles, upward pointing triangles, downward pointing triangles, and squares show the present results obtained on compression at ∼293, ∼475, ∼650, and ∼720 K, respectively. Data from previous work by Schiferl [4] and Degtyareva [5] at room temperature are shown by unfilled triangles and circles, respectively.

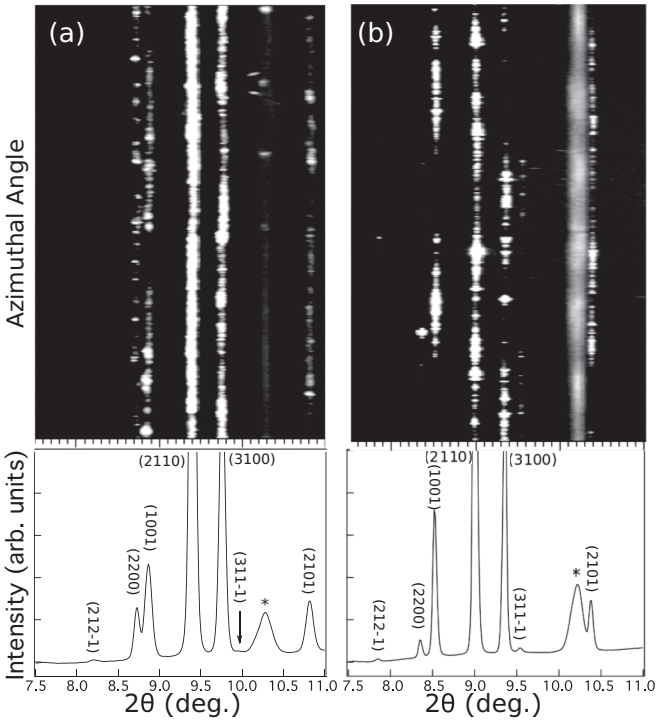

FIG. 4. 2D diffraction images and integrated profiles obtained from Sb-II at (a) 19.4 GPa and 475 K and (b) 6.2 GPa and 720 K. The 2D images are plotted as 2θ-azimuthal-angle plots, such that Debye-Scherrer rings of constant radii appear as vertical lines. Peaks from the rhenium gasket are marked with asterisks. Recrystallization of the sample results in increased visibility of the $(212\bar{1})$ and the $(311\bar{1})$ modulation peaks at higher temperatures in both the 2D images and in the integrated profiles.

the Sb-I → Sb-II transition at 7.1(1) GPa and the Sb-II → Sb-III transition at 25.1(5) GPa. We saw no evidence of the monoclinic Sb-IV composite phase. Tickmarks beneath the profiles in Fig. 2 show the calculated locations of the Bragg peaks from each of the three phases, while those peaks identified with asterisks arise from scattering from the rhenium gasket. The quality of the diffraction patterns is excellent, although the relative intensities of the peaks in Sb-I were strongly affected by preferred orientation, arising from the deposited nature of the Sb sample.

We observed no evidence of the simple cubic phase of Sb on pressure increase at any temperature, in agreement with the earlier high-temperature study of Iwasaki and Kikegawa to 11.5 GPa and ∼600 K [26]. Figure 3 shows the c/a ratio of Sb-I along each approximate isotherm, along with the previously-published room temperature data of Degtyareva *et al.* [5] and Schiferl [4]. While the c/a ratio approaches the value of $\sqrt{6}$ required for the transition to the simple cubic phase, that value is never reached at any temperature prior to the transition to Sb-II. Our results suggest that the c/a ratio at the transition to Sb-II does decrease slightly with increasing temperature, but linear extrapolation suggests that the simple cubic phase will not be observed prior to the sample melting at ∼840 K.

The diffraction profiles obtained from Sb-II, at all pressures and temperatures, contained $(hk0m)$ diffraction peaks from the guest substructure, showing that the guest chains remain ordered to the highest temperatures studied here. This is in contrast to previous results on the composite structures of Rb, K, and Sc, where the chains were found to become fully disordered, and the composite structure of Na at 147 GPa, where the chains were found to be partially disordered at 300 K [27]. The quality of the diffraction patterns from Sb-II also meant that it was possible to observe the weak $(hklm)$ modulation reflections that arise from the interactions between the host and guest subsystems. While these peaks are stronger in Sb-II than in the composite structures of any other element, peak overlap in the powder diffraction profiles means that too few are visible to determine the P-T dependence of the structural modulations, which would require single-crystal diffraction data [12]. However, the relatively intense $(212\bar{1})$ and the $(311\bar{1})$ modulation peaks were observed both at room temperature, in agreement with our previous powder-diffraction study [5], and also to the highest P-T conditions studied (see, for example, Fig. 4). Indeed, the $(311\bar{1})$ modulation reflection became sharper and *more* intense at higher temperatures. However, we believe these changes arose because of the recrystallization of the Sb sample at high temperatures, which gave rise to intense spots on the Debeye-Scherrer rings (see Fig. 4), rather than from increased structural modulations. However, it is clear that significant host-guest interactions are still present in Sb-II well above room temperature, suggesting that any disordering of the guest chains, if it occurs, will only take place at considerably higher temperatures than have been studied here.

In treating the guest subsystem of Sb-II as a series of one-dimensional chains, it is possible to determine their effective Debye temperature, as we have done previously for the composite structure of Rb-IV [16]. For Sb-II, we estimate $\Theta_D =\sim$ 540 K, considerably greater than the value of ∼178 K estimated for Rb-IV [16], and the value of 215 K obtained by Spal *et al.* for $Hg_{3-x}AsF_6$ at room temperature and ambient pressure [28].

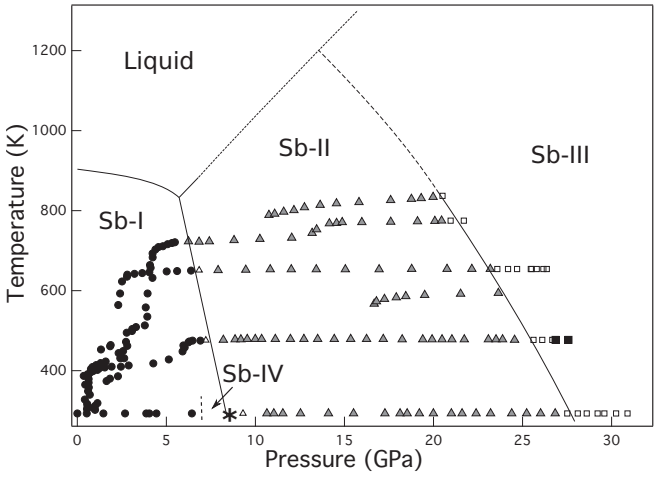

FIG. 5. The phase diagram of Sb to 31 GPa and 835 K. Circles, triangles, and squares show the P-T conditions under which the Sb-I, Sb-II, and Sb-III phases, respectively, were observed. Filled symbols indicate which single-phase profiles were observed, while unfilled symbols show where mixed phase profiles were obtained. The star symbol at 8.6 GPa and 300 K shows the location of the Sb-I → Sb-II transition reported by Degtyareva and Schiferl [4,5] and the Sb-IV phase, as reported by Degtyareva [5], is indicated by a dashed line at room temperature. The dashed melt curve is an extrapolation of the solid melt curve reported by Klement [19].

While Θ_D is greater in Sb-II than in the chain-melted phases of Rb-IV and $Hg_{3-x}AsF_6$, it is difficult to correlate this directly with the melting temperature of the guest chains, which occurs as a consequence of the loss of correlation between the chains rather than being a one-dimensional melting process within each chain.

The sample recrystallization observed above room temperature also reduced the effects of nonhydrostatic pressures on the diffraction profiles. In the data collected at room temperature, small azimuthal variations in the radii of the Debye-Scherrer (D-S) rings were clearly visible in the 2D diffraction patterns collected from Sb-II between 9.3 and 28.6 GPa, but were negligible in the diffraction patterns obtained from Sb-I and Sb-III at the same temperature. While Sb-I is observed at lower pressures than Sb-II, where nonhydrostatic effects would be expected to be smaller, the absence of such effects in Sb-III, above 28 GPa, suggests that they were relieved at the Sb-II → Sb-III transition. Analysis of the 2D images collected above room temperature again showed no azimuthal variations in radii in D-S rings of the Sb-I and Sb-III phases, and while variations in the radii in D-S rings from Sb-II were found to persist at high temperatures, they were much less pronounced than at room temperature.

The proposed phase diagram of Sb to 31 GPa is shown in Fig. 5. The phase boundaries, which were constructed such that they passed as closely as possible to the data points which marked the first appearance of a new phase, are completely consistent with the room temperature phase transition pressures reported by Degtyareva and Schiferl [4,5] although, as previously stated, the monoclinic Sb-IV phase is not observed in the current study. This is likely due to a gap in the coverage of the current data, as Sb-IV is stable over a very small pressure range on P increase, as discussed previously.

Our proposed phase boundary between Sb-I and Sb-II is in excellent agreement with that proposed by Khvostantsev and Siderov [29], and also agrees very well with the minimum in the melt curve previously observed at 5.7 GPa [19]. This minimum is thus confirmed as the triple point between the Sb-I, Sb-II, and liquid phases. The phase boundary between Sb-II and Sb-III is determined for the first time above room temperature and is found to also have a negative slope. Extrapolation of the known melting curve to 6.5 GPa and the newly-determined Sb-II/Sb-III phase boundary suggests that there will be a second triple point between the liquid, Sb-II, and Sb-III phases near 13 GPa and 1200 K (see Fig. 5), although the exact location will depend on the curvature of the melting curve above 7 GPa. Further data will be required to locate its exact position.

Throughout this paper, we have analyzed the data from Sb-II under the assumption that it has the incommensurate composite structure first proposed by McMahon *et al.* in 2000 [5,6], and subsequently confirmed by Schwarz [13]. In a recent publication, Arakcheeva *et al.* have proposed an alternative interpretation of incommensurate host-guest structures, detailing the influence of a density wave within the channels of the incommensurate Ba-IVb structure [30]. While this proposed structure for Ba-IVb is still incommensurate, it has an incommensurately modulated (referred to as "IM" in Ref. [30]) rather than an incommensurate composite ("COMP" in Ref. [30]) structure [8,31]. Arakcheeva *et al.* reported that the IM structure gave a better fit to their single-crystal diffraction data from Ba-IVb than the COMP structure and warned that determining whether the IM or COMP structural models best fitted other data would require refinements with the highest quality data.

However, there is an alternative and simpler method of determining which of the two structural models fits best, as they calculate different sample densities from the same diffraction data. In the COMP model there are $8 + 2q_3$ Sb atoms in a unit cell of volume $a_H \times a_H \times c_H$, while in the IM model, assuming the same structure proposed for Ba-IVb, there are 20 Sb atoms in a unit cell of volume $\sqrt{2}a_H \times \sqrt{2}a_H \times c_H$. As a result, assuming a value of ~1.31 for q_3 in Sb-II [5], the IM structure calculates a density for Sb-II that is ~6% *less* than that calculated assuming the COMP structure, using the same diffraction pattern in each case.

Fortunately, the density of Sb-I and Sb-II have been measured directly to 9.8 GPa by Bridgman [32], using the piston displacement method, and these absolute measurements are shown in Fig. 6. Also shown are the densities of Sb-II determined from the present room temperature diffraction data assuming both IM and COMP structural models. It is clear that the density calculated for Sb-II using the COMP structure is in excellent agreement with the data of Bridgman, as we noted previously [6], while the IM structure underestimates the density of Sb-II by ~5%. Indeed, the IM structural model calculates an unphysical *decrease* in the density of Sb at the Sb-I → Sb-II transition, rather than the 3.7% *increase* in density reported by Bridgman [32].

Finally, the absence of the simple cubic phase in this study, and indeed in all recent high-pressure studies of Sb, led us to wonder whether its presence in the earlier studies

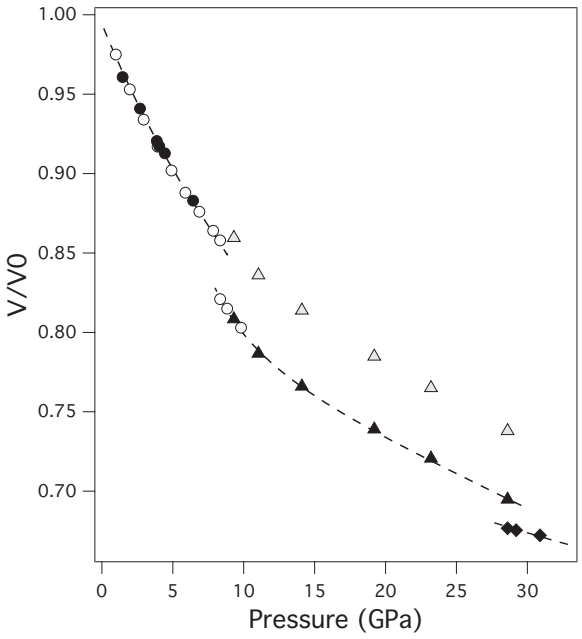

FIG. 6. The compressibility of Sb to 31 GPa at room temperature. Data points from Sb-I, Sb-II [analyzed as an incommensurate composite (COMP) structure], and Sb-III are shown by filled circles, triangles, and diamonds, respectively. The gray triangles show the volume of the Sb-II phase as calculated using the incommensurately modulated (IM) structure containing 20 atoms/cell described by Arakcheeva [30]. The data plotted with unfilled symbols are absolute volume measurements of Bridgman, made without phase determination [32].

of Vereschchagin, Kolobyanina, and Kabalkina [2,3,33] arose because of the effects of nonhydrostaticity in these studies. To investigate this further we conducted some additional high-pressure high-temperature studies without the use of any pressure transmitting medium, with the gasket hole containing only Sb and the copper pressure marker. We again found no evidence of a transition to the simple cubic phase above room temperature—the c/a ratio of the rhombohedral A7 structure decreased with increasing pressure but did not reach $\sqrt{6}$ before the sample transformed to the incommensurate composite structure at ∼8 GPa.

IV. CONCLUSIONS

In conclusion, the high-pressure phase diagram of Sb has been determined to 31 GPa and 835 K using synchrotron x-ray diffraction and resistively heated diamond anvil cells. The previously reported minimum on the Sb melt curve at 5.7 GPa marks the triple point between the Sb-I, incommensurate Sb-II, and liquid phases. The determination of the slope of the phase boundary between Sb-II and Sb-III suggests a second triple point near 13 GPa and 1200 K, although the exact location will depend on the curvature of the melting curve above 6.5 GPa. Further work is needed. Observation of the $(hk0m)$ diffraction peaks from the guest subsystem of Sb-II up to the highest temperatures reveals the guest chains to remain ordered, in contrast to the temperature-induced chain "melting" we have observed previously in Rb, K, and Sc [15–18]. Indeed, the clear observation of the $(hklm)$ ($l \neq 0$ and $m \neq 0$) modulation peaks in the integrated profiles up to 835 K suggests that the structural modulations of the host and guest subsystems in Sb-II remain relatively unchanged on heating and therefore remain greater than those observed in other composite structures of the elements at room temperature. Given the greatly increased thermal motion of the guest chains within the channels of the host framework at high temperatures, this is perhaps surprising.

ACKNOWLEDGMENTS

British Crown Owned Copyright 2018/AWE. Published with permission of the Controller of Her Britannic Majestys Stationery Office. We thank Diamond Light Source (DLS) for provision of synchrotron time and support, and thank Dominik Daisenberger of DLS, Craig Wilson of AWE, and Sarah Finnegan and Christian Storm of the University of Edinburgh for their help with the experiment. We thank Graeme Ackland and Andreas Hermann of the University of Edinburgh for helpful discussions on the Debye temperature of the guest chains.

[1] J. Donohue, *The Structures of the Elements*, A Wiley-interscience publication (John Wiley & Sons Incorporated, New York, 1974).

[2] L. F. Vereschchagin and S. S. Kabalkina, Sov. Phys. JETP **20**, 274 (1965).

[3] T. N. Kolobyanina, S. S. Kabalkina, L. F. Vereschangin, and L. V. Fedina, Sov. Phys. JETP **28**, 88 (1969).

[4] D. Schiferl, D. T. Cromer, and J. C. Jamieson, Acta Crystallogr. Sect. B **37**, 807 (1981).

[5] O. Degtyareva, M. I. McMahon, and R. J. Nelmes, High Press. Res. **24**, 319 (2004).

[6] M. I. McMahon, O. Degtyareva, and R. J. Nelmes, Phys. Rev. Lett. **85**, 4896 (2000).

[7] O. Degtyareva, M. I. McMahon, and R. J. Nelmes, Phys. Rev. B **70**, 184119 (2004).

[8] Incommensurate composite structures comprise two or more interpenetrating lattice-periodic subsystems that are mutually incommensurate. Incommensurately modulated structures are those in which atoms are displaced relative to their average lattice-periodic positions by a modulation whose wavelength is incommensurate with the average periodic lattice. The subsystems of an incommensurate composite structure may themselves be modulated as a result of the interactions between them.

[9] K. Aoki, S. Fujiwara, and M. Kusakabe, Solid State Commun. **45**, 161 (1983).

[10] R. J. Nelmes, D. R. Allan, M. I. McMahon, and S. A. Belmonte, Phys. Rev. Lett. **83**, 4081 (1999).

[11] M. I. McMahon and R. J. Nelmes, Chem. Soc. Rev. **35**, 943 (2006).

[12] M. I. McMahon, O. Degtyareva, R. J. Nelmes, S. van Smaalen, and L. Palatinus, Phys. Rev. B **75**, 184114 (2007).

[13] U. Schwarz, L. Akselrud, H. Rosner, A. Ormeci, Y. Grin, and M. Hanfland, Phys. Rev. B **67**, 214101 (2003).

[14] M. I. McMahon, T. Bovornratanaraks, D. R. Allan, S. A. Belmonte, and R. J. Nelmes, Phys. Rev. B **61**, 3135 (2000).
[15] M. I. McMahon and R. J. Nelmes, Phys. Rev. Lett. **93**, 055501 (2004).
[16] S. Falconi, M. I. McMahon, L. F. Lundegaard, C. Hejny, R. J. Nelmes, and M. Hanfland, Phys. Rev. B **73**, 214102 (2006).
[17] E. E. McBride, K. A. Munro, G. W. Stinton, R. J. Husband, R. Briggs, H. P. Liermann, and M. I. McMahon, Phys. Rev. B **91**, 144111 (2015).
[18] R. Briggs, M. G. Gorman, A. L. Coleman, R. S. McWilliams, E. E. McBride, D. McGonegle, J. S. Wark, L. Peacock, S. Rothman, S. G. Macleod, C. A. Bolme, A. E. Gleason, G. W. Collins, J. H. Eggert, D. E. Fratanduono, R. F. Smith, E. Galtier, E. Granados, H. J. Lee, B. Nagler, I. Nam, Z. Xing, and M. I. McMahon, Phys. Rev. Lett. **118**, 025501 (2017).
[19] W. Klement, A. Jayaraman, and G. C. Kennedy, Phys. Rev. **131**, 632 (1963).
[20] Z. Jenei, H. Cynn, K. Visbeck, and W. J. Evans, Rev. Sci. Instrum. **84**, 095114 (2013).
[21] G. W. Stinton, S. G. MacLeod, H. Cynn, D. Errandonea, W. J. Evans, J. E. Proctor, Y. Meng, and M. I. McMahon, Phys. Rev. B **90**, 134105 (2014).
[22] T. S. Sokolova, P. I. Dorogokupets, A. M. Dymshits, B. S. Danilov, and K. D. Litasov, Comput. Geosci. **94**, 162 (2016).
[23] A. P. Hammersley, S. O. Svensson, M. Hanfland, A. N. Fitch, and D. Häusermann, High Press. Res. **14**, 235 (2006).
[24] V. Petříček, M. Dušek, and L. Palatinus, Z. Kristallogr. **229**, 345 (2014).
[25] S. Merkel and N. Hilairet, J. Appl. Crystallogr. **48**, 1307 (2015).
[26] H. Iwasaki and T. Kikegawa, Physica B+C **139–140**, 259 (1986).
[27] L. F. Lundegaard, E. Gregoryanz, M. I. McMahon, C. Guillaume, I. Loa, and R. J. Nelmes, Phys. Rev. B **79**, 064105 (2009).
[28] R. Spal, C. E. Chen, T. Egami, P. J. Nigrey, and A. J. Heeger, Phys. Rev. B **21**, 3110 (1980).
[29] L. G. Khvostantsev and V. A. Sidorov, Phys. Status Solidi A **82**, 389 (1984).
[30] A. Arakcheeva, M. Bykov, E. Bykova, L. Dubrovinsky, P. Pattison, V. Dmitriev, and G. Chapuis, IUCrJ **4**, 152 (2017).
[31] S. van Smaalen, *Incommensurate Crystallography*, International Union of Crystallography Monographs on Crystallography (Oxford University Press, Oxford, 2007).
[32] P. W. Bridgman, Proc. Am. Acad. Arts Sci. **74**, 399 (1941).
[33] S. S. Kabalkina, T. N. Kolobyanina, and L. F. Vereshchagin, Sov. Phys. JETP **31**, 259 (1970).

IOP Conf. Series: Journal of Physics: Conf. Series **950** (2017) 042037 doi:10.1088/1742-6596/950/4/042037

Implementation of Hydrodynamic Simulation Code in Shock Experiment Design for Alkali Metals

A L Coleman[1], R Briggs[1], M G Gorman[1], S Ali[2] , A Lazicki[2], D C Swift[2], P G Stubley[3], E E McBride[4] , G Collins[2] , J S Wark[3] and M I McMahon[1]

[1] SUPA, School of Physics & Astronomy, and Centre for Science at Extreme Conditions, The University of Edinburgh, Edinburgh EH9 3FD, UK
[2] Lawrence Livermore National Laboratory, 6000 East Avenue, Livermore, California 94500, USA
[3] Department of Physics, Clarendon Laboratory, Parks Road, University of Oxford, Oxford OX1 3PU, UK
[4] DESY Photon Science, Notkestr. 85, D-22607 Hamburg, Germany

E-mail: s0936764@sms.ed.ac.uk

Abstract. Shock compression techniques enable the investigation of extreme P-T states. In order to probe off-Hugoniot regions of P-T space, target makeup and laser pulse parameters must be carefully designed. HYADES is a hydrodynamic simulation code which has been successfully utilised to simulate shock compression events and refine the experimental parameters required in order to explore new P-T states in alkali metals. Here we describe simulations and experiments on potassium, along with the techniques required to access off-Hugoniot states.

1. Introduction

The alkali metals are commonly considered to be "simple" at ambient conditions, and are well explained by the nearly-free electron model. At higher pressures these metals have been shown to depart from this simple behaviour and exhibit more complex, low-symmetry structures [1, 2, 3, 4]. Due to limitations in resistive and laser heating in DACs, the investigation of such exotic behaviour in alkali metals has been limited to moderate temperatures. There have, however, been several computational studies which predict transitions at higher temperatures than are inaccessible using static compression techniques [5, 6]. The use of dynamic compression techniques allows the study of these transitions in previously unexplored P-T regimes.

Shock compression generates states on a Hugoniot: the loci of P-T states that can be achieved with a single shock. Off-Hugoniot states can be accessed using ramp compression, were the ideal pathway is an isentrope [7], and the region between the Hugoniot and the isentrope can be explored with multiple shocks or ramps [8]. The Hugoniot and isentrope of potassium are shown in Figure 1, with the region accessible through multi-shock compression indicated by the shaded area. When combining multiple shocks in a multi-layered target, the complexity of the wave interactions is such that the final P-T states achieved must be determined with the aid of hydrodynamic simulations [9]. Such simulations are essential both in the choice of experimental parameters and also in aiding the interpretation of experimental data in real time.

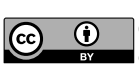

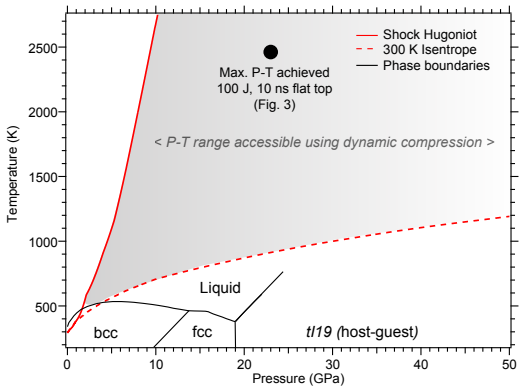

Figure 1. The potassium phase diagram [10, 11, 12] showing the P-T conditions accessible using laser compression techniques between the potassium principal Hugoniot and isentrope. The maximum P-T state achieved using a 100 J, 10 ns shock pulse is also shown.

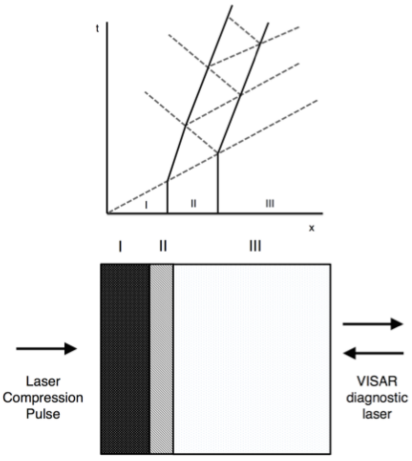

Figure 2. The lower image shows a typical target schematic while the upper image illustrates the interactions of a single shock entering the target [13].

The work presented here focuses on developing shock/multi-shock HYADES simulations in order to investigate unexplored regions of the P-T phase diagram of potassium. Potassium was chosen due to its structural similarities with Li and Na at high pressures, but with the phase transitions occurring at much lower pressures which are readily accessible at large-scale laser facilities. Preliminary laser compression data have been compared to the simulations presented here.

2. Methods

Simulations using the HYADES radiation hydrocode have been used to determine the laser compression parameters (pulse length, intensity, and double-shock pulse timing) and target parameters (ablator and sample thickness) required to compress potassium into previously unexplored P-T conditions. HYADES simulations utilise a Lagrangian mesh that moves with the target material [9]. Each zone in the mesh has a fixed mass and it is the movement of the mesh which determines the volume and the density of each zone through conservation of mass, energy, and momentum [14]. HYADES allows meaningful calculations to be executed rapidly with minimal computing expense which is advantageous in the planning of high shot-rate experimental campaigns and the interpretation of the results *in situ*.

The design of the target package is a crucial aspect of the experimental setup which must be optimised in order to access the required P-T conditions. Careful consideration of each target material's shock impedance [13] must be taken into account. The impedance matching technique allows a low-impedance material of interest to be layered between two higher-impedance materials such that a series of reverberating compression waves 'ring up' between the two higher-impedance materials until pressure uniformity in the target is achieved. These interactions are illustrated in figure 2 [13]. The lower image shows the target design consisting of the high impedance ablator (I), the lower impedance material of interest (II) and the high-impedance window material (III), while the upper image illustrates the ringing up of a shock wave through a series of reflections in the material of interest. For the potassium targets we used Al as the ablator material, with windows of LiF, as these two materials are well impedance matched, thus ensuring that there are no significant pressure gradients within the sample at peak compression. The SESAME database was used for equation of state and opacity data for

for Al, K and LiF [15].

The experimental work on potassium was conducted using the Janus laser at the Jupiter Laser Facility, LLNL, USA. This facility offers two Nd:glass (527 nm) laser beams which can provide flat-top pulses with energies up to 500 J and pulse lengths between 0.35 and 20 ns. A 1mm^2 phase plate was selected for use with pulses between 6 and 10 ns in length using varying energies.

3. Results and Discussion

Initially, single-shock simulations were used to understand the effects of a shock propagating through the multi-layer target package discussed above. This allowed the optimisation of the target parameters, laser pulse length and energy within the physical constraints of the Jupiter Laser Facility and the availability of materials. The effect of the 'ringing up' of the shock wave was determined, along with the length of pulse required in order to sustain compression through the ablator to the rear surface of the potassium. For a flat-top pulse length of 10 ns, a series of laser energies between 25 J and 175 J were simulated for a target consisting of 25 μm Al, 10 μm K and 500 μm LiF. These simulations showed initial pressures between 1 and 10 GPa in the K layer, with a subsequent jump to pressures between 2 and 17 GPa following the immediate re-shock from the K/LiF interface. After the ringing-up of the re-shocks between the high-impedance Al and LiF layers, the peak pressures in the K layer ranged from 4.5 to 32 GPa.

These simulations agreed well with the experimental data, as illustrated in Figure 3, which compares the experimentally-determined particle velocity in the K layer resulting from a 100 J, 10 ns flat-top pulse to the output from a HYADES simulation using the same parameters. The good agreement between the simulated and experimental velocity data means that the P and T obtained from the simulation (23 GPa and 2400 K) may be used to infer a location on a P-T diagram for the shock event (as shown on Figure 1).

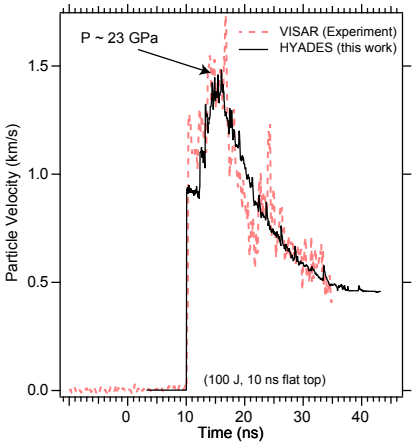

Figure 3. The experimental VISAR trace from a single 100 J, 10 ns flat-top pulse shows good agreement with the particle velocity data produced by the corresponding HYADES simulation.

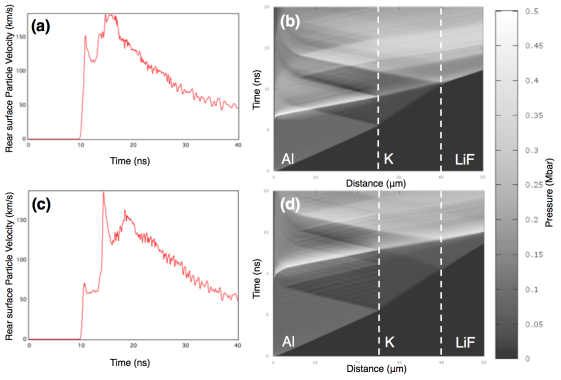

Figure 4. The upper VISAR trace and pressure plot show the results of a simulated double-shock event (50 J, 10 ns pulse and 150 J 10 ns pulse) with a delay of 6 ns between pulses, while the lower plots show the results of the same setup but with a delay of 9 ns between pulses.

More complex, double-shock experiments were then designed to further extend the range of off-Hugoniot P-T conditions that could be explored. This was achieved by first varying the initial shock in the system to take the potassium to an on-Hugoniot P-T state, with subsequent secondary shocks and further 'ring-ups' taking the compression pathway away from the Hugoniot

towards an isentrope. One important aspect of this design process is the relative timing of the two laser pulses, as illustrated in figure 4, which shows a double-shock simulation in which an initial 50 J, 10 ns flat-top pulse is followed by a 150 J, 10 ns flat-top pulse. Figure 4(a) shows a simulated VISAR trace and 4(b) shows the pressure distribution in the distance-time plane, for a 6 ns delay between the beginning of the first and second laser pulses. Figures 4(c) and 4(d) show the same information for a 9 ns delay between the laser pulses. In the case of the 6 ns delay, the first compression wave is overtaken by that produced by the second pulse before the former has fully propagated through the K layer and reached the K/LiF interface. As a result, the VISAR diagnostic used during the experiment to obtain the particle velocity at the K/LiF interface will be unable to identify the particle velocity resulting from just the first shock, and instead observes only the jump to the higher velocity resulting from the combination of the two compression waves. The loss of information about the on-Hugoniot state achieved by the initial shock means that the final P-T state is not obtainable from the VISAR data. However, for the 9 ns delay, the initial shock is able to propagate fully through the K layer before the second wave catches up, allowing the on-Hugoniot state achieved by the first pulse to be determined. The final P-T state produced by the second shock is then more easily determined.

4. Conclusions

HYADES has been used to plan a successful experimental campaign on shock-compressed potassium, by optimising target design and laser pulse parameters. It has proven to be an invaluable tool in the interpretation of the complex wave interactions, and the subsequent P-T states induced, in a laser-compressed multi-layer target. The results are directly applicable to our on-going campaigns on Li and Na.

5. Acknowledgements

We thank the Jupiter Laser Facility at Lawrence Livermore National Laboratory for provision of the laser facility time and support. This work was supported by research grant EP/J017256/1 from the UK Engineering and Physical Sciences Research Council.

References

[1] McMahon M I and Nelmes R J 2006 *Chem. Soc. Revs.* **35**, 943
[2] Guillaume C L, Gregoryanz E, Degtyareva O *et al* 2011 *Nat. Phys.* **7**, 211
[3] Gregoryanz E, Lundegaard L F, McMahon M I, Guillaume C L *et al* 2008 *Science* **320**, 1054
[4] Lundegaard L F, Stinton G W, Zelazny M, Guillaume C L, Proctor J E *et al* 2013 *Phys. Rev. B* **88**, 054106
[5] Ma Y, Oganov A R and Xie Y 2008 *Phys. Rev. B* **78**, 014102
[6] Kim H, Su J T and Goddard III W A *et al.* 2011 *PNAS* **108**, 15101
[7] Smith R F, Eggert J H, Jeanloz R, Duffy T S, Braun D G, Patterson J R *et al* 2014 *Nature* **511**, 330
[8] Boehly T R, Vianello E, Miller J E, Craxton R S, Collins T J B *et al* 2006 *Phys. Plasmas* **13**, 056303
[9] Larsen J T and Lane S M 1994 *J. Quant. Spectrosc. Radiat. Transfer* **51**, 179-186
[10] McBride E E, Munro K A, Stinton G W, Husband R J, Briggs R *et al* 2015 *Phys. Rev. B* **91**, 144111
[11] McBride E E, Narygina O, Stinton G W *et al* 2012 *Journal of Physics: Conference Series* **377**, 012040
[12] Narygina O, McBride E E, Stinton G W and McMahon M I 2011 *Phys. Rev. B* **84**, 054111
[13] Forbes J W 2012 *Shockwave compression of condensed matter* (Springer, New York)
[14] Swift D C and Kraus R G 2008 *Phys. Rev. E* **77**, 066402
[15] Lyon S P and Johnson J D *Private Communications on SESAME database*

Ultrafast X-Ray Diffraction Studies of the Phase Transitions and Equation of State of Scandium Shock Compressed to 82 GPa

R. Briggs, M. G. Gorman, A. L. Coleman, and R. S. McWilliams
SUPA, School of Physics and Astronomy, and Centre for Science at Extreme Conditions, The University of Edinburgh, Mayfield Road, Edinburgh EH9 3JZ, United Kingdom

E. E. McBride
European XFEL, Albert-Einstein-Ring 19, D-22761 Hamburg, Germany

D. McGonegle and J. S. Wark
Department of Physics, Clarendon Laboratory, Parks Road, University of Oxford, Oxford OX1 3PU, United Kingdom

L. Peacock and S. Rothman
Atomic Weapons Establishment, Aldermaston, Reading RG7 4PR, United Kingdom

S. G. Macleod
Atomic Weapons Establishment, Aldermaston, Reading, RG7 4PR, United Kingdom and Institute of Shock Physics, Imperial College London, SW7 2AZ, United Kingdom

C. A. Bolme and A. E. Gleason
Shock and Detonation Physics, Los Alamos National Laboratory, P.O. Box 1663, Los Alamos, New Mexico 87545, USA

G. W. Collins, J. H. Eggert, D. E. Fratanduono, and R. F. Smith
Lawrence Livermore National Laboratory, 6000 East Avenue, Livermore, California 94500, USA

E. Galtier, E. Granados, H. J. Lee, B. Nagler, I. Nam, and Z. Xing
Linac Coherent Light Source, SLAC National Accelerator Laboratory, Menlo Park, California 94025, USA

M. I. McMahon
SUPA, School of Physics and Astronomy, and Centre for Science at Extreme Conditions, The University of Edinburgh, Mayfield Road, Edinburgh, EH9 3JZ, United Kingdom and Research Complex at Harwell, Didcot, Oxon OX11 0FA, United Kingdom

(Received 22 January 2016; revised manuscript received 15 July 2016; published 9 January 2017)

Using x-ray diffraction at the Linac Coherent Light Source x-ray free-electron laser, we have determined simultaneously and self-consistently the phase transitions and equation of state (EOS) of the lightest transition metal, scandium, under shock compression. On compression scandium undergoes a structural phase transition between 32 and 35 GPa to the same bcc structure seen at high temperatures at ambient pressures, and then a further transition at 46 GPa to the incommensurate host-guest polymorph found above 21 GPa in static compression at room temperature. Shock melting of the host-guest phase is observed between 53 and 72 GPa with the disappearance of Bragg scattering and the growth of a broad asymmetric diffraction peak from the high-density liquid.

DOI: 10.1103/PhysRevLett.118.025501

The past 20 years have seen the discovery of a wealth of new and complex structures in the elements at high pressures [1], with perhaps the most outstanding examples being the incommensurate composite structures that comprise interpenetrating host and guest components [2]. Since their discovery in Ba [3], host-guest (HG) structures have been found in nine other elements, and are predicted to exist in aluminium at 3–5 TPa [4]. Such ultra-high-pressure states can be accessed routinely only via laser-compression techniques, but it is as yet unknown whether such complex structures can form on the nanosecond time scales and at the high temperatures produced in such experiments.

One element with a high-pressure HG structure, which has been studied using both static and shock compression techniques, is scandium. At ambient conditions, Sc has the hcp structure (hcp-Sc), which on heating transforms to the bcc structure (bcc-Sc) at 1607 K, before melting at 1812 K [5]. On compression at 300 K, hcp-Sc transforms at 21 GPa [6] to a HG structure (HG-Sc) [7,8], which remains stable to 104 GPa [9].

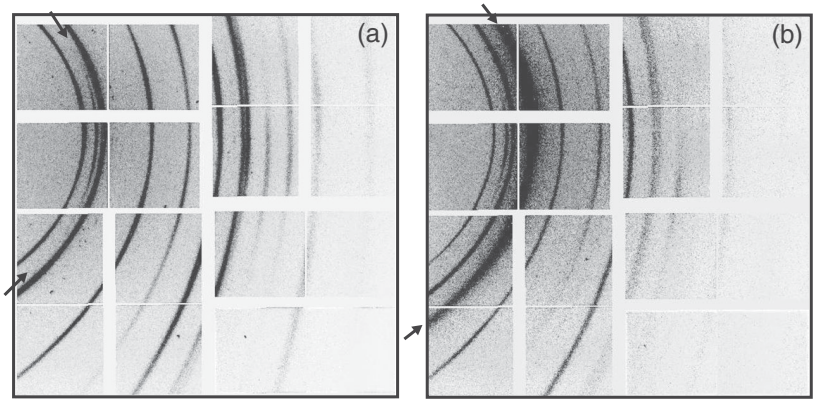

FIG. 1. 2D diffraction images collected on a single CSPAD detector from (a) uncompressed hcp-Sc and (b) Sc compressed to 51.1 GPa. The arrows in the two images highlight (a) the highly textured (002) Debye-Scherrer ring from uncompressed hcp-Sc and (b) the most intense Debye-Scherrer ring from the host-guest phase, the intensity distribution of which is much more uniform.

On the shock Hugoniot, the collection of states accessed by shock compression, a phase transition beginning at 16.5 GPa and completing by 38 GPa was identified from the deviation of existing shock Hugoniot data [10–12] from a calculated EOS for hcp-Sc and HG-Sc [13]; in the same study, *in situ* electrical measurements confirmed a transition. However, the earlier shock study by Carter *et al.* saw no evidence of a transition at 16.5 GPa, but saw a clear kink in $U_S - u_p$ (shock velocity—particle velocity) data at 35 GPa [12]. A phase transition to a further solid phase, or to the melt, was detected at 53 GPa [13]. Despite being unable to identify conclusively the phase transitions at 16.5, 35, and 53 GPa, since direct structural measurements were not available, the shock EOS of Sc is known to above 200 GPa [10–13].

To date, the measurement of an absolute EOS using laser-driven shock waves has been challenging, and reference to a standard EOS has generally been required. Furthermore, most modern laser-compression EOS data are reported on transparent materials, as an accurate and precise determination of the EOS of nontransparent materials, such as metals, poses major challenges. As a result, EOS data on opaque matter tend to exhibit considerable uncertainties, particularly in the density. However, the advent of x-ray free-electron lasers (XFELs) has resulted in an unprecedented improvement in the quality of diffraction data that can be obtained from dynamically compressed matter [14,15], making it possible to determine the crystal structure and density unambiguously with high precision. By combining such measurements with simultaneous velocimetry measurements, it is now possible to overcome previous limitations, and obtain EOS measurements without a reference, including for opaque materials.

Here we utilize x-ray diffraction at an XFEL to determine the EOS of scandium metal under shock compression and to study its structural evolution for direct comparison with prior isobaric heating and isothermal compression measurements. We observe a transition from hcp-Sc to bcc-Sc between 32 and 35 GPa, a second transition at 46 GPa from bcc-Sc to HG-Sc, and then melting beginning at 53 GPa and being complete at 72 GPa.

Two experiments were performed at the MEC end station of the Linac Coherent Light Source (LCLS) [16]. A Nd: glass optical laser (527 nm, 20 ns quasiflattopped pulses) was used to launch an ablation-driven shock wave through the samples, which comprised a 50 μm thick polyimide ablator glued to 25 μm thick Sc foil of 99% purity. The LCLS provided quasimonochromatic ($\Delta E/E \sim 0.5\%$, $\lambda = 1.4089$ or 1.2400 Å) x-ray pulses of 50 or 80 fs duration, each containing $\sim 10^{12}$ photons. The x-ray beam was focused to 50×50 μm^2 and then centered on the variable diameter focal spot of the drive laser, which, in turn, was centered on the target.

Two-dimensional diffraction images, as illustrated in Fig. 1, were recordered on multiple CSPAD detectors (Cornell-SLAC Pixel Array Detector) [17] placed in a transmission Debye-Scherrer geometry [18], which were then integrated azimuthally to produce 1D diffraction profiles. A velocity interferometer system for any reflector (VISAR) was used to both record the velocity-time histories of the rear free surface of the samples, thereby allowing the sample pressure to be determined, and to investigate any nonplanarity of the laser drive across the x-rayed region of the target.

The pressure was determined using the Rankine-Hugoniot equations from the measured densities and particle velocities, taken to be half the free-surface velocity [18]. In some cases, a LiF window was placed on the rear surface as a check on calculated pressures; in these cases, the pressure in the Sc was established from the value measured in the LiF [29] by impedance matching using prior Sc shock data [10–12]. Additional information on the experimental details and VISAR analysis is given in the Supplemental Material [18].

Data were collected between 0 and ~82 GPa, and contained clearly distinguishable diffraction patterns from

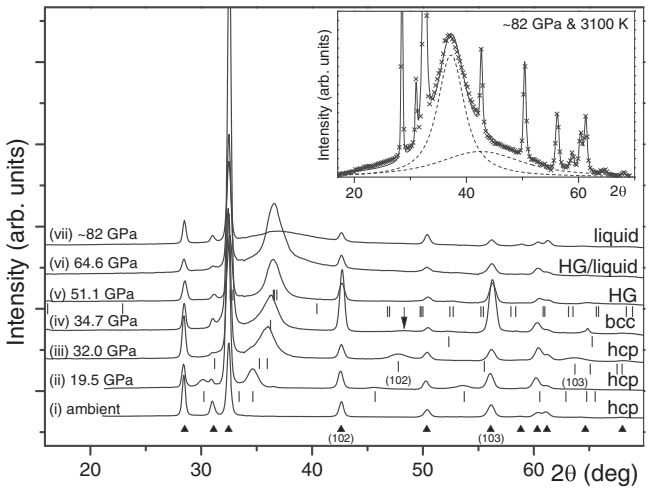

FIG. 2. Diffraction profiles from Sc on shock compression ($\lambda = 1.4089$ Å). The peaks from uncompressed hcp-Sc are identified by filled triangles below profile (i). The profiles show data from (i) uncompressed hcp-Sc; compressed hcp-Sc at (ii) 19.5 and (iii) 32.0 GPa; (iv) bcc-Sc at 35.6 GPa; (v) HG-Sc at 51.1 GPa; (vi) HG- and liquid-Sc at 64.6 GPa; and (vii) liquid-Sc at ~82 GPa. The peaks from the compressed hcp [profiles (ii) and (iii)], bcc [profile (iv)], and HG [profile (v)] phases are shown by tick marks beneath the profiles. The compressed hcp-Sc (102) and (103) reflections, the disappearance of which provides clear evidence of the hcp-to-bcc transition, are identified in profile (iii). A trace of the (102) peak is still observed at 34.7 GPa, as identified by the arrow in profile (iv). The inset shows an enlarged view of the ~82 GPa profile, where the asymmetry of the principal liquid peak is highlighted by fitting it with two Gaussians.

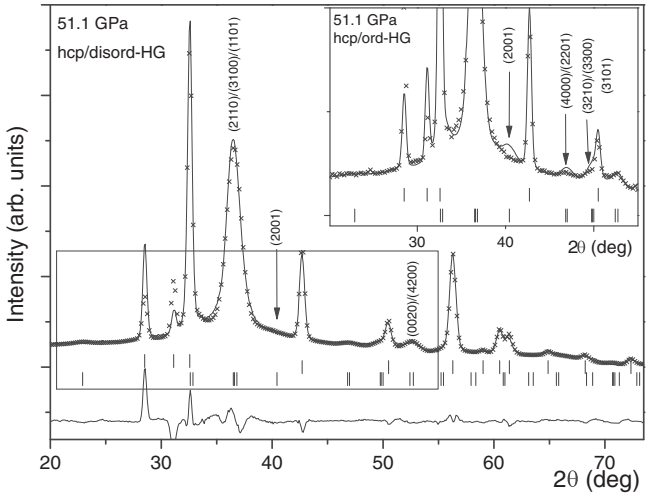

FIG. 3. A two-phase (62%:38% uncompressed-hcp:disordered-HG) Rietveld fit to the diffraction profile obtained at 51.1 GPa ($\lambda = 1.4089$ Å), with the most intense peaks indexed. The calculated peak positions of the best-fitting uncompressed-hcp and HG unit cells are shown by upper and lower tick marks beneath the profile. The inset shows an uncompressed-hcp:ordered-HG fit to the same profile. The additional (2001) guest-only peak, and the intensity mismatches caused by the intensities of the (2201) and (3101) guest-only peaks, are highlighted with arrows.

different solid phases and a liquid phase, as illustrated in Fig. 2. At pressures up to 32 GPa, only compressed hcp-Sc was observed, as identified from broadened hcp diffraction peaks displaced to higher angles; see profiles (ii) and (iii) in Fig. 2. Although the Debye-Scherrer rings from the compressed hcp-Sc are well defined and symmetric, they are both broader and noticeably less textured than those from the uncompressed material. This increased broadness and texture change is evident at all pressures, including data collected from samples compressed to only ~10 GPa which have undergone no phase transition, and is also present in samples released back to ambient pressure and arises from the many defects induced by the plastic deformation of the sample as it is strained beyond its elastic limit of ~0.4 GPa [28]. We have made a quantitative analysis of the microstress and grain size of the compressed samples, following the analysis conducted by Gleason *et al.* [23] in their shock compression study of quartz. We find that at 19.5 GPa, the grain size in compressed hcp-Sc is 25 (3) nm, considerably smaller than the measured grain size of 85(17) nm in the uncompressed Sc foil. The rms strain in the hcp-Sc phase at 19.5 GPa was measured to be less than $< 0.2\%$. Full details are given in the Supplemental Material [18].

Between 32 and 35 GPa, Sc undergoes a phase transition, resulting in the disappearance of the (102) and (103) hcp reflection at $2\theta \sim 48°$ and ~64°, respectively, and the appearance of an intense diffraction peak at $2\theta = 36.2°$ and a weaker peak at 52.2° [Fig. 2, profile (iv)]. The d-spacing ratio of these two peaks is $\sqrt{2}$, and they can thus be indexed as the (110) and (200) peaks of bcc-Sc with $a = 3.200$ Å at 34.7 GPa ($V/V_0 = 0.657$). However, the same ratio relates the d spacings of the (2110)/(3100)/(1101) and (0020)/(4200) peaks of HG-Sc [30] with $a = 7.16$ Å, $c = 3.20$ Å, and $\gamma = 1.28$ ($V/V_0 = 0.621$), where γ is the incommensurate wave vector.

Closer analysis of our highest-quality diffraction pattern at 51.1 GPa [Fig. 2, profile (v), and Fig. 3] revealed the existence of two much weaker diffraction features at 46.9° and 49.8°, neither of which are accounted for by bcc-Sc. While both peaks are predicted by the HG phase, this structure would also predict a more intense peak—the (2001)—at 40.4° that should be clearly visible (see inset of Fig. 3). This is a $(hk0m)$ "guest-only" peak, and arises from scattering from the chains of guest atoms only [30]. If these chains were disordered, as we have observed in HG-Rb at 300 K [31], and in HG-K at high temperatures [32], then this, and other, $(hk0m)$ guest-only peaks would be extremely weak and not visible. A Rietveld refinement of the 51.1 GPa profile using a disordered HG model is shown in Fig. 3, and is excellent, accounting for all observed features. Indeed, the use of a disordered model also

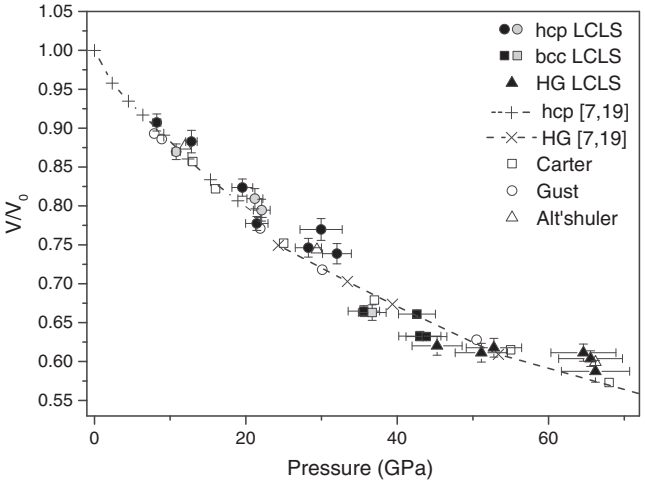

FIG. 4. Volumetric compression for Sc. Hugoniot EOS data obtained from this study are shown using filled black symbols, and points obtained using a LiF backing window are shown using filled gray symbols. The unfilled symbols show the previous shock compression data of Gust and Royce [11], Altshuler *et al.* [10], and Carter *et al.* [12]. The crosses and dashed lines show the corrected isothermal compressibility data at 300 K [7], assuming $\gamma = 1.280$ at all pressures for the HG phase [18].

improves the fit to the two peaks at 46.9° and 49.8°, both of which have an intensity contribution from ($hk0m$) guest-only peaks, and are calculated to be more intense in an ordered structural model (Fig. 3, inset). The best fitting lattice parameters at 51.1 GPa are $a = 7.095(2)$ Å, $c = 3.190(1)$ Å, and $\gamma = 1.280$ (constrained to the value found at 300 K [31]). For comparison, the lattice parameters of ordered HG-Sc at 51 GPa and 300 K are $a = 7.18$ Å and $c = 3.18$ Å [7].

Fitting all diffraction data between 35 and 53 GPa to a HG structure led to an unphysically small compressibility, and poor agreement with previous shock data. Fitting the same data with bcc-Sc led to exactly the same problems. However, further analysis of the diffraction data revealed that there was no evidence of the weaker HG-Sc peaks below 45 GPa, and that between 35 and 45 GPa the data were completely accounted for by bcc-Sc. A Rietveld fit to an uncompressed-hcp:bcc profile at 35.0 GPa is shown in Fig. S4 of the Supplemental Material [18]. As the sample density calculated from a diffraction pattern differs by ~3% depending on whether one assumes it is bcc-Sc or HG-Sc (see above). calculating the densities between 35 and 45 GPa assuming bcc-Sc, and between 45 and 53 GPa assuming HG-Sc, resulted in both a physically sensible compressibility and good agreement with previous studies (Fig. 4). There is no evidence of any volume change at the bcc-HG transition.

Above 53 GPa we observe a clear increase in the background level in the vicinity of the most intense HG diffraction peak [Fig. 2, profile (vi)], which we attribute to the first appearance of scattering from liquid-Sc. The observation of incipient melting at 53 GPa is in perfect agreement with the report of a phase transformation at 53 GPa by Molodets *et al.* [13]. The melting temperature is estimated from the shock temperature of the solid at 53 GPa to be ~2200 K [11].

As the sample pressure was increased above 53 GPa, the intense HG diffraction peak reduced in intensity, and disappeared at 72 GPa, above which only diffraction from liquid-Sc was observed [Fig. 2, profile (vii)]. This melting behavior suggests that the shock Hugoniot follows the Sc melting curve from 53 to 72 GPa before wholly entering the liquid phase. This agrees with one of the interpretations of Molodet *et al.* of their own data, where a mixed solid-liquid region is found between 53 and 72 GPa. The diffraction peak from the liquid is very distinctive, with a width that is 4–5 times that of the peak from HG-Sc [compare profiles (vi) and (vii) in Fig. 2], and is asymmetric (see inset of Fig. 2). Such an asymmetry suggests that Sc is not a simple liquid under such conditions [33–35].

Above 72 GPa, the free surface became entirely non-reflecting upon shock breakout, as is commonly observed as a consequence of melting and consistent with total melting above this pressure. Extrapolation of the liquid-diffraction peak position versus pressure [18] suggests that our highest-pressure liquid diffraction profile was obtained at ~82 GPa and 3100 K. The liquid diffraction data at this maximum pressure (see Fig. 2 inset) exhibits a high signal-to-noise ratio, and the diffraction profile contains scattering from only liquid-Sc and uncompressed hcp-Sc. While the q range of the data is limited by both the relatively long x-ray wavelengths used in this study and the limited angular coverage of the CSPAD detectors, the signal-to-noise ratio is perhaps better than that obtainable from a laser-heated diamond anvil cell (LHDAC) at the same $P - T$ conditions. The LCLS data also contain scattering only from the sample, and are free of parasitic scattering from the thermally insulating materials that typically encase the sample in a LHDAC experiment [36,37]. The LCLS liquid data are also free of diffraction peaks from contaminants, such as oxides and carbides, that can form as a result of extended laser heating in a DAC [38].

The phase diagram of Sc to 90 GPa and 3500 K obtained from our data is shown in Fig. 5. The Hugoniot shown is that of hcp-Sc [39]—a multi-solid-phase EOS for Sc is not yet available. The initial gradient of the hcp-HG phase boundary was confirmed in a high-pressure high-temperature static compression experiment at a synchrotron [18], and the phase transition points are shown. Up to 900 K, the HG-Sc was found to have ordered guest chains. The observation of a phase transition to bcc-Sc between 32 and 35 GPa along the Hugoniot is in excellent agreement with the transition reported in previous shock studies [12,13], while the lack of any volume change at the bcc-to-HG transition at 46 GPa probably prevented its detection in previous nondiffraction studies.

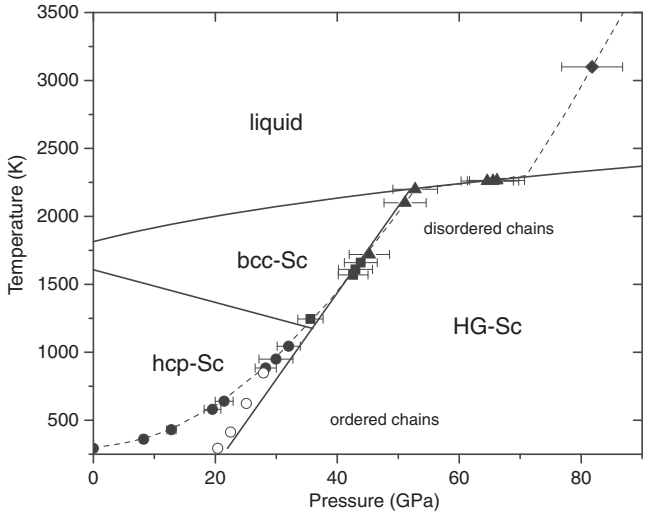

FIG. 5. The proposed phase diagram of Sc to 90 GPa and 3500 K. The short-dashed line shows the calculated hcp-Sc Hugoniot [39], a multiphase Hugoniot is not yet available, while the melt curve is a Simon-Glatzel fit to the ambient-pressure melting temperature and that at 53 GPa. Proposed phase boundaries between the hcp, bcc, and HG phases are shown with solid lines. The unfilled circles show the hcp-HG phase boundary, as determined in our static compression experiment.

The observation of the incommensurate HG structure of Sc is an important step in understanding the behavior of matter under shock compression. Not only is this complex incommensurate equilibrium phase formed on the subnanosecond time scales associated with laser-compression experiments, and observed up to 53 GPa and 2200 K, but the quality of the data obtained at the LCLS is sufficient to determine that the structure has undergone sublattice melting, as previously seen in other HG phases [31,32].

We believe this work represents an important benchmark on the path towards accurate EOS measurements in laser-driven dynamic compression experiments, particularly for opaque materials. The clarity with which both shock-induced solid-solid phase transitions and incipient or complete melting can be observed and distinguished in a relatively low-Z element like Sc ($Z = 21$) to 82 GPa holds great promise for future XFEL studies of similar phenomena in other materials to higher pressures. The quality and q range of the liquid diffraction data are almost sufficient to obtain a radial distribution function via Fourier transform of the diffraction profile. Unfortunately, the data extend to only $q = 5.5$ Å^{-1}, slightly too low to be analyzable via a Fourier transform. However, by increasing the energy of the x rays, and moving the detectors to obtain greater angular coverage, the q range can be extended to ~ 8 Å^{-1}, which simulations show is a sufficient range to obtain a quantitative radial distribution function sufficient to extend diffraction density measurements beyond the solid state. Obtaining such information from liquids at P-T conditions beyond those accessible with laser-heated DACs opens exciting possibilities for the study of liquids at planetary-core conditions.

In conclusion, by combining diffraction and velocimetry measurements, we have eliminated numerous uncertainties in the compression behavior of scandium, thereby showing the significant value of combining measurements of phase and equation of state to definitively interpret the dynamic compression response of materials.

M. I. M. and J. S. W. would like to acknowledge support from EPSRC under Grants No. EP/J017256/1 and No. EP/J017051/1. D. M. is supported by LLNS under Contract No. B595954. E. E. M. acknowledges funding from the VolkswagenStiftung. The work by J. H. E., D. E. F., R. F. S., and G. W. C. was performed under the auspices of the U.S. Department of Energy by Lawrence Livermore National Laboratory under Contract No. DE-AC52-07NA27344. C. A. B. would like to acknowledge support from Science Campaign 2 at Los Alamos National Laboratory, which is operated for the National Nuclear Security Administration of the U.S. Department of Energy under Contract No. DE-AC52-06NA25396. Use of the Linac Coherent Light Source (LCLS), SLAC National Accelerator Laboratory, is supported by the U.S. Department of Energy, Office of Science, Office of Basic Energy Sciences under Contract No. DE-AC02-76SF00515. The MEC instrument is supported by the U.S. Department of Energy, Office of Science, Office of Fusion Energy Sciences under Contract No. SF00515. We would like to thank Carol A. Davis of LLNL for her help in preparing the Sc targets, and Dr Giulia De Lorenzi-Venneri of LANL for supplying the Sc EOS used in Fig. 5. We thank Diamond Light Source (DLS) for provision of synchrotron time and support, and thank Craig Wilson and Dominik Daisenberger of DLS for their help with the experiment.

[1] M. I. McMahon and R. J. Nelmes, Chem. Soc. Rev. **35**, 943 (2006).
[2] M. McMahon and R. Nelmes, Z. Kristallogr. **219**, 742 (2004).
[3] R. J. Nelmes, D. R. Allan, M. I. McMahon, and S. A. Belmonte, Phys. Rev. Lett. **83**, 4081 (1999).
[4] C. J. Pickard and R. J. Needs, Nat. Mater. **9**, 624 (2010).
[5] B. J. Beaudry and A. H. Daane, Trans. Metall. Soc. AIME **224**, 770 (1962).
[6] Y. K. Vohra, W. Grosshans, and W. B. Holzapfel, Phys. Rev. B **25**, 6019 (1982).
[7] H. Fujihisa, Y. Akahama, H. Kawamura, Y. Gotoh, H. Yamawaki, M. Sakashita, S. Takeya, and K. Honda, Phys. Rev. B **72**, 132103 (2005).
[8] M. I. McMahon, L. F. Lundegaard, C. Hejny, S. Falconi, and R. J. Nelmes, Phys. Rev. B **73**, 134102 (2006).
[9] Y. Akahama, H. Fujihisa, and H. Kawamura, Phys. Rev. Lett. **94**, 195503 (2005).

[10] L. V. Altshuler, A. A. Bakanova, and I. P. Dudoladov, Sov. Phys. JETP **26**, 1115 (1968).
[11] W. H. Gust and E. B. Royce, Phys. Rev. B **8**, 3595 (1973).
[12] W. J. Carter, J. N. Fritz, S. P. Marsh, and R. G. McQueen, J. Phys. Chem. Solids **36**, 741 (1975).
[13] A. M. Molodets, D. V. Shakhray, A. A. Golyshev, and V. E. Fortov, Phys. Rev. B **75**, 224111 (2007).
[14] L. B. Fletcher, H. J. Lee, T. Doeppner, E. Galtier, B. Nagler, P. Heimann, C. Fortmann, S. LePape, T. Ma, M. Millot *et al.*, Nat. Photonics **9**, 274 (2015).
[15] M. G. Gorman, R. Briggs, E. E. McBride, A. Higginbotham, B. Arnold, J. H. Eggert, D. E. Fratanduono, E. Galtier, A. E. Lazicki, H. J. Lee *et al.*, Phys. Rev. Lett. **115**, 095701 (2015).
[16] B. Nagler, B. Arnold, G. Bouchard, R. F. Boyce, R. M. Boyce, A. Callen, M. Campell, R. Curiel, E. Galtier, J. Garofoli *et al.*, J. Synchrotron Radiat. **22**, 520 (2015).
[17] P. Hart, S. Boutet, G. Carini, M. Dubrovin, B. Duda, D. Fritz, G. Haller, R. Herbst, S. Herrmann, C. Kenney *et al.*, Proc. SPIE Proc. **8504**, 85040C (2012).
[18] See Supplemental Material at http://link.aps.org/supplemental/10.1103/PhysRevLett.118.025501 for additional information on the experiments, pressure determination in the liquid, and corrections to the previous static compression data, which includes Refs. [19–28].
[19] P. M. Celliers, D. K. Bradley, G. W. Collins, D. G. Hicks, T. R. Boehly, and W. J. Armstrong, Rev. Sci. Instrum. **75**, 4916 (2004).
[20] J. W. Forbes, *Shockwave Compression of Condensed Matter* (Springer, New York, 2012).
[21] B. Warren and B. Averbach, J. Appl. Phys. **21**, 595 (1950).
[22] J. A. Hawreliak, D. H. Kalantar, J. S. Stolken, B. A. Remington, H. E. Lorenzana, and J. S. Wark, Phys. Rev. B **78**, 220101 (2008).
[23] A. E. Gleason, C. A. Bolme, H. J. Lee, B. Nagler, E. Galtier, D. Milathianaki, J. Hawreliak, R. G. Kraus, J. H. Eggert, D. E. Fratanduono, G. W. Collins, R. Sandberg, W. Yang and W. L. Mao, Nat. Commun. **6**, 8191 (2015).
[24] https://www-s.nist.gov/srmors/certificates/674b.pdf.
[25] A. P. Hammersley, S. O. Svensson, M. Hanfland, A. N. Fitch, and D. Häusermann, High Press. Res. **14**, 235 (1996).
[26] L. M. Barker and R. E. Hollenbach, J. Appl. Phys. **45**, 4872 (1974).
[27] P. M. Celliers, G. W. Collins, D. G. Hicks, and J. H. Eggert, J. Appl. Phys. **98**, 113529 (2005).
[28] D. Geiselman, J. Less-Common Met. **4**, 362 (1962).
[29] D. Hayes, J. Appl. Phys. **89**, 6484 (2001).
[30] The Miller indices used to identify reflections from host-guest structures are of the form $(hklm)$. Reflections from the host component of the basic composite structure have indices $(hkl0)$, those from the guest have indices $(hk0m)$, and the $(hk00)$ reflections are common to both host and guest. Interactions between the host and guest will result in shifts with respect to the lattice periodic atomic positions, giving rise to extremely weak satellite reflections $(hklm)$ with both l and $m \neq 0$. These have been omitted from the refinements conducted here.
[31] M. I. McMahon and R. J. Nelmes, Phys. Rev. Lett. **93**, 055501 (2004).
[32] E. E. McBride, K. A. Munro, G. W. Stinton, R. J. Husband, R. Briggs, H. P. Liermann, and M. I. McMahon, Phys. Rev. B **91**, 144111 (2015).
[33] J. P. Hansen and I. R. McDonald, *Theory of Simple Liquids* (Academic Press, London, 1990).
[34] N. W. Ashcroft and J. Lekner, Phys. Rev. **145**, 83 (1966).
[35] G. Shen, V. B. Prakapenka, M. L. Rivers, and S. R. Sutton, Phys. Rev. Lett. **92**, 185701 (2004).
[36] A. Cadien, Q. Y. Hu, Y. Meng, Y. Q. Cheng, M. W. Chen, J. F. Shu, H. K. Mao, and H. W. Sheng, Phys. Rev. Lett. **110**, 125503 (2013).
[37] S. Anzellini, A. Dewaele, M. Mezouar, P. Loubeyre, and G. Morard, Science **340**, 464 (2013).
[38] A. Dewaele, M. Mezouar, N. Guignot, and P. Loubeyre, Phys. Rev. Lett. **104**, 255701 (2010).
[39] G. De Lorenzi-Venneri, Los Alamos National Laboratory, Technical Report No. LA-UR-12-25498.

Bibliography

[1] A. L. Coleman, M. Stevenson, M. I. McMahon, and S. G. Macleod, Physical Review B **97** (2018).

[2] E. Gregoryanz, O. Degtyareva, M. Somayazulu, R. J. Hemley, and H.-k. Mao, Physical Review Letters **94**, 185502 (2005).

[3] I. Loa, P. Adler, A. Grzechnik, K. Syassen, U. Schwarz, M. Hanfland, G. K. Rozenberg, P. Gorodetsky, and M. P. Pasternak, Physical Review Letters **87**, 125501 (2001).

[4] W. Zhang, A. R. Oganov, A. F. Goncharov, Q. Zhu, S. E. Boulfelfel, A. O. Lyakhov, E. Stavrou, M. Somayazulu, V. B. Prakapenka, and Z. Konôpková, Science **342**, 1502 (2013).

[5] D. Pan, Q. Wan, and G. Galli, Nature Communications **5**, 3919 (2014).

[6] P. F. McMillan, Nature Materials **1**, 19 (2002).

[7] E. C. Kemble and F. Birch, "Percy Williams Bridgman, 1882-1961: A Biographical Memoir," Columbia University Press (1970).

[8] R. L. Weber, *Pioneers of science: Nobel prize winners in physics* (IOP, 1980).

[9] C. E. Weir, E. R. Lippincott, A. VanValkenburg, and E. N. Bunting, Journal of Research of the National Bureau of Standards Section a-Physics and Chemistry **63**, 55 (1959).

[10] A. Van Valkenburg, Review of Scientific Instruments **33**, 1462 (1962).

[11] N. Dubrovinskaia, L. Dubrovinsky, N. A. Solopova, A. Abakumov, S. Turner, M. Hanfland, E. Bykova, M. Bykov, C. Prescher, V. B. Prakapenka, S. Petitgirard, I. Chuvashova, B. Gasharova, Y.-L. Mathis, P. Ershov, I. Snigireva, and A. Snigirev, Science Advances **2**, e1600341 (2016).

[12] W. J. M. Rankine, Philos. Trans. R. Soc. London **160**, 277 (1870).

[13] H. Hugoniot, J. LEcole Polytech. **58**, 3 (1889).

[14] P. O. K. Krehl, *History of Shock Waves, Explosions and Impact: A Chronological and Biographical Reference*, 1st ed. (Springer Berlin Heidelberg, 2008).

[15] W. J. Nellis, *P. W. Bridgman contributions to the foundations of shock compression of condensed matter*, Tech. Rep. (2009).

[16] J. W. Forbes, AIP Conference Proceedings **620**, 11 (2001).

[17] L. C. Chhabildas, L. Davison, and Y. Horie, *High-Pressure Shock Compression of Solids VIII*, The Science and Technology of High-Velocity Impact (Springer Science & Business Media, 2006).

[18] D. Bancroft, E. L. Peterson, and S. Minshall, Journal of Applied Physics **27**, 291 (1956).

[19] R. A. Graham, in *Sandia National Labs., Albuquerque, NM United States* (1993).

[20] G. A. Askaryan and E. M. Moroz, Soviet Journal of Experimental and Theoretical Physics **16**, 1638 (1963).

[21] N. C. Anderholm, Applied Physics Letters **16**, 113 (1970).

[22] J. D. O'Keefe, Journal of Applied Physics **44**, 4622 (1973).

[23] L. C. Yang, Journal of Applied Physics **45**, 2601 (1974).

[24] Q. Johnson and A. C. Mitchell, Physical Review Letters **29**, 1369 (1972).

[25] D. H. Kalantar, J. F. Belak, G. W. Collins, J. D. Colvin, H. M. Davies, J. H. Eggert, T. C. Germann, J. Hawreliak, B. L. Holian, K. Kadau, P. S. Lomdahl, H. E. Lorenzana, M. A. Meyers, K. Rosolankova, M. S. Schneider, J. Sheppard, J. S. Stölken, and J. S. Wark, Physical Review Letters **95**, 075502 (2005).

[26] R. F. Smith, J. H. Eggert, R. Jeanloz, T. S. Duffy, D. G. Braun, J. R. Patterson, R. E. Rudd, J. Biener, A. E. Lazicki, A. V. Hamza, J. Wang, T. Braun, L. X. Benedict, P. M. Celliers, and G. W. Collins, Nature **511**, 330 (2014).

[27] W. Klement, A. Jayaraman, and G. C. Kennedy, Physical Review **131**, 632 (1963).

[28] P. W. Bridgman, Physical Review **60**, 351 (1941).

[29] P. W. Bridgman, Proceedings of the American Academy of Arts and Sciences **74**, 425 (1942).

[30] L. F. Vereschchagin and S. S. Kabalkina, Soviet Physics JETP **20**, 274 (1965).

[31] S. M. Stishov and N. A. Tikhomirova, Soviet Journal of Experimental and Theoretical Physics **21**, 810 (1965).

[32] T. N. Kolobyanina, S. S. Kabalkina, L. F. Vereschangin, and L. V. Fedina, Soviet Physics JETP **28**, 88 (1969).

[33] S. S. Kabalkina, T. N. Kolobyanina, and L. F. Vereshchagin, Soviet Physics JETP **31**, 259 (1970).

[34] M. J. Duggin, Journal of Physics and Chemistry of Solids **33**, 1267 (1972).

[35] D. Schiferl, D. T. Cromer, and J. C. Jamieson, Acta Crystallographica Section B **37**, 807 (1981).

[36] J. C. Jamieson and A. W. Lawson, Journal of Applied Physics **33**, 776 (1962).

[37] L. G. Khvostantsev and V. A. Sidorov, Physica Status Solidi (a) **82**, 389 (1984).

[38] K. Aoki, S. Fujiwara, and M. Kusakabe, Solid State Communications **45**, 161 (1983).

[39] H. Iwasaki and T. Kikegawa, Physica B & C **139**, 259 (1986).

[40] H. Iwasaki and T. Kikegawa, International Journal of High Pressure Research **6**, 121 (2006).

[41] M. I. McMahon, O. Degtyareva, and R. J. Nelmes, Physical Review Letters **85**, 4896 (2000).

[42] U. Schwarz, L. Akselrud, H. Rosner, A. Ormeci, Y. Grin, and M. Hanfland, Physical Review B **67**, 214101 (2003).

[43] O. Degtyareva, M. I. McMahon, and R. J. Nelmes, High Pressure Research **24**, 319 (2004).

[44] O. Degtyareva, M. I. McMahon, and R. J. Nelmes, Physical Review B **70**, 184119 (2004).

[45] M. I. McMahon, O. Degtyareva, R. J. Nelmes, S. van Smaalen, and L. Palatinus, Physical Review B **75**, 184114 (2007).

[46] R. E. Duff and F. S. Minshall, Physical Review **108**, 1207 (1957).

[47] S. Katz, D. G. Doran, and D. R. Curran, Journal of Applied Physics **30**, 568 (1959).

[48] R. G. McQueen and S. P. Marsh, Journal of Applied Physics **31**, 1253 (2004).

[49] R. H. Warnes, Journal of Applied Physics **38**, 4629 (1967).

[50] B. R. Breed and D. Venable, Journal of Applied Physics **39**, 3222 (1968).

[51] G. E. Duvall and R. A. Graham, Rev. Mod. Phys. **49**, 523 (1977).

[52] D. B. Larson, Journal of Applied Physics **38**, 1541 (2004).

[53] J. W. Forbes and G. E. Duvall, in *High-Pressure Science and Technology* (Springer, Boston, MA, Boston, MA, 1979) pp. 210–216.

[54] "European XFEL Brilliance," `http://www.wayforlight.eu/en/fels?contentId=3021`, [Online; accessed 05-December-2017].

[55] C. J. Pickard and R. J. Needs, Nature Materials **9**, 624 (2010).

[56] A. L. Coleman, R. Briggs, M. G. Gorman, S. Ali, A. Lazicki, D. C. Swift, P. G. Stubley, E. E. McBride, G. Collins, J. S. Wark, and M. I. McMahon, Journal of Physics: Conference Series **950**, 042037 (2017).

[57] R. Briggs, M. G. Gorman, A. L. Coleman, R. S. McWilliams, E. E. McBride, D. McGonegle, J. S. Wark, L. Peacock, S. Rothman, S. G. Macleod, C. A. Bolme, A. E. Gleason, G. W. Collins, J. H. Eggert, D. E. Fratanduono, R. F. Smith, E. Galtier, E. Granados, H. J. Lee, B. Nagler, I. Nam, Z. Xing, and M. I. McMahon, Phys. Rev. Lett. **118**, 025501 (2017).

[58] V. E. Fortov, R. I. Ilkaev, V. A. Arinin, V. V. Burtzev, V. A. Golubev, I. L. Iosilevskiy, V. V. Khrustalev, A. L. Mikhailov, M. A. Mochalov, V. Y. Ternovoi, and M. V. Zhernokletov, Physical Review Letters **99**, 185001 (2007).

[59] S. N. Luo, B. J. Jensen, D. E. Hooks, K. Fezzaa, K. J. Ramos, J. D. Yeager, K. Kwiatkowski, and T. Shimada, Review of Scientific Instruments **83**, 073903 (2012).

[60] J. W. Forbes, *Shock Wave Compression of Condensed Matter: A Primer*, Shock Wave and High Pressure Phenomena (Springer Berlin Heidelberg, 2013).

[61] D. C. Swift, T. E. Tierney, R. A. Kopp, and J. T. Gammel, Physical Review E **69**, 036406 (2004).

[62] A. Higginbotham, J. Hawreliak, E. M. Bringa, G. Kimminau, N. Park, E. Reed, B. A. Remington, and J. S. Wark, Physical Review B **85**, 024112 (2012).

[63] D. Swift, R. Kraus, E. Loomis, D. Hicks, J. McNaney, and R. Johnson, Physical Review E **78**, 066115 (2008).

[64] J. Hawreliak, B. A. Remington, H. Lorenzana, B. E, and J. Wark, in *Lawrence Livermore National Laboratory LLNL, Livermore, CA* (2011) pp. 1–11.

[65] J. Wang, R. F. Smith, J. H. Eggert, D. G. Braun, T. R. Boehly, J. Reed Patterson, P. M. Celliers, R. Jeanloz, G. W. Collins, and T. S. Duffy, **114**, 023513 (2013).

[66] J. R. Asay, G. R. Fowles, E. Durall, M. H. Miles, and R. F. Tinder, Journal of Applied Physics **43**, 2132 (1972).

[67] J. R. Asay, G. R. Fowles, and Y. Gupta, Journal of Applied Physics **43**, 744 (1971).

[68] R. F. Smith, J. H. Eggert, M. D. Saculla, A. F. Jankowski, M. Bastea, D. G. Hicks, and G. W. Collins, Physical Review Letters **101**, 065701 (2008).

[69] J. W. Swegle and D. E. Grady, Journal of Applied Physics **58**, 692 (1985).

[70] D. C. Swift, Physical Review E **77**, 066402 (2008).

[71] J. R. Rygg, J. H. Eggert, A. E. Lazicki, F. Coppari, J. A. Hawreliak, D. G. Hicks, R. F. Smith, C. M. Sorce, T. M. Uphaus, B. Yaakobi, and G. W. Collins, Review of Scientific Instruments **83**, 113904 (2012).

[72] Larsen, J T and Lane, S M, Journal of Quantitative Spectroscopy and Radiative Transfer **51**, 179 (1994).

[73] A. Jayaraman, Reviews of Modern Physics **55**, 65 (1983).

[74] Z. Jenei, H. Cynn, K. Visbeck, and W. J. Evans, Review of Scientific Instruments **84**, 095114 (2013).

[75] A. K. Singh, C. Balasingh, H.-k. Mao, R. J. Hemley, and J. Shu, Journal of Applied Physics **83**, 7567 (1998).

[76] A. K. Singh, Journal of Physics and Chemistry of Solids **65**, 1589 (2004).

[77] F. Datchi, A. Dewaele, P. Loubeyre, R. Letoullec, Y. Le Godec, and B. Canny, High Pressure Research **27**, 447 (2007).

[78] T. S. Sokolova, P. I. Dorogokupets, A. M. Dymshits, B. S. Danilov, and K. D. Litasov, Computers and Geosciences **94**, 162 (2016).

[79] N. W. Ashcroft and N. D. Mermin, *Solid state physics* (Saunders College, 1976).

[80] J. R. Hook and H. E. Hall, *Solid State Physics* (John Wiley & Sons, 2013).

[81] C. Kittel, *lntroduction to Solid State Physics (Eighth Edition)* (John Wiley & Sons, Inc, 2005).

[82] Y. Waseda, E. Matsubara, and K. Shinoda, *X-Ray Diffraction Crystallography* (Springer, 2011).

[83] T. Hahn, *International tables for crystallography*, Volume A, Space-group symmetry (Kluwer Academic Pub, 1996).

[84] *16th BCA/CCG Intensive Teaching School in X-Ray Structure Analysis, Trevelyan College, Durham, UK*, Tech. Rep. (2017).

[85] P. M. De Wolff and IUCr, Acta Crystallographica Section A: Crystal Physics, Diffraction, Theoretical and General Crystallography **30**, 777 (1974).

[86] S. van Smaalen, *Incommensurate crystallography* (Oxford University Press, 2007).

[87] T. Janssen, A. Janner, A. Looijenga-Vos, and P. M. De Wolff, in *International Tables for Crystallography Volume C: Mathematical, physical and chemical tables* (Springer, Dordrecht, Chester, England, 2006) pp. 907–955.

[88] D. McGonegle, D. Milathianaki, B. A. Remington, J. S. Wark, and A. Higginbotham, Journal of Applied Physics **118**, 065902 (2015).

[89] A. Balerna and S. Mobilio, in *Synchrotron Radiation* (Springer, Berlin, Heidelberg, Berlin, Heidelberg, 2015) pp. 3–28.

[90] P. Duke, *Synchrotron Radiation*, Production and Properties (Oxford University Press, 2008).

[91] H. Wiedemann, *Synchrotron Radiation*, Advanced Texts in Physics (Springer Science & Business Media, Berlin, Heidelberg, 2013).

[92] G. Margaritondo and P. Rebernik Ribic, Journal of Synchrotron Radiation **18**, 101 (2011).

[93] B. W. J. McNeil and N. R. Thompson, Nature Photonics **4**, 1 (2010).

[94] H. Loos and others, in *Beam instrumentation. Proceedings, 14th Workshop, BIW10, Santa Fe, USA, May 2-6, 2010* (2010).

[95] P. Schmüser, M. Dohlus, and J. Dohlus, in *Ultraviolet and Soft X-Ray Free-Electron Lasers* (Springer, Berlin, Heidelberg, 2008) pp. 103–120.

[96] B. Nagler, B. Arnold, G. Bouchard, R. F. Boyce, R. M. Boyce, A. Callen, M. Campell, R. Curiel, E. Galtier, J. Garofoli, E. Granados, J. Hastings, G. Hays, P. Heimann, R. W. Lee, D. Milathianaki, L. Plummer, A. Schropp, A. Wallace, M. Welch, W. White, Z. Xing, J. Yin, J. Young, U. Zastrau, and H. J. Lee, Journal of Synchrotron Radiation **22**, 520 (2015).

[97] A. Le Bail, H. Duroy, and J. L. Fourquet, Materials Research Bulletin **23**, 447 (1988).

[98] H. M. Rietveld and IUCr, Journal of Applied Crystallography **2**, 65 (1969).

[99] P. M. Celliers, D. K. Bradley, G. W. Collins, D. G. Hicks, T. R. Boehly, and W. J. Armstrong, Review of Scientific Instruments **75**, 4916 (2004).

[100] K. T. Lorenz, M. J. Edwards, A. F. Jankowski, S. M. Pollaine, R. F. Smith, and B. A. Remington, High Energy Density Physic **2**, 113 (2006).

[101] D. H. Dolan, *Foundations of VISAR analysis* (Sandia Report, 2006).

[102] D. Milathianaki, S. Boutet, G. J. Williams, A. Higginbotham, D. Ratner, A. E. Gleason, M. Messerschmidt, M. M. Seibert, D. C. Swift, P. Hering, J. Robinson, W. E. White, and J. S. Wark, Science **342**, 220 (2013).

[103] J. S. Wark, R. R. Whitlock, A. Hauer, J. E. Swain, and P. J. Solone, Physical Review B **35**, 9391 (1987).

[104] D. Kraus, A. Ravasio, M. Gauthier, D. O. Gericke, J. Vorberger, S. Frydrych, J. Helfrich, L. B. Fletcher, G. Schaumann, B. Nagler, B. Barbrel, B. Bachmann, E. J. Gamboa, S. Göde, E. Granados, G. Gregori, H. J. Lee, P. Neumayer, W. Schumaker, T. Döppner, R. W. Falcone, S. H. Glenzer, and M. Roth, Nature Communications **7**, 10970 (2016).

[105] "LCLS Overview," `https://lcls.slac.stanford.edu/overview`, [Online; accessed 12-March-2018].

[106] E. C. Galtier, *LCLS private communication*, Tech. Rep. (2018).

[107] P. Hart, S. Boutet, G. Carini, and A. Dragone, in *Nuclear Science Symposium and Medical Imaging Conference NSSMIC, IEEE* (2012) pp. 538–541.

[108] S. B. Brown, A. Hashim, A. Gleason, E. Galtier, I. Nam, Z. Xing, A. Fry, A. MacKinnon, B. Nagler, E. Granados, and H. J. Lee, Review of Scientific Instruments **88**, 105113 (2017).

[109] D. Batani, H. Stabile, A. Ravasio, G. Lucchini, F. Strati, T. Desai, J. Ullschmied, E. Krousky, J. Skala, L. Juha, B. Kralikova, M. Pfeifer, C. Kadlec, T. Mocek, A. Präg, H. Nishimura, and Y. Ochi, Physical Review E **68**, 067403 (2003).

[110] V. Petricek, M. Dusek, and L. Palatinus, Zeitschrift für Kristallographie **229**, 345 (2014).

[111] T. Holland and S. Redfern, Mineralogical Magazine **61**, 65 (1997).

[112] D. Schiferl, Review of Scientific Instruments **48**, 24 (1977).

[113] A. Higginbotham and D. McGonegle, Journal of Applied Physics **115**, 174906 (2014).

[114] X. Wang, K. Kunc, I. Loa, U. Schwarz, and K. Syassen, Physical Review B **74**, 134305 (2006).

[115] P. Kalita, P. Specht, S. Root, N. Sinclair, A. Schuman, M. White, A. L. Cornelius, J. Smith, and S. Sinogeikin, Physical Review Letters **119**, 255701 (2017).

[116] A. Chiba, M. Tomomasa, T. Higaki, T. Hayakawa, and K. Tsuji, Journal of Physics: Conference Series **98**, 012011 (2008).

[117] M. G. Gorman, R. Briggs, E. E. McBride, A. Higginbotham, B. Arnold, J. H. Eggert, D. E. Fratanduono, E. Galtier, A. E. Lazicki, H. J. Lee, H. P. Liermann, B. Nagler, A. Rothkirch, R. F. Smith, D. C. Swift, G. W. Collins, J. S. Wark, and M. I. McMahon, Physical Review Letters **115**, 095701 (2015).

[118] Y. Katayama, T. Mizutani, W. Utsumi, O. Shimomura, M. Yamakata, and K.-i. Funakoshi, Nature **403**, 170 (2000).

[119] M. G. Gorman, *Martin 2018 Bi private communication*, Tech. Rep. (2018).

[120] K. Yaoita, K. Tsuji, Y. Katayama, M. Imai, J.-Q. Chen, T. Kikegawa, and O. Shimomura, Journal of Non-Crystalline Solids **150**, 25 (1992).

[121] E. E. McBride, A. Krygier, M. Harmand, Z. Konopkova, H. P. Liermann, A. Schropp, S. Toleikis, A. Pelka, M. Roedel, C. Spindloe, R. F. Smith, E. Galtier, H. J. Lee, B. Nagler, T. Tschentscher, J. S. Wark, and A. Higginbotham, APS Meeting Abstracts (2016).

[122] S. J. Turneaure and Y. M. Gupta, Applied Physics Letters **91**, 201913 (2007).

[123] R. F. Smith, J. H. Eggert, D. C. Swift, J. Wang, T. S. Duffy, D. G. Braun, R. E. Rudd, D. B. Reisman, J. P. Davis, M. D. Knudson, and G. W. Collins, Journal of Applied Physics **114**, 223507 (2013).

[124] G. V. Bunton and S. Weintroub, Journal of Physics C: Solid State Physics **2**, 116 (1969).

[125] J. M. Brown and R. G. McQueen, Journal of Geophysical Research **91**, 7485 (1986).

[126] S. Anzellini, A. Dewaele, M. Mezouar, P. Loubeyre, and G. Morard, Science **340**, 464 (2013).

[127] A. Dewaele, M. Mezouar, N. Guignot, and P. Loubeyre, Physical Review Letters **104**, 322 (2010).

[128] V. Sorkin, E. Polturak, and J. Adler, EPL (Europhysics Letters) **76**, 623 (2006).

[129] A. P. Hammersley, S. O. Svensson, M. Hanfland, A. N. Fitch, and D. Hausermann, International Journal of High Pressure Research **14**, 235 (2006).

[130] L. F. Lundegaard, E. Gregoryanz, M. I. McMahon, C. Guillaume, I. Loa, and R. J. Nelmes, Physical Review B **79**, 064105 (2009).

[131] M. I. McMahon and R. J. Nelmes, Physical Review Letters **93**, 055501 (2004).

[132] S. Falconi, M. I. McMahon, L. F. Lundegaard, C. Hejny, R. J. Nelmes, and M. Hanfland, Physical Review B **73**, 319 (2006).

[133] E. E. McBride, K. A. Munro, G. W. Stinton, R. J. Husband, R. Briggs, H. P. Liermann, and M. I. McMahon, Physical Review B **91**, 144111 (2015).

[134] S. Merkel, N. Hilairet, and IUCr, Journal of Applied Crystallography **48**, 1307 (2015).

[135] A. Arakcheeva, M. Bykov, E. Bykova, L. Dubrovinsky, P. Pattison, V. Dmitriev, and G. Chapuis, IUCrJ **4**, 152 (2017).

[136] P. Li, G. Gao, Y. Wang, and Y. Ma, Journal of Physical Chemistry **114**, 21745 (2010).